SYNTHESIS AND CHARACTERIZATION OF PROTEIN TEMPLATED MULTIFUNCTIONAL NOBLE METAL QUANTUM CLUSTERS FOR BIOMEDICAL APPLICATIONS

A Thesis submitted

in partial fulfillment for the Degree of

Doctor of Philosophy

By

MEEGLE S. MATHEW

Department of Chemistry

Indian Institute of Space Science and Technology

(A Deemed to be University u/s 3 of the UGC Act 1956)

Department of Space, Government of India

Valiamala, Thiruvananthapuram-695 547

Kerala, India

June 2019

To my beloved parents, husband, brother and sisters

CERTIFICATE

This is to certify that the thesis entitled **Synthesis and Characterization of Protein Templated Multifunctional Noble Metal Quantum Clusters for Biomedical Applications** submitted by **Meegle S. Mathew** to the Indian Institute of Space Science and Technology Thiruvananthapuram, in partial fulfilment for the award of the degree of **Doctor of Philosophy** is a *bona fide* record of research work carried out by her under my supervision. The contents of this thesis, in full or in parts, have not been submitted to any other Institution or University for the award of any degree or diploma.

Prof. Kuruvilla Joseph
Supervisor
Senior Professor
Dean (SA, SW and O)
Department of Chemistry

Counter signature of the HOD with seal

Thiruvananthapuram
June 2019

DECLARATION

I declare that this thesis entitled **Synthesis and Characterization of Protein Templated Multifunctional Noble Metal Quantum Clusters for Biomedical Applications** submitted in partial fulfilment of the degree of **Doctor of Philosophy** is a record of original work carried out by me under the supervision of Prof. Kuruvilla Joseph Department of Chemistry, Indian Institute of Space Science and Technology, Thiruvanathapuram and has not formed the basis for the award of any other degree or diploma, in this or any other Institution or University. In keeping with the ethical practice of reporting scientific information, due acknowledgments have been made wherever the finding of others have been cited.

Meegle S. Mathew

SC13D021

Thiruvananthapuram

June 2019

ACKNOWLEDGEMENTS

The completion of Ph.D thesis would not have been possible without my close association with many people. It is a great opportunity to extend my sincere gratitude to all those people, who made this Ph.D. thesis possible and contributed in different ways.

First and foremost, I would like to extend my sincere and deepest gratitude to beloved supervisor Dr. Kuruvilla Joseph, Professor and Dean (S.A, S.W & O), Department of Chemistry, IIST for his excellent guidance, constant encouragement and introducing me to this exciting field of science by making critical suggestions, posing challenging questions. He has given a complete freedom to grow as a researcher. His endless patience in his busy schedule is remarkable. His extensive discussions during my work, understanding attitude, and personal attention provided the good and smooth basis for my research work. I am thankful for his devoted contribution in reviewing my progress, writing, making corrections to improve and finalize the research papers as well as the thesis. I have developed the attitude of independent thinking in his association, and build the confidence to pursue independent research. I feel extremely proud and satisfied with his research guidance.

I gratefully acknowledge Director, Dr. V. K. Dadhwal and former Director, Dr. K.S. Das Gupta, for providing good infrastructure facilities during the tenure of my work. I express my sincere thanks to Dr. Prabhakaran K, Head of the Department for the academic support. My sincere thanks to former Head of the Department, Dr. Nirmala Rachael James, Department of Chemistry for her continuous support and encouragement. I also gratefully acknowledge the financial assistance from IIST.

I owe my most sincere gratitude to all my doctoral committee members, Dr. K. Sreenivasan Dr. Shijumon M.M, Dr. Mahesh S, Dr. Seena V for their critical comments. The suggestions they have given during each evaluation are highly appreciated. A special mention of thanks to one of my doctoral committee

member Dr. K. Sreenivasan, who spend extra time for evaluation of work and thesis corrections. I also thank all faculty members of the Department of Chemistry for their valuable suggestion which enabled the successful completion of the research work.

I extend my heartfelt thanks to Dr. T. Pradeep, Professor, IIT Madras, who gave me permission to work in his laboratory for one month and use the facilities available there for the completion of work presented in Chapter 1. Working with his group is a great achievement in my career. I would like to thank Dr. Ananya Baksi for giving valuable suggestion and academic help. I would like to thank sincerely Dr. Saritha A, Mr. Sreekumaran Nair for their effort to correct my manuscript and thesis.

I would like to thank Dr. R. S. Jayasree, Scientist F, SCTIMST Thiruvananthapuram and Mr. Jayaram for providing facilities for the biological studies.

I extend my sincere thanks to internship students Joyal Davis, Kavya Vinod and Anoop Philip.

I would like to give a special thanks to my seniors Dr. Manjunath Ganiga and Dr. Raneesh Konnola for their guidance and moral support. I sincerely admire the contribution of all my labmates Dr. Mohammed Mukthar Ali, Dr. Narasimman Rajaraman, Dr. Jalaja K, Dr. Sarah Titus, Dr. Sarika P.R, Dr. Sujith Vijayan, Dr. Rakesh R, Reshma C, Aswathi R, Neema P.M, Praveen Wilson, Haritha H, Yogesh Choudhary, B.D.S Deeraj, Arya S. Nair, Saisree S., Varsha M. V, Sanu Xavier, Roymon Joseph, and Linsha V, for their help provided in the tenure of Ph.D. I must thank staff members Dileep Kumar, Jayasree L., Jayasree Dinesh, Rehana, Bindu P. C, Remya T., Loveson Albert and Soumya for helping me in every possible way. I would like to thank Librarian and other staff members of IIST Library for their help.

I deeply acknowledge IIT Madras, M.G University Kottayam, STIC CUSAT, Amrita Cochin, NIIST Thiruvananthapuram, HLL Lifecare R&D Centre Thiruvananthapuram, RGCB Thiruvananthapuram, and SCTIMST BMT wing

Thiruvananthapuram for the characterization studies. I would like to thank Gopinath Clinic Nedumangad for giving blood samples for analysis.

A special mention of thanks to my friends in IIST, Devi Renuka K., Resmi S. and Karthika S. for the support provided during this period and their help and friendship shall always be remembered.

I would like to thank all my teachers who have inspired me throughout these years.

I express my deepest gratitude towards my better half for his eternal support and understanding of my goals and ambitions. His unconditional love and support have always been my strength.

A special thanks to my loving brother who cared, loved like a father and supported me in various aspects. Without his unconditional support, I could not reach here. I thank my beloved parents, sisters or their love, prayers, and affection. I also thank my father-in- law, mother-in-law, brother- in-laws and sister-in-laws for their support. I thank my aunt Sr. Lilly Grace for the prayers and support given till now. I also extend my sincere gratitude to my other family members for their constant encouragement.

Last but not least, I would like to praise the grace of God whose blessings are marvelous which I am experiencing throughout my life.

(Meegle S. Mathew)

ABSTRACT

Noble metal quantum clusters (NMQC) are sub-nanometer core sized materials made up of several tens of atoms with distinct optical, electrical, and chemical properties compared to those of their larger counterparts viz. plasmonic nanoparticles. Synthesis of atomically precise noble metal quantum clusters using novel synthetic strategies is an emerging area of recent research. In the past decades, the synthesis of AuQCs was achieved using various templates like phosphine, thiols, peptides, amino acids, enzymes, dendrimers, DNA, and proteins. Among these, protein template-based synthesis of the cluster, in particular, Au, Ag and Cu with molecule like properties have exhibited considerable attention in different fundamental fields from chemistry and biology to biomaterials due to its excellent luminescence, outstanding biocompatibility, ultra small size, large stocks shift etc. The protein protected metal quantum clusters provide more attractive features such as one-pot and green synthetic method, good aqueous solubility, relatively low environmental impact, mild reaction conditions, excellent biocompatibility, and versatile surface chemistry. Thus protein stabilized QCs are superior over other conventional fluorescent probes such as semiconductor quantum dots, organic dyes and engineered fluorescent proteins, which face limitations like intrinsic toxicity in biological systems, high rate of photobleaching and relatively large size. The combination of unique optical and electronic properties of the metal quantum cluster together with the inherent biological properties of protein make NMQCs promising candidates for various biomedical applications like imaging, sensing, delivery, and therapeutics. In spite of the notable progress recently made in the utilization of these clusters in medicine, they have been suffering from low quantum yield, less pH stability, and face oxidative decomposition by reactive oxygen species, unstable at high temperature and the high cost of protein. We are addressing some of these challenges by introducing some new proteins for the synthesis of QCs. This thesis discusses the synthesis of three different protein stabilized NMQC, particularly, AuQC, AgQC, AuAgQC and CuQC, characterization, photophysical studies, surface modification and explores the application of these QC in biosensing, imaging, and delivery.

Surface functionalization of bovine serum albumin-stabilized gold quantum cluster (AuQC@BSA) by an enzyme, acetylcholinesterase (AChE) via non-covalent interaction provide the ability of selective detection of acetylcholine (ACh). ACh is a neurotransmitter and AChE is a specific enzyme for ACh degradation, found in central and peripheral nervous system. It is a biomarker for various neuropsychiatric and neuropsychological diseases such as Alzheimer's and Parkinson. Successful incorporation of AChE over Ach is proved by various spectroscopic techniques. Electrospray ionization mass spectrometric (ESI MS) analysis proves the retention of enzymatic activity of AChE after immobilization on the AuQC@BSA surface. The fluorescence quenching of AuQC@BSA-AChE occurred with increasing the concentration of ACh. The systematic fluorescence study shows that the hydrolyzed product of ACh, choline (Ch) is the reason for the fluorescence quenching. It is a positively charged quaternary ammonium salt generated in the medium which interact with negatively charged QC and in turn changes the environment of QC and quenches the fluorescence. The lowest value

detected by this method was found to be 10 nM and shows excellent selectivity. A paper-based sensor shows the possibility of naked eye detection for ACh.

Contrary to the protein derived from animals, plant proteins are the suitable candidates for the sustainable synthesis of QC owing to its low cost, natural abundance, high stability, and sustainability. Gluten, a complex protein derived from wheat, made up of hundreds of different proteins was used for the 'green' and 'one-pot' synthesis of AuQC. The major drawback of conventional protein stabilized QCs, oxidative decomposition by reactive oxygen species (ROS) is prevented by the synthesized AuQC@gluten, owing to the large complex nature of the protein. A 'turn-on' sensing of creatinine is possible by using AuQC@gluten with the assistance of picric acid (PA). PA acts as a fluorescence quencher and creatinine is recovered 60 % of quenched fluorescence. Creatinine is a biomarker for kidney diseases. The mechanism of interaction of QC with the analyte is systematically studied.

The low quantum yield of the QCs can reduce the sensitivity of sensors. AuAg Alloy QC shows enhanced stability and QY due to its synergetic interaction and the 'silver effect'. Gluten stabilized AgAuQC (AgAuQC@gluten) shows high stability in acidic to extremely basic pH and much higher QY than AuQC@gluten. The sensitive and selective detection of bilirubin is established using the synthesized AgAuQC@gluten through fluorescence quenching. Bilirubin is a biomarker for liver disorder. The spectroscopic investigation implies that the electron transfer and inner filter effect is the leading cause of fluorescence quenching.

Ratiometric sensing method is considered as a more sensitive method for the detection due to the monitoring of two emission wavelengths. The thesis also discusses the design of a novel strategy for the preparation of sustainable dual emitting nanohybrid for ratiometric detection of mercury Hg (II) ion. The dual emitting composite contains blue-green emitting graphene quantum dot (GQD) and red emitting AuQC, prepared using gluten as the raw material. The in-situ growth of AuQC in gluten functionalized GQD, produces a dual emitting composite (AuQC@GQD). A uniform distribution of AuQC@GQD on the surface of nanofibre by electrospinning technique is an added score in sensing. A rapid visual detection of Hg (II) using the electrospun mat shows the practicality of the developed sensor.

Fabrication of polymer-QC composite is not much explored due to its less stability in the preparation conditions. The melt mixing of polyurethane and CuQC@gluten at 80 ^{o}C provides a complete dispersion of CuQC in the polymer matrix. The release of Cu(II) ion from CuQC-PU matrix at physiological condition leads to the utilization of this composite towards the fabrication of the intrauterine device for contraceptive applications since the action of Cu (II) ion in the uterus prevents the fertilization process. The proposed method can overcome the drawbacks of conventional intrauterine devices (CuT), such as bleeding in the initial days due to burst release of Cu (II) ion.

The biocompatible protein stabilized AuQC can act as a scaffold as well as a tracking agent for drug delivery applications. Curcumin (CUR) is an anticancer

hydrophobic drug, the poor aqueous solubility and rapid degradation limits its use in cancer therapy. A 99.8 % encapsulation of CUR in gliadin stabilized AuQC (AuQC@gliadin) is possible by simple mixing. The bioavailability of CUR can be enhanced by this strategy. It prevents the rapid degradation of CUR at physiological and alkaline pH condition. Photophysical properties of CUR are enhanced in aqueous solution of AuQC@gliadin. Folic acid (FA) conjugated AuQC@gliadin-CUR shows the targeted release of CUR in the cancer cell, without affecting the normal cell. Thus the protein stabilized AuQCs not only act as an encapsulating agent but also endows high aqueous stability and intense luminescence so that it can be used to track the delivery of CUR into cells.

TABLE OF CONTENTS

LIST OF TABLES

LIST OF FIGURES

ABBREVIATIONS

ACh	Acetylcholine
AChE	Acetylcholinesterase
Ala	Alanine
AuQC@BSA	Bovine Serum Albumin Stabilized Gold Quantum Cluster
BSA	Bovine Serum Albumin
CD	Circular Dichroism
CD	Carbon Dot
Ch	Choline
Chole	Cholesterol
CIE	Commission Internationale de l'eclairage
CNT	Carbon Nanotube
CUR	Curcumin
Cys	Cysteine
EDS	Energy-Dispersive X-ray Spectroscopy
EE	Encapsulation Efficiency
ESI MS	Electrospray Ionization Mass Spectrometry
ESIPT	Excited State Intramolecular Proton Transfer
FA	Folic acid
FRET	Fluorescence Resonance Energy Transfer
Fruct	Fructose
FTIR	Fourier-Transfer Infrared Spectroscopy
GA	Glutaraldehyde
GER	Galvanic Exchange Reaction
Glu	Glucose
Gly	Glycine
GO	Graphene Oxide
GQD	Graphene Quantum Dot
GSH	Glutathione

HCys	Homocysteine
HRP	Horseradish Peroxide
HRTEM	High Resolution Transmission Electron Microscope
HSA	Human Serum Albumin
IFE	Inner Filter Effect
IUD	Intrauterine Device
Lact	Lactose
LDPE	Low Density Polyethylene
Lf	Lactoferrin
Lys	Lysine
Lyz	Lysozyme
MALDI TOF MS	Matrix Assisted Laser Desorption/Ionization Time-Of-Flight Mass Spectrometry
MPC	Monolayer Protected Cluster
NC	Nanocluster
NIR	Near InfraRed
NMQC	Noble Metal Quantum Custer
NP	Nanoparticle
PA	Picric Acid
PET	Photo Induced Electron Transfer
PL	Photoluminescence
Prol	Proline
PU	Polyurethane
PVA	Polyvinyl Alcohol
QC	Quantum Cluster
QD	Quantum Dot
QY	Quantum Yield
ROS	Reactive Oxygen Species
RSD	Relative Standard Deviation
SAED	Selected Area Electron Diffraction
SEM	Scanning Electron Microscope
Ser	Serine

SHE	Standard Hydrogen Electrode
SPR	Surface Plasmon Resonance
SUS	Simulated Uterine Solution
TCSPC	Time Correlated Single Photon Counting
TGA	Thermo Gravimetric Analysis
Tyr	Tyrosine
Val	Valanine
XPS	X-ray Photoelectron Spectroscopy
XRD	X-ray Diffraction Analysis

NOTATIONS

χ^2	chi-square
C	Concentration
F	Fluorescence intensity
I/F	Intensity
τ	Lifetime
ns	Nanosecond
Φ	Quantum yield
η	Refractive index
K	Slope
σ	Standard deviation
T	Temperature
t	Time
λ	Wavelength

CHAPTER 1

INTRODUCTION

This chapter briefly summarises the general features of protein stabilized noble metal quantum clusters (NMQCs), advantages of protein stabilized NMQCs, over other protecting QCs. The various synthetic strategies applied for the preparation of protein protected fluorescent NMQCs and the characterization methods employed to study these systems are discussed. The novel physical, chemical and optical properties and their potential applications in the biomedical field including, biosensing, imaging, delivery, and therapy has been discussed. At the end of this chapter, the motivation and objectives of the research work, the organization of the whole thesis and a brief outline of each chapter is provided.

1.1. Fluorescent metal quantum cluster

Functional nanomaterials are considered as versatile nanomaterials owing to their intrinsically different features from bulk materials. Their unique optical and electronic properties are exploited in various areas such as biomedical, electronics and photovoltaic (Cheng *et al.*, 2014; Dwivedi *et al.*, 2015; Liu *et al.*, 2018) . Among the functional nanomaterials, the fluorescent materials have received vast attention in the field of bio-nanotechnology, due to their unique and fascinating optical and functional properties. Particularly, atomically precise molecules of fluorescent noble metal quantum clusters (NMQC) with quantum confinement effect have been the most attracting materials of contemporary material science.

NMQCs are sub-nanometre core sized clusters composed of several tens of metal atoms. The size of QCs is in the range of 1-2 nm (Lu & Chen, 2012; Mathew & Pradeep, 2014). Thus it is considered as a missing link between atoms or molecules and the nanoparticles. Therefore, the properties of metal quantum clusters are entirely different from nanoparticles (NP) or bulky metals. The metal nanoparticles exhibit surface plasmon resonance (SPR) due to scattering of electrons at the surface of the particle, where the size of the NP is comparable to or smaller than the electron mean free path (Qian *et al.*, 2012). Whereas in the case of NMQCs, the ultrasmall size is comparable with the Fermi wavelength of conduction electrons in metal (e.g., Fermi energy of Au 5.53 eV and Ag-5.49 eV, and for Cu- 7 eV) which leads to the splitting of continuous density of states into discrete energy levels and exhibit molecule like optical features such as optical absorption and luminescence in the UV-Vis to near IR (NIR) region. Figure 1.1 shows the major optical phenomenon of NP and QC (Chakraborty & Pradeep, 2017; Hu. *et al.*, 2015; Mathew & Pradeep, 2014).

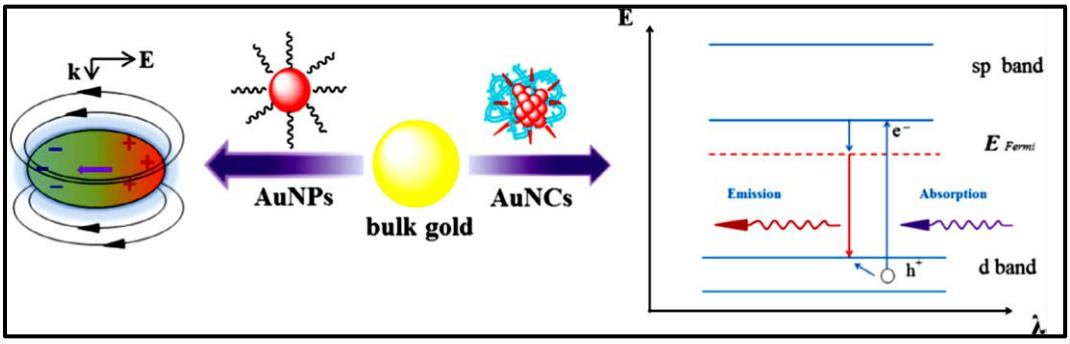

Figure 1.1. Schematic representation of surface plasmon resonance from gold nanoparticle (AuNP) and energy splitting of fluorescent AuQC (Cui *et al.*, 2014).

The metal quantum cluster is also named as nanoclusters (NCs), monolayer protected clusters (MPCs) etc. We are using the term as 'metal quantum clusters (MQCs)' throughout this thesis. The widely studied NMQCs are gold quantum cluster (AuQCs), silver quantum cluster (AgQCs) and copper quantum clusters (CuQCs).

Compared with other conventional fluorescent nanomaterials, such as semiconductor quantum dots (QDs), iron oxide nanoparticle (Fe_3O_4), dye-doped nanoparticles, silica nanoparticle, upconverting NPs, the fluorescent NMQCs have following notable advantages, particularly applicable for biomedical applications (Jiang *et al.*, 2018).

1. NMQCs are composed of elements with low toxicity or even no toxicity, providing excellent biocompatibility.
2. Good chemical stability of QCs due to their inert nature and they exhibit extraordinary photostability.
3. Ultrasmall sizes of QCs make them suitable candidates for biolabeling, without disturbing the functions of the to-be-labeled bio-entities and also, the ultrasmall sizes enable them to be easily drained out after in vivo treatment.
4. The fluorescent emissions can be tuned from UV-Vis to NIR by monitoring the size and composition of the MQCs.

Owing to these fascinating features, the QCs are exploited in the field of medicine and biology (Bhattacharyya & Mukherjee, 2018; Tao *et al.*, 2015).

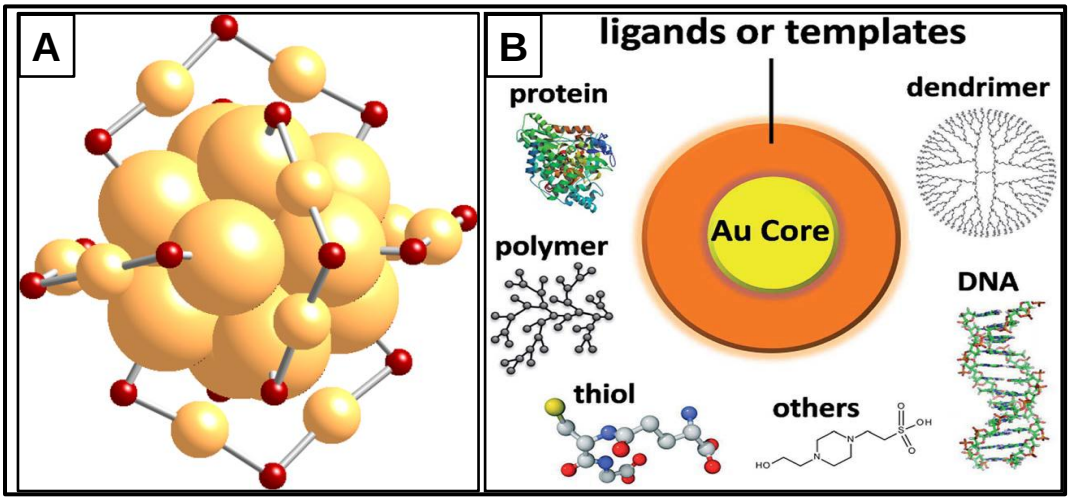

Figure 1.2. The schematic illustration of the core and shell-like structure of AuQC and the conventional ligand or template used for the synthesis of QC (Chevrier *et al.*, 2012).

The structures of fluorescent NMQCs have been extensively studied and various structures have been proposed, which depends on the number of atoms present in the cluster. The most studied QCs are $Au_{25}(SR)_{18,}$ $Au_{102}(SR)_{44}$, and $Au_{38}(SR)_{24}$, and the structure of these QCs are typically core and shell-like structures (Figure 1.2A) (Yu *et al.*, 2015). The core is made up of several tens of metal atom and the shell consist of -S(R)-[Au-S(R)-]$_X$ oligomers of different lengths (x = 1 and 2. This oligomer motif arises from the ligands used for stabilizing QCs (Mathew & Pradeep, 2014). The conventional ligand used to stabilize the QCs are phosphine, small thiol molecules such as glutathione, mercaptopropionic acid (MPA) etc. or bulky molecules like polymers, proteins, DNA, dendrimers etc (Mathew & Pradeep, 2014) (Figure 1.2B). These protecting ligands or templates play a key role in providing stability to the QCs and are also related to the origin of photoluminescence (PL). The QCs with different ligands exhibit different features, even though, it has the same number of metal atoms or similar core size. Based on the type of ligand used for protection/stabilization, the QCs are named as thiolated protected cluster, polymer/dendrimers protected cluster, DNA protected cluster and protein/peptide protected cluster etc (Cantelli

et al., 2016; Chen *et al.*, 2016; Zheng *et al.*, 2007). The following section discusses on the choice of ligands used for the synthesis of QCs.

1.2. Stabilizing/protecting ligands for NMQC synthesis

The cluster science starts from gas phase clusters, where the metal clusters are formed by evaporation and it is unprotected. Thus it will become very reactive and form a larger sized particle or structure (Xavier *et al.*, 2012c). In this case, the possibility of uncontrolled growth and formation of the larger sized metal nanoparticles cannot be ruled out. Thus the selection of ligand is a crucial step in the controlled synthesis of the NMQCs. The first ligand choosen for the synthesis of NMQC was phosphine due to its high affinity towards metal ions. Example for phosphine protected MQCs are $Au_{24}(PPh_3)_{10}(SC_2H_4Ph_5)Cl_2^+$, $[Au_{20}(PPhPy_2)_{10},Cl_4]Cl_2$ (Pradeep *et al.*, 2014a; Xavier *et al.*, 2012c). Followed by phosphine stabilized cluster, various thiol stabilized QCs were reported due to the comparatively high affinity of sulfur towards metal ion. The organic thiols have been used for stabilizing the QCs are hexane thiol, octane thiol, phenyl ethanethiol (PET), dodecanethiol, tertiary butyl benzyl mercaptan, etc (Pradeep *et al.*, 2014a; Xavier *et al.*, 2012b). Due to the insolubility of organic thiol stabilized QCs in an aqueous medium, water-soluble thiols were introduced to synthesize the QCs. Whetten and his group first introduced glutathione (GSH) as a capping agent for the synthesis of water-soluble QCs (Schaaff *et al.*, 1998). After his pioneer work, a series of research was carried out to understand the structure and properties of GSH stabilized QCs (Negishi *et al.*, 2004; Negishi *et al.*, 2005). Other water-soluble thiol stabilized QCs are mercaptopropionic acid (MSA), penicillamine and captopril protected clusters (Cathcart & Kitaev, 2010; Nishida *et al.*, 2007). Thereafter a new window of opportunity has opened up for the formation of the quantum cluster using the macromolecular template. In this category, macromolecules such as various DNA, dendrimers, and polymers have been used for cluster stabilization and protection (Sun *et al.*, 2003; Chen., *et al.*, 2012; Pandya *et al.*, 2016). New entity to this interesting group is the protein and

peptide protected clusters (NMQC@Protein) (Goswami *et al.*, 2014a; Xie *et al.*, 2009). The NMQCs@protein also belong to the category of thiolated metal clusters because here the metallic cores are protected through thiols containing highly folded proteins. The schematic representation of the recent trend in the synthesis of QCs is shown in Figure 1.3.

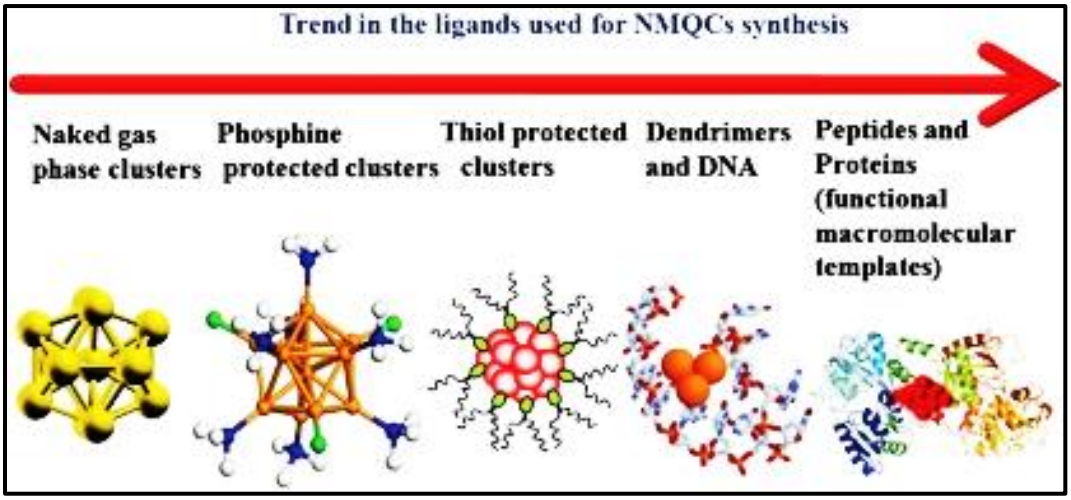

Figure 1.3. Schematic illustration of trends in the ligand used for the synthesis of NMQC (Xavier *et al.*, 2012c).

The protein stabilized QCs are considered as a more suitable candidate for biological imaging and sensing applications by considering its high advantage over other organic molecule protected clusters. The major advantages of QCs@proteins are good aqueous solubility, excellent biocompatibility, green and one-pot synthetic strategy, rich surface chemistry for functionalization, and distinctive molecular structures for specific bio-recognition. Further, the biogenic shell of the QCs formed by proteins can provide good colloidal stability and solubility in biological medium. Moreover, compared to other monolayer protected QCs, protein-stabilized NMQCs have several folds of enhanced luminescence (Chevrier *et al.*, 2012; Xavier *et al.*, 2012c). The detailed investigation of the synthesis, properties, characterization, and its major biomedical applications are discussed in the following sections.

1.3. Protein protected NMQC-Synthesis

Proteins are macromolecules, composed of 20 different amino acids connected through peptide bonds. It is having a different structure in which primary structure is held together by peptide bonds, the secondary structure formed through hydrogen bonds between main chain peptide group, three-dimensional tertiary structure formed by folding of α-helixes and β-sheets. Quaternary structure through a combination of different protein subunits (Goswami *et al.*, 2014a).

The protein stabilized AuQCs synthesized through the biomineralisation process was first reported by Xie et al in 2009 (Xie *et al.*, 2009). Biomineralisation is a natural process that takes place in biological organisms, which intake metal ions to produce minerals (Yang., *et al.*, 2017). In this case, the AuQCs formed without the use of external reducing agent and the protein itself acts as a protecting and stabilizing agent. Xie et al used bovine serum albumin (BSA) as a template for this one-pot synthesis of AuQC. Figure 1.4 shows the schematic illustration of the synthesis of AuQC@BSA. The synthesis was carried out by simple mixing of Au^{3+} ion and protein at alkaline pH at 37 ºC. It is reported that at alkaline pH, the aromatic amino acid can donate electrons to reduce Au ions and the broken disulfide can bind to Au and stabilize the cluster core and prevent further growth (Pradeep *et al.*, 2014a). The reducing capability of BSA is originated from the tyrosine and tryptophan amino acid in BSA at alkaline pH. The cysteine residues of BSA can bind and stabilize the resultant AuQC through Au–S bonding. BSA is having 35 cysteine groups. It has been also shown that histidine residue in the protein can facilitate the nucleation of gold atoms to form clusters inside the protein (Chaudhari *et al.*, 2011). The MALDI-TOF MS data confirm that BSA protected Au QCs consisting of 25 gold atoms and cluster is named as Au_{25}@BSA. It exhibits intense red emission centered at 640 nm when excited at 480 nm. The quantum yield (QY) of the as formed AuQC@BSA was moderately high (6%). The small amount of Au(I) (~17%) present on the surface

of the Au core in AuQC@BSA helps to stabilize the QCs. Moreover, the optical property of Au@BSA was found to be stable at physiological temperature and pH (Xie *et al.*, 2009). This synthetic strategy is considered as a 'green' and 'sustainable' due to its low environmental impact during synthesis, mild reaction conditions, aqueous solubility and formation of QC without the use of strong reducing agents.

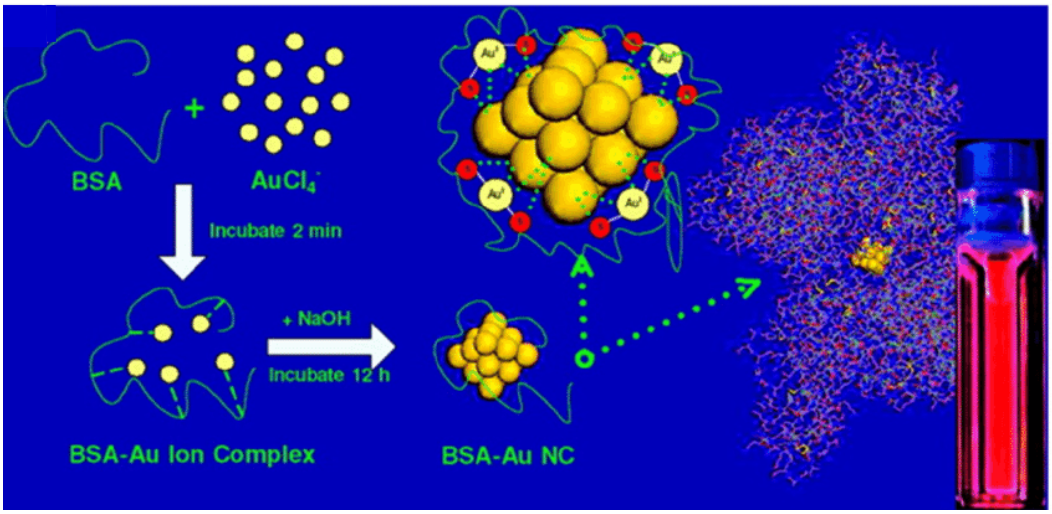

Figure 1.4. Schematic illustration of the formation of BSA stabilized fluorescent AuQC (AuQC@BSA) (Xie *et al.*, 2009).

Subsequently this synthetic strategy has been adopted to synthesize various fluorescent NMQCs using other proteins, such as lysozyme (Lyz), insulin, apoferritin, ovalbumin, lactoferrin (Lf), pepsin, human serum albumin (HSA) ribonuclease A, horseradish peroxidase, bovine pancreatic ribonuclease-A, chymotrypsin, as a protecting/stabilizing agent (Chan & Chen, 2012b; Kawasaki *et al.*, 2011; Kong *et al.*, 2013; Lin & Tseng, 2010a; Liu *et al.*, 2014; Liu *et al.*, 2011; Shamsipur *et al.*, 2015; Shi *et al.*, 2015; Wen *et al.*, 2011a; Xavier *et al.*, 2010). This exposes the flexibility of this system and each protein can behave differently and produce unique clusters. One of the important criteria for choosing proteins for synthesizing the clusters is the presence of sulfur-containing the amino acid (Eg., cysteine (Cys)) and aromatic amino acid in the protein. Kawasaki et al studied the effect of pH on the reducing ability of amino acids present in the protein to synthesize AuQC. They used pepsin as the template for

the AuQC formation and it produces multi-color emission at different pH values. The blue luminescence arises form Au_5@pepsin and Au_8@pepsin, green emission arises from Au_{13}@pepsin and red emissions from Au_{25}@pepsin. The generation of different core sized QC is due to the reducing ability of various amino acids at different pH conditions. At alkaline pH (pH 12), tyrosine residue present in pepsin reduces Au^{3+} and produce red emitting AuQC. At acidic pH, aspartic acid reduces Au^{3+} and form green emitting AuQC. At pH 9, blue emitting AuQC are formed after prolonged reaction time, which is also due to the reducing ability of acidic amino acids in the pepsin (Kawasaki *et al.*, 2011).

Another advantage of protein stabilized metal QC is the retention of biological functions of protein after the formation of QCs. For example, Liu et al. have shown the growth of AuQC in solution and also in insulin crystals. They have proven that the AuQC@insulin retained the intrinsic bioactivity of the insulin (Liu *et al.*, 2011). Similarly, the enzyme activity of horseradish peroxide (HRP) enzyme was retained after the formation of AuQC@HRP, which has been further exploited for the detection of hydrogen peroxide (Wen *et al.*, 2011b).

Recently scientists have given more focus on plant protein directed synthesis of fluorescent metal QCs. Unlike the proteins derived from animals and insects (BSA, HSA, Lyz, Lf, chitosan etc), the proteins derived from plants have specific advantages such as natural abundance, sustainability, high accessibility, and cost-effectiveness. Li et al selected pea protein isolate (PPI) as a protein to synthesize AuQCs. (Li., *et al.*, 2018). The major protein derived from animal and plant used for the synthesis of QCs are shown in Figure 1.5.

The protein stabilized AuQCs were also synthesized by the assistance of microwave irradiation (MWI) (Yan *et al.*, 2012; Zheng *et al.*, 2015). Yue et al synthesized the BSA protected AuQC using microwave irradiation. The red emitting Au_{16}QC@BSA was prepared by treating BSA and $HAuCl_4$ under basic conditions (pH 12) at 37˚C and irradiated MW for 6 hours. They have proven that compared to the ormal heating method, the MWI assisted synthesis can produce smaller sized QC. The another advantage of MWI assisted synthesis is the fast

reaction without the ssistance of high temperatures or high pressures (Yue *et al.*, 2012).

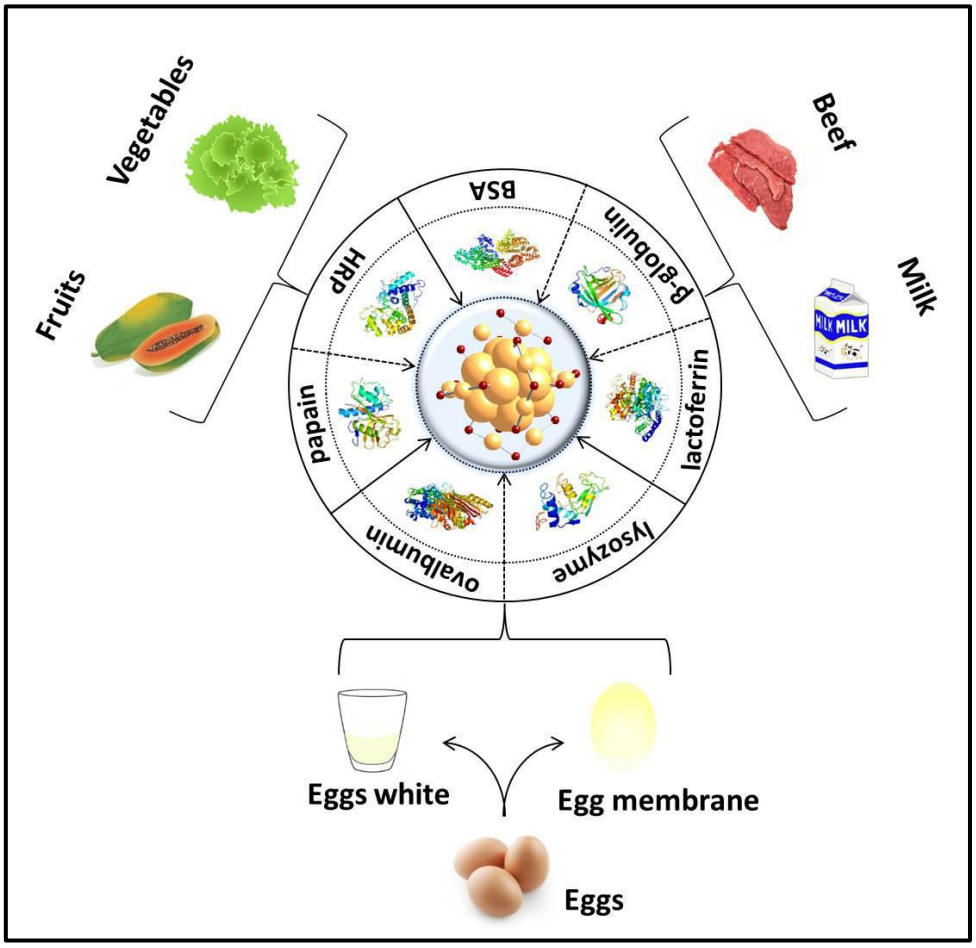

Figure 1.5. Schematic representation for the preparation of metal QC using various proteins derived from animals and plants (Li, *et al.*, 2018).

In another case, the metal QCs were synthesized on a solid platform, such as on hair fiber, eggshell membrane (ESM) etc, which enable a new strategy for the synthesis of stable QC. Shao et al. synthesized fluorescent Au QC and Ag QC using ESM as a solid template since ESM is a cysteine-rich protein. The freshly stripped membrane from egg-shell is soaked and treated with $HAuCl_4$ or $AgNO_3$ solution followed by incubation with a reducing agent ($NaBH_4$) to produce intense emitting AgQC and AuQC (Shao *et al.*, 2011). Haveli et al. demonstrated the synthesis luminescent AuQC on hair fiber as the solid platform (Haveli *et al.*, 2012).

In certain cases, protein protected AuQCs were synthesized by the assistance of mild reducing agent such as ascorbic acid. In 2011, Xavier et al. reported the synthesis of human apo-transferrin stabilized AuQCs by using ascorbic acid as a reducing agent. Usually, the use of reducing agents for the protein directed synthesis of QCs is avoided to improve the biocompatibility and retain the native protein structure. Here, ascorbic acid was added to support the reduction of gold ions with a small amount of protein. The excessive use of costly protein can be avoided by this strategy (Xavier Le *et al.*, 2011).

Another accepted strategy used for the synthesis of metal QC is core etching, which is a top-down method. In this approach, the highly fluorescent MQCs are formed from larger sized metal nanoparticles or metal QCs with the assistance of another thiol containing ligands, which dissociate the large particle into smaller ones. Muhammed et al reported the synthesis BSA protected AuQCs from MSA-capped AuNPs via core etching. Here AuNP@MSA are taken as the precursor for the synthesis of QCs and BSA used as the etching agent. The BSA etched the surface atoms of nanoparticles and form intense emitting AuQC@BSA with sub-nanometre core size (Muhammed *et al.*, 2009).

1.3.1. General strategies for synthesis of bimetallic/alloy QCs

Other than monometallic QCs, bimetallic QCs emerged as a new class in noble metal QCs (AuAgQC, AuCuQC, AuPt QC, etc). Moreover, it exhibits enhanced optical features than monometallic QCs because, the integration of two metal species with its unique property in a single cluster. The bimetallic QCs provide more quantum yield than monometallic cluster due to the synergistic effects. It can be prepared with two strategies, which are co-reduction and post-treatment methods. In co-reduction, simultaneous reduction of two metal ions can take place in the presence of single protecting ligand (Figure 1.6 a). Post-treatment method progress via a two-step process. The first step involves the preparation of precursor/intermediate such as monometallic particle or larger sized QC. In the second step, post-treatment of the precursors/intermediates by incorporating a second metal ion or etching of mono-MQCs/MNPs intermediates

provide bimetallic QC. This can take place via galvanic replacement, anti-galvanic replacement, thiol-etching, and re-organization process (Figure 1.6 b) (Yuan *et al.*, 2015). Both strategies have been applied for the synthesis of protein stabilized bi-metallic QCs.

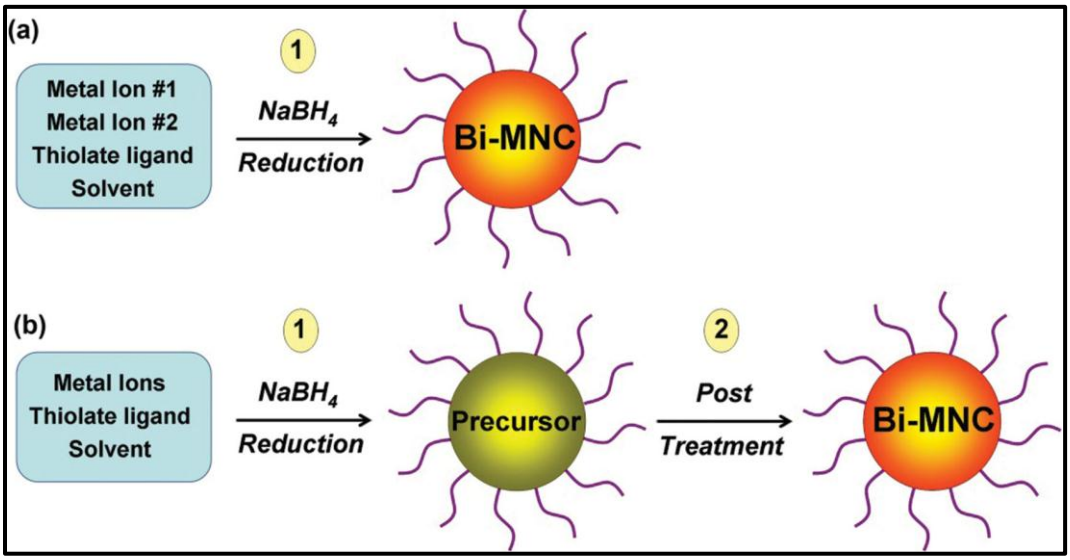

Figure 1.6. Schematic illustration of the general strategies involved in the synthesis of bimetallic QCs (Yuan *et al.*, 2015).

1.3.2. Formation mechanism of NMQC@Protein

Though the cluster is formed in a protein template via the biomineralization process, the actual mechanism behind the biomineralization is not yet clear. The proposed mechanism for cluster formation by biomineralization is that, when protein interacts with Au3+, it unfolds and accommodates the Au ions inside. Then at alkaline pH condition, the breakage of disulfide bonds occurs and it will bind to Au via Au-S linkage. Thus the secondary structure of the protein will change after cluster formation (Baksi et al., 2015). Pradeep and co-wokers systematically investigated the evolution of QC in protein by XPS and MALDI TOF analysis. They have proven that the cluster formation takes place via a two-step process. In the first step, upon the addition of protein to Au3+ ion, an Au1+-protein adduct will form and in the second stage, at alkaline pH, rearrangement and nucleation of protein lead to the formation of intense emitting AuQC.

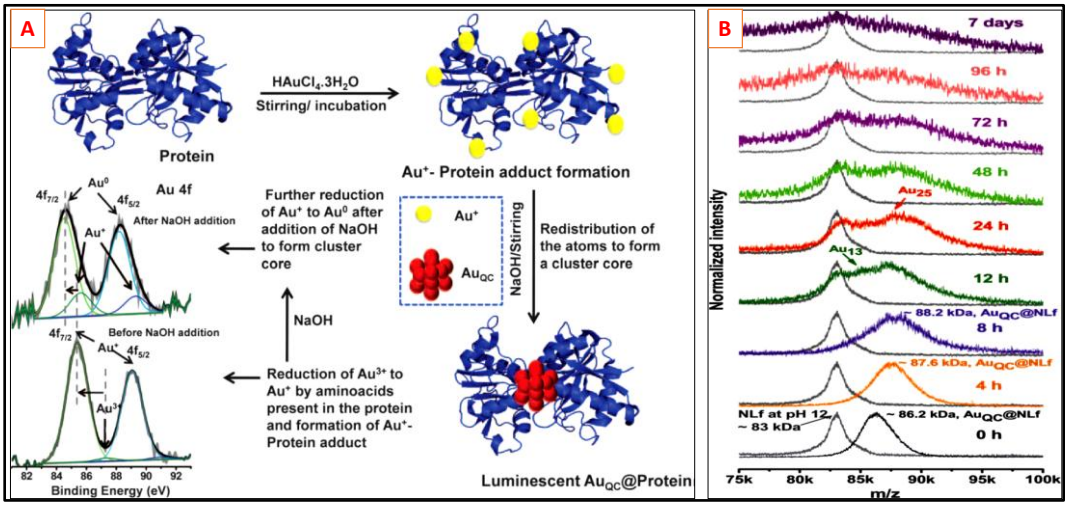

Figure 1.7. (A) The general scheme for the formation mechanism for the fluorescent AuQC@protein. (B) MALDI MS data of AuQC@NLf at different time interval (Pradeep *et al.*, 2014b).

The XPS data of each stage proven the presence of Au(I) in the Au^{1+}-protein adduct and Au (0) in AuQC formation (Figure 1.7 A). They have monitored the growth of clusters at the different composition of Au^{3+} and native lactoferrin (NL) by using MALDI TOF MS analysis. After the addition of Au ions to Lf, an immediate uptake of Au^{3+} by NL was observed at a pH of 4–5, and Au^{3+} is reduced to Au^{1+} and form Au^{1+}–Lf conjugate. Parent Lactoferrin alone shows a broad peak at m/z 83 kDa in mass spectra. The mass spectra of Au^{1+}–Lf conjugates shows a peak around 86.2 kDa, which corresponds to 16 Au atoms attached to the Lf. At alkaline pH (pH= 12.4), the aromatic amino acids will further reduce Au^{1+} to Au^{0} and disulfide bonds are broken and stabilize the cluster core through Au-S linkage. During the initial 4 hours of incubation, the cluster core was developed and it starts emitting under UV light. The mass spectra shows a shift in peak from 86.2 kDa to 87.6 kDa after 4 hours of incubation, corresponding to $Au_{22–23}$@NLf. After 12 hours of incubation, the mass peak corresponding to Au_{13} appeared along with re-emergence of free protein. After 25 hours, Au_{25}@NLf was observed and after 48 hours there was no change in the spectrum and it also remains the same after 7 days (Figure 1.7 B). They proposed that the emergence of free protein in-between cluster synthesis is due to the redistribution or inter-protein transfer of gold ions (Chaudhari *et al.*, 2011). Baksi

et al further proven the same mechanism using combined small angle X-ray scattering and mass spectrometric (MS-SAXS) study (Baksi *et al.*, 2015).

Xu et al. have systematically investigated the role of protein and amino acid content on the protein for the formation and fluorescent properties of the AuQC. They have used four model proteins viz BSA, lysozyme, trypsin, and pepsin and showed that the balance between the amine and tyrosine/tryptophan residues in the protein is the major critical factor for the formation of AuQCs. For example, pepsin with a few amine-containing residues and higher amount of tyrosine/tryptophan residue was not able to produce AuQC, whereas AuNPs could be formed. Moreover, protein having lesser cysteine residue causes blue shifts in the fluorescent emission of the AuQCs (Xu *et al.*, 2014).

1.3.3. Common purification strategies of NMQC@Protein

Different strategies were employed to purify the protein protected metal QCs. The most common method of purification is dialysis. Dialysis is a separation technique used for removing small or unwanted compounds from macromolecules in solution. The process takes place via selective and passive diffusion through a semi-permeable membrane (Luo *et al.*, 2011). It depends on the size of the protein and the molecular weight cut off of the membrane used to dialyze. Protein stabilized MQCs with a molecular weight larger than the membrane-pores are retained inside the membrane, whereas other small molecules and salts passed freely through the membrane. Thus changing of the dialysate medium with different time intervals aids the complete removal of unwanted molecules. Therefore this method can be used for the removal of small contaminants within protein stabilized QCs in the solution phase. BSA protected metal QCs has been purified by various researchers using a dialysis membrane with a molecular weight cut off 12 kDa (Durgadas *et al.*, 2011; Habeeb Muhammed *et al.*, 2010).

Another method of purification is the precipitation method. Recently, Guan and co-workers have developed co-precipitation method for isolating BSA-protected Au_{25} clusters from free BSA (Figure 1.8) (Guan *et al.*, 2014).

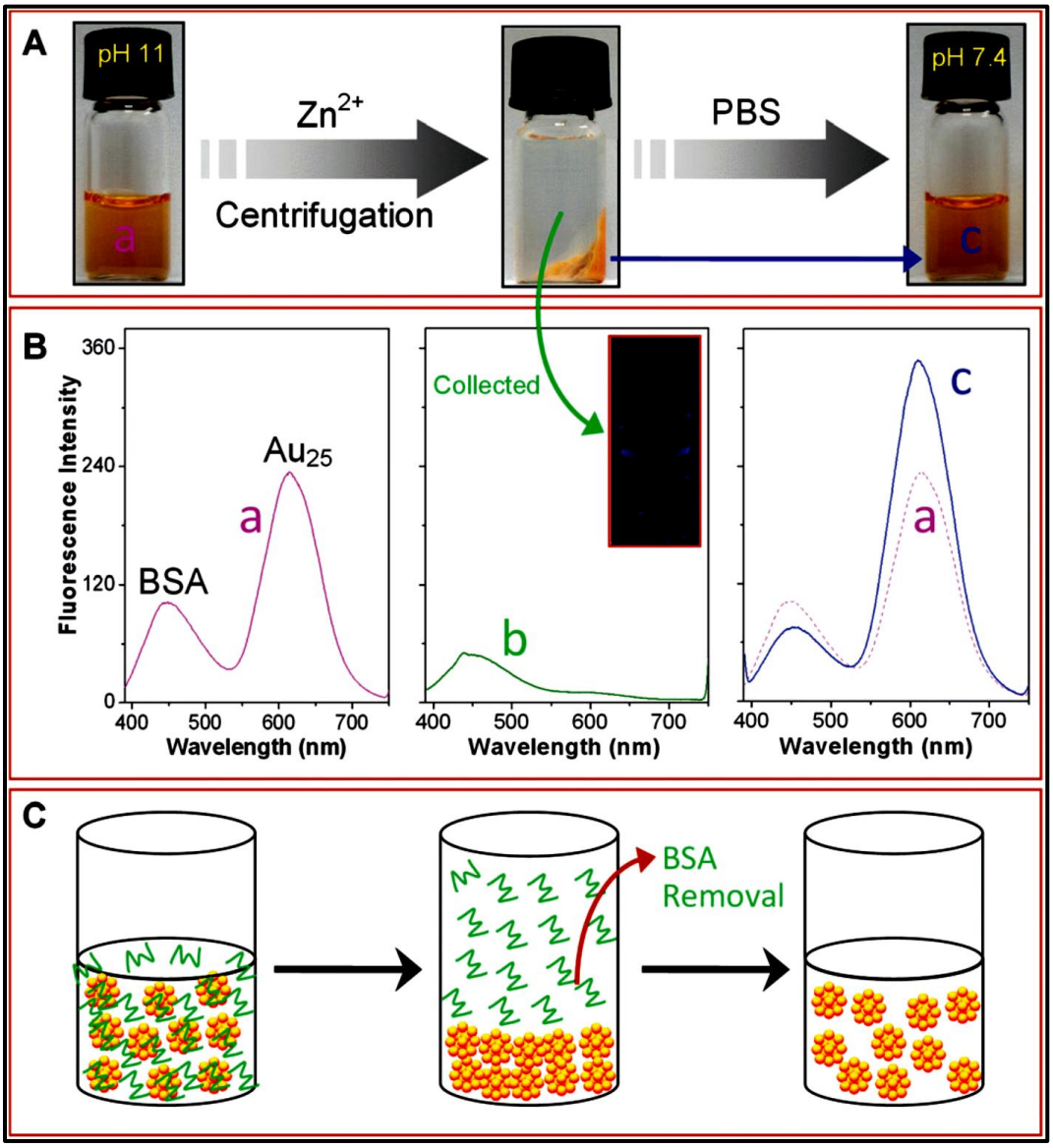

Figure 1.8. Purification strategy by co-precipitation method. (A) and (B) shows the photographs of QC and fluorescence emission spectra of QC during the purification by the addition of Zn^{2+}. (C) Schematic illustration of the purification of AuQC (Guan *et al.*, 2014).

Au_{25}@BSA clusters precipitated out by addition of Zn^{2+} solution at pH 11. The precipitate was collected by centrifugation and washed with distilled water followed by re-dispersion into PBS buffer (pH = 7.4) to form a transparent solution of clusters with intense emission. They proposed the mechanism of precipitation in such a way that, upon the addition of Zn^{2+} at extremely high pH, the OH group present on the surface of Au^{+} can strongly interact with Zn^{2+} to

form zinc hydroxide, leading to the precipitation of clusters. This was further confirmed by density functional theory (DFT) study.

Xiong et al. purified the BSA protected AuQC by precipitation method under acidic conditions (Xiong *et al.*, 2017). They have treated AuQC@BSA with acetic acid and the grey precipitate formed was centrifuged, washed and re-dispersed into basic media to yield the purified AuQCs. They proposed that in acidic media, the protective ability of BSA was lost due to conformation changes of BSA and AuQCs quickly aggregates to form larger sized AuNPs. Then at basic pH, the protective ability was recovered by changing the conformation of BSA.

1.3.4. General properties and characterization methods

The unique optical and electronic properties of metal QCs are strongly dependent on their size, structure, composition, and protecting ligand on the cluster. Various experimental techniques have been applied to the structural investigation of metal QCs. The protein stabilized metal QCs are generally characterized by UV-Vis absorption spectroscopy, Fluorescence, MALDI TOF MS, TEM, FTIR, CD, and XPS methods.

1.3.4.1. Photophysical properties

Optical absorption

The optical properties of NMQCs are entirely different from metal NPs. In the case of the metal NPs, the SPR is the major optical property which is mainly used for bio-sensing applications. The SPR is the collective oscillations of electrons in the particle surface after excitation by light. When the particle size reduces further to ~2 nm, this smaller particle behave like molecules and show strong quantum confinement, which leads to the discretization of energy states (Shang *et al.*, 2011). Thus the SPR band of AuNP at ~520 nm get diminished when size reduces below 2 nm. In the UV-Vis absorption spectra of QC, the absence of the surface plasmon resonance is the direct indication of the formation of sub-nanometre core sized AuQC. The absorption bands of metal QCs is

dependent on ligand and metal core size. The protein protected metal QCs exhibit a featureless absorption spectrum with a peak nearly at 280 nm due to the absorption of aromatic amino acids of the protein. In addition, a small hump was observed around 350 nm which is attributed to oxidized aromatic amino acid residues of protein (Mathew *et al.*, 2016; Mathew & Joseph, 2017).

Photoluminescence emission and excitation

The size-tunable photoluminescence is the one of the unique optical properties of metal QC. Most of the reported QCs@protein are red emissive in nature. Generally, the fluorescence emission spectra of QCs have two emission maxima, when excited at 365- 400 nm range. One near at 450 nm which is attributed to emission from protein and another NIR emission centered around 630–690 nm, arises from cluster core, which mainly depends on the core and the protein. Another case, small-sized QC exhibit only one emission maxima, for example, Au_8 cluster have emission maxima around 450 nm and they are blue emissive. The fluorescence of quantum clusters arises due to the molecular like transitions between HOMO-LUMO energies. Moreover, generally, the protein stabilized QCs exhibit two excitations (nearly 365 nm and 500 nm), which are attributed to the multiple electronic transitions in noble metal quantum clusters (Mathew *et al.*, 2016; Mathew & Joseph., 2017). A detailed explanation of the origin of photoluminescence is discussed in section 1.3.5.

Quantum yield and lifetime

Quantum yield (QY) of a fluorophore is defined as the ratio of a number of emitted photons to the number of absorbed photons (Sommer *et al.*, 2015). The protein stabilized QCs are having a comparatively good quantum yield (QY). The QY of the quantum cluster is varied by different factors, such as the protein template which used for stabilization, mode of synthesis and core size of the QC. The QY of a few QCs with different size and stabilization are given as follows. The Au_{25}@BSA provides 6 % (Xie *et al.*, 2009), Au38@BSA having 6.8 % (Mohanty *et al.*, 2012a), AuQCs@Lf produce 6% (Xavier *et al.*, 2010) and AuQCs@Lyz shows 15% (Baksi *et al.*, 2013) of QYs.

The lifetime of the excited state of the fluorophore is defined as the average time the fluorophore molecule spends in the excited state prior to return to the ground state (Lakowicz, 2013). The lifetime is also an important factor to understand about the structure of QCs since it measures the time available for the QCs to interact with or diffuse in its environment. Usually, decay profile of protein stabilized QCs is fitted by multiexponential and exhibit a fast component with few tens of picoseconds and several slow components of nanoseconds. The lifetime data of a few QC@protein are given below. The AuQCs@Lf shows lifetime of 0.18 ns (58%), 0.82 ns (22%), 3.58 ns (11%) and 110.70 ns (9%) (Xavier *et al.*, 2010). In the case of AuQCs@BSA these values are 0.10 ns (59.6%), 0.86 ns (21.9%), 4.5 ns (08.6%) 174.7 (09.9%). The AuQCs@Lyz shows lifetime values of 0.1 ns (40%), 1.1 ns (55%) and 19.0 ns (5%) (Pradeep *et al.*, 2014a). In the case of lactoferrin stabilized AuQC excited state lifetime with long lifetime value provide proof for fluorescence resonance energy transfer between protein and cluster (Xavier *et al.*, 2010). Le Gue´vel et al. proved that long lifetime component emerges from the bigger cluster (Au_{25}) with red luminescence (Le GueÌ • vel *et al.*, 2011). Zheng et al. proposed that the long lifetime component could be due to the triplet-singlet intraband transition (Zheng *et al.*, 2007).

1.3.4.2. Spectroscopic and microscopic investigations

X-ray photoelectron spectroscopy (XPS)

XPS method has been used to understand the structure of protein protected cluster as well as core oxidation state of the metal. For the case of Au_{25}@BSA, the Au $4f_{7/2}$ spectrum is deconvoluted into two distinct components with binding energies of 84.0 and 85.1 eV, which is attributed to Au(0) and Au(I), respectively. The small amount of Au(I) (~17%) present on the surface of the Au core is from S-Au-S shell which helps to stabilize the cluster core (Xie *et al.*, 2009). This will give an idea about the cluster structure in which the cluster core is made up of. Au(0) and the shell is made up of S-Au(I)-S binding. In the case of smaller sized QCs such as $Au_{8,}$ only Au(0) composition is detected (Le GueÌ • vel *et al.*, 2011).

Fourier- transform infrared spectroscopy (FTIR) and circular dichroism (CD)

Infrared spectroscopy is one of the most important methods used for analyzing conformational change and the secondary structure of the protein in MQC@protein. As mentioned in earlier sections, proteins exhibits primary, secondary, tertiary and quaternary structure. The QC formation is mainly affected by the secondary structure of proteins because it originates from hydrogen bonds between the amino acids and the carboxylic groups in the peptide backbone. The secondary structure of the protein is arranged by α-helix, β-sheets or random coils. For example in the case of AuQC@BSA, at extremely high pH, the disulfide bonds present in the protein will break and the cysteine residues, which are located in the α-helix regions bind to the cluster. This leads to the change in the secondary structure of protein after QC formation (Pradeep *et al.*, 2014a). Noticeable changes were found in the amide I, II and III region of protein after formation of QC. The peaks in the range of 1600 to 1690 cm^{-1} arises from the stretching frequency of amide I. It is mainly from C=O stretching and a small contribution from the out of plane stretching of C–N bond. Amide II shows peak in the range of 1480 – 1575 cm^{-1}, due to the NH in-plane bending and a small contribution from C=O in the plane as well as C–C and C–N stretching. Amide III exhibits a peak in between 1229 - 1301 cm^{-1}. Other than this, a broad peak was observed at 3500–2900 cm^{-1} which arises from O–H, N–H and C–H vibrations. After QC formation, changes are mainly noted in the amide I and II region. For example in the case of AuQC@BSA, the shifting of amide bands to a higher frequency and the broadening of the bands were observed after cluster formation (Pradeep *et al.*, 2014a).

Far-UV circular dichroism (CD) is another spectroscopic method used to probe the conformation of proteins. Compared to FTIR spectroscopy, the CD gives more precise details about the secondary structure of protein such as the α-helix, β-sheets or random coils structure. A double minimum at 208 and 222 nm corresponds to α-helical structure, whereas a single minimum at 217 nm

originates from β-sheets and a single minimum at 204 arises from random coil structures (Pradeep *et al.*, 2014a). Xie and his co-workers used CD for understanding the conformational change of BSA after the formation of AuQC. Different conformations of BSA can provide different sized Au QCs (Yu *et al.*, 2013b).

Transmission electron microscopic technique (TEM)

Even though TEM images were used to analyze the size of the cluster core, it is not considered as an accurate method to obtain actual core sizes or the number of atoms present in each cluster. The sub-nanometre sized QCs are sensitive to electron beam from high-resolution transmission electron microscopy, which leads to the aggregation of QC and provides a larger size than the actual size (Habeeb Muhammed *et al.*, 2010). Most of the protein protected QCs shows the core size in the range of 1-2 nm (Liu *et al.*, 2011; Mathew & Joseph, 2017).

Matrix assisted laser desorption ionization time of flight mass spectrometry (MALDI-TOF MS)

As described above, TEM is not considered as a reliable technique for evaluating the core diameter as well as number of atoms in each cluster due of their extremely small size and instability towards electron beam. So it is a big challenge to determine the exact size and numbers of metal atoms in a single QC. In 1996, Whetten and co-workers found that MS is a powerful technique to measure the sizes/structure of small QCs and they were used laser-desorption/ionization and time-of-flight MS to analyze AuQC (Whetten *et al.*, 1996). Followed by his invention, MS have been widely used for structural investigation of various QCs. The protein stabilized QC generally studied by MALDI-TOF MS analysis by analyzing the molecular weight of the protein and MQCs@protein. For example in the case of BSA stabilized QC, the parent BSA shows molecular ion peak at 66 kDa and the AuQC@BSA shows a peak at 71 kDa, which is corresponding to 25 Au atoms in a single BSA and the cluster was named as Au_{25}@BSA (Xie *et al.*, 2009). Similarly Ag/CuQC@BSA, Au/AgQC@Lyz, AuQC@Lf, etc. have been studied using MALDI TOF MS. The

detailed study of NMQC@Protein using MALDI TOF MS is discussed in section 1.3.1 and 1.3.5

1.3.5. Structure of NMQC@protein and origin of luminescence

Understanding the structure of QC is crucial to look into their optical properties. Even though the crystal structure determination is considered as the best option to find out the exact structure of protein stabilized MQCs, the QC@protein is not yet crystallized. Thus a complete understanding of the structure and the origin of luminescence of QCs@proteins is not yet completely explored. Several hypotheses are put forward and studied by many Scientist for understanding the structure and origin of luminescence in protein stabilized QCs. Generally, for assigning cluster composition of QC@protein, mass spectrometry (MS) and X-ray spectroscopic methods are the widely used techniques. Along with this advanced theoretical studies support the proposed hypothesis.

The mass spectrometric analysis provides information about the number of atoms present in the QCs. In the case of BSA stabilized QC, MALDI TOF MS termed the cluster as Au_{25}@BSA. XPS reveals the presence of Au(0) and Au(I) state in an AuQC@BSA system, which proposes the core and shell structure (Chevrier *et al.*, 2012). The core is made up of 13 Au (0) atoms and forms an icosahedral structure, which is surrounded by 6 $Au_2(SR)_3$ staples. Using time-resolved photoluminescence and transient absorption techniques, Wen et al. investigated the fluorescence origin of the Au_{25}@BSA (Wen *et al.*, 2012). They found that the fluorescence of Au_{25}@BSA consists of two bands. The band I emerged from the icosahedral core structure containing 13 Au(0) atoms. Additionally, its features are similar to semiconductors, where the red shift of the emission band and bandwidth broadening were observed with increasing temperatures. It is due to electron-phonon and electron–defect/surface scattering phenomenon, like semiconductors. Whereas, the band II predominantly arises from the [S- Au(I)- S- Au(I)- S] semi rings. They found that Au_{25}@BSA have two types of emission. They are prompt fluorescence (PF) on a nanosecond time scale and delayed fluorescence (DF) on a microsecond time scale. The origin of

the red emission from DF is by efficient intersystem crossings (ISC). The Au(I) in the Au(I)-S semirings can form an Au(I) complex at triplet states. The excited electrons in this band can intersystem cross to the triplet state and finally contribute to the red band. Figure 1.19 shows the schematic representation of the luminescence origin from Au_{25}@BSA.

Chevrier et al. explained the core structure and origin of luminescence by Synchrotron-based X-ray absorption fine structure (XAFS) spectroscopy analysis (Chevrier *et al.*, 2018). They have proven that the Au@BSA shows an interlocked gold-thiolate (Au-SR) ring structure known as $Au_{10}(SR)_{10}$ catenane. The stronger aurophilic interactions between interlocking Au(I)-SR ring structures induces ligand to metal-metal charge transfer (LMMCT) process.

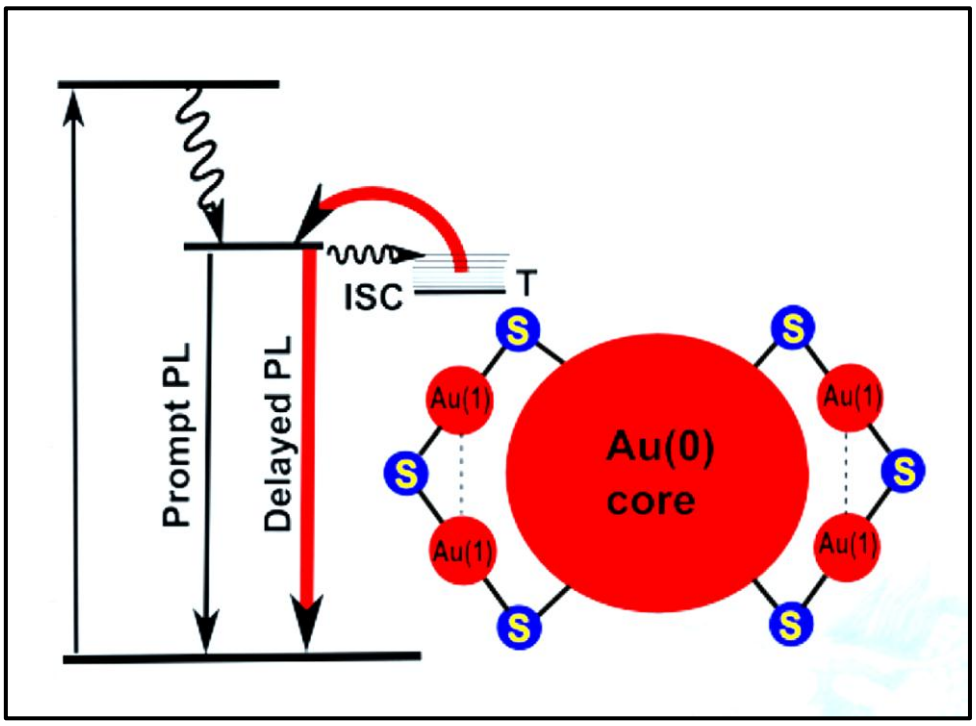

Figure 1.9. Schematic illustration for the origin of photoluminescence from Au25@BSA (Wen *et al.*, 2012).

1.3.5.1. Spherical Jellium Model

Spherical jellium model is used for the theoretical prediction of number of atoms present in the QC by correlation with the emission wavelength. Equation

1.1 represents the relationship between size and emission wavelength. The energy gap between adjacent levels of a QC is on the order of E_f/N, where E_f is the Fermi energy of the bulk metal and N is the number of metal atoms present in the QC. According to the Jellium model, the emission frequency (ω) of QC depends to its radius (R) and number of atoms (N) as shown in Equation (1.1) where r_s is the Wigner−Seitz radius of the metals.

The emission frequency (ω) of a QC is inversely proportional to the size (radius, R) of the cluster. Thus, when the size QC decreases, a blue shift in the emission maximum occurred. (Chattoraj & Bhattacharyya, 2014)

$$\frac{h\omega}{2\pi} \cong \frac{E_f}{\sqrt[3]{N}} = \frac{E_f r_s}{R} \qquad (1.1)$$

For example, Au_{25}@BSA shows an emission maximum at 685 nm, whereas Au_8@BSA shows an emission maximum at 450 nm (Le GueÌ • vel *et al.*, 2011).

1.3.6. Surface modifications of NMQC@protein

It is essential to modify the surface of QC with other substances such as targeting molecules, proteins, enzymes, polymers, other nanoparticles etc to benefit and broaden their uses in biomedical field. The common modification methods used for protein stabilized metal QCs are covalent bio-conjugation and non-covalent interaction.

1.3.6.1. Covalent modification

Surface modification of QC by covalent interaction has been used in bio-labeling and a targeted imaging and delivery applications. Irudayaraj and co-workers demonstrated the conjugation of AuQC@BSA with Herceptin for targeted imaging and localization in ErbB2 over-expressing breast cancer cells and tumor tissue for cancer therapy (Wang., *et al.*, 2011). They have cross-linked the BSA with gluteraldehyde and conjugation of Herceptin over the AuQC@BSA was done by EDC/NHS coupling chemistry. Chen and coworker's conjugated

methionine and indocyanine green (ICG) derivative dye, (MPA) covalently on BSA stabilized Au QCs by EDC/ NHS chemistry and DCC coupling respectively for tumor-selective optical imaging in methionine-dependent malignant cells (Chen., Li., *et al.*, 2012).

1.3.6.2. Non-covalent modification

Surface modification by non-covalent interaction is widely used because of its ease of preparation, absence of toxic coupling agent etc. There are several reports that demonstrate the modification of QC through non-covalent interactions for different applications (Song *et al.*, 2016; Zheng *et al.*, 2017). The non-covalent interactions such as electrostatic interaction, hydrogen bonding, hydrophobic etc. have been used to functionalize the formed QC for specific applications. For example, the enzyme urease was conjugated over glutathione protected Au cluster through simple mixing of Au cluster and urease (Nair *et al.*, 2013).

Ligand exchange is also used as a strategy for functionalization of protein stabilized MQCs. By this method one can alter the property of QC, since ligand plays a crucial role in the optical, electronic and morphological features of the particle, For example, Bhattacharyya and co-workers demonstrated the replacement of BSA stabilized AuQCs with glutathione ligand in the breast cancer cell, which leads to the higher uptake in the cancer cell (Chattoraj & Bhattacharyya, 2014).

1.3.6.3. Metal QC-based nanocomposite

The improvement of materials performance by incorporating other nanoparticle can provide further opportunity to broaden their utility in practical applications. The inclusion of other nanoparticles such as carbon-based material, silica nanoparticle, metal nanoparticle (AuNP) and quantum dots provide improved performance along with some new properties resulting from the synergistic effects of metal QC and other nanoparticles. The presence of a variety of proteins with enormous surface charges can also help in the fabrication of nanocomposites. There are several reports on the carbon dot-AuQC (CD-AuQC)

composites for ratiometric sensing and imaging applications. For example, Yang and co-workers prepared dual emitting nanocomposite by cross-linking CD prepared from papain enzyme and AuQCs@ papain for visualizing and detecting H_2O_2, doxycycline, and I^-(Yang., *et al.*, 2017).

Apart from CD, carbon nanotubes (CNTs) and graphene oxide (GO) were also used for fabricating QC-based nanocomposite through different strategies. Yan and co-workers fabricated a nanocomposite of transferrin-functionalized AuQC (AuQC@Tf) and GO to form AuQC@Tf/GO through hydrogen bond and a hydrophobic interaction between Tf and GO (Wang., *et al.*, 2013).

In another case, Qu and coworker integrated lysozyme-stabilized Au QCs and GO through the electrostatic interactions between positively charged AuQC and negatively charged GO. Bhandari and co-workers embedded Au QC and QD complex in proteins for the generation of white light emission (Bhandari *et al.*, 2016).

Silica coating is another widely used strategy for the surface modification of MQCs for biological applications because of the advantages of silica such as good water-solubility and excellent stability as well as a low nonspecific binding with the biological matrix. For example, Yang and his group demonstrated a silica coating on AuQC@BSA for fluorescence imaging-guided photodynamic therapy (PDT). They have coated silica on the surface of AuQCs to form a fluorescent core-shell nanostructure using a modified Stöber method. Thereafter they modified the surface of silica by using a silane coupling agent, 3-aminopropyltrimethoxysilane (APTS) for further conjugation of Ce6, which is a chlorin e6 (Ce6) photosensitizer. Covalent binding of Ce6 to the AuNCs@SiO_2NH_2 was performed using EDC-NHS reaction (Huang., *et al.*, 2013; Le *et al.*, 2010).

Moreover, the researchers have also demonstrated the incorporation of MQCs on polymer substrates by simple mixing and electrospinning process for specific applications (George *et al.*, 2012; Senthamizhan *et al.*, 2014).

1.4. Biomedical applications of NMQC@Protein

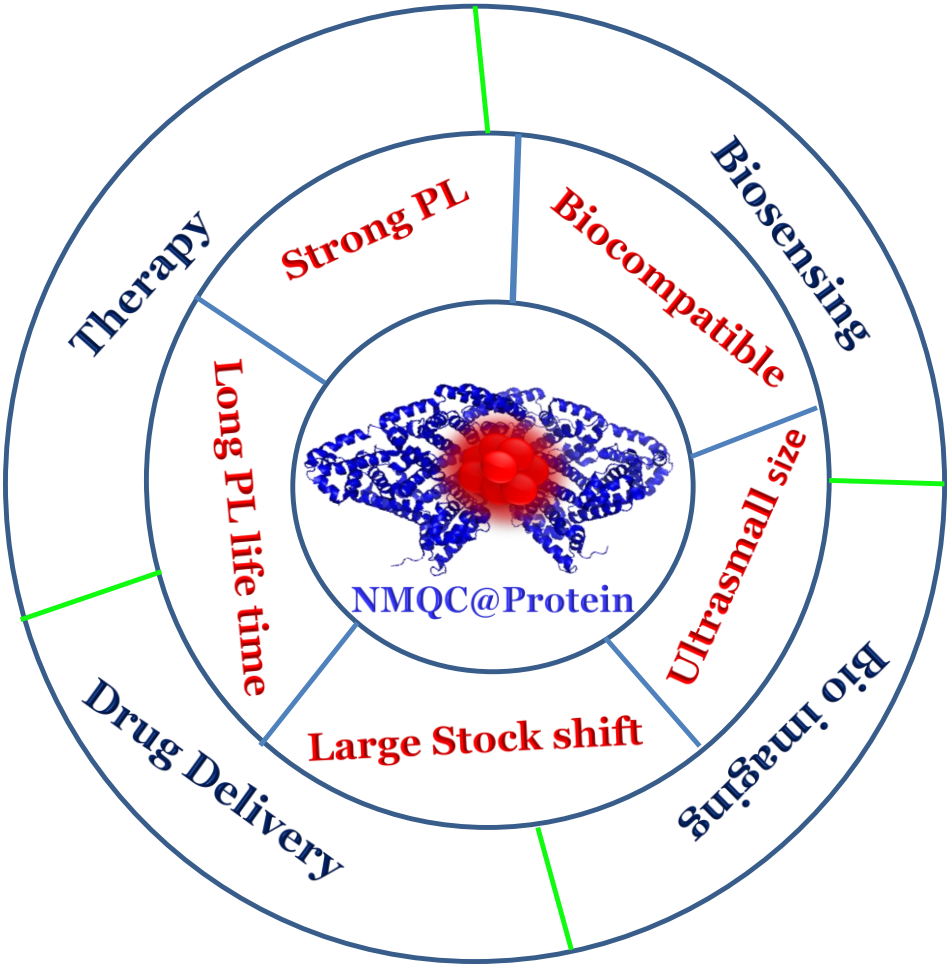

Figure 1.10. Schematic representation for the properties and various biomedical applications of fluorescent noble metal quantum clusters (Cui *et al.*, 2014).

Fluorescent NMQCs have received much attention in the field of biosensing, bioimaging, and therapy owing to their unique optical and functional properties, such as long fluorescence lifetime, ultrasmall size, large Stokes shift, strong photoluminescence, as well as excellent biocompatibility and photostability. The major application of QC in the biomedical fields are given in Figure 1.10. This section summarizes the biomedical applications of protein stabilized metal quantum clusters and highlight the desirable features of these QCs for biosensing, bioimaging, biolabelling, and targeted cancer therapy.

1.4.1. Biosensor

Biosensor is an analytical device used to detect the presence or concentration of a biological analyte, such as a biomolecule, metal ion etc. Biosensors consist of three parts: (i) Bioreceptor, a component that recognizes the analyte and produces a signal. (ii) Transducer, which measures the signal produced during biorecognition, and (iii) reader device, which converts it into a measurable signal (Figure 1.11). Different methods such as optical, electrochemical, mass sensitivity etc are employed to develop biosensors. Among these, optical sensing method is the widely used one. Optical sensing method uses two techniques, absorption and fluorescence to detect the analyte. Fluorescence sensing method is more sensitive than absorbance-based method because of its diverse ways of measuring both absorbance and fluorescence. In the case of UV-Vis absorption spectroscopy, light absorbance is measured as the difference in intensity between light passing through the reference and the sample. But in fluorescence, the intensity is measured directly, without comparison with a reference beam. The sensitivity for the detection also very high for the case of fluorescence when compared to absorption technique. The advantage is due to the measurement of the fluorescence relative to a dark background, as compared to the bright reference beam in an absorbance measurement (Lakowicz, 2013). Fluorescent sensing is based on the fluorescence phenomenon that occurs when electromagnetic radiation is absorbed by fluorophores. The generated signal is mostly determined by employing one of the following methods (Nawrot *et al.*, 2018) (Figure 1.11).

- FRET (Förster Resonance Energy Transfer),
- FLIM (Fluorescence Lifetime Imaging),
- FCS (Fluorescence Correlation Spectroscopy)
- FI (changes in Fluorescence Intensity).

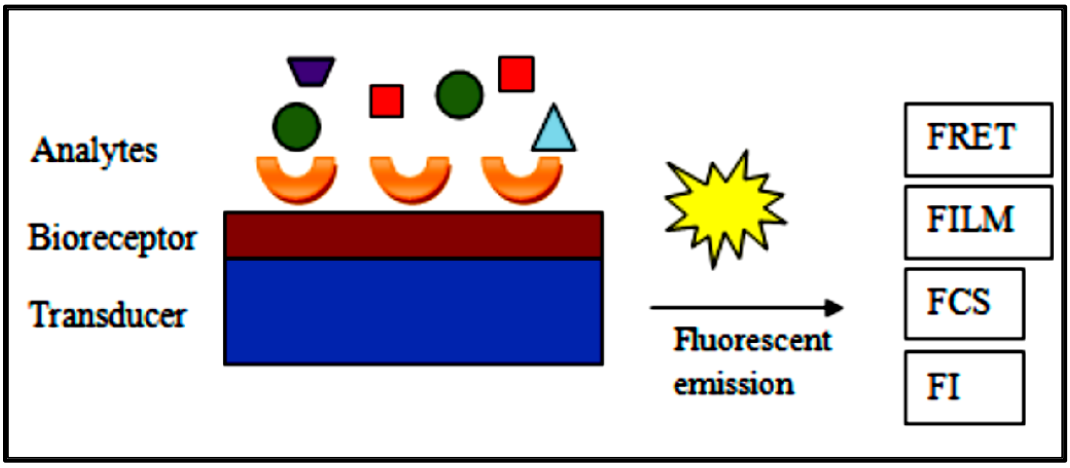

Figure 1.11. Schematic representation of different strategy used for the preparation of fluorescence biosensors. (Nawrot *et al.*, 2018)

The strong luminescence emerges from ultra-small NMQCs has enabled it as an emerging fluorescent probe for detecting various analytes, such as heavy metal ions, inorganic anions, and various biomolecules. Before discussing the different types of biosensors, the various sensing approaches used for fluorescence sensing has to be described. Here we are mainly dealing with the fluorescence intensity based sensing strategies.

1.4.1.1. General approaches in fluorescence sensing

Fluorescence quenching/turn-off sensing

Fluorescence quenching is the decrease in the fluorescence intensity of fluorophore at a particular wavelength with increasing concentration of quencher. Quenching requires a molecular contact between the fluorophore and quencher. Several processes can result in quenching such as collisional or dynamic quenching, complex formation or static, excited state reactions, energy transfer etc. Dynamic fluorescence quenching arises from collisions between the fluorophore in its excited state and quencher and the fluorophore returns to the ground state without emission of light. In the case of static fluorescence quenching, a non-fluorescent complex is formed between the fluorophore and the quencher (Lakowicz, 2013). Another process is energy transfer between fluorophore and quencher, which leads to fluorescence quenching. For example

fluorescence resonance energy transfer (FRET) between fluorophore/Donor and quencher/acceptor, leads to decreases the intensity of the donor (fluorophore) and transfers the energy to an acceptor. The efficiency of the FRET is dependent on the distance between the two donors and acceptor (minimum 10 Aº) and overlap between the donor emission and acceptor absorption. Another mechanism for fluorescence quenching is photoinduced electron transfer (PET) mechanism in which a complex is formed between the electron donor and the electron acceptor. This charge transfer complex can return to the ground state without emission of a photon. Here the excited fluorophore can act as either the electron donor or acceptor (Sun *et al.*, 2015).

Inner filter effect (IFE)

IFE based fluorescent quenching is another strategy used to develop fluorescent sensor. It is a non-radiation energy conversion models in fluorometry, and fluorescence quenching is due to the absorption of the excitation and/or emission light of fluorophore by absorbers (quenchers). The IFE takes place only when a significant spectral overlap between the absorption spectrum of quencher and emission or excitation spectrum of a fluorophore occurs. The advantage of this method is that it does not require any molecular interaction or any other strict criteria as like FRET for quenching (Liu *et al.*, 2017).

Fluorescent enhancement/turn-on sensing

Compared to the fluorescence quenching strategy, the turn-on or enhancement method exhibit more specificity. In this case, in the presence of an analyte, the fluorescent enhancement or the recovery of quenched fluorescence takes place. The fluorescent enhancement occurs by several processes such as aggregation-induced emission, chelation induced enhancement etc. Turn-on fluorescence sensing can take place two-step process. In the first step, the intensity of the fluorescent probe is quenched by a quencher, which can be another nanoparticle, or small molecule. In the second step, the quenched fluorescence is recovered in the presence of an analyte by the blocking of electron transfer or energy transfer (Hu *et al.*, 2014; Qin *et al.*, 2015; Yuan *et al.*, 2013).

Ratiometric sensing

Ratiometric sensing can be done using dual emitting nanomaterials or hybrid nanomaterials. Here the sensing is carried out by monitoring two emission intensities at their emission maxima. Thus ratiometric sensing methods exhibit advantages over sole responsive signal based method. A sole responsive signal is readily fluctuated by environmental factors such as variation in probe concentration, instrumental efficiency etc. Whereas ratiometric sensor can eliminate these environmental factors and give more precise measurement because of its self-referencing capability by calculation of two emission intensity ratios (Zhang *et al.*, 2014).

Moreover, the combination of the above-mentioned strategy also has been applied for sensor development. For example turn-off-on/ turn-on-off sensor, in which the fluorescence quenching can take place in the presence of an analyte and it is recovered by another analyte or vice versa (Hu *et al.*, 2014; Zhang., *et al.*, 2015)

1.4.1.2. Metal ion sensing

The detection of heavy metal ions in biological systems got great attention owing to their hazardous effects on the human health especially to the central nervous system, kidneys, skin, liver, and bones. Therefore, the detection of a heavy metal ion by an environmentally friendly strategy is highly desirable.

Protein stabilized metal QCs are widely used for the detection of various heavy metal ions, such as Hg^{2+}, Pb^{2+}, Cu^{2+}, Ag^{+}, Cd^{2+}, As^{3+}, Cr^{3+}, Cr^{6+}, Fe^{3+}, etc by turn-off or turn-on method. The fluorescence quenching or enhancement is either due to the direct interaction of analyte to the core of metal nanocluster or interaction with the protein, For example, Xie et al. reported the detection of mercury ion using Au_{25}@BSA based on quenching strategy (Xie *et al.*, 2010). The reason for fluorescence quenching is the metallophilic interaction between Hg^{2+}–Au^{+} ^{1} (d^{10}-d^{10}). The QC contains 17% of Au^{+} on the surface, which can interact with Hg(II) through strong and specific metallophilic interaction. The

proposed scheme of metallophilic interaction and fluorescence quenching is shown in Figure 1.12. It exhibits excellent selectivity due to the high specificity of Hg^{2+} with Au^{+}. The limit of detection (LOD) of this method was 0.5 nM (0.1 ppb) which was lower than the maximum permissible level of mercury in drinking water announced by the U.S. Environmental Protection Agency (2.0 ppb).

Subsequently, several others have used similar strategy for the detection of mercury by using various other protein protected metal QCs (Guo & Irudayaraj, 2011; Pyng *et al.*, 2013; Shi *et al.*, 2015; Yang., *et al.*, 2017).

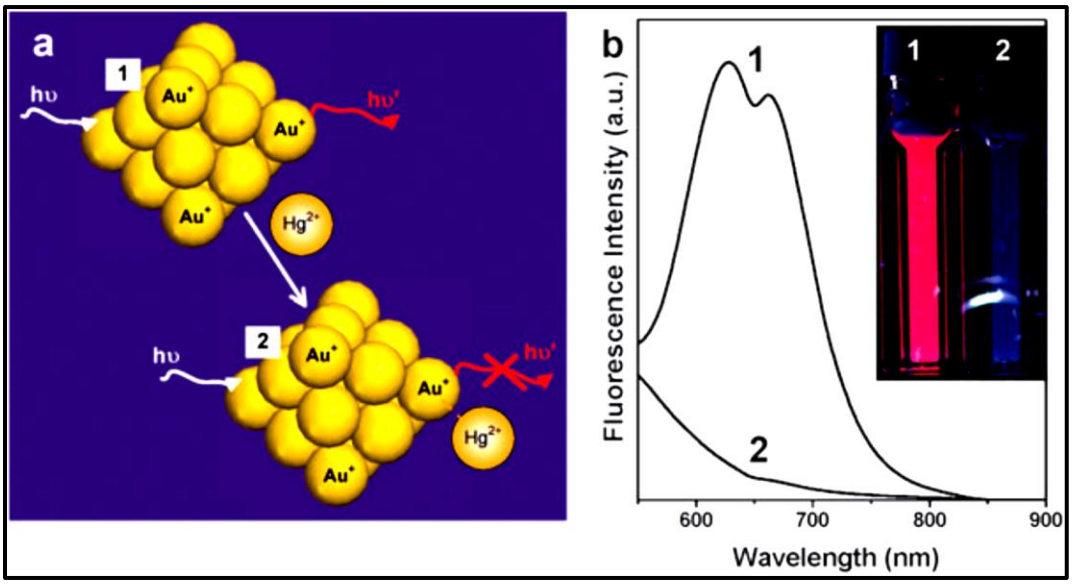

Figure 1.12. (a) Schematic representation of Hg^{2+} sensing using AuQC based on metallophilic bond induced fluorescence quenching (b) Fluorescence emission spectra of AuQC (1) and AuQC-Hg (2) respectively. The inset shows the photographs of QC in the absence (1) and presence (2) of Hg^{2+} ions under UV irradiation (354 nm) (Xie *et al.*, 2010a).

Lin and Tseng used Lysozyme VI (Lys VI) stabilized AuQCs for the sensing of Hg^{2+} and CH_3Hg^{+} through metallophilic interaction. The LODs for Hg^{2+} and CH_3Hg^{+} were found to be 3 pM and 4 nM, respectively. They found that compared to AuQCs@BSA, Lys VI stabilized QC provided an approximately 330-fold enhancement in the sensitivity of detection, which is due to the more Au^{+} in Lys VI-AuQC (41%) than the AuQCs@BSA (17%) (Lin & Tseng, 2010b).

Hu et al. proposed a photo-induced electron transfer process for Hg (II) sensing using AuQC@BSA. Here, Hg^{2+} form a complex with AuQC@BSA through S–Hg bond. The electrons from AuQC@BSA are firstly excited under photo-irradiation and, then Hg^{2+} can directly intercept one of the charge carriers which is reduced to Hg^{+}, which can disrupt the radiative recombination of the holes and the excited electrons, and further lead to the quenching the fluorescence of the AuQC@BSA. The LOD of the probe was 80 nM (Hu *et al.*, 2010).

Pyang and co-workers proposed that along with metallophilic interaction, electron transfer from Au_{25}QCs to Hg^{2+} ions can lead tofluorescence quenching. When the Hg^{2+} is bound to the outer shell of the QC, the electron transfer from the triplet state of AuQC to the Hg^{2+} causes fluorescence quenching. Upon excitation of QCs, two possible transitions can take place. (I) The excited electrons can recombine with hole in the singlet state via prompt fluorescence. (II) electrons can move to the triplet state through ISC process. Repopulated electrons from triplet to singlet state will emit fluorescence with the same spectra with a much longer decay component. This was supported by fluorescence lifetime measurement studies. With an increasing concentration of Hg^{2+} ions, the amplitude of the slow component evidently decreases (Figure 1.13 B).

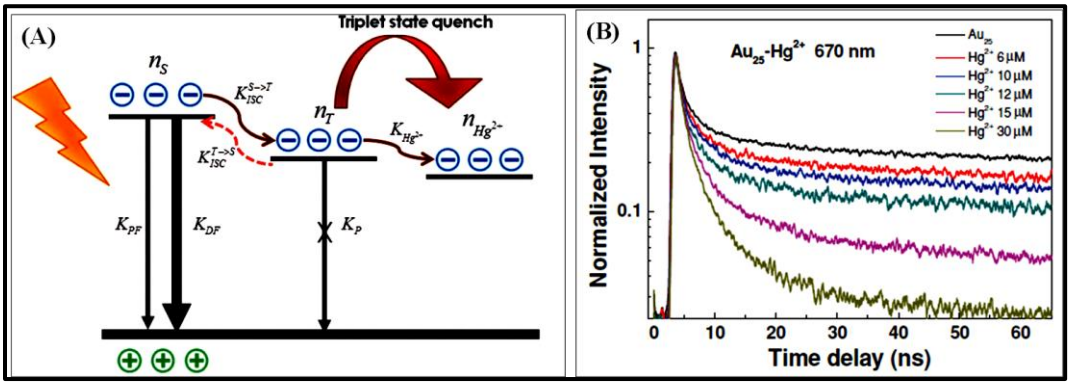

Figure 1.13. (A) Schematic representation for the mechanism for fluorescence quenching by Hg (II) by triplet electron transfer between AuQC and Hg(II). The n_S and n_T represent the singlet and triplet states of Au25@BSA; ISC represent the intersystem crossing $K_{Hg}{}^{2+}$ is the electron transfer rate from the triplet state of QC to Hg^{2+}. (B) Quenching of delayed fluorescence of AuQC with increasing concentration of Hg^{2+} ions (Pyng *et al.*, 2013).

The relative amplitude of the delayed fluorescence decreases with increasing Hg^{2+} concentrations (Pyng *et al.*, 2013). Figure 1.13 shows the proposed mechanism of quenching and variation in the lifetime with increasing concentration of Hg(II).

Other than monometallic QCs, bimetallic QCs also used for the detection of Hg (II). Compared to monometallic QCs, bimetallic QC exhibits a superior property such as high QY and high sensitivity for sensing.

Zheng et al described the sensitive detection of Hg (II) by using yellow emitting BSA stabilized AuAg alloy QCs. They have proven that the sensitivity of the AuAgQC is much higher than AuQC for the detection of Hg^{2+}. The limit of detection of Hg (II) is 13 nM (Zheng *et al.*, 2015b).

Ratiometric sensing strategy also was applied for the more sensitive detection of Hg (II) (Zhao *et al.*, 2017). For Example, AuQC@BSA incorporated electrospun nanofibre was used for Hg (II) detection. A green emitting dye, FITC (fluorescein isothiocyanate) was precoated on the fiber for visual detection. The luminescence of FITC is insensitive to Hg^{2+} and Hg^{2+}quenched the red emission of the QC completely. Thus the green emission of the fiber appeared under a dark field fluorescence microscope enabling sensing (Ghosh *et al.*, 2014).

Even though copper is considered as an essential element for all living systems for its key role biological process, it is a critical environmental pollutant. The wide use of Cu in various industries causes soil, water, and food contamination. Excessive uptake of Cu^{2+} in the human body can cause liver or kidney damage (Chen., *et al.*, 2013). Much efforts have been devoted to detecting Cu^{2+} using protein stabilized fluorescent metal QCs as probes, mainly based on fluorescence quenching. Durgadas et al. demonstrated AuQC@BSA as a probe for determination of Cu^{2+} in live cells over a range of 100 mM to 5 mM with a LOD of 50 mM. The binding of Cu^{2+} with BSA leads to electron transfer which in turn causes fluorescence quenching. Interestingly the fluorescence was recoverable by adding glycine (Durgadas *et al.*, 2011).

Redox-induced fluorescence quenching was established for the sensing of Cu^{2+} by HSA stabilized fluorescent Au/Ag core/shell nanocrystals. The Cu^{2+} reduced to Cu^{+} upon the interaction of HSA and subsequent interaction between Cu^{+} and Ag causes fluorescent quenching. The limit of detection (LOD) of this method was 5 nM (Gui & Jin, 2013).

CdTe/Silica/AuQCs hybrid spheres were developed for the ratiometric determination of Cu^{2+}. The hybrid was prepared through covalent linking of Au QC@BSA to the surface of the amino-functionalized CdTe/SiO2 spheres. The green emission from CdTe/SiO2 is insensitive to Cu (II), while the red emission from AuQCs was quenched (Wang., *et al.*, 2014).

The excess use of silver in the electronics, photographic and imaging industries produce high doses of Ag which causes environmental pollution and is toxic to the human beings. The Ag^{+} inactivate the functions of many biological systems by binding with amine, imidazole and carboxyl groups of various metabolites, and displace essential metal ions such as Ca^{2+} and Zn^{2+} in hydroxyapatite in bone. Even though it shows antibacterial activities to a biological organism, an excess amount of silver can lead to environmental and biological contamination (Sun *et al.*, 2013; Zhang & Wang, 2014; Zhang., *et al.*, 2015).

Wu group reported a turn-on fluorescence detection of silver ions (Ag (I)) by utilizing Au_{16}QCs@BSA as the fluorescent probe. The detection limit for Ag (I) was found to be 0.10 mM. Upon the addition of Ag(I) to AuQC, a blue shift assisted linear enhancement was observed. The main reason for the blue shift and enhancement is due to the interaction of Ag(I) with AuQC@BSA. A metallic bond was formed between Ag(I) ion and Au core, and then Ag(I) was reduced by BSA and deposited on the surface of AuQC inside the BSA until its further enlargement is ultimately prevented by the template. Thus surface electron energy of Au_{16}QCs was changed which subsequently leads to the blue shift and enhancement in fluorescence intensity with Ag(I) ion. In 2013 they have further carried out a detailed investigation to understand fluorescent sensing mechanism

by using same QCs and proven that Ag(I) reduced by Au_{25}, and the gold atoms in Au_{25} were replaced by silver and formed hybrid Au@AgQCs (Li., *et al.*, 2013; Yue *et al.*, 2012). This result suggests a redox reaction occurs between Au(0) in the core and Ag+, which induces the oxidation of Au(0) to Au(I) and finally lead to an increase of Au(I) proportion. The increased binding energy of Au (I) in XPS study further supports this observation. Figure 1.14 shows the sensing strategy and XPS data of Au_{16} QC and Au@AgQCs.

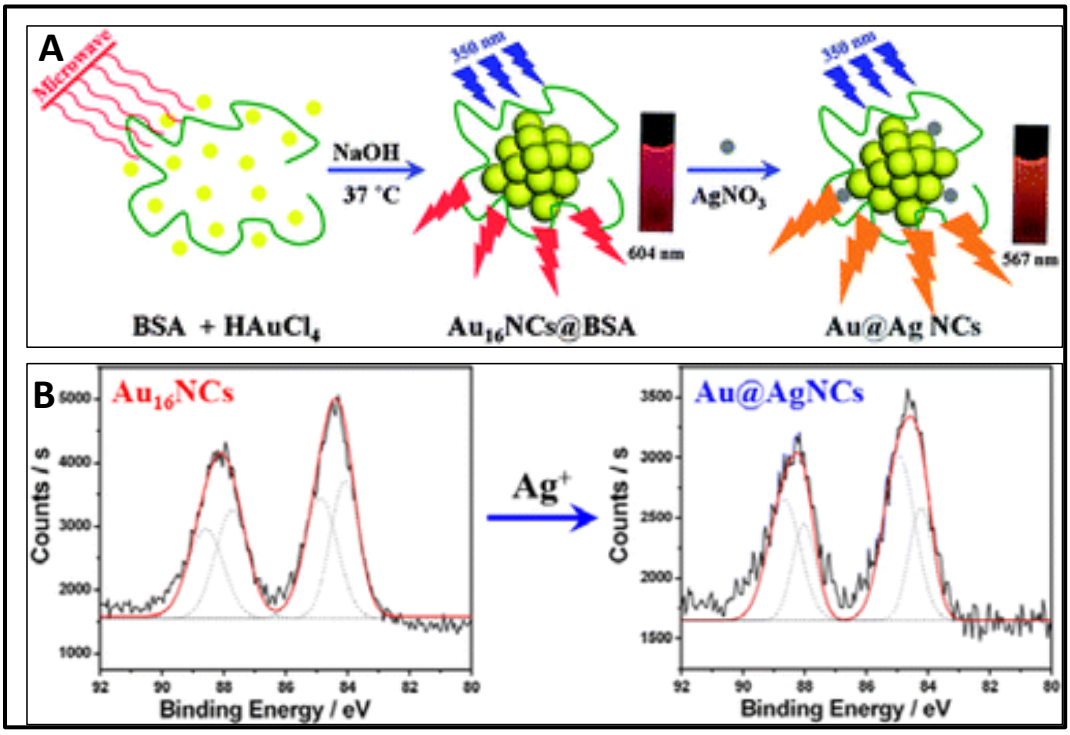

Figure 1.14 (A) Schematic representation of synthesis of AuQC and thereafter the detection of Ag (I) by Au@Ag QC formation. (B) Au 4f XPS spectra of Au_{16}NCs@BSA (A) before and (B) after adding silver nitrate.(Li., *et al.*, 2013)

Chromium mainly exists in two valence states as Cr(III) and Cr(VI) in aqueous solutions. Cr(III) in trace amounts is an essential nutrient required for sugar and fat metabolism, while its high concentration in the human body leads to cancer and induce oxidative DNA damage. Cr(VI) also create a severe problem in humans due to its strong oxidizing properties. Trace amounts of Cr(VI) can damage the liver, kidneys and other organs leading to hemolysis, liver failure and, even cancer (Dayan & Paine, 2001; Zhang & Wang, 2014).

Feng group developed the Chromium (VI) sensor by using AuQC@BSA based on fluorescence quenching. They found that in the presence of Br^-, the standard electron potential of Au(I)/Au(0) is lower than that of Cr(VI)/Cr(III), which enables gold to be oxidized by Cr(VI). The fluorescence intensity of Au QCs decreased gradually due to the leaching processes of gold. The detection limit of the sensor was found to be 0.6 nM (Jian-feng *et al.*, 2016; Zhang., Zeng., *et al.*, 2016).

Zinc ion is (Zn^{2+}) an essential trace element found in the human body. It is an important factor in many biological processes such as the regulation of gene expression, cellular apoptosis etc. The abnormal level of Zn^{2+} can cause serious neurological diseases such as Alzheimer's disease, Parkinson's disease, cerebral ischemia, and epilepsy (Huang., *et al.*, 2013; Li., *et al.*, 2017). Liu et al. developed a novel fluorescence turn-on sensor for Zn (II) using AuQC@BSA with the assistance of salicylic aldehyde (SA). SA interacted with amino groups of AuQC@BSA and form a fluorescent Schiff base, which leads to fluorescent quenching. Upon the addition of Zn(II), it forms a strong bond with the Schiff base ligands, leading to blue-shift and increase of the fluorescence from Schiff base–metal coordination complexes and simultaneous recovery of fluorescence from AuQCs. The LOD of Zn(II) by this method is 29.28 nM (Liu., *et al.*, 2015). The similar strategy was applied by Bothra et al. for detection of Zn(II). In this case, they have used lysozyme cocooned gold QC and vitamin B6 cofactor pyridoxal5′-phosphate (PLP). The red emission from AuQCs@Lyso changed to yellow upon conjugation with PLP due to the formation of a Schiff base between the free $–NH_2$ present in the lysozyme and the –CHO group of PLP. The PLP conjugated AuQCs@Lyso was further applied for the selective turn-on recognition of Zn^{2+} ions. The limit of detection for Zn^{2+} ions was 39.0 nM (Bothra *et al.*, 2018).

Lead (Pb^{2+}) is another highly toxic, carcinogenic and bio-accumulative heavy metal ion. The accumulation Pb^{2+} in the human body causes various neurological, cardiovascular, gastrointestinal, reproductive disorders (Wang, Z. *et al.*, 2015; Zhong *et al.*, 2015). Lee et al. used AuQC@BSA for the detection of

Pb^{2+} through fluorescence quenching. They proposed that the red emission of AuQC@BSA was quenched by Pb^{2+}-mediated interparticle aggregation mechanism through the interaction between the amino, carboxylic, mercapto groups of BSA with Pb (II). The limits of detection for Pb^{2+} ions was 4.8 nM (Lee *et al.*, 2016).

Wang et al. also developed BSA stabilized silver/gold alloy QC based fluorescent Pb (II) sensor based on aggregation-induced quenching strategy. The high-affinity between protein and Pb^{2+} ion produces a complex which acts as a quencher of fluorescence. The limit of detection of the probe was 2 nM (Wang., *et al.*, 2015).

1.4.1.3. Anions sensing

Cyanide (CN^-) is the most poisoned chemical and trace amount of CN^- in the human body can arrest the function of the central nervous system which leads to sudden death. The extensive use of CN^- in the metallurgical industry causes environmental pollution. The CN^- forms a strong complex with ($Au(CN)_2$) through Elsner reaction (Lu *et al.*, 2014). This recognition chemistry is applied for CN^- detection. Liu et al. detected cyanide using BSA stabilized AuQCs for the first time. Upon the addition of cyanide to AuQC@BSA solution, the etching of Au by CN^- leads to the decomposition of AuQCs, which causes fluorescent quenching.

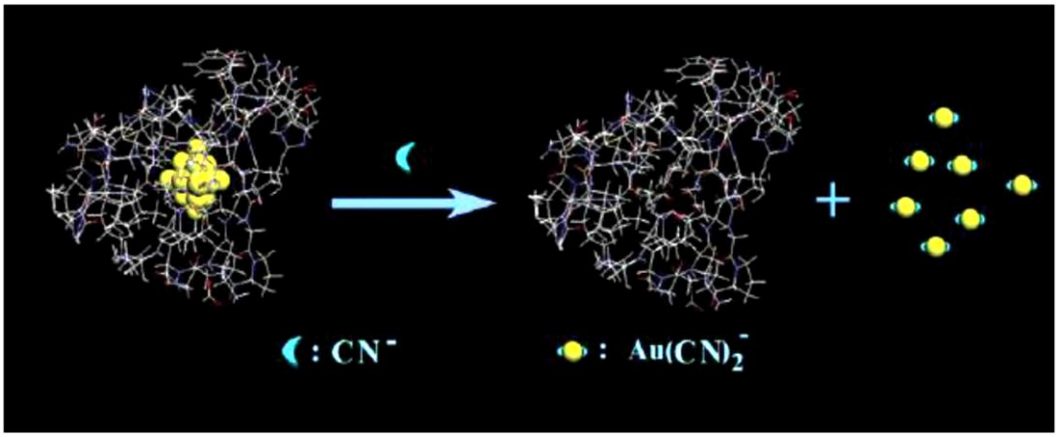

Figure 1.15. Schematic representation of the CN− detection using AuQC@BSA based on the etching method (Liu *et al.*, 2010).

The sensor shows excellent selectivity over other environmentally relevant anions owing to the specific interaction between cyanide and Au atoms. The schematic representation for the fluorescence sensing is shown in Figure 1.15. The LOD for this probe was ~200 nm, which is ~14 times lower than the maximum level (2.7 mm) of cyanide in drinking water allowed by the World Health Organization (WHO) (Liu *et al.*, 2010).

Nitrite (NO_2^-) ion is another anion creates several environmental and health problems. NO_2^- typically used in food preservative causes cancer, neuropsychiatric disorders, methemoglobinemia etc (Unnikrishnan *et al.*, 2014). In 2013, Liu et al. developed a nitrite sensor by using AuQC@BSA for the first time based on aggregation-induced fluorescence quenching (Liu., *et al.*, 2013). Later, Yue et al. also demonstrated the application of AuQC@BSA for nitrite detection (Yue *et al.*, 2013). One of the limitations of their study is the poor selectivity, interference from Hg^{2+}, Cu^{2+}, CN^- cannot be avoided. Thereafter Unnikrishnan et al. carried out a detailed investigation of the mechanism and application of AuQC@BSA for nitrite detection (Unnikrishnan *et al.*, 2014). The mechanism for fluorescence quenching is due to the oxidation of Au(0) atoms to Au(I) by nitrite ions/nitrosyl cations (NO^+). The limit of detection of this sensor was found to be 100 nM.

In another study at 2015, Xu et al. developed a nanohybrid fluorescence probe for the ratiometric detection of NO_2^-. The nanohybrid contains red emissive AuQC@HSA on the surface of blue emissive graphene oxide (GO-C_6NH_2).

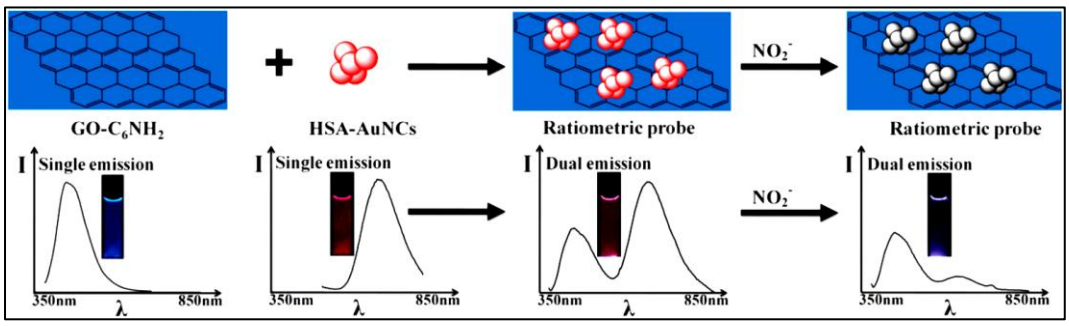

Figure 1.16. Schematic representation of the ratiometric probe structure and the visual detection principle for NO_2^-(Xu., *et al.*, 2015).

The nitrite selectively quenches the red emission of AuQC@HSA, while the blue emission from GO-C6NH_2 remains constant, which leads to the distinguishable fluorescence colour evolution. The LOD for nitrite detection was found to be 46 nM (Xu., *et al.*, 2015). Schematic representation for the formation of hybrid and thereafter the sensing of NO_2^- and their corresponding fluorescence spectra are shown in Figure 1.16

Nitrite ion detection was carried by another indirect method using BSA stabilized AuQCs by Zhang et al. Upon the addition of NO_2^- and H_2O_2 to the AuQC@BSA, the emission of the AuQC was completely quenched as a result of the oxidation of the Au by the peroxynitrous acid (HOONO) generated from the specific reaction of HNO_2 with H_2O_2. The same mechanism has been applied for the detection of iodide (Cao *et al.*, 2015; Sun & Jin, 2014; Zhang., *et al.*, 2013).

Sulfide ions (S^{2-}) also belong to the category of environmental pollutants. Widely distributed in water, it produce serious environmental problem and trace amount of S^{2-} in living systems is hazardous especially to human health. The long-term existence of S^{2-} causes chronic diseases and digestive disturbance (Gao *et al.*, 2016). Using AuQC@BSA, an S_2^- sensor was developed based on the formation of Au_2S by the reaction between Au in AuQCs and S_2^- which destruct the structure of AuQC@BSA leading to fluorescence quenching. The detection limit was found to be 0.029 μM (Liu., *et al.*, 2013).

Gao et al prepared three type of Lysozyme stabilized AgQC named as dLys-AgQCs 1, dLys-AgQCs 2 and dLys-AgQCs 3 for the detection of S_2^- through different strategies. In the first case, dLys-AgQCs 1 is quenched by S^{2-} by forming Ag_2S and destructing the nanostructure of dLys-AgQC 1. The fluorescence intensity of dLys-AgQCs 3 is enhanced by S^{2-}, as S^{2-} combined with Ag(I) contained in dLys-AgQCs 3 and altered the ligand-to-metal-metal charge transfer process. For the case of dLys-AgQCs 2, the photoluminescence was enhanced firstly with a small amount of S^{2-} and then quenched with the addition of more S^{2-}. This could be due to the combination of S^{2-} with Ag(I) at low concentrations and then with Ag(0) at high concentrations (Gao *et al.*, 2016).

Similarly, anions like chloride, Iodate etc are detected by protein stabilized metal QCs (Li., *et al.*, 2014; Xiong *et al.*, 2015).

1.4.1.4. Small biomolecule sensing

Small biomolecules, such as glucose, biothiol, amino acids, urea, dopamine, GSH, bilirubin, FA, ATP, Cholesterol, and H_2O_2, play an important role in many biological processes and abnormal level of this molecule have been considered as an important factor in several diseases and their therapy. Protein stabilized fluorescent MQCs have been successfully used for the development of such biomolecule sensors.

Glucose is considered as an important biologically relevant molecule. It is the main source of energy in living cells and metabolic intermediate in the synthesis of other complex molecules. Furthermore, it is a clinically relevant molecule. The abnormal level of glucose in the blood provides significant information on many diseases such as diabetes or hypoglycemia (Yoo & Lee, 2010).

In 2013, Xia et al. utilized glucose oxidase functionalized gold QC for glucose detection with a detection limit of 0.7×10^{-6} M. The glucose oxidase is functionalized by etching reaction. In the first step, tetrakis (hydroxylmethyl) phosphonium-protected gold nanoparticles were prepared and in the second step etching of AuNP by thioctic acid-modified glucose oxidase provide glucose-oxidase functionalized AuQCs. The glucose oxidase generates H_2O_2 in the presence of glucose, which causes fluorescence quenching via aggregation of QC (Xia *et al.*, 2013).

The Lysozyme stabilized CuQC was used for the detection of glucose with a detection limit of 1.9 nM. The fluorescence quenching of CuQC is due to the reduction of Cu(I) on the surface of the QC by glucose (Wang., *et al.*, 2015).

Jin et al. detected glucose by using AuQC@BSA (Jin *et al.*, 2011). In the presence of glucose oxidase and O_2, oxidation of glucose and generation of H_2O_2

takes place. They have shown that H_2O_2 quenches the fluorescence of AuQCs@BSA by destructing the structure of QC. Thus both H_2O_2 and glucose can be detected by this method. The detection limit for the glucose was 5 mM. Followed by this several groups have detected glucose and H_2O_2 employing the same strategy (Li., *et al.*, 2013; Liu., *et al.*, 2016).

H_2O_2 has received considerable attention in the chemical, biological, clinical, and environmental field. Abnormal levels of H_2O_2 is harmful to the biological systems and damage neuropathology of central nervous functions. Moreover, H_2O_2 was produced during the oxidation reactions catalyzed by glucose oxidase, urease, cholesterol oxidase, etc. The advantage of the enzymes special binding on the target material has been utilized for the detection of glucose, cholesterol, uric acid, and H_2O_2 (Liu., *et al.*, 2016).

Uric acid is a byproduct formed during the purine catabolism of nuclear proteins and nucleic acids in the body. The excess amount of uric acid in the body leads to serious diseases, such as gout, renal and cardiovascular diseases (Wang *et al.*, 2019). AuAg@BSA was used as the fluorescent probe for the ratiometric detection of uric acid. The detection is based on the inner filter effect (IFE) between AuAg@BSA and 2,3-diaminophenazine (DAP) in the presence of horseradish peroxidase (HRP). Upon the addition of HRP, uric acid was degraded and produce H_2O_2 and at the same time, o-phenylenediamine (OPD) catalytically oxidized to DAP in the presence of H_2O_2. The detection limit for this probe was 5.1×10^{-6} M (Wang *et al.*, 2019).

Meng et al developed catalase conjugated gold QC for the detection of hydrogen peroxide, glucose and uric acid with a detection limit of 25 nM, 3 µM and 40 nM respectively (Meng *et al.*, 2018).

Wen et al. used red emitting AuQCs@HRP (horseradish peroxidase) for the detection of hydrogen peroxide with LOD of 30 nM (Wen *et al.*, 2011b).

Moreover, protein-templated QCs exhibit enzyme mimetic activity, which has been further exploited for the detection of clinically relevant biomolecules

(Wang *et al.*, 2019). For Example, Wang et al. demonstrated the peroxidase-like activity of AuQC@BSA and successfully applied it for the determination of xanthine (Wang., *et al.*, 2011).

The intrinsic peroxidase-like activity of copper QC was reported and used for the colorimetric detection of both glucose and H_2O_2 with a detection limit of 10 µM and 100 µM respectively (Hu.*et al.*, 2013).

Cholesterol plays a key role in the functioning of the nerve system and brain cells. An excess amount of cholesterol in the blood causes a disease known as atherosclerosis. The abnormally low concentration of cholesterol results in hypocholesterolemia, which may cause hemorrhagic stroke (Chang & Ho, 2015).

An inner filter effect based fluorescent sensor was developed for the detection of cholesterol using AuQC@BSA. poly(vinyl pyrrolidone)-protected gold nanoparticles (AuNP@PVP) and AuQC@BSA was used as an IFE absorber/fluorophore pair. In the presence of cholesterol oxidase, H_2O_2 was generated and the interaction of H_2O_2 with AuNP causes an expansion of AuNP size.

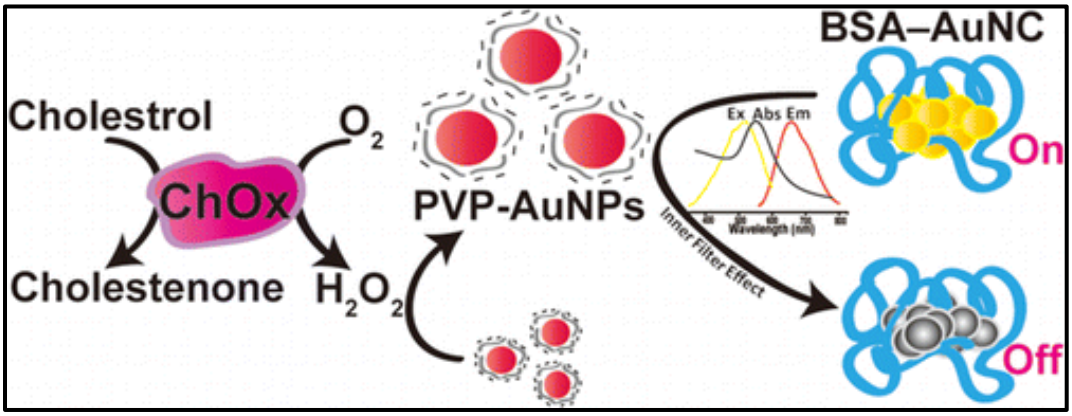

Figure 1.17. Schematic representation for the sensing of cholesterol based on inner filter effect (Chang & Ho, 2015).

Thus the SPR band of AuNP@PVP was enhanced with increasing concentration of H_2O_2 and, subsequently, induced significant fluorescence quenching of AuQC@BSA due to the overlap between the SPR absorption of

AuNP@PVP and the excitation of AuQC. The limit of detection of cholesterol by this method was 1.4 μM (Chang & Ho, 2015) (Figure 1.17).

Folic acid (FA) is an essential vitamin required for the healthy functioning of all cells. Deficiency of FA in the human body causes megaloblastic anemia and fetal development defects in humans (Hemmateenejad *et al.*, 2014). The analyte induced fluorescence quenching was established for the detection of FA using AuQC@BSA. The interaction between FA and BSA, changes in the local environment around the AuQCs causes fluorescence quenching. The detection limit of this probe was 18.3 ng/ mL.

Dopamine (DA) has been detected by various group by using protein stabilized QCs. It is an important neurotransmitter found in the central nervous system which controls the emotions. It helps to the real functioning of the central nervous, renal, hormonal, and cardiovascular systems. Abnormal concentrations of DA in the brain may result in neuropsychological diseases, such as Parkinsonism, Alzheimers, schizophrenia etc (Tao *et al.*, 2015).

Tao and co-workers reported BSA-stabilized AuQCs for the detection of dopamine (DA) by a colorimetric and fluorimetric method with a detection limit of 10 nM. The fluorescence quenching was due to the photo-induced electron transfer process from the electrostatically attached DA to the AuQCs@BSA. The colorimetric approach for DA detection was demonstrated by inhibiting the peroxidase-like activity of AuQCs in the presence of DA. Thus, the peroxidase substrate 3,3′,5,5′-tetramethylbenzidine (TMB) was unanalyzed when H_2O_2 is introduced and thus remained colorless. In the absence of DA, AuQC@BSA catalyzed the oxidation of TMB to form a blue-colored product (Tao *et al.*, 2013) (Figure 1.18).

In another case, AuQC@BSA were used for label-free detection of DA based on fluorescence quenching strategy. The quenching is due to an electron transfer process between QC and dopamine. They also demonstrated the DA detection in cerebrospinal fluid (Govindaraju *et al.*, 2017). Recently Miao et al.

reported that CuQC can be used for the detection of dopamine with a detection limit of 0.28 µM (Miao *et al.*, 2018).

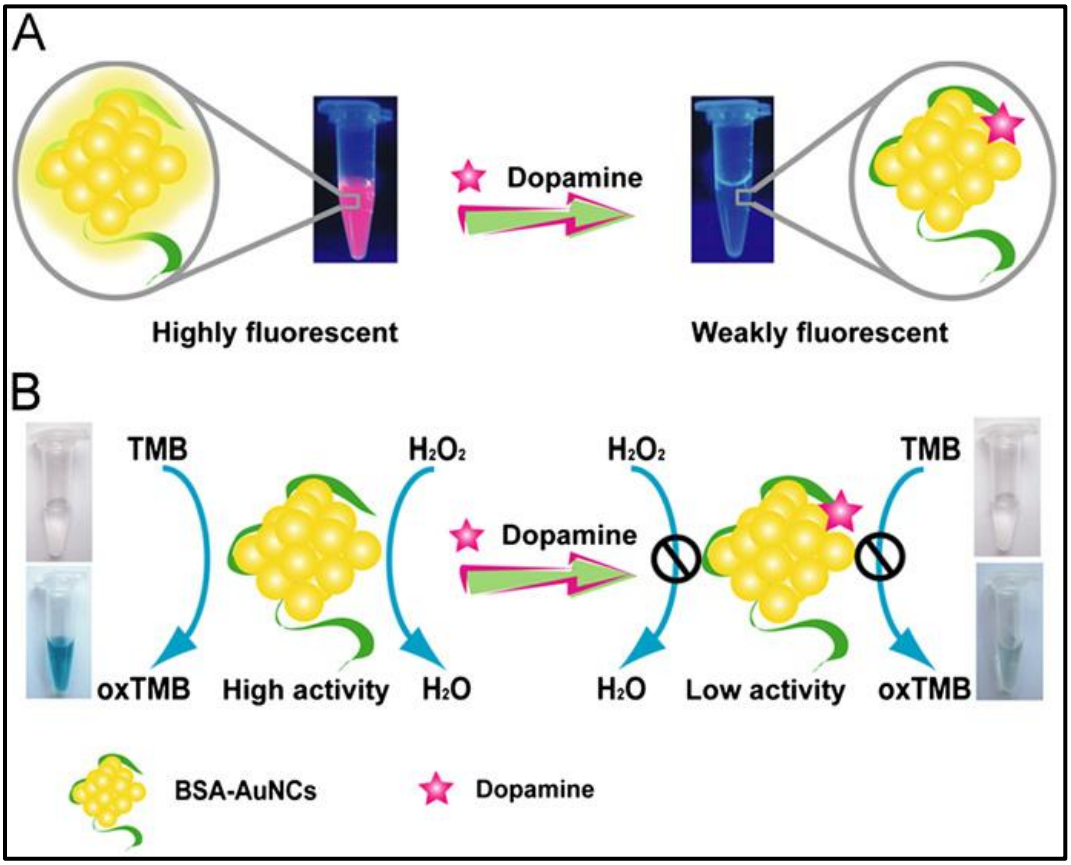

Figure 1.18. (A) Schematic illustration of the fluorescence response of the AuQC@BSA with DA. B) Schematic representation of peroxidase-like catalytic color reaction for sensitive sensing of DA (Tao *et al.*, 2013).

Biothiols such as cysteine (Cys), homocysteine (Hcy) and glutathione (GSH) etc play a vital role in human cellular functions and reversible redox reactions. The detection of their levels in human body fluids plays an important role in the early diagnosis of many diseases.

Tseng et al demonstrated glutathione (GSH) detection using lysozyme stabilized blue emitting Au_8QC through GSH-induced core-etching. They have validated the practicality of the sensor by detecting the level of GSH in a single drop of blood (Chen & Tseng, 2012; Zhai *et al.*, 2018).

The amino acid screening was carried out by using a dual emitting QC by the assistance of various metal ions. The dual emission originated from proteins and QCs respectively. The dual emission changed by four different metal ions and the combination of metal ions and amino acids together provide a sensor array for different amino acids such as leucine (Leu), alanine (Ala), proline (Pro), valine (Vla), serine (Ser), glutamine (Gln), cysteine (Cys), etc (Wang *et al.*, 2012).

Trypsin, the digestive enzyme, is utilized for the degradation of proteins into peptides. Moreover, trypsin plays a key role in controlling the pancreatic exocrine function and is a biomarker for pancreatitis (Wang., *et al.*, 2015). Trypsin detection was done by using AuQC@BSA. It is found that the AuQC@BSA shows enzyme mimicking activity at visible light. The QCs upon visible light irradiation used for the colorimetric detection of trypsin through trypsin digestion. The trypsin-digested the protein template of AuQC and decreased the catalytic activity of AuQC@BSA which leads to the colorimetric detection. The detection limit was found to be 0.6 μg/mL (Wang., *et al.*, 2015).

Cystatin C (Cys C) is a cysteine protease inhibitor found in the human body, which is a marker of glomerular filtration rate for kidney injury detection. Lin et al. detected Cys C using AuQC@BSA based on the BSA scaffold degradation caused by the cysteine protease activity of papain and the specific inhibition of papain activity by Cys C. The fluorescence of AuQC@BSA was quenched by papain, and restored by the coexistence of Cys C. The LOD was 4.0 ng mL^{-1}(Lin *et al.*, 2013).

Moreover, enzyme activity such as inorganic pyrophosphate, pyrophosphatase, acetylcholinesterase and alkaline phosphatase activity could be effectively analyzed by protein stabilized QC (Halawa *et al.*, 2017; Rong *et al.*, 2018; Selvaprakash & Chen, 2014; Xu *et al.*, 2017). For example, AuAgQC@BSA was utilized for the fabrication of inorganic pyrophosphatase (PPase) activity sensor in the presence of copper ion (Cu^{2+}) and inorganic pyrophosphate ion (PPi). Cu^{2+} was used as the fluorescent quencher, while PPi was employed as the hydrolytic substrate of PPase. In the absence of PPase, retention of fluorescence was

observed (Zhou., *et al.*, 2016). Schematic representation for the synthesis of bimetallic QC and its sensing strategy is shown in Figure 1.19.

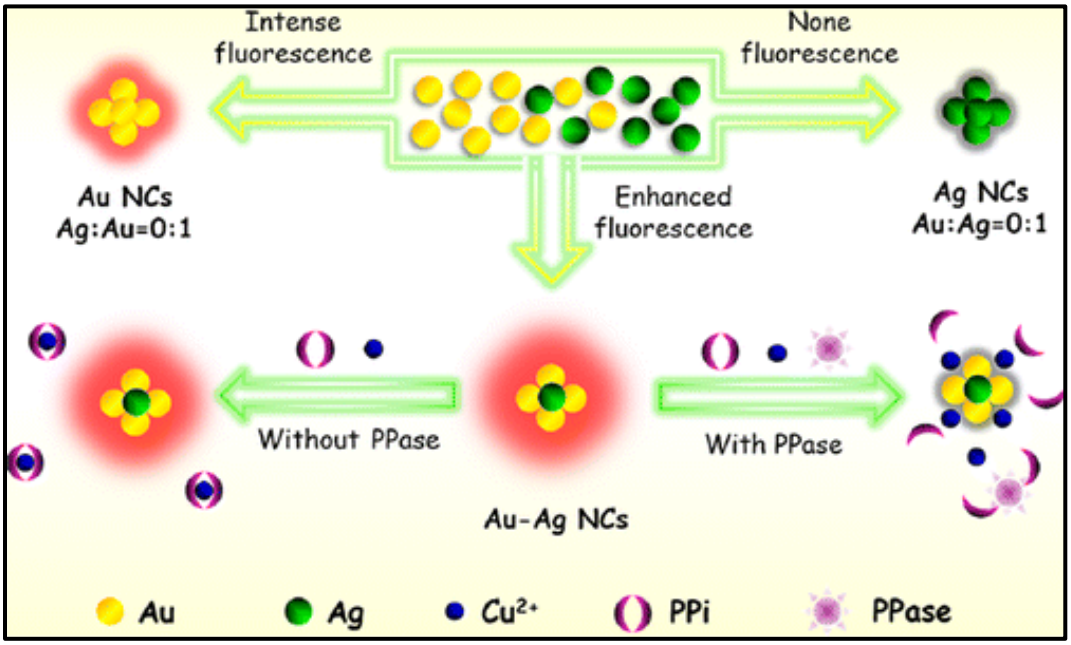

Figure 1.19. Schematic representation for the Synthesis of AuAgQC and thereafter the sensing of pyrophosphatase (PPase) activity (Zhou., *et al.*, 2016).

Rajamanikandan et al. prepared red emissive CuQC@BSA and applied it for the detection of creatinine in human urine samples (Rajamanikandan & Ilanchelian, 2018).

Ovalbumin (OVA) stabilized AuQC was used for the label-free detection of ascorbic acid (AA). The fluorescence of Au QC was found to be quenched effectively through the oxidation state change of AuQC by AA (Li., *et al.*, 2015).

1.4.1.5. Bacteria detection

The lysozymes stabilized AuQC retains the specific recognition ability for bacteria such as Escherichia coli (E. coli) and hence is used for the specific detection E.coli. Meanwhile the BSA stabilized AuQCs could not recognize E. coli and no fluorescence enhancement was observed (Chan & Chen, 2012; Liu., *et al.*, 2015).

Chan et al used HSA stabilized AuQC for the detection of pathogenic bacteria -Staphylococcus aureus and methicillin-resistant S. aureus (MRSA). The AuQC@HSA exhibit specific binding affinity with S. aureus and MRSA due to the interaction of the peptide motifs on HSA of AuQC@HSA with the cell wall of the bacteria. The limit of detection of bacteria by the naked eye was $\sim 10^6$ cells/mL (Chan & Chen, 2012).

1.4.2. Biological labeling and imaging

In recent times, Scientists have taken much efforts for exploring the use of metal quantum clusters for biological labeling and imaging. Among various fluorescent QCs, the protein stabilized QCs are much suitable candidates for this application due to their unique functionality, large Stoke shifts, easy bio-conjugation, and excellent biocompatibility. Generally, the fluorescent QCs can be internalized by cells via either receptor-mediated or non-specific endocytosis (Zheng *et al.*, 2017).

In-vivo tumor fluorescence imaging using near IR emitting BSA protected AuQC was first reported by Wu et al in 2010. They demonstrated the ability of AuQC for high tumor uptake in MDA-MB-45 and Hela tumors in mice (Wu *et al.*, 2010).

Chen and co-workers studied the tumor imaging ability of AuQC@BSA. The QCs were conjugated with two different near-infrared fluorescent dyes, methionine (Met) and MPA, to form Au-Met-MPA and found that the nanoprobe was internalized in MCF-7 tumor cells and had little effect to a normal cell (L02) (Chen, H., Li, *et al.*, 2012).

The targeted imaging was carried out by conjugating bio-recognition elements to MQC through reactions with amino, carboxyl and thiol functional group on the protein shell of QC. Examples of targeted moieties that have been used for the targeted imaging are Herceptin and folic acid, which will specifically bind to cancer cells. Archana et al. have proven for the first time that folic acid (FA) conjugated AuQC@BSA can be used for folate-targeted imaging of oral

carcinoma cells. Followed by this work, protein templated metal QCs have been widely applied for in-vitro and in-vivo imaging of cancer cells (Archana *et al.*, 2010).

Wang and co-workers demonstrated Herceptin conjugated BSA-protected AuQCs for specific targeting and nuclear localization in ErbB2 over-expressed breast cancer cells and tumor tissues (Wang., *et al.*, 2011).

Recently Nebu et al. have developed a nanocomposite that contains, super paramagnetic iron oxide core with erlotinib conjugated Au@BSA. The resulting Fe_3O_4@AuNC@erlotinib was used for the targeted imaging of pancreatic cancer cell, e PANC-1 (Nebu *et al.*, 2018).

Zhou et al prepared FA-conjugated AuQC@SiO_2 nanoprobe for targeted imaging in FR (+) MGC-803 cells and in-vivo gastric cancer tissues using fluorescence imaging. Along with fluorescence imaging (FI) technique, a computed tomography (CT) imaging technique was also used for tumor imaging due to the fact that AuQCs inherently possess both FI and X-ray capability (Zhou., *et al.*, 2013). These type of multimodal imaging can provide complementary information and allow reliable and accurate diagnosis of diseases.

In another case, gadolinium(III) functionalized AuQC@BSA was used as a multimodal imaging probe. The AuQC@BSA-Gd(II) probe facilitate triple modal imaging based on fluorescence/MRI/CT for in vivo tumor-bearing mice. All the three imaging technique provide information about tumor site by the noticeable accumulation of nanoprobe (Hu., *et al.*, 2013) (Figure 1.20). Moreover, the probe quickly clears by renal excretion, indicating its capacity of low body residues. After this work, several groups employed Gd functionalized protein stabilized quantum cluster for multimodal imaging (You *et al.*, 2017).

Shibu et al. fabricated a nanohybrid by conjugation of biotinylated AuQC@BSA to streptavidin-functionalized Fe_3O_4 nanoparticles. An epidermal growth factor was (EGF) conjugated into Fe_3O_4 nanoparticles, and both nanoparticle and AuQC could be delivered into the cells.

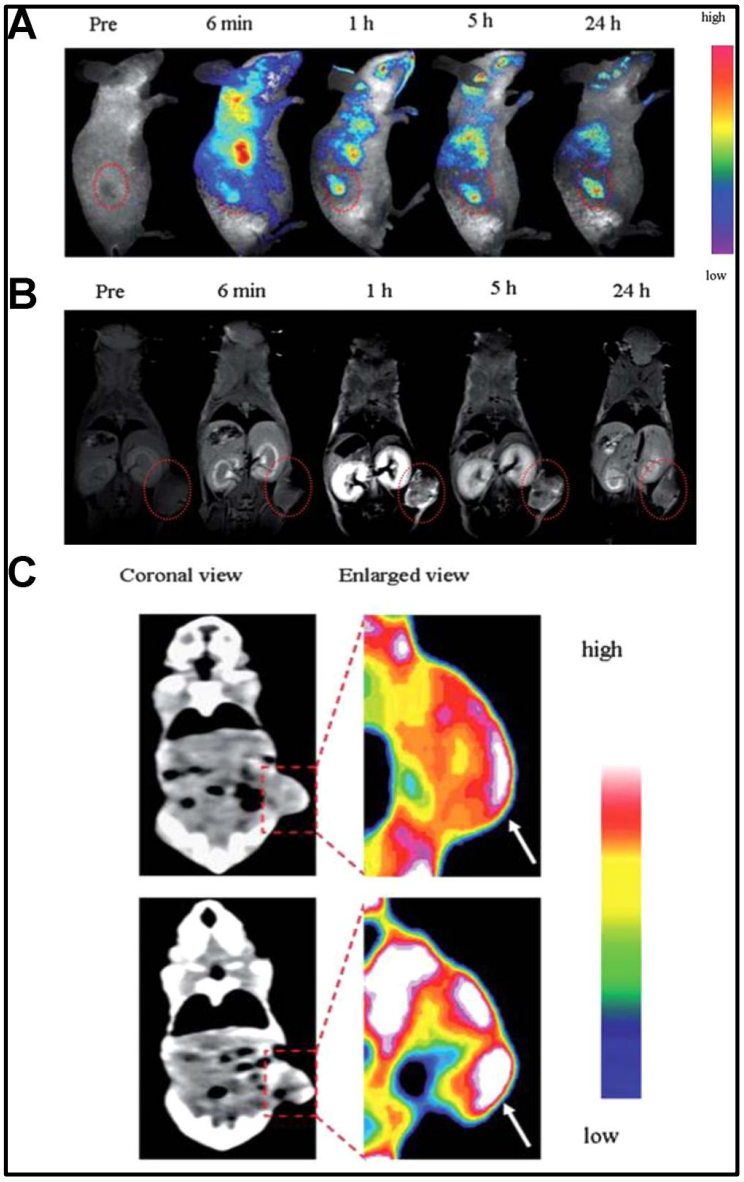

Figure 1.20. In vivo (A) fluorescence, (B) MRI, and (C) CT imaging of tumor-bearing mice after the tail injection of AuQC@BSA based multimodal imaging probe (Hu., *et al.*, 2013a).

This is recognized by both NIR fluorescence and magnetic resonance imaging (MRI) technique for live cell imaging (Shibu *et al.*, 2013). Similar to BSA stabilized AuQC, other protein protected MQCs also expand the area of bio-imaging. In some cases, protein protected QCs retains the biological activity of the protein, after QC formation can be used directly to targeted imaging of specific cells without altering the surface chemistry of QC. For example, insulin and human transferrin stabilized AuQC used for fluorescence imaging. In the

case of insulin stabilized AuQCs, it can directly target insulin receptor overexpressed C2C12 cells through receptor-mediated endocytosis (Liu *et al.*, 2011).

Transferrin stabilized AuQCs also applied for targeted imaging in transferrin receptor overexpressed A549 cells (Le, Daum, *et al.*, 2011). Wang et al fabricated a nanocomposite contains transferrin (Tf)-functionalized AuQC and graphene oxide (GO) as a turn-on near-infrared (NIR) fluorescent probe for bioimaging in cancer cells and small animals. Tf acted not only as a stabilizer and a reducer but also as a functional ligand for targeting the transferrin receptor (TfR). GO quenches the fluorescence of TfAuQCs. When the composite enters into the TfR overexpressed cell (Hela cell),

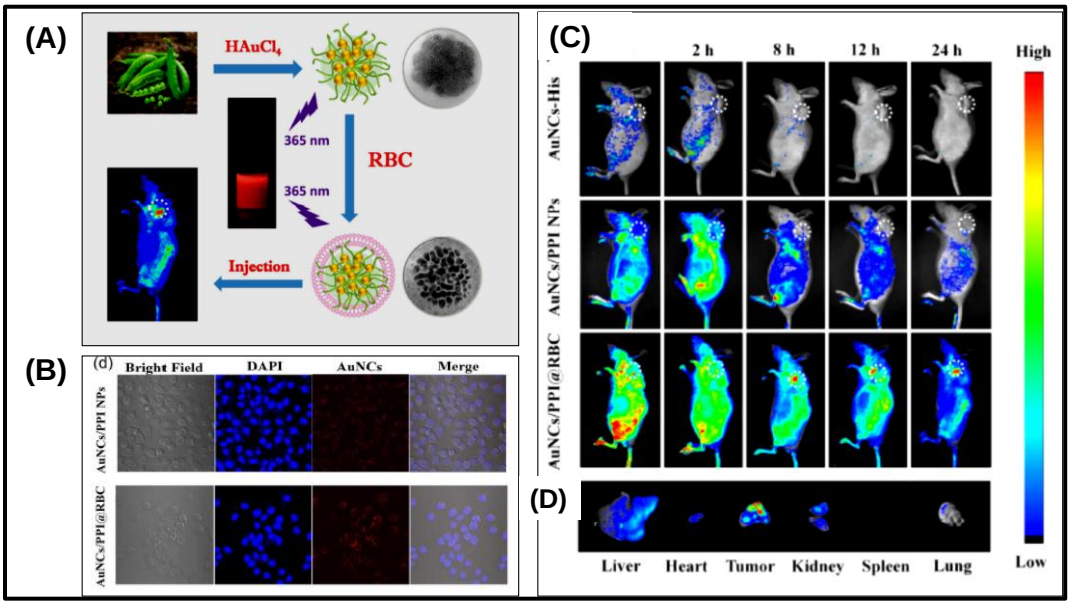

Figure 1.21. (A) Schematic representation of the synthesis of AuNCs/PPI@RBC and its bioimaging application in a tumor-bearing mouse. (B) Confocal images of MCF-7 cells incubated with AuNCs/PPI NPs and AuNCs/PPI@RBC for 4 h. (C)(a) Real-time NIR fluorescence images in vivo after intravenous injection of AuNCs reduced by His (upper panel), AuNCs/PPI NPs (middle panel) and AuNCs/PPI@RBC (lower panel) in tumor-bearing mice for 1 h, 2 h, 8 h, 12 h and 24 h; (b) Ex vivo tissue images of tumor bearing-mouse injected with AuNCs/PPI@RBC (from left to right: liver, heart, tumor, kidney, spleen, and lung).(Li., *et al.*, 2017)

the fluorescence of the QC was restored due to the specific interaction between Tf and TfR (Wang., *et al.*, 2013). Qiao and co-workers used ovalbumin stabilized Au QCs for targeted cancer cell imaging using homopolymer N-acryloxysuccinimide as the linker and folic acid as a targeted moiety (Qiao *et al.*, 2013).

Recently, Li et al. demonstrated the use of plant protein protected AuQC for imaging. The protein derived from pea- (pea protein isolate (PPI)) has been used as a stabilizing agent (Li., *et al.*, 2018).

The AuQC/PPI was encapsulated into RBC membrane-derived vesicles to extend the blood circulation and avoid the macrophages uptake. The confocal and real-time NIR fluorescence images shows the enhanced uptake of AuNCs/PPI@RBC in the tumor site, which is due to the longer blood circulation and enhanced permeability and retention (EPR) effect of AuQC (Figure 1.21)

1.4.3. Drug delivery and cancer therapy

Protein stabilized metal QCs have been used for drug delivery and cancer therapy applications due to the presence of functional groups of proteins that facilitate easy loadings of therapeutic drugs. There are several drugs that have been incorporated and delivered using protein stabilised QC, which include, doxorubicin, cisplatin, camptothecin, and sorafenib (Bhattacharyya & Mukherjee, 2018; Chen, H., Li, B., *et al.*, 2012; Zhou, F. *et al.*, 2016).

Chen et al. shows that the folic acid (FA) conjugated AuQCs@BSA could be utilized for targeted doxorubicin (DOX) delivery. DOX is a widely used clinical anticancer drug. Additionally, they have conjugated a near-infrared (NIR) fluorescent dye, MPA on AuQC-FA for in vitro and in vivo fluorescence imaging. The DOX-loaded on AuQC–FA (AuQC–FA–DOX) shows high anti-tumor activity (Chen., Li., *et al.*, 2012).

Later, Khandelia et al demonstrated the in-vitro delivery of doxorubicin (DOX) to cancer cells using Au@BSA by the assistance of both one- and two-

photon imaging techniques (Khandelia *et al.,* 2015). The same group used lysozyme stabilized AuQCs for efficient delivery of doxorubicin-to cancer cell and noticed that a 90% cell death was observed in breast cancer cell- MCF7 and a 40 % cell death was observed in normal breast cell- MCF 10A (Chattoraj *et al.*, 2016).

Shamsipur et al. developed hemoglobin stabilized AgQCs and conjugated it with hyaluronic acid (HA) and doxorubicin drug (DOX) as DOX/HA/AgQC for targeted imaging and delivery of DOX into CD44-overexpressing cancer cells, which lead to an increased suppression of tumor cell growth (Shamsipur *et al.*, 2018).

Retnakumari et al. have demonstrated the delivery of an anticancer drug sorafenib using hybrid nanoconjugate that contains antibodies, polymeric linkers, and AuQCs@HSA. They have loaded with STAT5 inhibitor (sorafenib) on the QC and conjugated with transferrin (Tf) ligands for TfR specific delivery. They found that the nanoconjugate shows enhanced antileukemic activity and maximum uptake was observed in samples containing the highest level of STAT5 and TfR expression (Retnakumari *et al.*, 2012).

Zhou et al. show the targeted delivery of cisplatin drug in breast cancer cells using folic acid conjugated AuQC. The schematic representation for the development of nanocarrier and delivery is shown Figure 1.22A. They found that the nanoconjugate significantly inhibit the growth and lung metastasis of the orthotopically implanted 4T1 breast tumors (Figure 1.22 B) (Zhou., *et al.*, 2016).

Chen et al. synthesized core-shell structured multifunctional nano carriers for anticancer drug camptothecin. Here the AuQC acted as a core and FA-conjugated sulfated polysaccharide (GPPS–FA) as a shell, based on poly(l-lactide) (PLA) inner arm. The hybrid product Au NCs–PLA–GPPS–FA was used for targeted anticancer therapeutics. They observed that a controlled release into HeLa cell and damaging of the cell was possible using the nanohybrid (Chen., *et al.*, 2012).

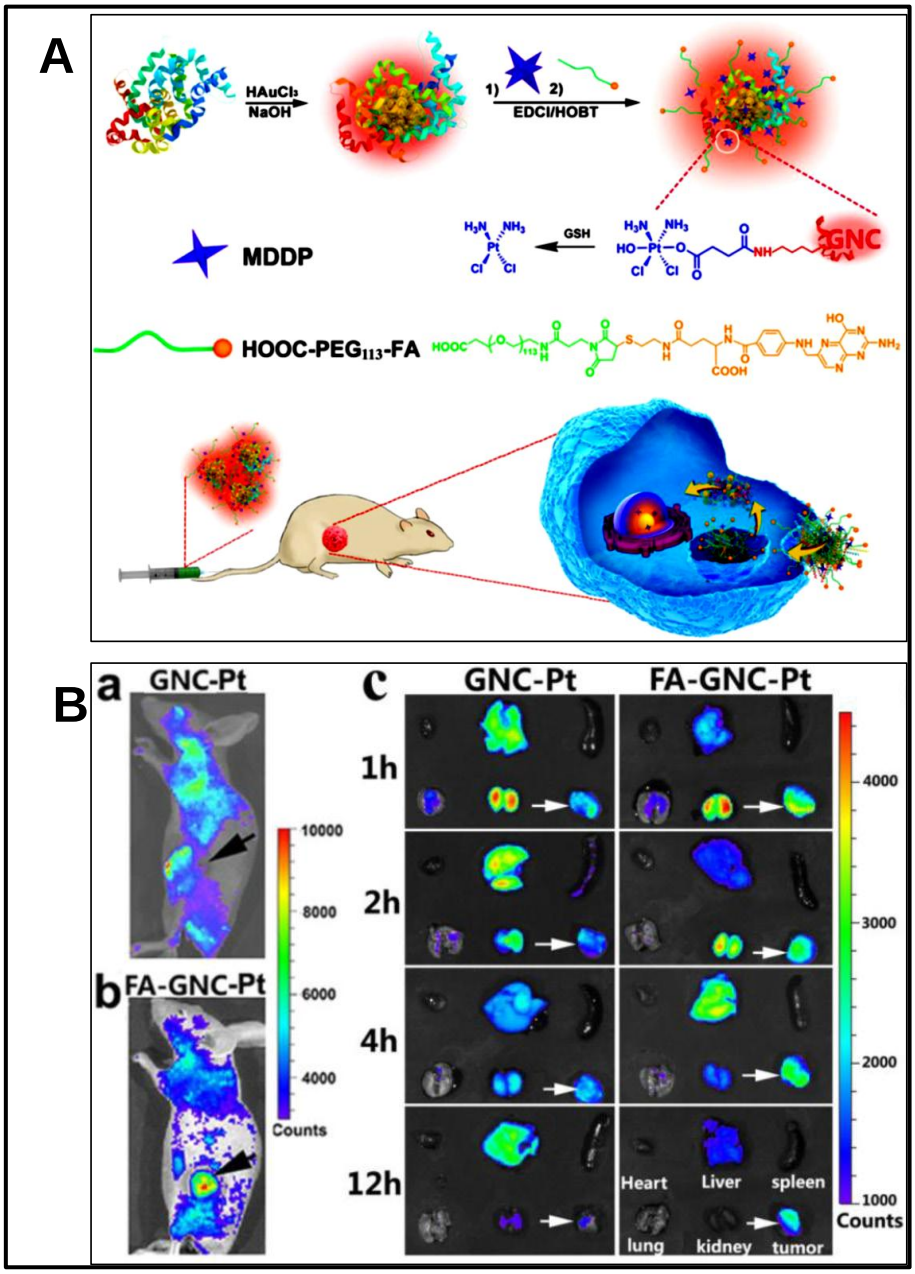

Figure 1.22. (A) Schematic illustration of synthesis and modification of GNC-based nanoconjugate for tumor-targeted chemotherapy and fluorescence imaging. (B) In vivo (a and b) and ex-vivo (c) fluorescence imaging and organ distribution of the FA-GNC-Pt and GNC-Pt nanoparticles in 4T1 tumor-bearing nude mice at a different time interval. The white arrows showed the location of the tumor. (Zhou., *et al.*, 2016)

Cui et al. prepared gold cluster nanoassembly (Au CNA) by protein cross-linking approach. The nanoprobe exhibited noticeable cellular uptake and tumor targeting. The probe was also used for photodynamic therapy (PDT). Upon the irradiation of 660 nm laser, Au CNA generated a large amount of reactive oxygen

species (ROS) for photodynamic therapy (PDT) (Cui., *et al.*, 2017). Similarly, Yu et al. demonstrated the potential use of Ag_{13}BSA in photodynamic therapy (PDT). They found that the QC has the ability to generate strong singlet oxygen and effectively killed the breast cancer cells, MCF-7 (Yu *et al.*, 2016).

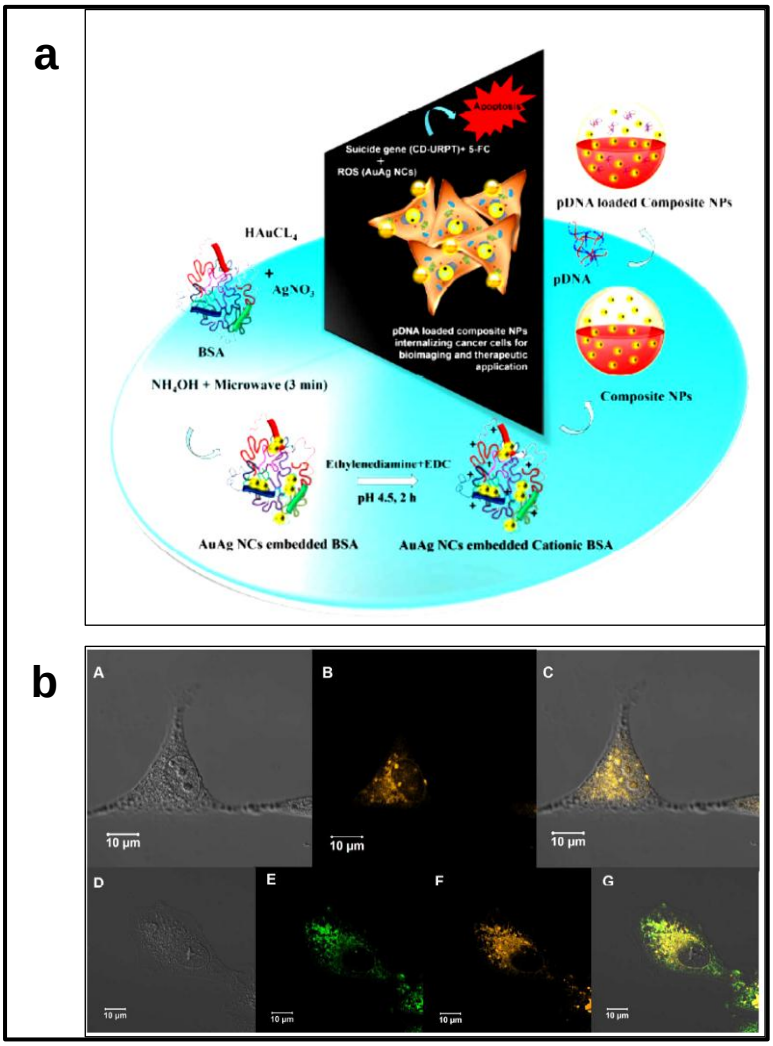

Figure 1.23. (a) The schematic representation for the synthesis of cationic AuAgQC@BSA composite NPs for suicide gene delivery therapy. (b) Confocal microscopic images. (A) Bright field image, (B) fluorescence image and (C) merged fluorescence image (D) Bright field image of HeLa cells treated with pDNA loaded composite NPs and cytopainter green lysosomal staining kit, (E) fluorescence image showing green fluorescence from stained lysosomes of HeLa cells treated with pDNA loaded composite NPs and cytopainter green lysosomal staining kit, (F) fluorescence image showing fluorescent pDNA loaded composite from NPs inside HeLa cells treated with pDNA loaded composite NPs and cytopainter green lysosomal staining kit, (G) merged fluorescence image. (Dutta *et al.*, 2016)

Gene delivery is another approach used in the clinical treatment of cancer diseases. Dutta and co-workers demonstrated the delivery of therapeutic suicide gene (CD-UPRT) in cancer cells by using cationic BSA stabilized AuAg bimetallic quantum clusters. The QC loaded with pDNA, was effectively entrapped by cancer cells and the luminescence of QC was used for tracking the delivery of pDNA into cells (Figure 1.23). Moreover, the QCs produces ROS (reactive oxygen species), which caused apoptosis-mediated cell death (Dutta *et al.*, 2016). The schematic description of the formation of nanoprobe and its therapeutic response is shown in Figure 1.23 a. The confocal studies confirm the uptake of the composite into the lysosomal compartments (Figure 1.23 b).

1.5. Scope and objectives of the work

From the forgoing discussions, it is found that, NMQCs have intrinsically attractive optical, electronic and chemical features broaden the applications in various areas, from bio-sensing to bio-imaging, drug delivery and therapy. Compared with other protected QCs, protein protected clusters shows advantages such as one- pot and green synthesis, the formation of QC at mild reaction conditions, good aqueous solubility, superb biocompatibility, versatile surface chemistries etc. Even though the protein protected clusters are advantageous in many of these aspects, it has several challenges such as the cost of the proteins derived from animals and insects are comparatively high and the stability towards various other biological species and the condition is comparatively less which limits its biomedical application. Thus we attempted to address some of the challenges by synthesizing new protein protected clusters and exploring it for biomedical applications. The major objectives of present research are

- Synthesis and characterization of various metal QC using sustainable protein as protecting and stabilizing agent
- Surface modification of the synthesised quantum clusters for particular applications
- Development of biosensors using the synthesized QCs and underlying the possible sensing mechanism

The major strategies employed for the development of fluorescent sensors are

1. Enzymatic sensing
2. Turn-on sensing
3. Fluorescence quenching
4. Ratiometric sensing

- Explore the use of QC as a nanocarrier for drug delivery and bio-imaging application

  The strategies applied for Drug delivery are

  1. Diffusion-controlled delivery
  2. Targeted delivery

1.6. Organization of the thesis

Chapter 1 discusses the recent progress in the synthesis of protein-directed approaches for QC. The synthetic protocols, formation mechanisms, characterizations, purification, surface functionalization and key applications in the biomedical field such as bio-sensing, imaging, and therapy are discussed.

Chapter 2 demonstrates the synthesis of BSA protected AuQC and the conjugation of an enzyme AChE for the highly selective and sensitive sensing of acetylcholine (ACh). Real-time monitoring of the hydrolysis of ACh using electrospray ionization mass spectrometry was carried out to find out the mechanism of interaction.

Chapter 3 describes the sustainable one-pot synthesis of water-soluble fluorescent gold quantum clusters using plant-derived protein, gluten, as a protecting and stabilizing ligand. Then an elaborative discussion on the turn-on detection of creatinine in the human blood using AuQC@gluten and a detailed discussion on the mechanism of sensing is included.

Chapter 4 elaborates the synthesis of highly stable gold-silver alloy quantum cluster using gluten as a protecting and stabilizing ligand through GER. This chapter also discusses the development of bilirubin sensor based on

AgAuQC@gluten by fluorescence quenching strategy. A detailed investigation on the probable mechanism for fluorescence quenching by bilirubin is also discussed in this chapter.

Chapter 5 discusses the synthesis of sustainable resource-based dual emitting GQD-AuQC (AuQC@GQD) composite for ratiometric sensing of Hg^{2+}, using gluten protein as raw material. A detailed investigation on the formation mechanism of dual emitting nanocomposite and optimization of the reaction condition is explained in this chapter. Incorporation of this nanohybrid on PVA nanofibre by the electrospun process, and thereafter the efficient visual detection of Hg^{2+} is also demonstrated.

Chapter 6 outline the synthesis of gluten stabilized CuQC and incorporation of QC into a polymer matrix for the development of intrauterine device application. The Cu (II) ion release kinetics from the composite was studied. The biocompatibility of the composite is also discussed.

Chapter 7 explains the synthesis of gliadin protected AuQC and loading of hydrophobic drug CUR into the AuQC@gliadin for improving its bioavailability and increasing the therapeutic effect of cancer. The Photophysical studies of CUR in QC, release kinetics of CUR from QC, and the cellular uptake is also explained in this chapter.

Chapter 8 summarizes the conclusions drawn from the present thesis and highlights on the future scope of the work.

CHAPTER 2

ENZYME CONJUGATED BSA PROTECTED GOLD QUANTUM CLUSTER FOR ACETYLCHOLINE SENSING

This chapter deals with fluorescent detection of acetylcholine (ACh) using bovine serum albumin (BSA) protected atomically precise clusters of gold. The gold quantum clusters (Au_{QC}@BSA) synthesized using bovine serum albumin and conjugated with acetylcholinesterase (AChE), an enzyme specific for acetylcholine, resulting in Au_{QC}@BSA-AChE. The enzyme, AChE hydrolyzes acetylcholine (ACh) to choline (Ch) which in turn interacts with Au_{QC}@BSA-AChE and quenches its fluorescence, enabling sensing. The validity of present method for determination of concentration of acetylcholine in real system such as blood was demonstrated. Further, the sensor, Au_{QC}@BSA-AChE can be easily coated on paper and an efficient and cheap sensor can be developed and detection limit for ACh is found to be 10 nM.

Part of this chapter has been published in Biosensors and Bioelectronics (2016), Vol: 81, 8168–74

2.1. Introduction

Acetylcholine (ACh) is one of the most important neurotransmitters found in the human central and peripheral nervous systems. Acetylcholinesterase (AChE) catalyses the hydrolysis of ACh to choline and acetate (He *et al.*, 2014). It is mainly found at the neuromuscular junction and in animal synapse. An abnormally low concentration of ACh can cause various neuropsychological and neuropsychiatric disorders such as Alzheimer's disease, Parkinson's disease (Blokland, 1995) etc. The main reason behind the Alzheimer's disease is the decreased levels of ACh and the enzymes responsible for its synthesis and degradation in the brain (Mueller *et al.*, 2005). Thus, by monitoring the activity of AChE and measuring the concentration of ACh in the human body, one could detect Alzheimer's in its early stage. The level of ACh of a healthy person in blood can be varied from 0.20 to 1.31 µM/L with a geometric mean of 0.49 µM /L (Watanabe *et al.*, 1986). Clearly, a patient suffering from Alzheimer's will have still lower level of ACh than 0.20 µM Ach (Mueller *et al.*, 2005; Watanabe *et al.*, 1986).

Recently, Wei and co-workers have detected ACh using carbon dots (Wei *et al.*, 2014). They have developed a biosensor for the detection of acetylcholine based on the detection of H_2O_2. In this process, ACh decomposes into choline and acetate by AChE. The product choline is decomposed further by another enzyme, choline oxidase (ChOx) to betaine and H_2O_2, followed by Fenton reaction and the resulting hydroxyl group quenches fluorescence of carbon dot. Johnson et al. designed a semi-synthetic fluorescence-based probe, ACh-SNIFIT, for direct, real-time detection of acetylcholine and anticholinesterase (Schena & Johnsson, 2014). Liu and co-workers utilized Rhodamine B modified gold nanoparticles for sensing AChE (Liu *et al.*, 2012). The above mentioned sensors are based on the principle of fluorescence quenching or enhancement and typically employ organic dyes. However, many of organic fluorophore are toxic and unstable with a poor selectivity for the target analyte and hence practical applications for real systems are difficult to achieve. In comparison, protein protected noble metal QCs are bio-compatible and can be used as effective probes for sensing (Hu.,*et al.*, 2015a).

Chen and his co-workers developed a sensor for detection of activity of acetylcholinesterse enzyme using denatured BSA protected cluster. They have indirectly detected activity of acetylcholinesterase using acetylthiocholine iodide as substrate (Li., *et al.*, 2014). Compared to other nanomaterial based sensor such as semiconductor quantum dots, metal QC based sensor got tremendous attention because of their biocompatibility and non-cytotoxicity over other nanomaterials, whose biomedical application is restricted due to their toxicity in biological systems and relatively large size.

Here, we report a novel bio-friendly fluorescence based direct detection of ACh using AChE conjugated BSA protected gold quantum clusters (QCs), (AuQC@BSA-AChE). The selective and sensitive detection of ACh via its hydrolysis to choline and acetate by AChE on AuQC@BSA. The generated choline interacts with the Au QCs and quenches the fluorescence of AuQC@BSA-AChE. The practicality of the Au_{QC}@BSA-AChE sensing system was validated through the detection of ACh in real blood samples. The Au_{QC}@BSA-AChE can be easily coated on a filter paper and an efficient sensor for onsite detection of acetylcholine was developed. Thus, our sensor (AuQC@BSA-AChE) can be used for early stage diagnosis of neuropsychiatric diseases such as Alzheimer's, Parkinson's etc.

2.2. Experimental Section

2.2.1. Materials

All the reagents were used as obtained without further purification unless stated otherwise. $HAuCl_4.3H_2O$, BSA, the membrane dialysis bag (molecular weight cut-off 12 kDa), AChE (Type C3389, 500 U mg^{-1} from electric eel), acetylcholine chloride, choline chloride, glucose, fructose, glycine, lysine, sodium dihydrogen phosphate, and disodium hydrogen phosphate were purchased from Sigma Aldrich. All solutions were prepared using Millipore water. Stock solutions of ACh, choline and AChE were prepared using phosphate buffer of pH 8 (0.05M).

2.2.2. Instrumentation

UV-visible absorption spectra were recorded in the range of 200-800 nm using the Varian model, Cary win Bio 100 spectrometer. All steady-state fluorescence measurements were made using the Fluoro Max-4C spectrofluorometer (Horiba Instruments, USA). The emission spectra were recorded upon excitation at 400 nm; the slit width for excitation and emission were set at 5 nm. HRTEM images were obtained with a JEOL 3010 instrument. Here the dilute solution of QC was drop casted over the carbon coated grid, dried at room temperature and used for TEM analysis. For MALDI -TOF MS analysis, the Applied Biosystems Voyeger-DE-pro instrument was used and sinapic acid was used as the matrix. Hydrodynamic volume and zeta potential measurements were performed using particle size analyzer (Zetasizer Nano ZS series, Malvern instruments).

2.2.3. Preparation of Au_{QC}@BSA

The red luminescent Au_{QC}@BSA was synthesized by a previously reported method (Mohanty *et al.*, 2015). Briefly, 10 mL aqueous solution of $HAuCl_4$ (6 mM) was added to 10 mL BSA (25 mg/mL in water) with vigorous stirring for 5 min, followed by the addition of 1 mL of 1 M NaOH solution to maintain the basicity (pH 12) of the system. The reaction was continued for 24 h under mild stirring. The golden yellow solution slowly changed to dark orange with intense red luminescence under UV irradiation, indicating the formation of gold QCs. Purification of Au_{QC}@BSA was performed by dialysis against distilled water for 24 h in a dialysis membrane of molecular weight cut-off 12 kDa. The cleaned gold clusters were then freeze dried and stored at 4 ºC for further use.

2.2.4. Preparation of synthesis of Au_{QC}@BSA-AChE

Synthesis of Au_{QC}@BSA-AChE was carried out by mixing of AChE with Au_{QC}@BSA. The dialysed and freeze dried gold clusters were dissolved in a phosphate buffer at pH 8, since the optimum pH for AChE activity is 8-9.

Au_{QC}@BSA-AChE was prepared by treating 10 mL of the gold cluster solution with 1 mL of AChE (0.4 µM) dissolved in phosphate buffer (pH 8) at room temperature under mild stirring, followed by a reaction time of 2 h and stored at 4^0C for further use.

2.2.5. Development of test strips for detection of ACh

The Au_{QC}@BSA-AChE coated sensor was developed in a simple way. Briefly, Whatman No 41 filter paper were cut into small pieces (2cm x 2cm) and soaked in 10 mL Au_{QC}@BSA-AChE (at a concentration of 0.4 µM) solution taken in a beaker for about 24 h. After drying in air (approximately 2 hour), 20 µL of different concentration of ACh is drop casted. The Au_{QC}@BSA-AChE coated sensor before and after the treatment of ACh is placed under UV light (360 nm) and changes in the color has been noted.

2.2.6. Method of detection of acetylcholine in blood

Blood samples were collected from a healthy adult volunteer and samples were spiked with different concentration of acetylcholine and incubated for 30 min. The above ACh spiked blood and blood without ACh spike is treated with 3 mL of Au_{QC}@BSA-AChE and changes in fluorescent intensity at 670 nm was monitored. This study was approved by ethical committee of Indian Institute of Space Science and Technology (IIST) (IIST/IEC/2016/CHE-01).

2.3. Results and Discussion

2.3.1. Synthesis of Au_{QC}@BSA-AChE conjugate

A schematic of our experiment is shown in Figure 2.1. We have synthesized highly fluorescent BSA protected gold quantum clusters (Au_{QC}@BSA). MALDI MS showed the presence of Au core containing 30 atoms with a molecular ion peak at m/z 72 kDa, based on which the cluster was assigned as Au_{30}@BSA. Parent BSA exhibits a mass peak at m/z 66 kDa (Figure.2.2 (a)).

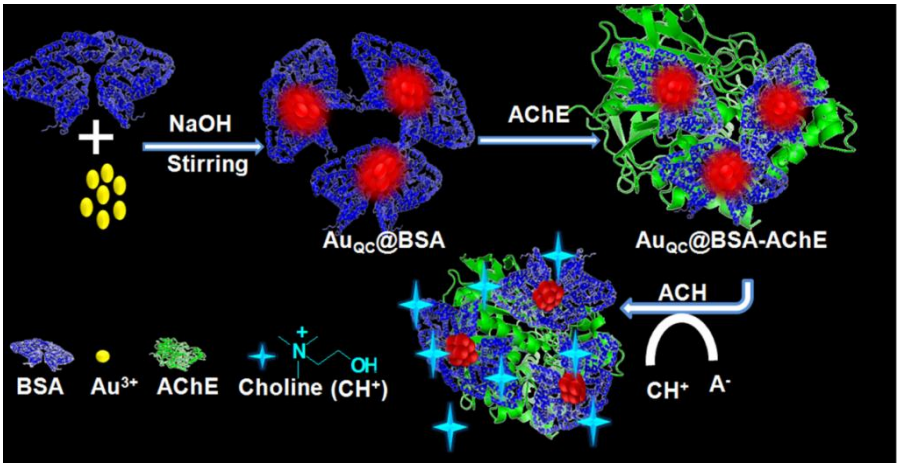

Figure 2.1. Schematic representation of synthesis of Au_{QC}@BSA, Au_{QC}@BSA-AChE and consecutive detection of acetylcholine via fluorescence quenching.

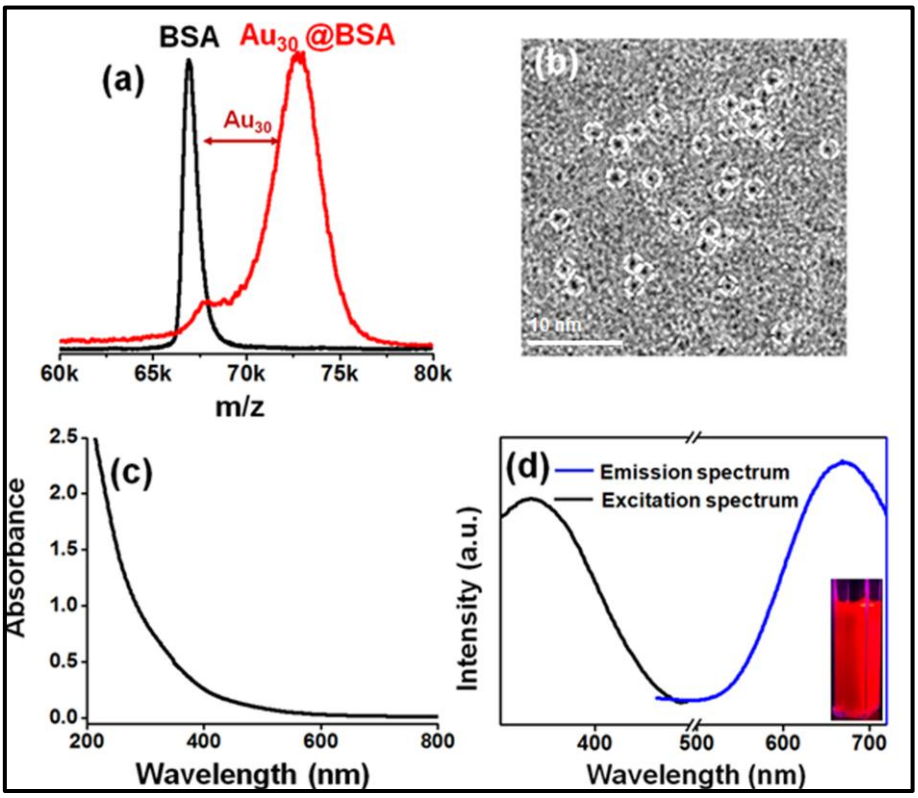

Figure. 2.2. (a) MALDI TOF MS of BSA (black trace) and Au_{QC}@BSA (red trace). (b) TEM image of Au_{QC}@BSA, some of them are circled. (c) UV –Visible absorption spectrum of Au_{QC}@BSA (d) Fluorescence excitation (black trace) and emission spectrum (blue trace) of Au_{QC}@BSA. Photograph of Au_{QC}@BSA under UV light irradiation (365 excitation) is shown in the inset.

Presence of larger plasmonic nanoparticles in the sample was ruled out by UV-Vis absorption spectra (absence of plasmon band at 520 nm) (Figure.2.2 (c)) and TEM

image (size of the particles seen was of about 1 nm) (Figure.2.2 (b)). The cluster solution shows a red luminescence under UV exposure. The emission maximum is at 677 nm with an excitation maximum at 365 nm (Figure. 2.2 (d)).

Recently, Mohanty et al. have shown that BSA can form conjugate with lysozyme (Lyz) by simple mixing with each other (Mohanty *et al.*, 2015). Proteins are well known to form aggregates mostly due to salt bridge interaction between one units with the other. Mixed protein conjugates are also possible when multiple proteins are present in the same mixture.

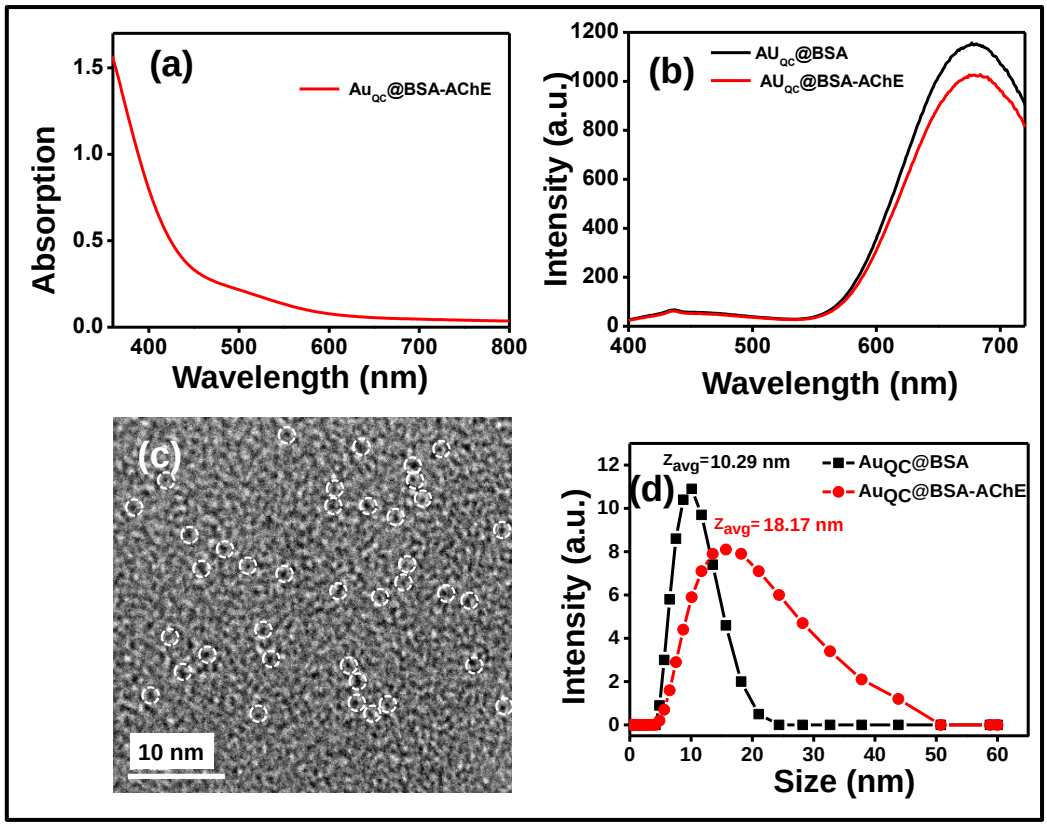

Figure. 2.3. (a)UV-visible absorption spectrum of Au_{QC}@BSA-AChE.(b)Fluorescence emission spectra of BSA protected cluster (Au_{QC}@BSA)(black) and acetylcholinesterase conjugated cluster (Au_{QC}@BSA-AChE) (red). (c) TEM image of AChE conjugated cluster (Au_{QC}@BSA-AChE) with cluster core of 1 nm. Some of them are circled. (d) Particle size distribution of Au_{QC}@BSA and Au_{QC}@BSA-AChE.

Nair et al. also reported that conjugation of glutathione protected Au cluster and urease can be accomplished by mixing Au cluster and urease (Nair *et*

al., 2013). We have carried out conjugation of AChE over Au_{QC}@BSA by mixing AChE with Au_{QC}@BSA and stirred for 2h. There was no considerable change in the optical properties of cluster before and after the treatment of AChE. UV-Visible absorption spectra and PL spectra of Au_{QC}@BSA before and after the addition of ACh are shown in Figure 2.3. Due to the instrumental limitation, number of AChE conjugated to the cluster were unable to found out because of the large mass of AChE (260 kDa for AChE whereas mass of the Au_{QC}@BSA is around 72 kDa). TEM image shows that size and morphology of the cluster remains same after conjugation of AChE (Figure 2.3 (c)). Further we have analysed the change in hydrodynamic volume of Au_{QC}@BSA before and after conjugation of enzyme using dynamic light scattering technique. Here after conjugation of AChE, average diameter of Au_{QC}@BSA is changed from 10. 29 nm to 18.17 nm, which implies the adsorption of AChE over AuQC@BSA (Figure 2.3 (d)). Zeta potential measurements were performed before and after the treatment of AChE. The studies showed a significant decrease in zeta potential of Au_{QC}@BSA from -20 mV to -12 mV after AChE treatment. This reflects the conjugation AChE to Au_{QC}@BSA through strong electrostatic interaction between Au_{QC}@BSA and AChE.

2.3.2. Sensing of acetylcholine

The fluorescence emission intensity of Au_{QC}@BSA-AChE was readily quenched in the presence of ACh. Figure 2.4 shows the hydrolysis of ACh to choline and acetate in presence of AChE.

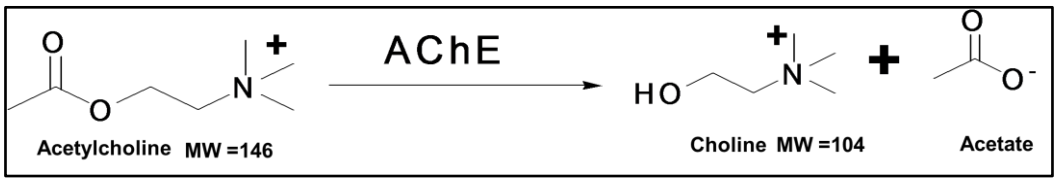

Figure 2.4. Hydrolysis of acetylcholine catalysed by AChE generate choline and acetate.

Figure 2.5a illustrates the decrease in fluorescence of Au_{QC}@BSA-AChE as a function of increasing concentration of ACh. Specifically, on addition of 6.4 µM

ACh, nearly 60% of the fluorescence emission intensity of Au_{QC}@BSA-AChE was quenched. A linear correlation between the two quantities, i.e. emission intensity and concentration, is clearly visible from the Stern–Volmer plot, displayed in Figure. 2.5b. The plot is constructed based on the Stern–Volmer equation (Equation (2.1)).

$$\frac{F_0}{F} = 1 + K_{SV}[Q] \qquad (2.1)$$

where the F_0 and F represent the fluorescence intensity of Au_{QC}@BSA-AChE in the absence and the presence of ACh respectively, K_{SV} is the Stern–Volmer quenching constant, and [Q] is the concentration of analyte. The figure shows that a good linear correlation was found over the concentration range from 0.08 µM to 6.4 µM (R^2= 0.98). The Stern-volmer plot is constructed using a subset of data points taken from Figure 2.5a. It is observed from the figure 2.5a that rate of quenching is more at lower concentration of ACh (0-0.04 µM) compared to higher concentration. The quenching of fluorescence is also easily noticeable from the photographs (insets in Figure. 2.5b) of Au_{QC}@BSA-AChE solution before and after treatment with ACh (6.4 µM). Detailed mechanism of the fluorescence quenching of Au_{QC}@BSA-AChE by ACh is given in section 2.3.5.

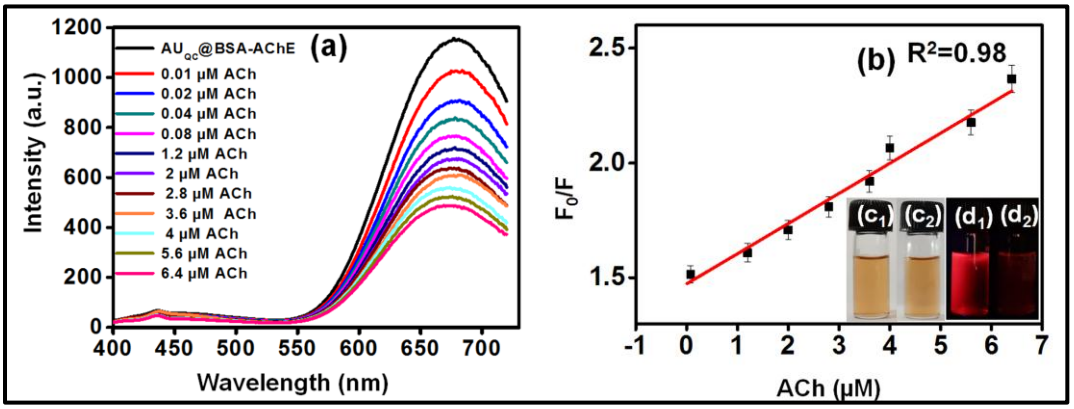

Figure 2.5. (a) Variation of the fluorescence emission spectrum of Au_{QC}@BSA-AChE with increasing concentration of ACh. (b) The Stern-Volmer plot depicting the linear correlation between fluorescence emission intensity at 677 nm and ACh concentration. c_1 and c_2 are the photograph of Au_{QC}@BSA-AChE before and after treatment with ACh (6.4 µM) in visible light and d_1 and d_2 in UV light respectively.

2.3.3. Selectivity studies

We have investigated the selectivity for detection of ACh by comparing the fluorescence response of Au_{QC}@BSA-AChE to the presence of other biologically relevant molecules and a neurotransmitter, dopamine under similar reaction conditions. Concentration of ACh and the analytes were maintained at 6.4 µM. We have tested several molecules and salts (ions derived from them), namely, glucose (Glu), fructose (Fruct), lactose (Lact), glycine (Gly), lysine (Lys), cysteine (Cys), homocysteine (Hcys), glutathione (GSH) NaCl and KCl, which are normally present in blood and could therefore be responsible for fluorescence quenching in a real system. We found that amongst these, only ACh led to significant decrease of fluorescence intensity of Au_{QC}@BSA-AChE, while other molecules did not affect it much as shown in Figure. 2.6. Furthermore another neurotransmitter, dopamine slightly enhanced the fluorescence intensity when 6.4 µM concentration of dopamine is introduced as can be seen in Figure. 2.6a. On the contrary, no variation in the fluorescence signal of Au_{QC}@BSA-AChE is observed when the concentration of dopamine is <6.4 µM.

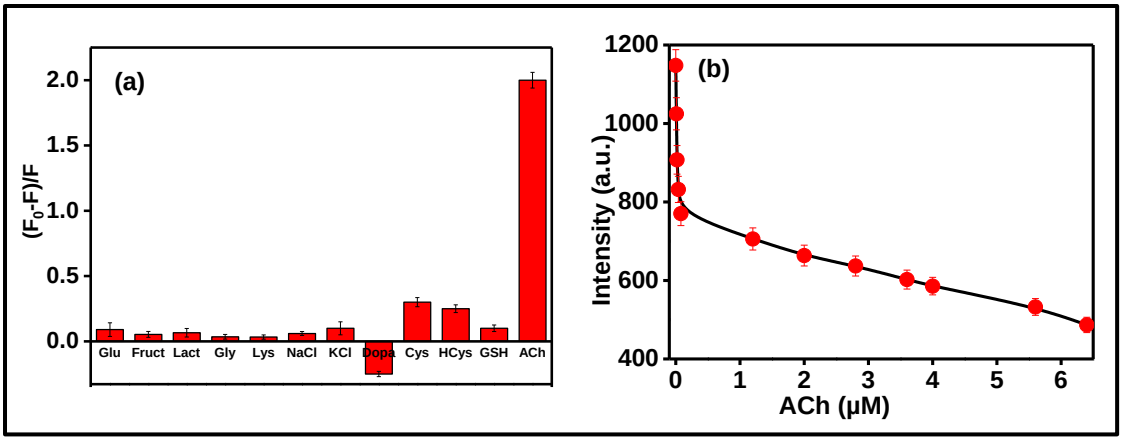

Figure 2.6. (a) Effect of various biologically relevant molecules and dopamine, a neurotransmitter on the luminescence intensity of Au_{QC}@BSA-AChE (concentration of all analytes were kept at 6.4 µM). (b) Variation of fluorescence intensity with different concentrations of ACh. The error bar represent standard deviations based on three independent measurements.

This clearly indicates that, dopamine is less likely to interfere in the acetylcholine detection in real systems, as its concentration is much below 6.4 µM

(Zhang *et al.*, 2003). Detection limit of the present sensor towards ACh is 10 nM, a noticeable quenching in the fluorescence intensity of Au_{QC}@BSA-AChE is found at this concentration (Figure. 2.6 b).

Table 2.1. Comparison of analytical performance of present method with other methods for the detection of ACh.

Method	LOD	Linearity	References
Amperometry	1.0 µM	0.005- 0.4 mM	(Hou *et al.*, 2012)
Electrochemical	26.7 µM	0.25- 5.88 mM	(Sattarahmady *et al.*, 2010)
Potentiometry	10.0 µM	10-100 µM	(Barsoum *et al.*, 2004)
Chemiluminescence	0.05 µM	0.05-100 µM	*(Tsai & Doong, 2005)*
Fluorescence	0.5 µM	0.5-60 µM	(Chen *et al.*, 2011)
Fluorescence	10.0 nM	80-(6.4×10^3)	This Study

We have compared the analytical performance of the current method with various other analytical tools used for ACh detection in recent times (Table 2.1). It is clear from the table that, the analytical parameters such as detection limit, linear range of the present sensor is comparable/superior to the many of the mentioned methods.

2.3.4. Kinetics of interaction of acetylcholine with Au_{QC}@BSA-AChE

To understand the kinetics of fluorescence quenching, the ESI MS spectra of the enzymatic reaction was monitored over real time. The decrease in signal intensity of acetylcholine and a gradual increase in choline intensity with increasing time of reaction was observed (Figure. 2.7a). Under the optimized conditions, at pH 8 the conversion of ACh (0.4 µM AChE) to choline was completed within 1 hour.

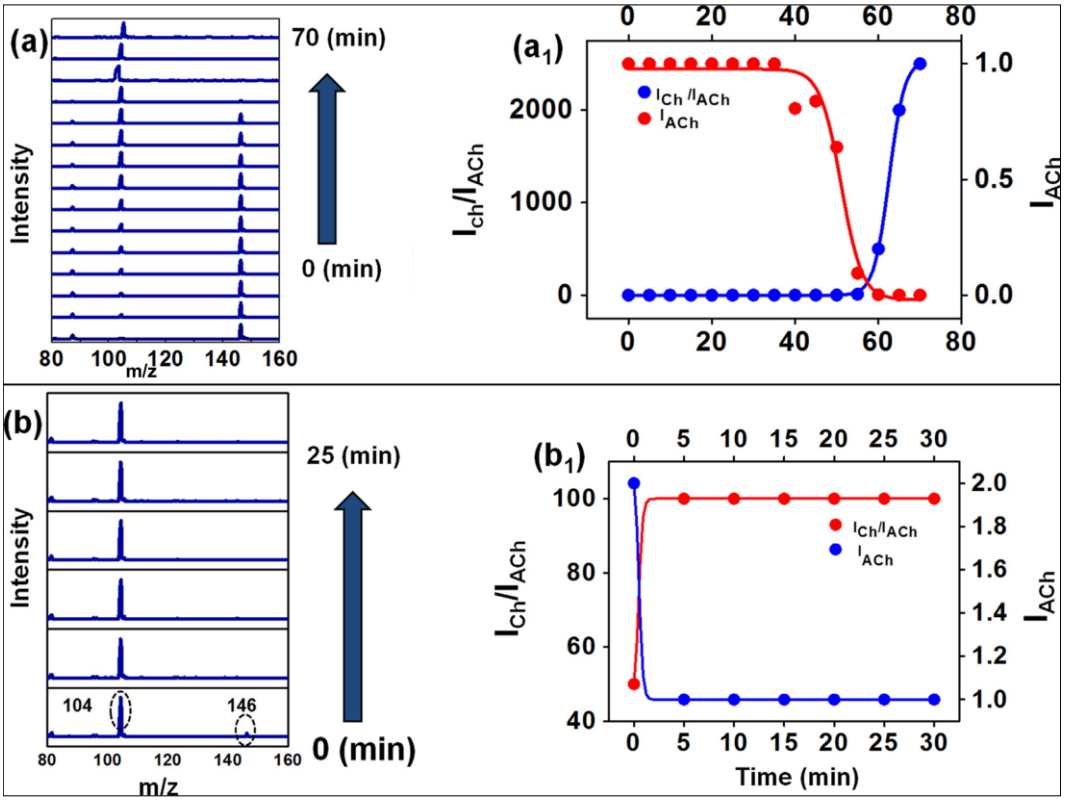

Figure. 2.7. Real time monitoring of ESI MS of hydrolysis of (a) ACh by AChE over a reaction time of 0-70 min and (b) ACh by Au_{QC}@BSA-AChE over a shorter reaction time of 0-25 min. (a_1) and (b_1) are the corresponding calibration plots.

In comparison, when Au_{QC}@BSA-AChE was used at pH 8 (at a concentration of 0.4 μM), ACh was consumed and transformed to choline in ≈5 min (see Figure. 2.7b). Thus, it is evident from the time variation of ESI MS that rapid detection of acetylcholine is possible by using the Au_{QC}@BSA-AChE conjugate system.

2.3.5. Mechanism of fluorescence quenching

The high concentration of choline that is produced rapidly near the enzyme as confirmed by the above MS investigation could interact with the cluster system and can lead to fluorescence quenching. To confirm this, we performed control experiments in which similar concentrations of choline were allowed to interact with the Au_{QC}@BSA-AChE cluster and found that choline effectively quenches the fluorescence intensity (Figure 2.8(b)). Note that choline

consists of an electron deficient quaternary ammonium group and an alkyl hydroxyl group, either of which can interact with the cluster.

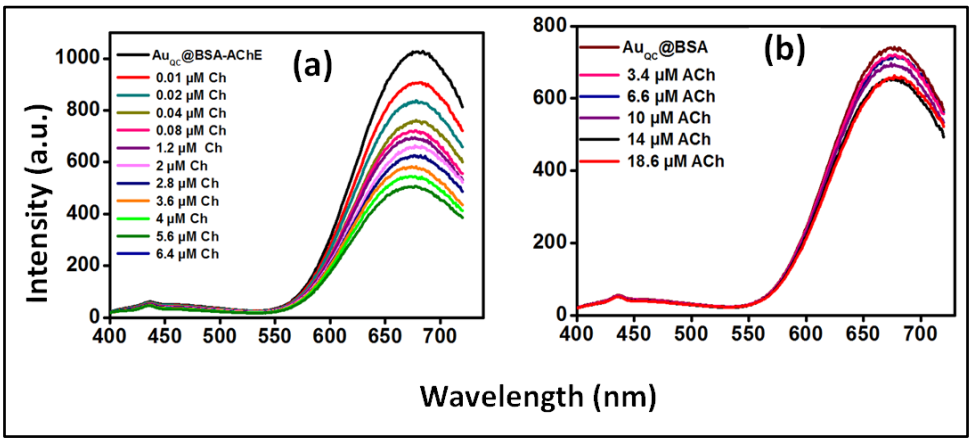

Figure 2.8. (a) Variation of the fluorescence emission spectrum of Au_{QC}@BSA-AChE with different concentrations of choline (Ch). (b) Emission spectrum of Au_{QC}@BSA with different concentration of ACh.

To identify the underlying mechanism, we examined the interaction between Au_{QC}@BSA-AChE and different molecules containing these two functional groups individually. We mimicked the quaternary ammonium group using quaternary ammonium bromide and found that these compounds are efficient quenchers of Au_{QC}@BSA-AChE (Figure 2.9a), while alkyl alcohols do not show such activity (MeOH, EtOH, etc.) (Figure 2.9 c&d), hence we confirmed that interaction is mostly through quaternary ammonium group. Further, interaction of acetate group towards cluster was ruled out by fluorescence study. There is no substantial variation in fluorescence intensity of gold cluster after the treatment of different concentration of acetic acid (Figure 2.9 b).

To support the proposed mechanism, Au@BSA alone was treated with ACh. As displayed in Figure 2.7 (b), in comparison with Au_{QC}@BSA-AChE (Figure 2.5 (a)), the fluorescence intensity of Au_{QC}@BSA did not vary significantly even on addition of a high concentration of ACh (10 - 14 µM). This suggests that in the absence of AChE, Au_{QC}@BSA alone cannot hydrolyze acetylcholine to choline. Hence, the observed fluorescence quenching of

Au_{QC}@BSA-AChE can only be related to the choline generated through the hydrolysis of ACh by the binding of AChE to the cluster.

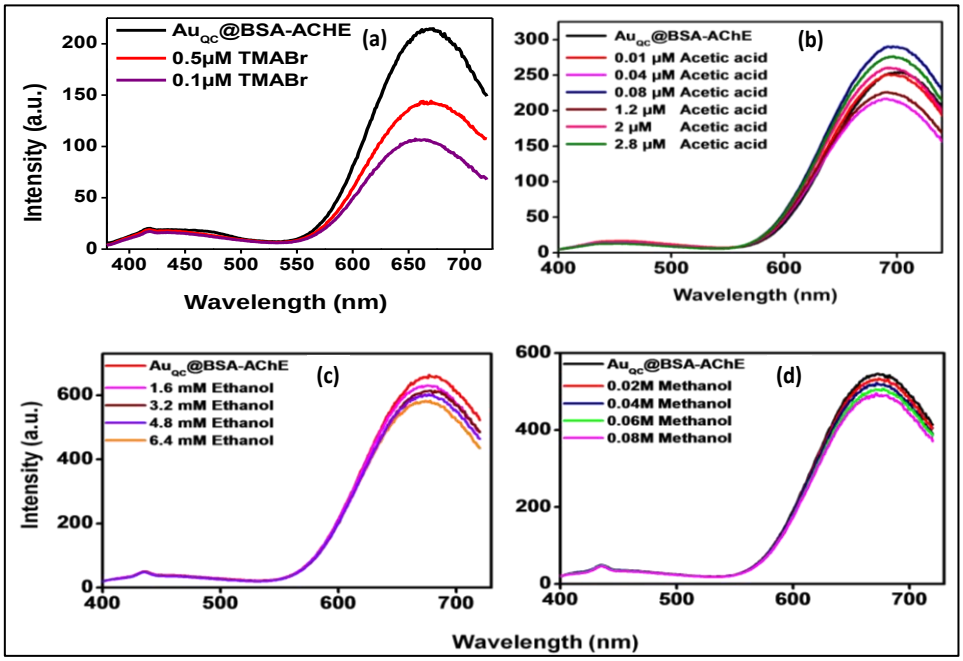

Figure 2.9. Flourescence emission spectra of Au_{QC}@BSA-AChE with different concentrations of tetramethylammonium bromide (TMABr) (a), acetic acid (b), ethanol (c) and methanol (d) respectively.

The actual mechanism of sensitive response of Au_{QC}@BSA-AChE towards acetylcholine has been investigated. It is well reported that, the stern-volmer plot will give an idea about the fluorescence quenching mechanism (Lakowicz 2013). Here the linear stern-volmer plot depicts that only one type of quenching takes place, which may be either static or dynamic quenching. To further understand the actual mechanism for fluorescent quenching, we have carried out a detailed study in this system. It is noticed that the fluorescence quenching is not due to the fluorescence resonance energy transfer (FRET) since there is no overlapping between absorption spectrum of acetylcholine and emission spectra of Au_{QC}@BSA-AChE. Another possible mechanism for fluorescence quenching is analyte induced nano aggregation. The analyte induced aggregation may not be possible since gold quantum clusters are stabilized by BSA mainly by covalent interaction between AuQCs and the thiol groups of the

cysteine. Here choline is not able to substitute BSA and induce aggregation of clusters.

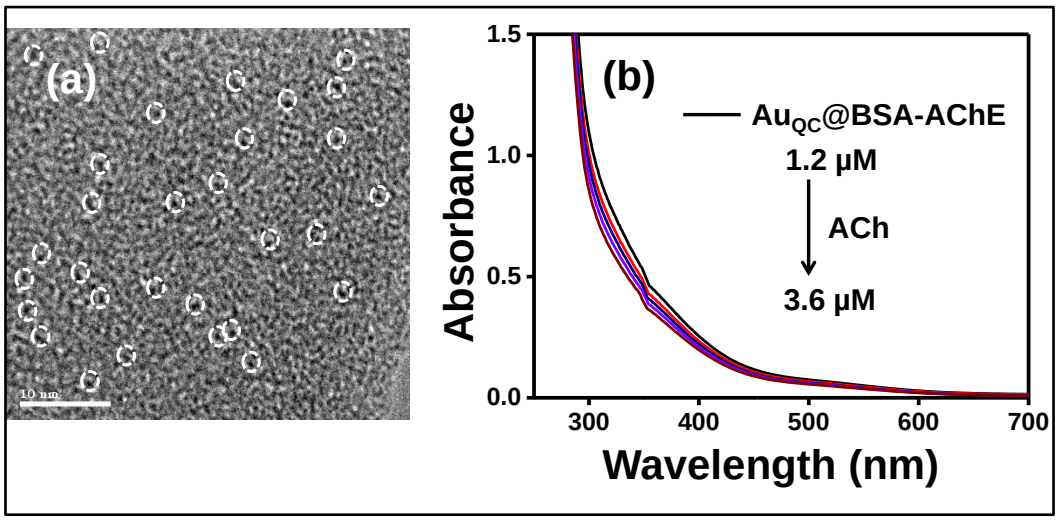

Figure 2.10. (a) TEM image of Au_{QC}@BSA-AChE) after the treatment of ACh (6.4 µM). Some of them are circled. (b) UV -Visible absorption spectrum of Au_{QC}@BSA-AChE with different concentration of ACh.

Moreover, we did not observe any aggregation even for a long time after addition of ACh to Au_{QC}@BSA-AChE (Figure. 2.10 (a)). It is well reported that interaction of analyte towards the surface of protein protected cluster can alter its fluorescent intensity (Chen., *et al.*, 2012; Hemmateenejad *et al.*, 2014). The probable reason for quenching effect of acetylcholine could be attributed to hydrolysis of acetylcholine and the electrostatic interaction between positively charged choline and negatively charged Au_{QC}@BSA-AChE. Consequently changes the environment of the Au_{QC}@BSA-AChE leads to the static fluorescence quenching of the cluster. It is confirmed from absorption spectrum of Au_{QC}@BSA-AChE before and after addition of acetylcholine (figure. 210 (b)). There is decrease in absorbance of Au_{QC}@BSA-AChE after each addition of acetylcholine.

2.3.6. Analysis of ACh in blood samples

To check the validity of the present fluorescent sensor towards the detection of ACh in real system, pre-treated blood samples were spiked with known amount of

ACh and fluorescence analysis were performed. Details on sample preparation are included in the experimental section (Section 2.2.5).

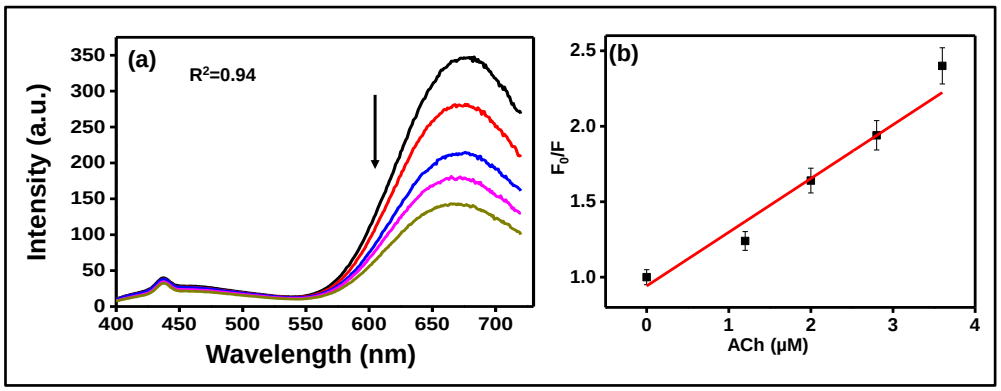

Figure 2.11. Emission spectra of Au_{QC}@BSA-AChE with different concentration of ACh spiked blood sample. The arrows indicate the signal changes as increases in ACh concentrations (1.2, 2, 2.8 and 3.6 μM). (b) a plot of the values of F_0/F at 677 nm versus the concentrations of ACh.

The blood samples were diluted to 1000-fold prior to analysing of ACh to avoid interference from matrix. An apparent decrease in fluorescence at 677 nm of the Au_{QC}@BSA-AChE was observed after the treatment of ACh spiked blood samples (Figure 2.11).

Table 2.2. Detection of ACh in real blood samples by standard addition method.

Test No	**Standard addition in blood (μM)**	**Amount found (μM)**	**RSD (%) (n=3)**
1	0	0.8	1.7
2	1.2	1.97 (98.5%)	1.2
3	2.0	2.75 (98.21%)	1.35
4	2.8	3.4 (95%)	2.0

The mean recoveries for ACh at three spiked levels (1.2, 2 and 2.8 μM) ranged from 95 to 98% and the fluorescence responses against the concentrations of ACh spiked into whole blood was linear. These results suggest that this probe

is largely free from the matrix effect of the blood sample and accuracy and reliability of the present method for ACh determination in real samples.

2.3.7. Sensor development

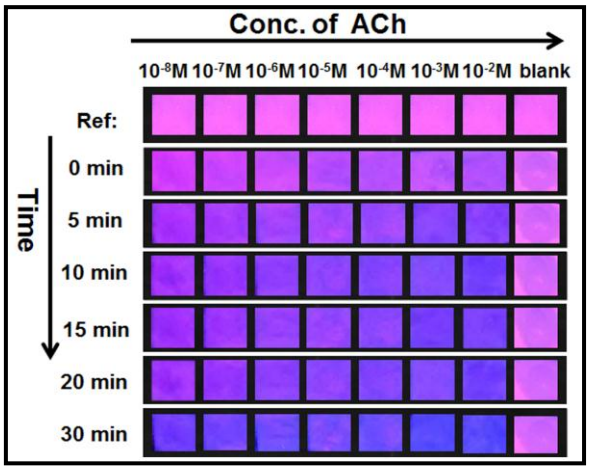

Figure.2.12. Shows photographs of the Au_{QC}@BSA-AChE test paper strips with different concentrations of acetylcholine taken under UV light at several time intervals.

From the previous studies, we know that Au_{QC}@BSA is stable in the presence of various polymeric supports like fibres. Recently, single fibre based detection of Hg^{2+} (Ghosh et al. 2014) and TNT (Mathew et al. 2012) have been reported, confirming the stability of such clusters on polymeric matrices also. With this motivation, we proceeded to develop a paper based sensor for the visual detection of acetylcholine using Au_{QC}@BSA-AChE. To achieve this, we soaked small pieces of filter paper in Au_{QC}@BSA-AChE overnight and then dried them. Using the Au_{QC}@BSA-AChE test paper, we were able to detect different concentrations of acetylcholine. As the reaction time progressed from 0 to 30 min, color of the paper changed from red to blue under UV the light (Figure. 2.12). As can be seen from Fig. 2.12, the emission color is depended on the concentration of ACh. From the time-dependent photographs of the test paper strips in the figure, it is evident that complete quenching occurs within 30 minutes. We believe that extending the stability of the luminescence on the filter paper would make Au_{QC}@BSA-AChE test strips useful for practical applications.

2.4. Conclusions

In the present study, we have effectively conjugated the enzyme, acetylcholinesterase (AChE) with BSA protected gold quantum clusters (Au_{QC}@BSA) and used the conjugate for the selective detection of acetylcholine (ACh). The conjugate, Au_{QC}@BSA-AChE exhibits optical properties similar to Au_{QC}@BSA. During the detection of ACh, AChE bound to the Au_{QC}@BSA hydrolyzes ACh to choline, which in turn quenches fluorescence of Au_{QC}@BSA-AChE through the interaction of choline to the gold quantum clusters. A detection limit of ACh of 10 nM is achieved by this method which is far lower than the methods reported so far. Real time monitoring of the hydrolysis via ESI MS shows that the reaction is faster with Au_{QC}@BSA-AChE than with AChE alone. Au_{QC}@BSA-AChE is stable and they exhibit similar fluorescence on a solid substrate like filter paper, which led to the design of a highly selective, sensitive and cost effective fluorescence based optical sensor for ACh. The validity of present method tested by detecting the concentration of ACh in blood samples, which suggested its great potential for diagnostic purpose. Compared to other sensors, our sensor exhibits several practical advantages, including simple reagent preparation, sensitivity, selectivity, accuracy, cost-effective detection etc. Moreover conjugation of different enzyme on protein protected cluster can be used for development of specific sensor, which can be possible in future by following our strategy.

CHAPTER 3

SYNTHESIS AND CHARACTERIZATION OF GLUTEN PROTECTED GOLD QUANTUM CLUSTERS FOR CREATININE DETECTION

This chapter describes the cost-effective synthesis of novel, water-soluble and stable fluorescent gold quantum clusters via a facile and green method using wheat gluten protein as a stabilizing agent (Au_{QC}@gluten). Gluten, a cysteine-rich protein serves as an effective stabilizing agent for these clusters. The Au_{QC}@gluten shows intense red emission at ~680 nm and is characterized using UV-Vis spectroscopy, fluorescence, Fourier-transform infrared spectroscopy, transmission electron microscopy and X-ray photoelectron spectroscopy. The red emitting Au_{QC}@gluten has been applied in the detection of creatinine with high sensitivity and selectivity. The detection limit is found to be 2 nM in the linear range from 20 μM to 520 μM. This method allows for the accurate detection of creatinine in clinical blood samples, indicating its promising biomedical applications.

Part of this chapter has been published in ACS Sustainable Chemistry & Engineering, (2017), Vol 6: 4837–4845.

3.1. Introduction

Gluten proteins are the major proteins found in the starchy endosperm family such as wheat. It is one of the most complex protein families comprising hundreds of different proteins (Shewry *et al.*, 2002). The precise number of proteins present in the gluten has not yet been determined. Gliadin and glutenin are the major components of wheat gluten protein. Gliadin is a monomeric protein with molecular weight between 30 to 80 KDa and contains single polypeptide chains whose conformations are stabilized by intramolecular disulfide bonds. Glutenin, a polymeric protein, however, consists of subunits of MWs between 30 to 90 kDa linked through intermolecular disulfide bonds. Elasticity to the dough is imparted by a group of proteins present in glutenin. Cysteine is one of the major amino acids present in the gluten protein and it stabilizes the protein through either intra-chain disulfide bond within the protein or inter-chain disulfide bonds. Other major amino acids present in the protein are proline, glutamine, tyrosine etc (Bietz & Wall, 1972; Shewry *et al.*, 2002; Shewry & Tatham, 1997; Wieser, 2007). Due to the presence of cysteine and other aromatic amino acids in the gluten protein, we employed it as a template for developing a new gold quantum cluster. Gluten stands out as an excellent candidate among different plant-derived proteins owing to its ease of availability and low cost (Day *et al.*, 2006; Reddy & Yang, 2007). To the best of our knowledge, this is the first report for the synthesis of gold quantum clusters using gluten, a complex protein as a template. The resulting Au_{QC}@gluten is highly stable and can be used for the selective and sensitive detection of creatinine.

Creatinine is the best indicator for checking renal function and muscle damage in humans. The normal level of creatinine in blood serum is in the range of 0.6 - 1.2 mg/dl (53 - 106 µM/L) (Hanif *et al.*, 2016). The increased level of creatinine in the blood leads to different renal diseases like urinary tract obstruction, renal failure, diabetic nephropathy, chronic nephritis and glomerulonephritis whereas the decreased level of creatinine in the blood causes skeletal muscle diseases like muscular dystrophy and myasthenia (He *et al.*, 2015;

Parmar *et al.*, 2016; Ruedas-Rama & Hall, 2010). Thus monitoring the level of creatinine in the blood can be used as a useful diagnostic tool for patients with kidney malfunctions.

There are several reports on biosensors for the detection of creatinine, most of which are based on electrochemical or colorimetric sensing. Recently, Parmar and co-workers have colorimetrically detected creatinine using PA (picric acid) caped silver nanoparticle (Parmar *et al.*, 2016). Most of the creatinine detection is based on the Jaffe's reaction, which follows the principle that in an alkaline medium, PA binds with creatinine to form an orange creatinine-picrate complex. The main drawback of Jaffe's reaction is its less specificity towards creatinine since other biomolecules that are present in blood, such as creatine, urea, glucose etc can interfere in the reaction and might lead to an inaccurate result (Mali & Nicholas, 1988).

Herein, we present a cost-effective, one-pot, environmentally benign, gluten-based synthesis of gold quantum clusters, in which gluten act as both reducing as well as the stabilizing agent. It is interestingly observed that the synthesized Au_{QC}@gluten is highly stable towards reactive oxygen species like H_2O_2 revealing its promising application in the biomedical field such as bio-imaging, bio-labeling, etc. Further, the AuQC@gluten was used for the highly selective, sensitive and cost-effective, novel turn-on fluorescent sensing of creatinine with PA acting as a quencher. Turn-on fluorescence sensing using gold quantum clusters are still rare since most of the sensors reported in the literature are based on the fluorescence quenching of gold quantum clusters. Here creatinine could selectively recover the PA- quenched fluorescence of Au_{QC}@gluten owing to the higher binding affinity of PA towards creatinine. Further, the practicality of the Au_{QC}@gluten sensing system was validated through the detection of creatinine in real blood samples.

3.2. Experimental Section

3.2.1. Materials

All the reagents were used as obtained without further purification unless stated otherwise. $HAuCl_4.3H_2O$, gluten, the membrane dialysis bag (molecular weight cut-off 14 kDa), cholesterol, cysteine, homocysteine, glutathione, glycine, lysine, tyrosine, adenine, creatine, folic acid, urea, and creatinine were purchased from Sigma-Aldrich. Sodium dihydrogen phosphate and disodium hydrogen phosphate, glucose, fructose, and galactose were purchased from Merck. All solutions were prepared using Millipore water.

3.2.2. Instrumentation

UV-Visible absorption spectra were recorded in the range of 200 - 800 nm using the Varian model, Cary win Bio 100 spectrometer. All luminescence measurements were recorded using the Fluoro Max-4C spectrofluorometer (Horiba Instruments, USA). The emission spectra were recorded upon excitation at 380 nm; the slits for excitation and emission were set at 5 nm. We have used time-correlated single photon counting (TCSPC) for lifetime analysis with a pulse width of 1.3 ns. Here the excitation wavelength was fixed at 440 nm and decay profile was collected at 680 nm. The QY of AuQC@gluten was calculated using Quinine sulfate as standard. HRTEM images were obtained with a JEOL JEM 2100 instrument with an acceleration voltage of 200 kV. XPS analysis was carried out using an Omicron ESCA Probe spectrometer with unmonochromatized Al Kα X-rays. FTIR spectra were measured using Perkin Elmer FTIR spectrometer. pH measurement was done by using EUTECH pH meter.

3.2.3. Preparation of AuQC@gluten

Synthesis of Au_{QC}@gluten is briefly explained herein. The gluten protein solution was prepared by dissolving gluten (25 mg/mL) in alkaline solution (25 mM NaOH) and heating (40°C) for 15 minutes. In a typical experiment 5 mM (5 mL) $AuCl_4$ is treated with 25 mg/mL (5 mL) of the above-prepared gluten in

alkaline solution and kept for vigorous stirring at 55°C. The stirring is continued for 3 hours till the color of the solution changed from light yellow to deep brown. The cluster formation is preliminarily confirmed by intense red emission under table top UV light (365 nm excitation). Purification of Au_{QC}@gluten was performed by dialysis against distilled water for 24 hours in a dialysis membrane of molecular weight cut-off of 14 kDa. The cleaned gold clusters were then freeze-dried and stored at room temperature for further use.

3.2.4. Method of sensing of creatinine

The Au_{QC}@gluten solution was diluted 10 times prior to all studies. 2.5 mL of the cluster solution was treated with different concentrations of PA (Final concentration of PA - 1.6 mM) and the fluorescence intensity variation was measured at 680 nm by an excitation of 380 nm. Then the Au_{QC}@gluten-PA mixture was treated with various concentrations of creatinine (20 µM -520 µM) and fluorescence recovery at 680 nm was monitored.

3.2.5. Method of detection of creatinine in the blood

Blood samples were collected from 3 volunteers and diluted to 1000 times before doing the analysis. An authentically signed consent was obtained from the patients. 50 µL of diluted blood samples were spiked with different concentrations of creatinine (20 µM -520 µM) and incubated for 15 minutes. Blood with and without creatinine spike was treated with 2.5 mL of Au_{QC}@gluten-PA and the fluorescent intensity at 680 nm was monitored. This study was approved by the ethical committee of Indian Institute of Space Science and Technology (IIST) (IIST/IEC/2016/CHE-01).

3.2.6. Calculation of quantum yield (QY)

The QY was calculated using quinine sulfate as standard and calculated based on Equation 3.1

$$\varphi_s = \varphi_0 \times \frac{A_s}{A_0} \times \frac{I_0}{I_s} \times \frac{n_s^2}{n_0^2} \text{ -----} \quad (3.1)$$

Where, φ_0: Reference QY, φ_s: Sample QY, A_0 and I_0 are the absorbance and area under the fluorescence curve of reference respectively, I_s and A_s are the areea under the fluorescence curve and absorbance of the sample respectively, η_0 and η_s are the refractive index of the solvent used for reference and sample respectively.

3.3. Results and Discussion

3.3.1. Synthesis of Au_{QC}@gluten

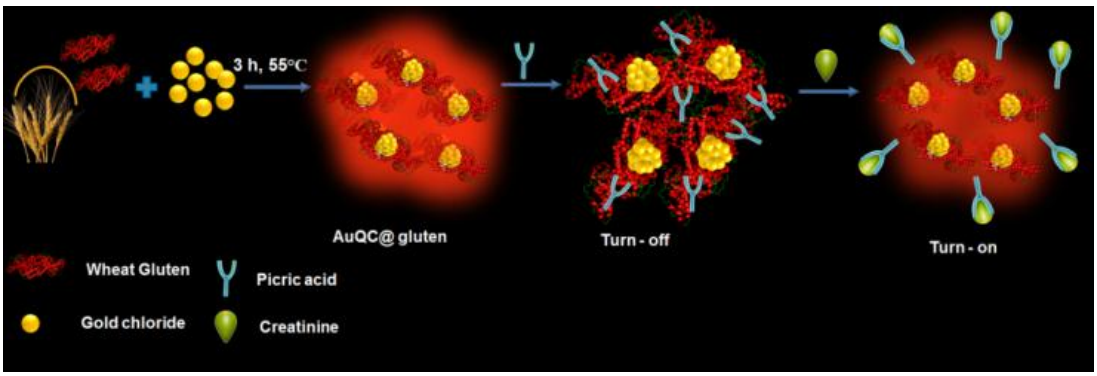

Figure 3.1. Schematic representation for the synthesis of Au_{QC}@gluten, fluorescent quenching of Au_{QC}@gluten in the presence of PA and consecutive turn-on sensing of creatinine.

Schematic representation of the formation of Au_{QC}@gluten is shown in Figure 3.1. Synthesis of Au_{QC}@gluten was accomplished in a single step within 3 hours, which was much faster than any other protein protected cluster synthesis.[18] Here the Au_{QC}@gluten was formed by the mixing of gluten and $AuCl_4$ under basic pH and continuous stirring at 55°C for 3 hours. The formed Au_{QC}@gluten shows a broad featureless absorption peak with a small hump at 280 nm, which is due to the presence of aromatic amino acid present on gluten as in BSA protected cluster (Mathew *et al.*, 2016). The absence of surface plasmon resonance peak (around 520 nm) clearly a rule out the possibility of Au nanoparticle formation in the solution mixture. The Au_{QC}@gluten solution exhibit light brown color under

visible light (Inset of Figure 3.2, a) and intense red emission under UV light (365 nm) (Inset of Figure 3.2, b). The formed cluster exhibit emission maximum centered at 680 nm by an excitation of 380 nm and weak emission observed around 450 nm arises due to the aromatic amino acid present in the gluten (Figure 3.2), which was further confirmed by observing an emission spectrum of gluten at an excitation of 380 nm (Figure 3.3A).

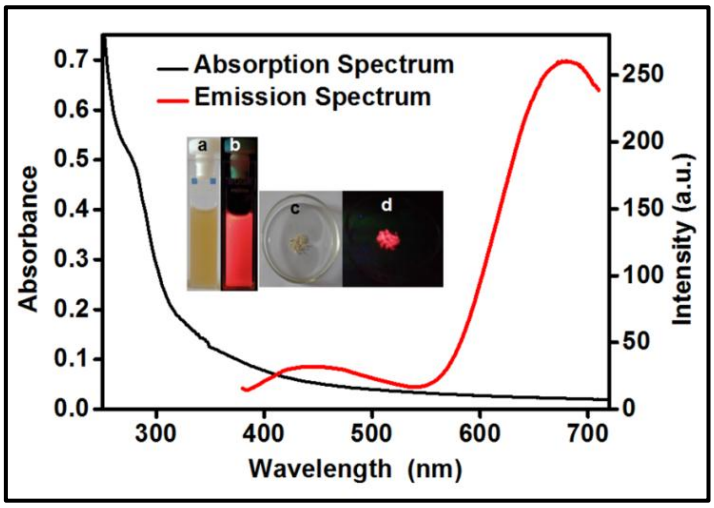

Figure 3.2. The optical absorption (black trace) and emission (red trace, λ_{ex} = 380 nm) spectra of Au_{QC}@gluten. The inset shows the photographs of aqueous solution Au_{QC}@gluten (a & b) and powder (c & d) under visible light (a & c) and UV light (b & d).

The excitation spectrum of Au_{QC}@gluten exhibit two peaks, one intense peak at 380 nm and a hump at 480 nm, which are the typical characteristic peaks of protein protected quantum clusters (Figure 3.3B). The different excitation peaks may be due to the multiple electronic transitions in noble metal quantum clusters (Le Guevel *et al.*, 2012). The formed

Au_{QC}@gluten was purified against distilled water for 24 hours. The cluster solution obtained after dialysis was subjected to freeze-drying to get QCs in powder form, which exhibit light brown color under visible light (Inset of Figure 3.2, c) and intense red emission under UV light (Inset of Figure 3.2, d).

According to the spherical Jellium model, the wavelength of the fluorescent quantum cluster depends on the size of the cluster core (Zheng *et al.*,

2004). A red emission of Au_{QC}@gluten was observed with an emission maximum at 680 nm with an excitation of 380 nm.

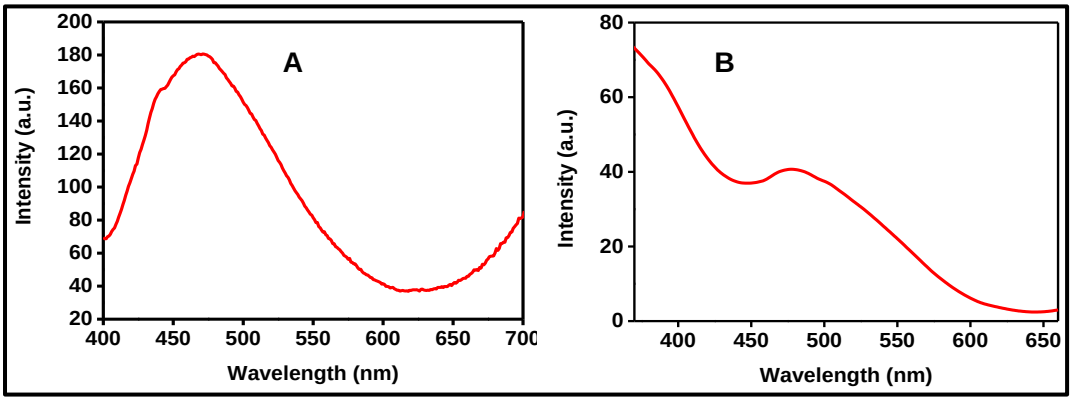

Figure 3.3. (A) Fluorescence spectra of gluten (λ_{ex} = 380 nm) and (B) Excitation spectrum of Au_{QC}@gluten.

This red emission wavelength is close to other protein protected clusters like Au_{25}@BSA (λ_{em} = 670 nm), Au_{25}@lactoferrine (λ_{em} = 650 nm) and Au_{25}@pepsine (λ_{em} = 680 nm) (Ghosh *et al.*, 2014; Kawasaki *et al.*, 2011; Xavier *et al.*, 2010). Thus it is assumed that the gluten protected quantum cluster also contains 25 gold atoms (Au_{25}@gluten). This was further supported by glutathione study in which Tsukuda and co-workers reported high stability of 25 gold quantum cluster towards glutathione (Shichibu *et al.*, 2007). Thus, we analyzed the stability of Au_{QC}@gluten towards various concentrations of glutathione (Concentration of glutathione- 4 µM to 4 mM). The cluster does not produce any noticeable changes in fluorescence intensity in the presence of glutathione, confirming the presence of 25 gold atoms (Figure 3.4). Due to the complexity of wheat gluten protein (composed of hundreds of different protein), number of gold atoms present in the cluster could not be detected using MALDI TOF- MS analysis.

Excitation independent fluorescence emission is another exciting property of quantum clusters. Excitation of AuQC@gluten at different wavelength does not change the emission maximum of cluster implying the higher optical stability of these clusters (Figure 3.4B). In addition, higher stability of Au_{QC}@gluten in a

wide range of pH (pH = 5.5 - 12) in different buffer solutions exhibits its possibility of potential application in several biological fields (Figure 3.5A).

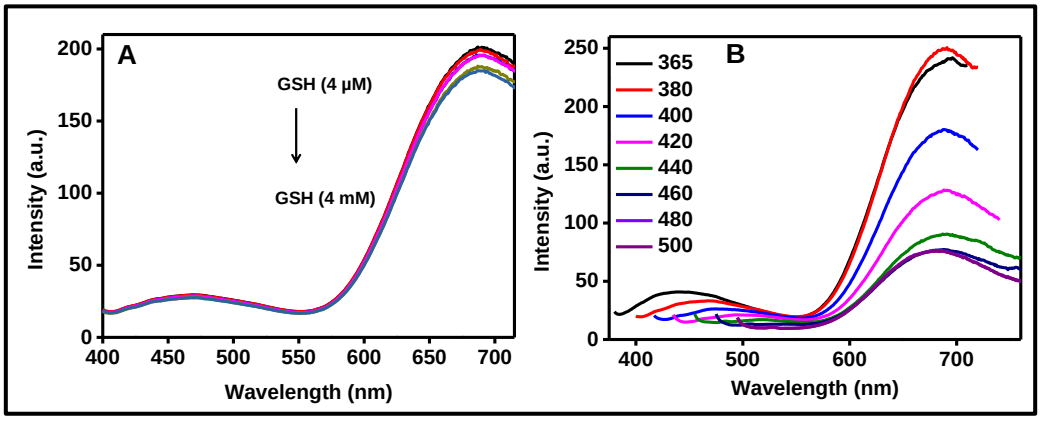

Figure 3.4. (A) Fluorescence emission spectra of Au_{QC}@gluten with various concentration of glutathione (λ_{ex} = 380 nm) (B) Emission spectra of AuQC@gluten at the different excitation wavelength.

The stability of the cluster towards Na^+ ions was also investigated by subjecting the cluster to different concentrations of NaCl (Figure 3.5B). It is observed that the ionic strength did not affect the fluorescence intensity of Au_{QC}@gluten.

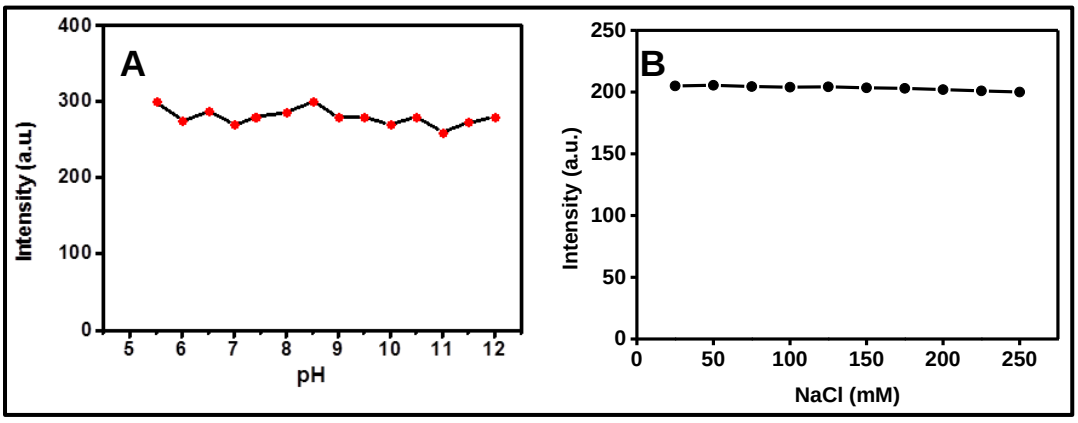

Figure 3.5. (A) The stability of Au_{QC}@gluten at various pH ranges from 5.5 to 12 pH. (B) The fluorescence intensity Au_{QC}@gluten with various concentrations of aqueous NaCl solution (25 mM to 250 mM). Fluorescence spectra were collected by an excitation of 380 nm with an emission maximum at 680 nm.

Contrary to other protein protected gold quantum clusters, whose application as biological labels is limited due to their oxidative decomposition by reactive oxygen species (ROS),

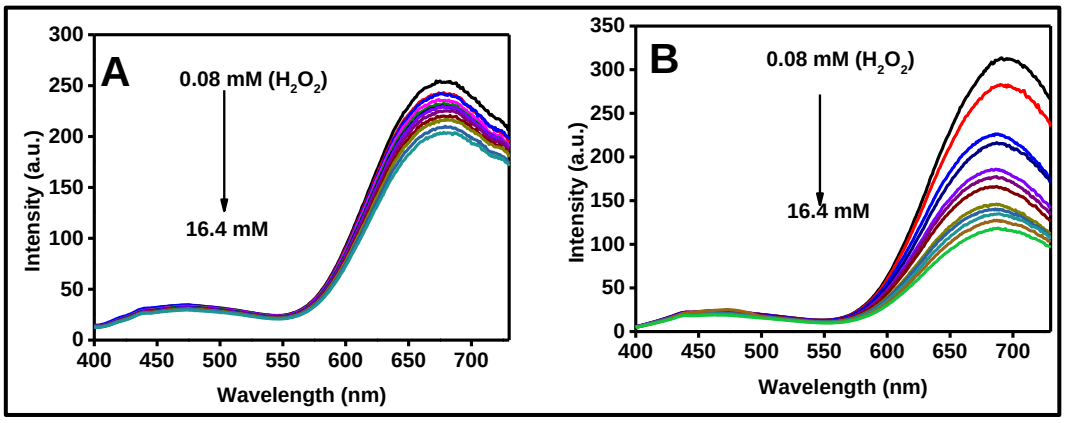

Figure 3.6. (A) The stability of Au_{QC}@gluten with various concentration of H_2O_2. (B) The fluorescence changes of Au_{QC}@BSA with various concentration of H_2O_2 (λ_{ex} = 380 nm).

gluten stabilized gold quantum cluster shows more stability against ROS, which can provide a new and even better choice in this field (Figure 3.6). The enhanced stability of gluten protected gold quantum cluster against reactive oxygen species may be due to the presence of a large number of high molecular weight and complex nature of the protein, which can prevent the diffusion H_2O_2 through the protein and further prevent oxidation of cluster core. A comparative study of the stability of Au_{QC}@BSA and Au_{QC}@gluten against H_2O_2 is given in Figure 3.6. The synthesis of Au_{QC}@BSA was explained in chapter 2 (Mathew *et al.*, 2016). According to the previous reports, the reason for the poor stability of BSA protected quantum cluster is due to the flexible structure of BSA which facilitates the diffusion of reactive oxygen species towards the cluster core which in turn destabilizes the quantum cluster (Zhou.,*et al.*, 2016). Zhou and co-workers modified BSA protected gold clusters with a polymer-like shielding layer for stabilization against reactive oxygen species (Zhou, W. *et al.*, 2016). But our system does not require any further modification for improving the stability of QC.

The quantum yield of Au_{QC}@gluten was determined to be 6.45 % with quinine sulfate (Qy=0.54) (Dawson & Windsor, 1968) as standard (Table 3.1,), which is comparable with other protein protected clusters (Xavier *et al.*, 2012b).

Table 3.1 Calculation of Quantum yield of AuQC@gluten

Sample	**λ_{Exc} (nm)**	**φ_0**	**A_0**	**I_0**	**n_o**	**A_s**	**I_s**	**n_s**	**φ_s (%)**
AuQC	380	0.54	0.063	$2.3x10^8$	1.33	0.03	$1.6x10^7$	1.33	6.45

Synthesis conditions including the molar ratio of gluten and Au^{3+} ions, the reaction temperature and reaction time, pH of the medium were studied. When the concentration of $HAuCl_4$ is maintained constant (5 mM) and the concentration of gluten was varied from 5 mg/mL to 40 mg/mL, it is noted that the cluster formation starts at 10 mg/mL and at this concentration emission intensity is very poor and fluorescent intensity at 680 is maximum at 25 mg/mL of gluten (Figure 3.7A).

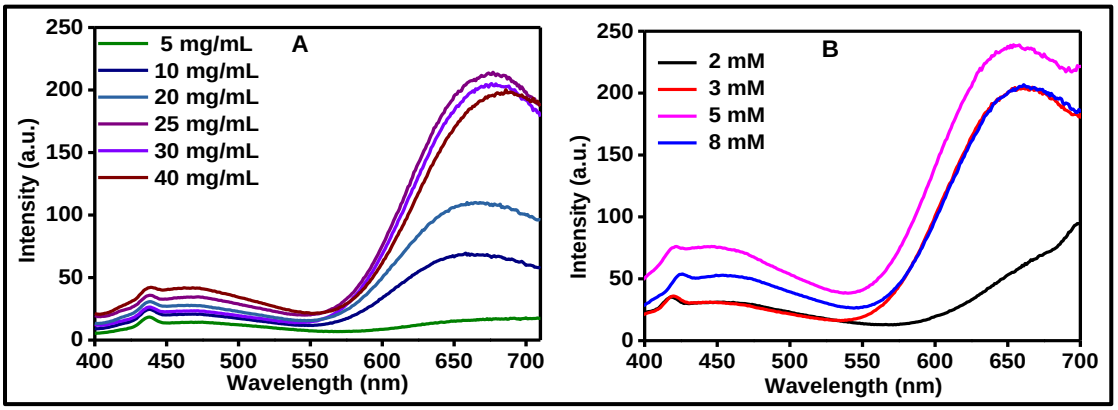

Figure 3.7. (A) Fluorescence emission spectra (λ_{ex} = 380 nm) for the evolution of clusters with different concentration of gluten and (B) different concentration of $HAuCl_4$.

Thus it is confirmed that the optimum concentration of gluten required for the formation of the cluster is 25 mg/mL. Further, when we varied the

concentration of $HAuCl_4$ from 2 mM to 8 mM by keeping the concentration of gluten as constant (25 mg/mL), it was noticed that optimum concentration of gold chloride required for the formation of the intense emitting cluster was 5 mM (Figure 3.7B). The optimum temperature required for the formation of the cluster was found out by carrying out the reaction at four different temperatures (room temperature (25° C), physiological temperature (35°C), medium temperature (55°C) and high temperature (80° C). At 55°C, the fluorescence intensity of gold quantum cluster reached the maximum at 3 hours of reaction (Figure 3.8B).

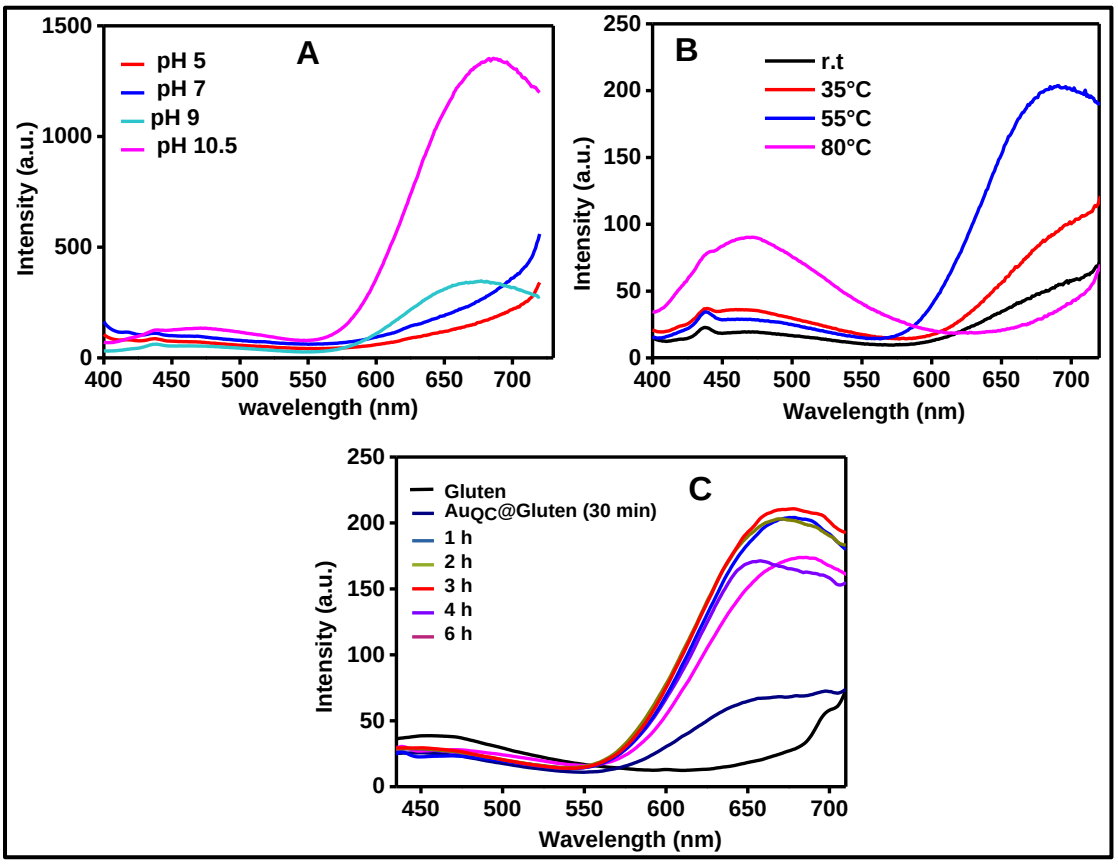

Figure 3.8. Fluorescence emission spectra (λ_{ex} = 380 nm) for the evolution of clusters with different pHs (A), different Temperature and (B), and different time points (C) respectively.

Further increasing or decreasing the temperature led to non-fluorescence and the optimum temperature required for formation of the cluster was found to be around 55°C. We have monitored the cluster formation by checking fluorescent spectra of Au_{QC}@gluten at regular intervals of time and it was observed that the cluster starts forming from the initial time itself (30 minutes). As

the reaction time progressed, a gradual increase in fluorescence was observed from the cluster solution and the fluorescence reached maximum after at 3 hours. Upon increasing the reaction time from 3 to 6 hours, at 55 °C, the fluorescent intensity of the cluster starts decreasing. This might be attributed to the beginning of cluster degradation at 55 °C (Figure 3.8C). Thus the minimum time required for the formation of the fluorescent quantum cluster was estimated to be 3 hours. The effect of pH on the formation of the quantum clusters were investigated, it is observed that the intense red emitting quantum cluster formed at high pH (pH=10.5) (Figure 3.8A). Thus the reaction carried out in an optimal composition of 25.0 mg/mL gluten, 5.0 mM $HAuCl_4$ at 55 °C for three hours at pH =10.5, produces the intense red emitting gold quantum clusters (Au_{QC}@gluten).

3.3.2. Characterization of Au_{QC}@gluten

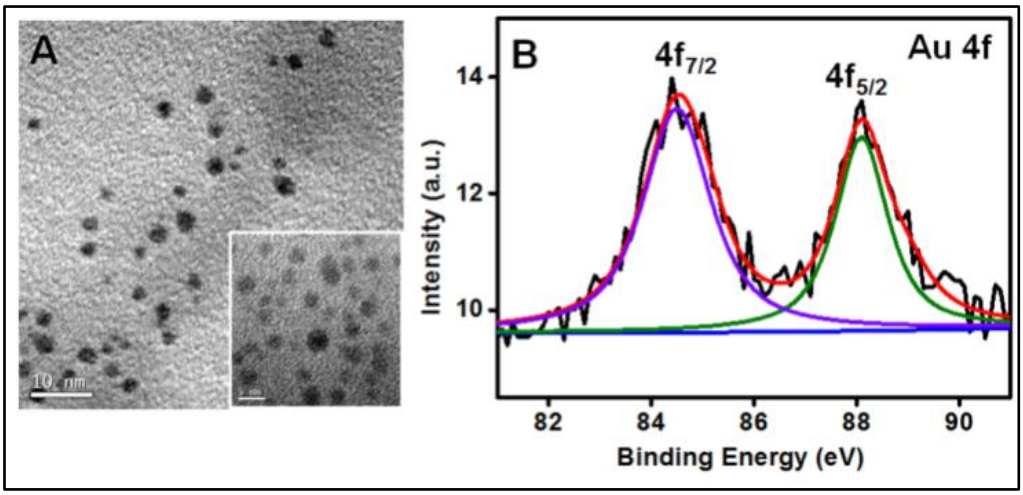

Figure 3.9. (A) The TEM images of Au_{QC}@gluten; (B) XPS spectra of Au 4f for Au_{QC}@gluten.

The cluster formation was confirmed by XPS, TEM and FTIR analysis. TEM images of Au_{QC}@gluten revealed that the formed quantum cluster has an average diameter of around 1.5 nm (Figure 3.9A). The oxidation state of the cluster was determined by XPS in which the binding energy for Au $4f_{7/2}$ and $4f_{5/2}$ of Au_{QC}@gluten was found to be 84.5 and 88.0 eV respectively, which confirms the formation of the cluster by reduction of Au(III) to Au(0) (Figure 3.9B) The minor shift to the higher binding energy is due to reduced size of QC. The binding

energy increases with decreasing the particle size. (Xaviar, 2010). The stabilization of AuQC by gluten as analyzed by FTIR spectroscopy (Figure 3.10) by taking gluten as the control.

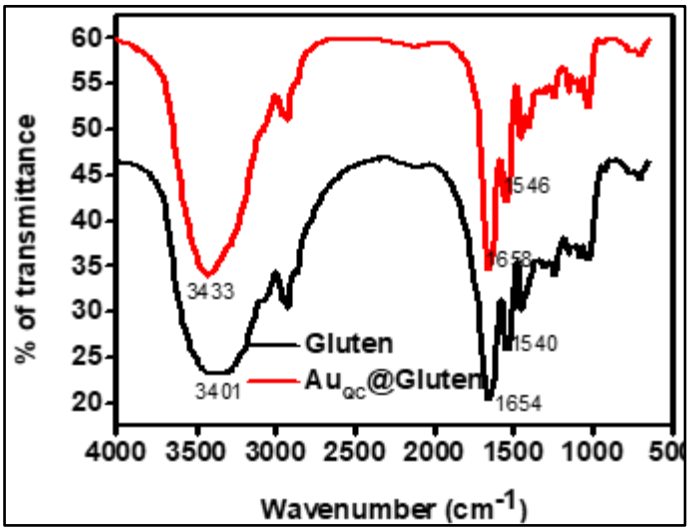

Figure 3.10. Fourier transform infrared (FTIR) spectra of gluten and Au_{QC}@gluten

In FTIR spectra of both gluten and gluten stabilized cluster, the peaks are matching depicting that the cluster is formed inside the gluten protein. As shown in Figure 3.10, the peaks in the range of 1600 to 1690 cm^{-1} are the stretching frequency of amide I. Amide II is in the range of 1480 – 1575 cm^{1} and amide III is in between 1229 - 1301 cm^{-1}. Broad peak 3500 - 2900 cm^{-1} is due to the OH, CH, and NH vibration (Xavier *et al.*, 2010). The secondary structure of the protein will mainly affect the amide I band. Here the peak corresponding to amide I is shifted to higher wavenumber from 1654 to 1658 cm^{-1} after cluster formation with a reduction in the peak intensity, which is due to the increase in the disordered structure of the protein. Along with amide I, amide II is also affected here, which is observed by the shift in peak from 1540 to 1546 cm^{-1}.

3.3.3. Sensing of creatinine

The fluorescence of the AuQC@gluten were employed for the highly sensitive and selective fluorescence turn-on sensing of creatinine. Schematic

representation for the turn-on fluorescence sensing of creatinine is represented in Figure 3.1. All experiments were carried out at pH 9.0 in phosphate buffer since PA can form complex with creatinine only in basic medium (Chen & Lin, 2012). Here we have observed that the addition of PA to the Au_{QC}@gluten could drastically quench the red fluorescence of Au_{QC}@gluten at 680 nm (excitation at 380 nm) owing to the interaction of PA with the amino group of gluten.

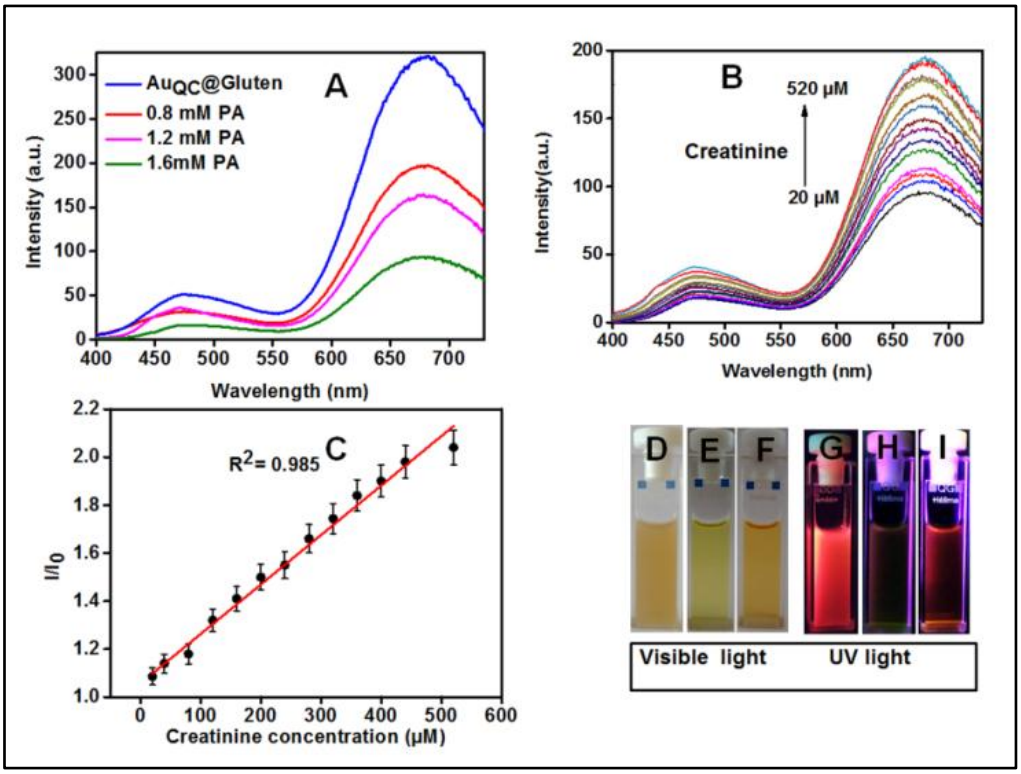

Figure 3.11. (A) Fluorescence quenching of Au_{QC}@gluten to different concentrations of PA (0.4 mM- 1.6 mM) and (B) Fluorescence recovery of PA-treated Au_{QC}@gluten at various concentration of creatinine (20 µM - 520 µM). (C) The linear relationship between fluorescence responses (I/I_0) towards various concentration of creatinine, where, I_0 and I are the fluorescent intensity of Au_{QC}@gluten-PA mixture in the absence and presence of creatinine. Photographs of Au_{QC}@gluten (D), Au_{QC}@gluten-PA (E), Au_{QC}@gluten-PA-Creatinine (F) under visible light and (G),(H) and (I) are the same under UV light (λ_{ex} = 365 nm).

As the concentration of PA increases from 0.4 mM to 1.6 mM, the fluorescence of Au_{QC}@gluten is quenched (Figure 3.11A). Upon the introduction of creatinine into Au_{QC}@gluten –PA mixture solution, a gradual recovery of quenched fluorescence is observed with increasing concentration of creatinine,

owing to the strong and stable complexation of PA with creatinin (Figure 3.11B). As the concentration of creatinine increases, fluorescent intensity at 680 nm is linearly increasing. A 61% recovery of fluorescent intensity at 680 nm observed at a 520 µM concentration of creatinine. This linear recovery of luminescence on the addition of creatinine can be used as a turn-on creatinine sensor. Figure 3.11C represents the fluorescence enhancement (I/I_0) plotted with respect to the concentration of creatinine, where I_0 and I are the fluorescent intensity of Au_{QC}@gluten-PA mixture in the absence and presence of creatinine, respectively. We have obtained a very good linear relationship of creatinine over the range of 20 to 520 µM with an R^2 value of 0.985. The detection limit is calculated based on 3σ/K (Wu., *et al.*, 2015), where σ is the standard deviation from the blank measurement in the absence of creatinine and K is the slope of the calibration plot. The detection level of creatinine at a signal-to-noise ratio of 3 is estimated to be 2 nM, which is much lower than the normal level of creatinine found in human blood (Hanif *et al.*, 2016). The quenching and recovery of fluorescence are also easily noticeable from the photographs shown in Figure 3.11(G), (H) and (I). The color of the cluster solution changes from light brown to yellow after the addition of PA, which further changes to orange-red due to creatinine-picrate complex formation (Figure 3.11E and Figure 3.11F). The detailed mechanism for the fluorescence sensing of creatinine is given in Section 3.3.5.

3.3.4. Selectivity Study

One drawback of the usual optical sensors for the detection of creatinine is its low specificity towards creatinine (Parmar *et al.*, 2016). We have investigated the selectivity of fluorescence detection of creatinine towards other biologically relevant molecules present in blood under similar reaction conditions. Fluorescence study was applied to several molecules and salts like glucose (Glu), fructose (Fruct), galactose (Gal), cholesterol (Chole), cysteine (Cys), homocysteine (Hcys), glutathione (GSH), glycine (Gly), lysine (Lys), tyrosine (Tyr), Adenine, creatine, folic acid (FA), urea and salts including NaCl and KCl. Further, we have extended the selectivity study towards metal ions, which include

Fe^{3+}, Mg^{2+}, Zn^{2+}, Ca^{2+}, Li^{+}, Cu^{2+}, NO_3^{-}, SO_4^{2-}, S_2^{-}, PO_4^{3-}, F^{-}, Cl^{-}, I^{-}, CH_3COO^{-}, $S_2O_3^{2-}$, Citrate, and CO_3^{2-} at a concentration of 100 µM.

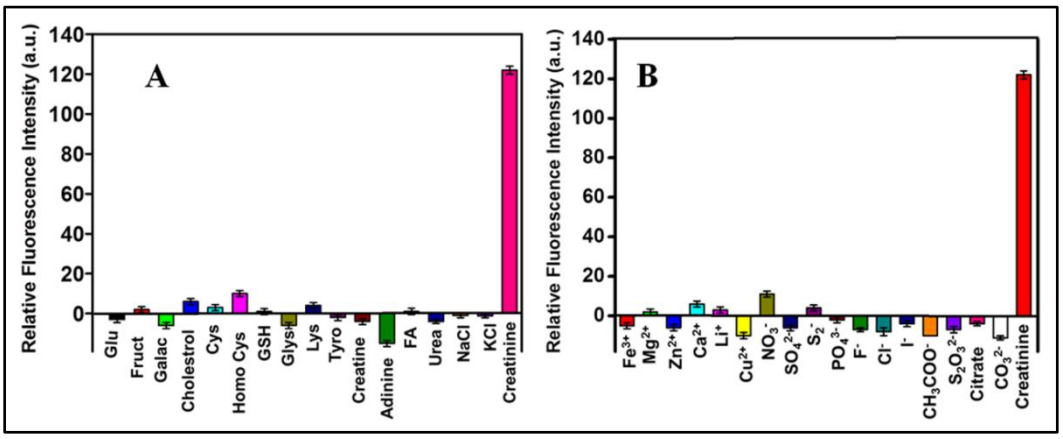

Figure 3.12. (A) Fluorescence response of Au_{QC}@gluten in the presence of creatinine (100 µM) and other biologically relevant molecule and (B) shows the effect of various ions on the fluorescence of Au_{QC}@gluten. Concentrations of all analytes were maintained constant (100 µM).

As shown in Figure 3.12, we observed that only creatinine could induce noticeable fluorescence recovery with a relative standard deviation (RSD) of 2.3%. Thus the other molecules do not interfere with the detection of creatinine in the blood. This indicates that this method can be used for highly selective and sensitive detection of creatinine.

Table 3.2. Comparison of current method with other Analytical methods for the creatinine sensor.

Methods	**LOD**	**Linearity**	**References**
Amperometric	0.3 µM	1-150 µM	(Schneider *et al.*, 1996)
Colorimetric	0.0084 µM	0.01–1 µM	(Parmar *et al.*, 2016)
Electrochemical	0.3 µM	1-80 µM	(de Araújo *et al.*, 2012)
Chemiluminescence	0.072 µM	0.1-30 µM	(Hanif *et al.*, 2016)
Fluorimetric	0.002 µM	20-520 µM	Current method

Further, the better analytical performance of the current sensing method is analyzed by comparing the performance of various other analytical tools used for creatinine detection in recent times (Table 3.2). It is clear from the table that, the analytical parameters such as detection limit and linear range of the present sensor is comparable/superior to the many of the mentioned methods.

3.3.5. Mechanism of fluorescence sensing

To elucidate the mechanism of fluorescence quenching and recovery of Au_{QC}@gluten with PA and creatinine, we carried out optical absorption, excitation spectrometry, and lifetime analysis. The acid-base interaction induced electron transfer quenching mechanism has been reported for detection of PA based on the fluorophore having basic groups such as amine, pyridine etc (Liu., *et al.*, 2016; Sun *et al.*, 2014; Zhang., *et al.*, 2016). Recently Sun and co-workers developed a protein-based fluorescence detection of PA via acid-base pairing interactions (Sun *et al.*, 2014). PA is a well-known electron-deficient nitro aromatic due to the strong electron withdrawing effect of the nitro group. The hydroxyl group present in the PA (2, 4, 6-trinitrophenol) is highly acidic owing to the presence of strong electron withdrawing effect of the three nitro group present in the PA (Structure of picric acid is given in Figure 3.13). The protein, gluten has a large number of amino groups, where PA can effectively adsorb by acid-base pairing interaction. When PA is added to the solution of Au_{QC}@gluten, it can interact with amine moieties of protein present on the surface of the gold quantum cluster through acid-base interaction. The close vicinity between Au_{QC}@gluten and PA greatly facilitates the electron transfer process. The electron transfer from the electron-rich Au_{QC}@gluten to electron-deficient PA leads to fluorescence quenching. When creatinine is added to Au_{QC}@gluten-PA, PA forms a stable complex with creatinine by replacing PA from AuQC@gluten. The increase in the concentration of creatinine causes an elevation in the level of the creatinine-picrate complex in the medium and consequently turning-on the fluorescence of the cluster. The reaction scheme for the formation of the creatinine-picrate complex through Jaffe reaction is shown in Figure. 3.13 (Debus *et al.*, 2015).

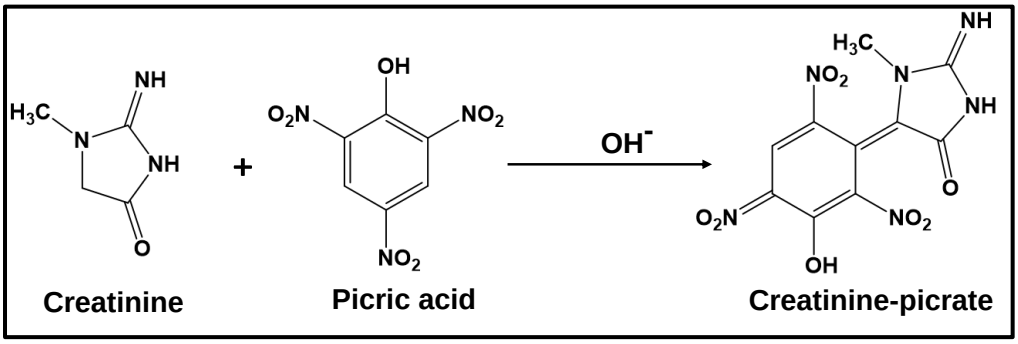

Figure 3.13. Reaction scheme for the formation of creatinine –picrate complex by Jaffe reaction.

The excitation spectra and absorption spectra of Au_{QC}@gluten at various PA concentrations (0.4 - 1.6 mM) are shown in Figure 3.14A and 3.14C respectively.

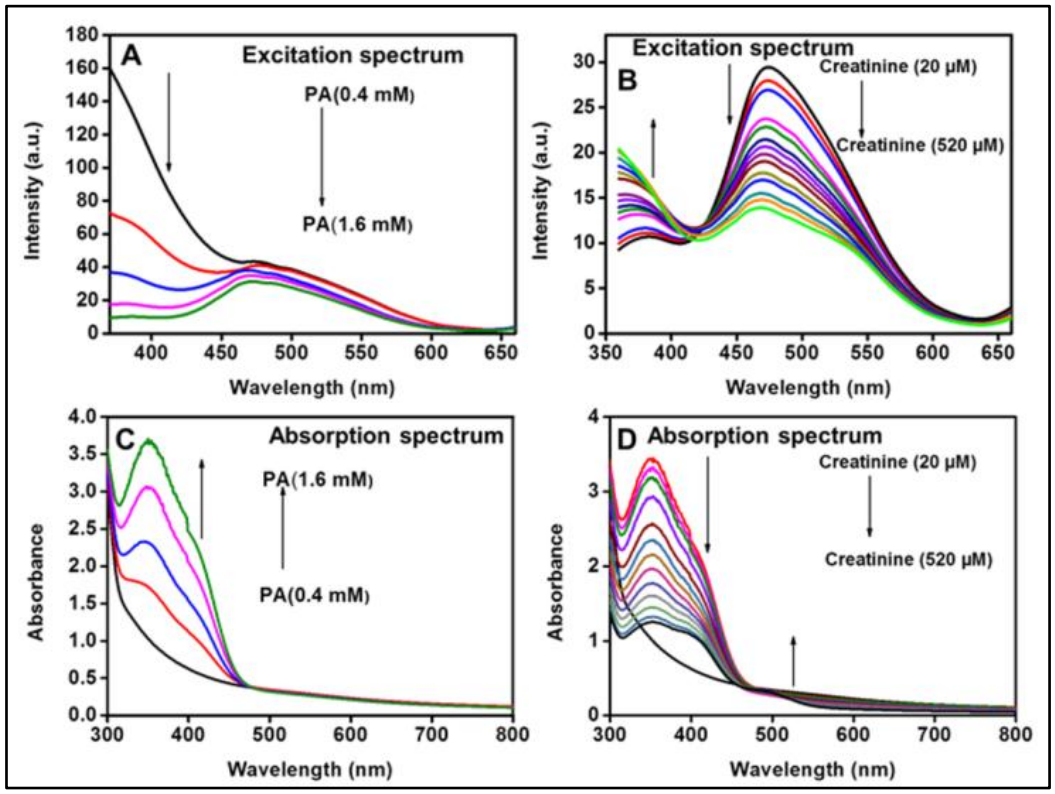

Figure 3.14. (A) and (B) shows the variation in the excitation spectrum of Au_{QC}@gluten with different concentration of PA and PA-creatinine mixture respectively. (C) and (D) shows the absorption spectrum of Au_{QC}@gluten with different concentration of PA and with PA-Creatinine mixture respectively.

In excitation spectra of Au_{QC}@gluten, the peaks corresponding to quantum cluster (380 nm) is decreasing with increasing concentration of PA (Figure 3.14A). When creatinine is introduced into the mixture of Au_{QC}@gluten & PA, the peak for the cluster emerges with decreased signal intensity at 480 nm (Figure 3.14B). There is a noticeable change observed in the UV-Vis absorption spectra of Au_{QC}@gluten with various concentration of PA (0.4 - 1.6 mM). A new peak emerges at 352 nm due to the presence of PA, which is further confirmed by taking the absorption spectrum of PA as given in Figure 3.15D with an absorbance maximum at 355 nm. The absence of covalent bond formation between amine moieties of gluten with PA was confirmed by the analysis of the absorption spectrum of Au_{QC}@gluten in the absence and presence of PA. The introduction of PA into Au_{QC}@gluten causes a slight blue shift in the λ_{max} of PA from 355 to 352 nm, which is due to the interaction/ adsorption of PA towards gluten stabilized cluster. When PA is added to the gold quantum cluster solution, there is no emergence of a new peak, but a shift in 3 nm wavelength of PA occurs which corresponds to the adsorption of picrate on the surface of the gold quantum cluster and not due to complex formation. Thus creatinine can easily replace picrate from the surface of the gold cluster and can form a creatinine-picrate complex. It is well known that PA can form a complex with creatinine in an alkaline medium as creatinine-picrate (Figure 3.13). When an aqueous solution of creatinine is added to PA (1.6 mM) treated Au_{QC}@gluten, a creatinine-picrate complex formation takes place in the medium, which leads to a change in the color of the solution from yellow to orange-red. The creatinine-picrate complex formation was further confirmed from UV-Vis absorption spectra. UV-Vis absorption spectrum of Au_{QC}@gluten-PA mixture with various concentrations of creatinine is shown in Figure 3.14 D. As the concentration of creatinine increases, the absorbance for PA (350 nm) decreases and a new peak) emerges at 490 nm, which is due to the formation of the creatinine-picrate complex. Further, the effect of pH upon sensing of the creatinine was studied. We have varied the pH of the medium from 6 to 11 and it is clear that the rate of recovery is maximum at basic pH whereas at acidic pH, the rate of recovery is negligible due to the lack of complex formation (Figure 3.15, A).

Additionally, the electron transfer mechanism was investigated by time-resolved fluorescence spectroscopy studies. We used pulsed laser excitation (455 nm) to avoid interference from gluten and measure the lifetimes of these Au quantum clusters at their fluorescence peak maxima. Figure 3.15B shows the time-resolved fluorescence decay curves of Au_{QC}@gluten, Au_{QC}@gluten with PA (1.6 mM) and Au_{QC}@gluten with PA-creatinine mixture. All the data were fitted well by a bi-exponential fit and the data is given in Table 3.3. Upon interaction of PA with Au_{QC}@gluten, a shortening of the average decay time of gold quantum clusters is observed, indicating the strong interaction of PA towards Au_{QC}@gluten which leads to electron transfer from Au_{QC}@gluten to electron deficient PA.

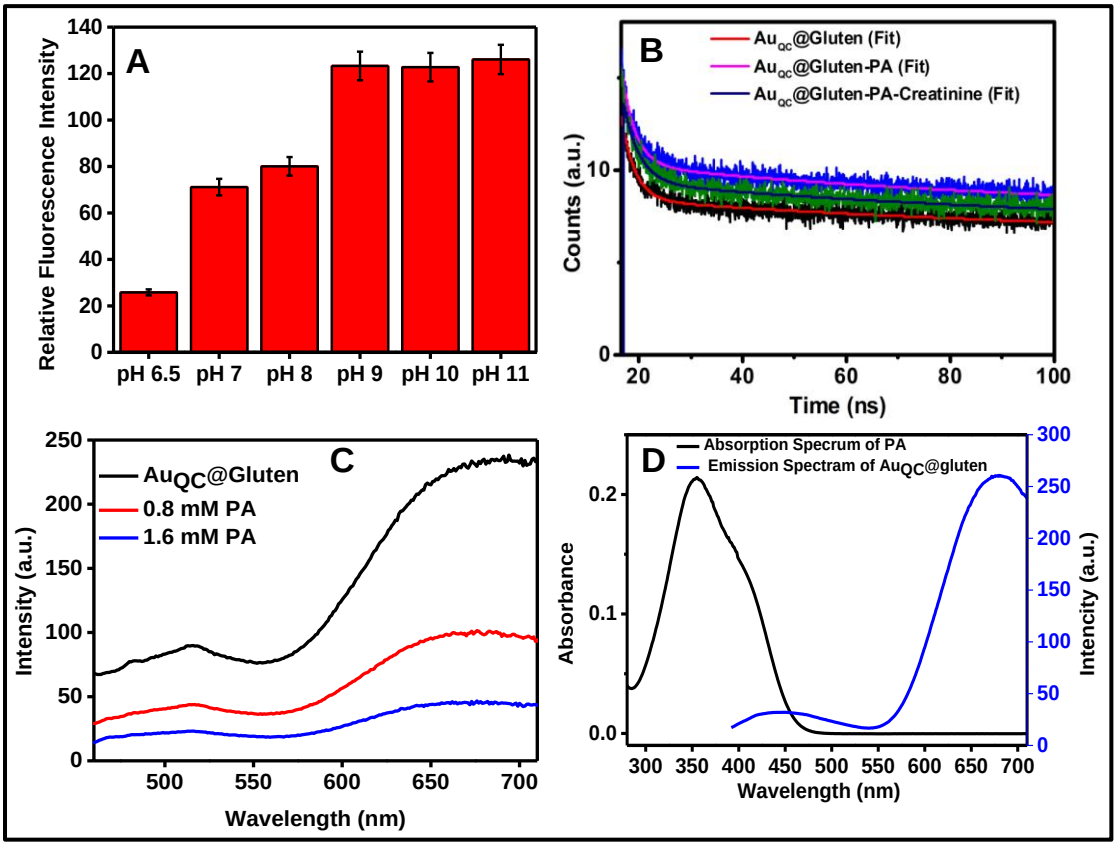

Figure 3.15. (A) Fluorescence recovery of Au_{QC}@gluten-PA with creatinine (520 µM) at different pH values, (B) Fluorescence decay profile of Au_{QC}@gluten (Red line), Au_{QC}@gluten-PA (Pink Line) and Au_{QC}@gluten-PA-Creatinine (blue line). (C) Fluorescence quenching of AuQC@gluten to different concentrations of PA (0.4 mM- 1.6 mM) at an excitation of 440 nm. (D) Absorption spectrum of PA (black line) and emission spectrum of Au_{QC}@gluten (blue line).

The average lifetime of Au_{QC}@gluten was found to be 95.84 ns with time component 96 ns (94%) and 2.5 ns (6%). It has been observed that with the addition of PA, the lifetime of slow decaying component decreases and the average lifetime reduces to 85.83 ns. Further, fluorescent recovery of Au_{QC}@gluten-PA with creatinine restores its average lifetime to 98.84 ns. This observation confirms that the main contribution to this change originates from the longest lifetime component and the interaction occurred in the excited state of the quantum cluster. The possible mechanism for fluorescence quenching of Au_{QC}@gluten in the presence of PA is its non-radioactive relaxation via electron transfer between the excited state gold quantum clusters to PA.

Table 3.3. Lifetime data of pure Au_{QC}@gluten, Au_{QC}@gluten-PA, and Au_{QC}@gluten-PA Creatinine.

Sample	**τ_1 (ns)**	**A_1**	**τ_2 (ns)**	**A_2**	**$<\tau>$ (ns)**	**χ^2**
Au_{QC}@gluten	96	94	2.5	6	95.84	1.30
Au_{QC}@gluten-PA	86	94	2.6	6	85.83	1.28
Au_{QC}@gluten-PA-Creatinine	99	95	3.09	5	98.84	1.27

Here we have eliminated Fluorescence Resonance Energy Transfer (FRET) mechanism for fluorescence quenching since there is no spectral overlapping between the absorption spectrum of PA and emission spectrum of Au_{QC}@gluten (Figure 3.15D). Furthermore, the effect of the inner filter effect on fluorescence quenching has been evaluated, since the fluorophore is excited at 380 nm, where the PA can have absorption around 355 nm. It has been reported that the absorption of the excitation and/or emission of light by absorbers might reduce the fluorescence intensity of the fluorophore (Li., *et al.*, 2016). For analyzing the effect of inner filter effect on fluorescence quenching, we have changed the excitation wavelength from 380 nm to 440 nm, where the absorption of PA is negligible and still a decrease in fluorescent intensity of cluster was observed in the presence of PA (figure 3.14C). Thus inner filter effect might not be

completely responsible for fluorescence quenching. In conclusion, the fluorescence quenching of the Au_{QC}@gluten by PA might partly result from the inner filter effect related to the specific absorption of PA. Since we have excited at 380 nm, the effect of the inner filter effect cannot be completely neglected. Hence, on the basis of the above discussion, it can be concluded that the fluorescence quenching and recovery of Au_{QC}@gluten is attributed to both the efficient electron transfer process as well as the inner filter effect.

3.3.6. Sensing of creatinine in the blood

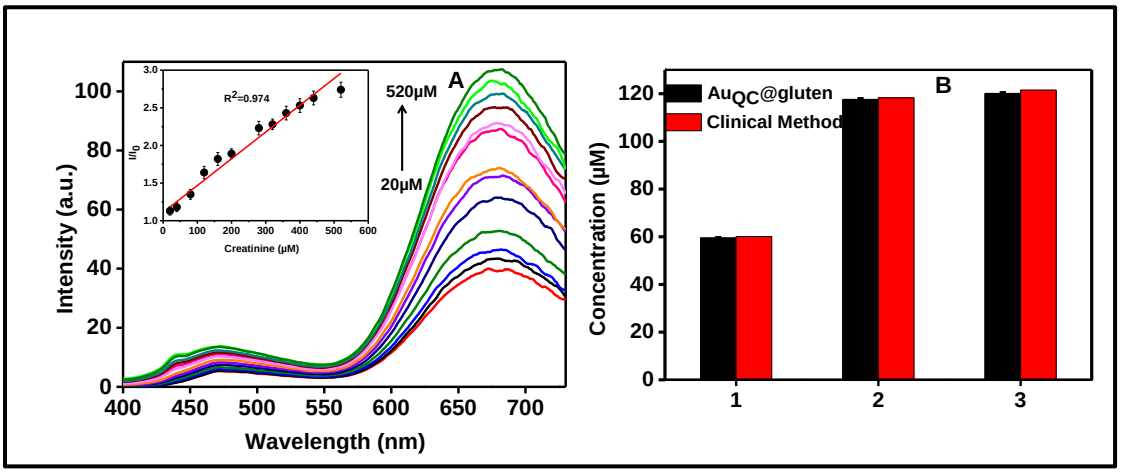

Figure 3.16. The determination of the concentration of creatinine in blood using Au_{QC}@gluten clusters. Fluorescence emission spectra of PA-treated Au_{QC}@gluten with various concentrations of creatinine spiked blood samples. Inset shows the plot of the values of (I/ I_0) at 680 nm versus the concentrations of creatinine. (B) Comparison of creatinine levels detected by our method with clinical detection method. 1, 2& 3 are different blood samples containing varying amounts of creatinine.

Table 3.4. Analytical results for creatinine in the spiked blood sample.

Added (μM)	**Found (μM)**	**Expected (μM)**	**Recovery (%)**	**RSD (%)**
0	59.50	60.10	98.16	3.5
40.00	98.25	100.10	98.25	2.1
120.00	219.60	220.10	99.50	2.8
240.00	457.8	460.10	99.50	2.3

To check the validity of the proposed sensor for the detection of creatinine in a real system, pre-treated blood samples were spiked with a known amount of creatinine and fluorescence recovery analysis were performed. Details of the sample preparations are given under the experimental section. The blood samples were diluted to 1000 times prior to analysis. A noticeable recovery of fluorescent intensity of Au_{QC}@gluten-PA was observed after the introduction of blood spiked with various concentration of creatinine (Figure 3.16A). The recovery of the creatinine is tested at three spiked concentrations (40, 120, and 240 µM) and is given in the Tables 3.4. This proposed method exhibits good recovery and acceptable RSD values, suggesting that the matrix effect of blood does not interfere with the detection of creatinine. From the calibration curve, the concentration of creatinine in whole blood was estimated to be 59.50 ± 0.3 µM, 117.60 ± 0.5 µM and 120.10 ± 0.5 µM using our method and the result was compared with normal clinical method (Figure 3.16B). These results confirm that the proposed method has a great potential for application of creatinine detection in the real sample.

3.4. Conclusions

We have demonstrated a cost-effective, green, one-pot approach to synthesize water-soluble fluorescent gold quantum clusters with a complex protein, gluten, as a protecting and stabilizing ligand. The resulting bright red emitting quantum clusters have 6.45% quantum yield. The Au_{QC}@gluten is highly stable against reactive oxygen species like H_2O_2. Hence, it can be utilized in many biological applications, such as bio-imaging, bio-labeling etc. The XPS, TEM, fluorescence, FT-IR, etc. validate the formation of the quantum cluster in a protein template. Au_{QC}@gluten with a core diameter of 1.5 nm has been applied to successfully develop the turn-on fluorescent sensor for the selective detection of creatinine with a detection limit of 2 nM. A detailed investigation was carried out to find out the response mechanism.

CHAPTER 4

SYNTHESIS AND CHARACTERIZATION OF GLUTEN PROTECTED SILVER- GOLD ALLOY QUANTUM CLUSTERS FOR BILIRUBIN DETECTION

This chapter presents the development of a facile and cost-effective method for the preparation of highly stable near infrared emitting wheat gluten stabilized AgAu alloy quantum clusters (AgAuQC@gluten) through galvanic exchange reaction (GER). The prepared AgAuQC@gluten displayed intense luminescence with an appreciable quantum yield of 9.5 %, and excellent stability under various pH values and photostability for a few hours of photo-irradiation. Additionally, AgAuQC@gluten were utilized as a fluorescent probe for highly selective sensing of bilirubin. The detection limit was found to be 50 nM. Photoinduced electron and inner filter effect (IFE) are responsible for the strong quenching of fluorescence of these QCs. Furthermore, this method has been validated by applying it to the determination of bilirubin in real blood samples.

The results of this chapter have been communicated for publication in Particle and particle systems characterization

4.1. Introduction

Bilirubin is a yellow compound present in bile, which is produced during the breakdown of old red blood cells by the liver (Fevery, 2008; Stocker *et al.*, 1987). Measuring the level of bilirubin is essential for monitoring liver disorders in human beings. The normal level of bilirubin found in blood is <25 μM, whereas the increased level of bilirubin (>25 μM) indicates various liver disorders like hepatitis, jaundice, cirrhosis etc (Stocker *et al.*, 1987). Further, the excess bilirubin in the blood causes unwanted deposition in the body which eventually leads to gallstones, pancreatic tumors, brain damage, or even death (Hopkins *et al.*, 1996). Therefore, it is of necessity to develop a simple, rapid, and highly sensitive detection method for bilirubin, especially in human body fluids.

To date, many analytical technologies have been developed to detect bilirubin such as various electrochemical sensing methods, colorimetric assays, and fluorescence detection methods (Du *et al.*, 2017; Thangamuthu *et al.*, 2018). The clinical method used to detect the level of bilirubin is a diazotization reaction between sulphanilic acid and bilirubin, but it is a time-consuming method (30 min is needed to achieve the maximum color) (Fevery, 2008). Among these analysis methods, fluorescent detection methods are ideal due to distinct advantages such as high specificity and sensitivity, simplicity, and short response time (Zhang *et al.*, 2017). Organic dyes are utilized as fluorescent probes for the detection of bilirubin in recent times (Ellairaja *et al.*, 2017; Senthilkumar & Asha, 2015). However, organic dyes might suffer from small Stokes shift, short lifetime, low water solubility and poor photostability (Durgadas *et al.*, 2011). Alternatively, considerable attention has been drawn to the preparation and applications of fluorescent metal QCs due to their small size, excellent biocompatibility, large Stokes shift, intense fluorescence emission, and high photostability (Chen, L.-Y. *et al.*, 2014; Mathew & Joseph, 2017).

Recently, Basu et al. developed a probe for detection of hyperbilirubin in blood by using gold QC incorporated in a polymer film (Basu *et al.*, 2016). The yellow luminescence of chitosan stabilized AuQC incorporated polymer film was

quenched in presence of Cu^{2+} ions and subsequently recovered in the presence of bilirubin. Human serum albumin protected AuQC were used as a fluorimetric probe for the sensing of bilirubin in blood was also reported (Santhosh *et al.*, 2014). The proteins derived from animal/insects such as albumin, gelatin, collagen, etc are widely used for synthesizing nanomaterials and thereafter used for sensing and drug delivery applications (Hu., *et al.*, 2015b). However, the stability, cost, and storage of these proteins are the main challenges faced in the biomedical field. To overcome these limitations, the plant-derived proteins have been investigated as an alternate source for synthesizing fluorescent metal QCs owing to its specific advantages such as natural abundance, high accessibility, and cost-effectiveness (Goswami *et al.*, 2014b; Gui & Jin, 2013; Li., *et al.*, 2018; Malekzad *et al.*, 2017; Mathew, Joseph, 2017). Here we have synthesized AgAu alloy QC using gluten as a template. Among NMQCs, bimetallic QCs, particularly AgAu QCs has received great attention due to their high stability against oxidation, high quantum efficiency etc by the integration of two metal species with its unique property in a single cluster (Barcaro *et al.*, 2015; Ganguly *et al.*, 2016) (Le, Hotzer, *et al.*, 2011; Yuan *et al.*, 2015). Several synthetic strategies have been applied for the synthesis of AgAu alloy quantum clusters including, solid-state synthesis, template-assisted synthesis, galvanic exchange, doping and core etching of nanoparticle or conversion of large-sized quantum clusters to few atom quantum clusters (Jupally & Dass, 2014; Murugadoss *et al.*, 2012)(Jin & Nobusada, 2014; Wang., *et al.*, 2014; Zhou., *et al.*, 2013). Recently, synthesis of several monolayer protected alloy clusters like $AuAg_{144}$, $Au_{25-x}Ag_x(SR)_{18}$, $Au_{\sim 98}Ag_{\sim 46}$, $AuAg_{38}$, $Ag_{19}Au_{19}$@BSA, Ag_7Au_6 were reported (Jupally & Dass, 2014; Kauffman *et al.*, 2013; Kumara & Dass, 2011; Liu, J. *et al.*, 2016; Udayabhaskararao *et al.*, 2012). The $Ag_{19}Au_{19}$@BSA were prepared by simple mixing of AgQCs@BSA and AuQC@BSA (Mohanty *et al.*, 2012b).

In this study, we have demonstrated a facile route for the synthesis of water-soluble, AgAu alloy quantum cluster stabilized by a green and cost-effective protein, wheat gluten. The intense near-infrared emitting AgAuQC@gluten were synthesized based on galvanic exchange reaction, in which AgQCs act as a sacrificial template. These QCs were found to be stable at

all pH (1-12) and UV light irradiation for a few hours. Consequently, the as-prepared AgAuQCs were further investigated as a fluorescent probe for the selective sensing of bilirubin. Herein we have developed a novel and extremely sensitive AgAu alloy QCs based fluorimetric method for detecting bilirubin. The practicality of the sensing system was validated through the detection of bilirubin in human blood samples. Moreover, the fluorescent AgAuQC@gluten can be easily coated on a cotton bud and an efficient sensor can be constructed for rapid and routine monitoring of bilirubin.

4.2. Experimental Section

4.2.1. Materials

All the reagents were used as obtained without further purification unless stated otherwise. $HAuCl_4.3H_2O$, $AgNO_3$, gluten, the membrane dialysis bag (molecular weight cut-off 14 kDa), cholesterol, cysteine, homocysteine, glutathione, glycine, lysine, tyrosine, adenine, creatine, folic acid, bilirubin, and creatinine were purchased from Sigma-Aldrich. Sodium dihydrogen phosphate and disodium hydrogen phosphate, glucose, fructose, stearic acid, urea, and galactose were purchased from Merck. Cotton buds were procured locally. All solutions were prepared using Millipore water.

4.2.2. Instrumentation

The optical absorption spectra were collected using the Varian model, Cary win Bio 100 spectrometer. The experiments were carried out at room temperature and collected data in the range of 200-800 nm. Fluoro Max-4C spectrofluorometer (Horiba Instruments, USA) was used for luminescence measurements. The emission spectra were recorded upon excitation at 400 nm; the slit width for excitation and emission were set at 5 nm. We have used TCSPC accessory for lifetime analysis with a pulse width of 1.3 ns. Photostability study was carried out by irradiating an aqueous solution of AgAuQC@gluten with multi lamp instrument containing 32 W UV light sources. The HR-TEM images were recorded on a JEOL JEM 2100 instrument with an acceleration voltage of 200 kV.

XPS analysis was carried out using a Multilab 2000, Thermo Fisher Scientific using Al K-α radiation. The sample were spotted as drop-cast films on a sample stub. Energy dispersive X-ray analysis was carried out using HRSEM, Quanta FEG200, FEI, USA equipped with Energy dispersive spectroscopy (EDS). For SEM, the powder sample were coated over a carbon coated stub followed by gold sputtering. FTIR spectra were measured using Perkin Elmer FTIR spectrometer, the spectra of powder sample recorded using Attenuated total reflection (ATR) accessory.

4.2.3. Preparation of AgAuQC@gluten

The first step in the synthesis of AgAuQC@gluten involved the preparation of AgQC@gluten. For this gluten, the protein solution was prepared by dissolving gluten (25 mg/mL) in alkaline solution (0.5 M NaOH) and heating (40 °C) it for 15 minutes. In a typical experiment, 5 mL (6 mM) $AgNO_3$ solution was treated with 5 mL (25 mg/mL) of the above-prepared gluten in alkaline solution and was vigorously stirred at room temperature for 20 minutes. The color of the solution changed from pale yellow to dark brown. 2 mL of the as-synthesized AgQC@gluten was mixed with 2 mL 1mM $HAuCl_4$ and the pH of the medium was adjusted in the range of 5-6 by adding HCl (0.1M). This mixture was stirred for 3 hours at 55 ° C. The color of the solution changed from dark brown to yellowish brown. The cluster formation was preliminarily confirmed by an intense red emission under table top UV light (365 nm excitation). Purification of AgAuQC@gluten was performed by dialysis against distilled water for 24 hours in a dialysis membrane of molecular weight cut-off of 14 kDa. The purified AgAuQC@gluten clusters were then freeze-dried and stored at room temperature for further use.

4.2.4. Method of sensing of bilirubin

The AgAuQC@gluten solution was diluted 10 times prior to all studies. A volume of 2.5 mL of the QC solution was treated with different concentrations of

bilirubin (2.5 μM -70 μM) and the fluorescence intensity variation was measured at 690 nm by an excitation at 400 nm.

4.2.5. Method of detection of bilirubin in blood samples

Blood samples were collected from a volunteer and were diluted 1000 times before analysis. An authentically signed consent was obtained from the volunteer. 50 μL of diluted blood sample were spiked with different concentrations of bilirubin (2.5−70 μM) and incubated for 15 minutes. Blood with and without bilirubin spike was treated with 2.5 mL of AgAuQC@gluten and the fluorescence intensity at 690 nm was monitored.

4.2.6. Development of test probe for detection of bilirubin

The AgAuQC@gluten sensor was developed using a simple strategy by coating the QC on cotton buds. For this, the cotton buds were soaked in 10 mL of AgAuQC@gluten solution for about 24 hours. After drying in air (approximately 24 hours), the buds were dipped in different concentrations of bilirubin solution (2.5−70 μM). The AgAuQC@gluten coated sensor before and after the treatment with bilirubin was placed under UV light (360 nm) and changes in the color have been noted.

4.3. Results and Discussion

4.3.1. Synthesis and characterizations of fluorescent AgAuQC@gluten

The synthesis of AgAu quantum clusters in a protein template was carried out by galvanic exchange reaction method as shown in Figure 4.1. The capping agent used for the formation of AgQC and AgAuQC is gluten, a protein derived from wheat. In the first step of the AgAuQC synthesis, the template, AgQC was synthesized by the bio-mineralization method (Mathew *et al.*, 2016). Mixing of $AgNO_3$ and gluten at pH- 12 at room temperature produced brownish colored non-fluorescent AgQC. This was followed by the addition of $HAuCl_4$ into AgQC

solution in an acidic medium (pH-5-6) which enabled the replacement of a few silver atoms to form AgAu alloy quantum clusters.

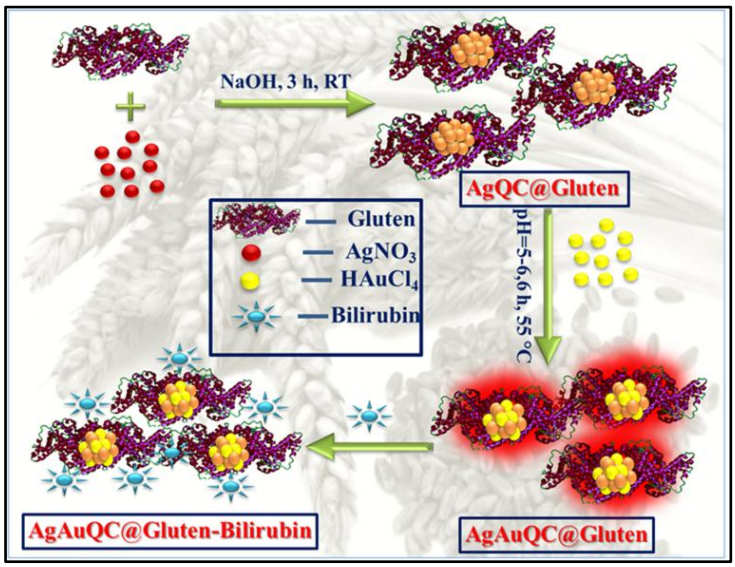

Figure 4.1. Schematic representation for the synthesis of gluten protected AgQC@gluten, AgAuQC@gluten followed by the sensing of bilirubin.

This replacement reaction occurs due to the higher standard reduction potential of Au^{3+}/Au (0.99 V versus the standard hydrogen electrode, SHE) over Ag^{+}/Ag (0.80 V versus SHE) (Wang., *et al.*, 2013). In this reaction, two processes can happen, which leads to the generation of intense emitting AgAuQC. (1) The Ag (0) was oxidized to Ag^{+} and got converted to AgCl in the solution. (2) The Au^{3+} was reduced to Au(0). The UV- Vis absorption spectra of gluten, AgQC@gluten, AgAuQC@gluten are shown in Figure 4.2A. The peak at 280 nm corresponds to the absorption of aromatic amino acid present in gluten. A small hump observed at 320 nm, which is not seen in gluten, confirms the AgQC formation. In the case of the alloy, an extended broad absorption in the range of 300-600 nm is observed, this is an indication for the formation of AgAu alloy QCs. Furthermore, the absence of surface plasmon resonance (SPR) peak rules out the possibility of the formation of gold and silver nanoparticles in the medium. The AgQC@gluten is non-fluorescent/weakly fluorescent as shown in Figure 4.2B. When $HAuCl_4$ is introduced in the AgQC@gluten, the replacement of Ag by Au atoms produce intense red emitting AgAuQC. The fluorescent emission of

AgAuQC@gluten is shown in Figure 4.2B. The as-prepared AgAuQC@gluten in aqueous solution shows strong near-infrared fluorescence with λmax at 690 nm, which is 90-times intense than AgQCs at the same concentration. The Near-infrared (NIR) emitting nanomaterials are much attractive in the field of in vivo deep-tissue imaging due to the improved tissue penetration of lights and decreased tissue autofluorescence in the NIR range (Tao *et al.*, 2015).

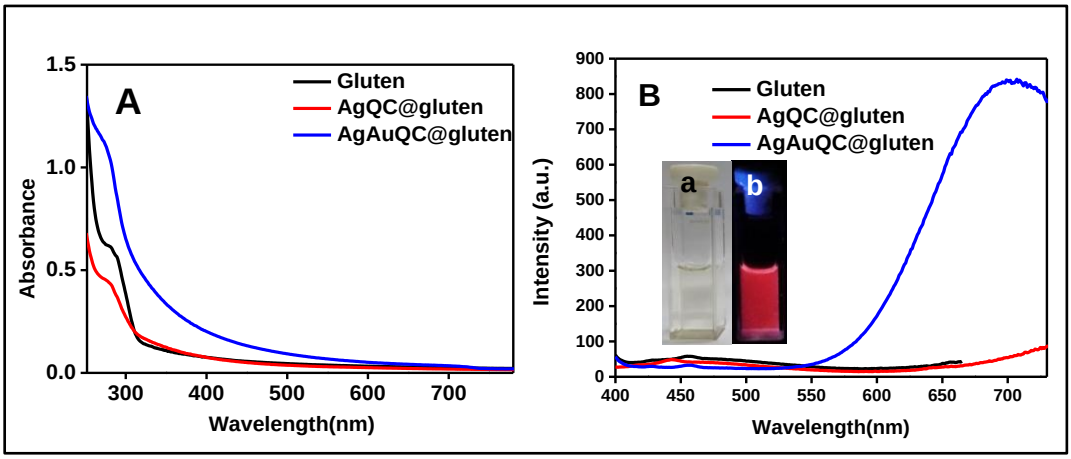

Figure 4.2. UV-Visible absorption (A) and emission spectrum (B) of gluten (black trace), AgQC@gluten (red trace) and AgAuQC@gluten (blue trace) respectively The inset shows the photograph of AgAuQC@gluten taken in visible light (a) and UV light (b).

The fluorescent emission maximum of the alloy QC cluster exhibits a red shift (λ_{max}=690 nm) at this composition compared to the AuQC@gluten (λ max=680 nm) when excited at 400 nm (Mathew, & Joseph, 2017). The quantum yield (QY) of AgAuQC@gluten is found to be 9.5% using Coumarin 153 (QYs, 0.54 in ethanol) as the standard (Rurack & Spieles, 2011), which is greater than most of the reported alloy QCs. The Equation for QY calculation is given in Section 3.2.5 (Equation 3.1). The calculation of quantum yield is given in Table 4.1. The enhanced quantum yield is due to the well-known 'Silver effect'(Cheng *et al.*, 2014). The presence of gold and silver in the same system produce enhanced fluorescence due to the synergetic interactions (Liu *et al.*, 2018; Lu & Chen, 2012).

Table 4.1. Quantum Yield Calculation

Sample	**λEx. (nm)**	**Φ_0**	**A_0**	**I_0**	**n_o**	**A_s**	**I_s**	**n_s**	**Φ_s (%)**
AgAuQC	400	0.54	0.012	$1.7x10^8$	1.33	0.037	$4.0x10^7$	1.33	9.5

The HRTEM of AgQC@gluten and AgAuQC@gluten are shown in Figure. 4.3. The average size of both AgQC and AgAuQC is in the range of 1 -1.5 nm (Figure 4.3A &4.3B). The formation of AgAuQC was further confirmed by XPS and EDS analysis. The XPS spectrum of AgAuQC shows the presence of both Ag(0) and Au(0) states in the system.

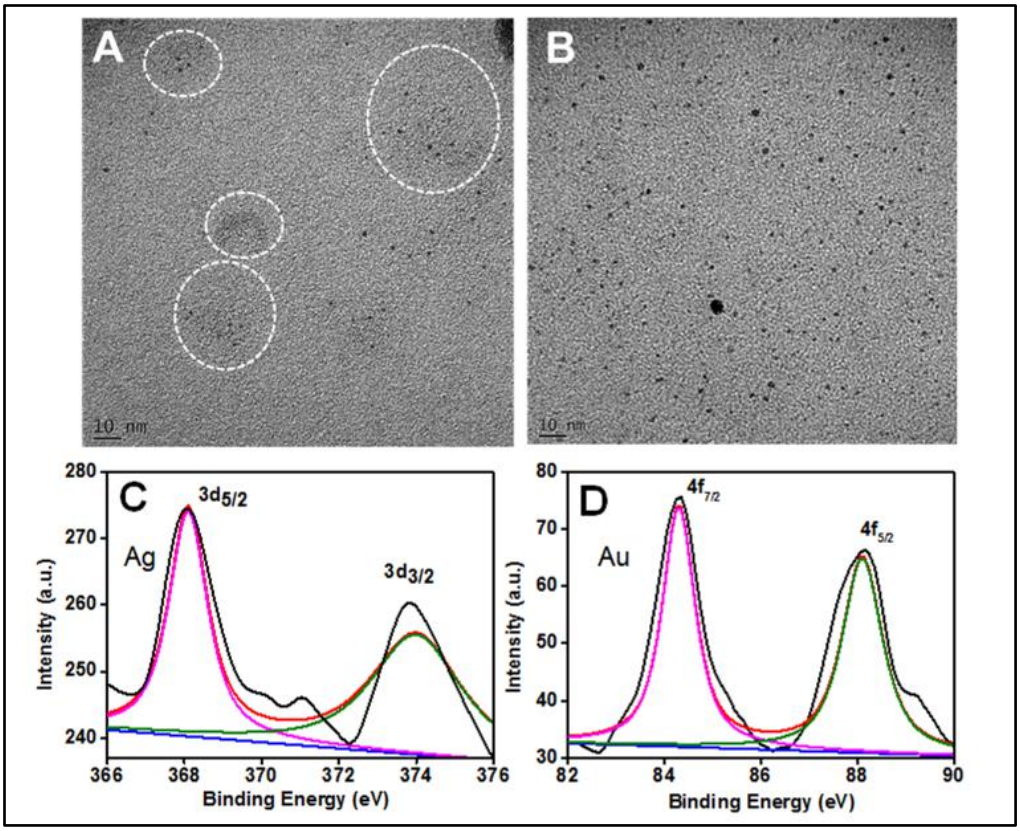

Figure 4.3. **(**A) & (B) shows the TEM image of AgQC@gluten and AgAuQC@gluten respectively. (C)&(D) shows the XPS of Ag 3d and Au 4f of AgAuQC@gluten respectively.

The binding energy for Ag $3d_{5/2}$ and Au $4f_{7/2}$ are at 368.1 eV and 84.3 eV respectively, which corresponds to the metallic form of Ag and Au (Figure 4.3C & 4.3D).

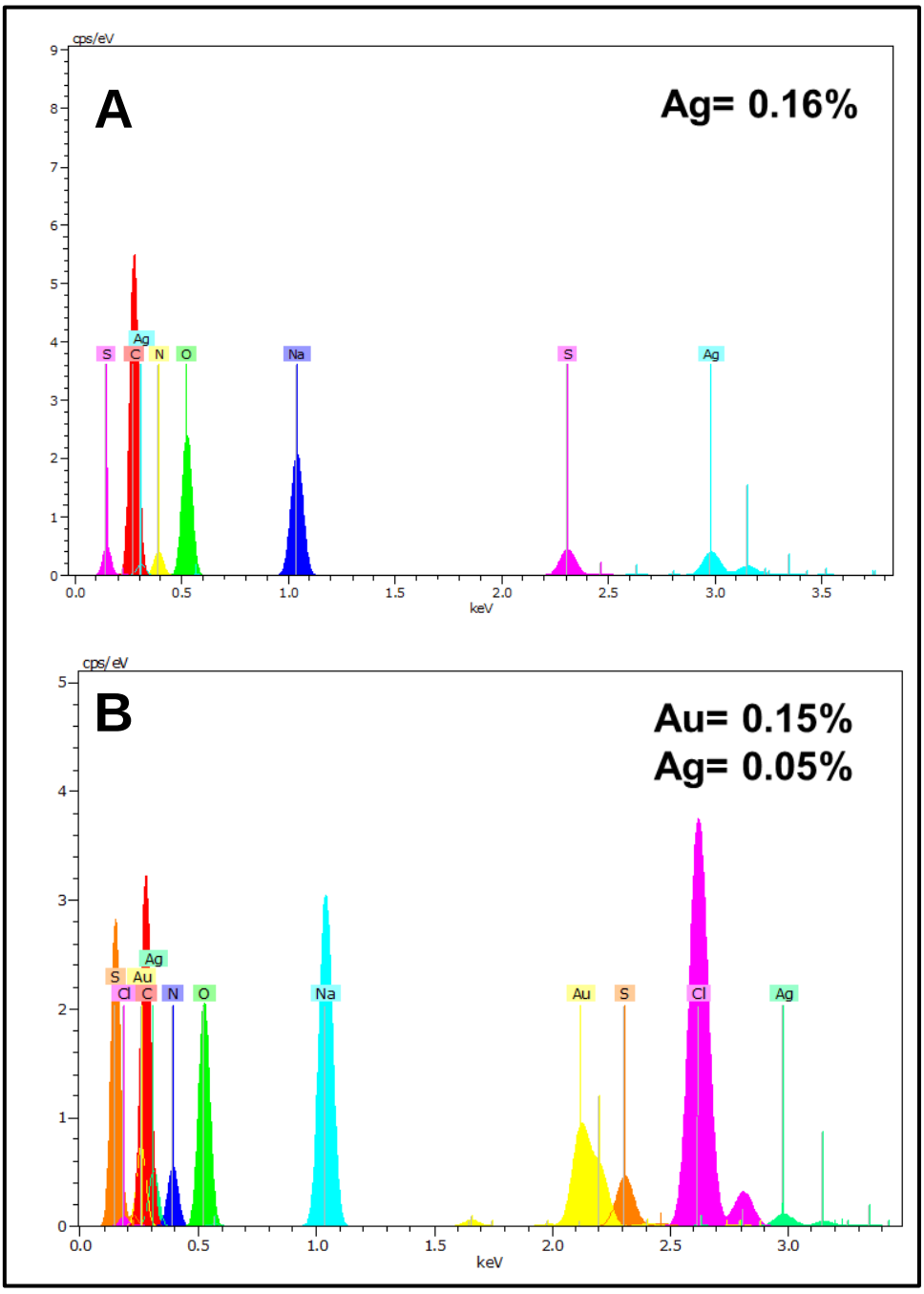

Figure 4.4. (A)&(B) shows the EDS result of AgQC@gluten & AgAuQC@gluten respectively.

The EDS analysis of AgQC and AgAuQC is carried out separately. The analysis indicates the presence of 0.16% Ag in AgQC, while the AgAuQC system shows 0.05 % and 0.15 % Ag and Au respectively (Figure. 4.4A & 4.4B). The decrease in Ag composition from 0.16% to 0.05 % in AgAuQC further confirms the formation of AgAuQCs through galvanic exchange reaction. Due to the complexity of wheat gluten protein (composed of hundreds of different protein), the number of Ag and Au atoms present in the cluster could not be detected using MALDI TOF- MS analysis.

Highly stable fluorescent nanomaterials are significant candidate for various biomedical applications such as biolabelling, bioimaging etc (Chevrier *et al.*, 2012; Goswami *et al.*, 2014b). The limitations of the conventional fluorophore (organic dyes, quantum dots) used for bio-imaging purposes are its high toxicity and photobleaching effect (Chan *et al.*, 2002; Richards *et al.*, 2008). Thus the synthesized AgAuQC cluster can broaden the biomedical application of luminescent nanomaterials owing to their ultra-stable nature. Figure 4.5A shows the fluorescence intensity of AgAuQC@gluten at various pH values from 1 to 12. The fluorescence intensity of the QCs does not change with pH, indicating that these QCs possess a relatively high pH-stability. Further, the photostability of AgAuQC was investigated by exposing it to a 32 W UV light source (Figure 4.5 B). The fluorescence intensity of the AgAuQC@gluten was monitored at different time intervals up to 200 minutes. The fluorescence intensity remained consistent even after prolonged exposure to UV light. Moreover, we optimized the galvanic replacement reaction conditions for synthesizing strongly fluorescent and highly stable AgAuQCs by adjusting the concentrations of $HAuCl_4$, altering the reaction temperatures and pH of the medium. Fluorescence spectra of the resultant AgAuQCs synthesized under different reaction conditions are given in Figure 4.6. Initially, the effect of concentration of $HAuCl_4$ was investigated. On varying the concentration of $HAuCl_4$ from 0.6 mM to 3.0 mM, the maximum fluorescence intensity was achieved at 1.0 mM concentration of $HAuCl_4$. Further increase in the Concentration leads to the decrease in the fluorescence intensity as a consequence of larger sized nanoparticles formation.

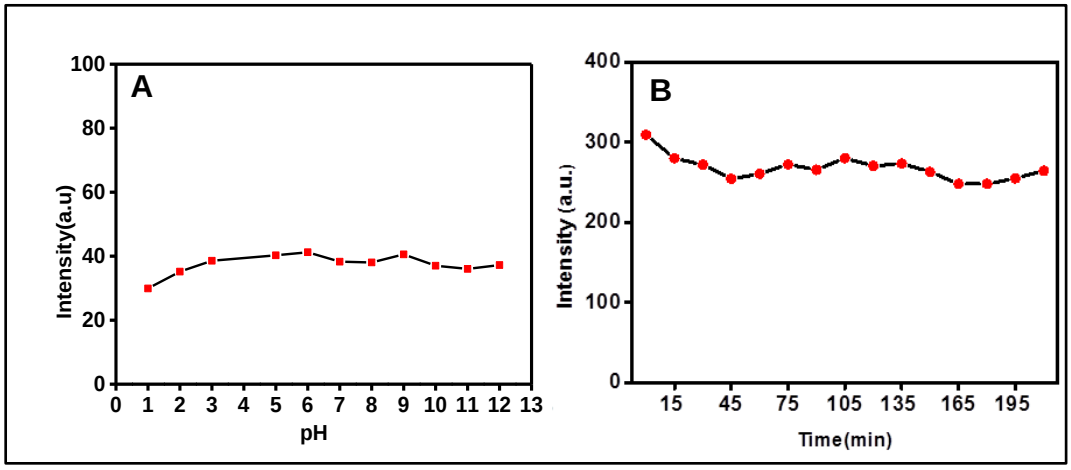

Figure 4.5. (A) Fluorescence intensities of AgAuQC@gluten as a function of pH. (B) Fluorescence intensity of AgAuQC@gluten with UV irradiation at different time interval.

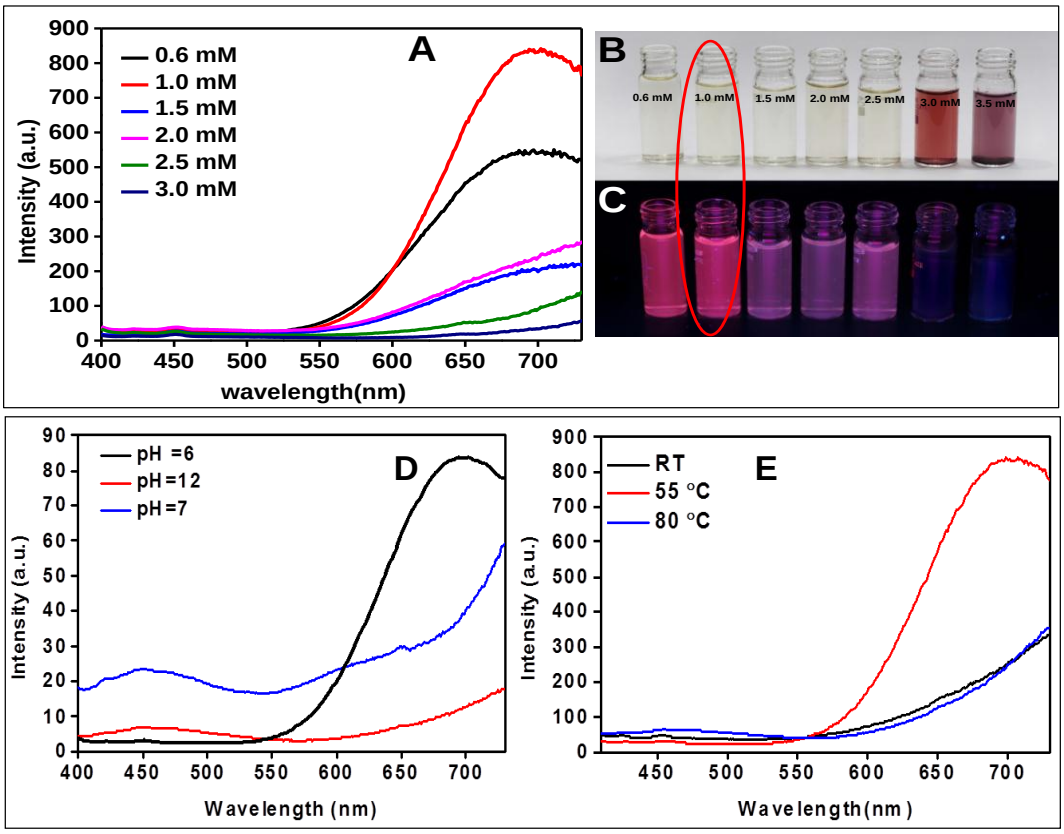

Figure 4.6. (A) Fluorescence emission spectra for the formation of AgAuQC@gluten with different concentration of $HAuCl_4$ and (B) &(C) shows the corresponding photograph under visible light (B) and UV light (C) respectively. D and E show the formation of AgAuQC@gluten with different pH condition and temperature respectively.

The emergence of red coloration in the solution at higher concentrations of $HAuCl_4$ further provides the confirmation of nanoparticle formation in the medium. Thus the optimum concentration of $HAuCl_4$ for the formation of intense emitting AgAuQCs was 1.0 mM. The fluorescent spectra of AgAuQC synthesized at different concentrations of $HAuCl_4$ and the corresponding photographs of the solutions are shown Figure 4.6A, B&C. Additionally, the influence of pH for galvanic exchange reaction was analyzed, and we serendipitously observed that the galvanic exchange reaction takes place only at acidic pH (pH~5-6) (Figure 4.6D). The effect of temperature on the formation of the alloy was studied by varying the temperature of the mixture from room temperature to 80 °C. It was observed that the AgAuQC synthesized at 55 °C exhibited the highest emission intensity. (Figure 4.6E). Hence, the synthesis conditions like the concentration of $HAuCl_4$, the reaction temperature and the pH of the medium were optimized as 1 mM, 55 °C and 5-6 pH, respectively.

The influence of the solution pH on the mechanism and products in GERs has not been addressed in most of the published works as the acid and base have no influence on the redox potential of metal ions (Susman *et al.*, 2015). Thus, GER is considered to be a pH-independent reaction. So, the pH can only influence the protecting ligand used for the stabilization of the nanoparticle. It is well known that the protein shows different conformations at different pH values which would definitely reflect on the synthesis of metal nanoclusters (Cao *et al.*, 2013; Yu *et al.*, 2013). It is assumed that, because of the highly complex and folded structure of gluten, the replacement of metal ions from the AgQC@gluten may not be possible at basic pH, which could be the reason why the alloy formation was inhibited at basic pH. When gluten protected AgQC is treated with $HAuCl_4$ at acidic pH, the confirmation of the protein might have changed, enabling the Au^{3+} ions to effectively diffuse and thereby replace the Ag atoms. In the case of other protein protected clusters, the GER is feasible at basic pH and neutral pH itself (Mohanty *et al.*, 2012b).

The secondary structures of gluten in the reaction system were investigated by FT-IR spectroscopy. As shown in Figure. 4.7, a broad peak at

3500 - 2900 cm^{-1} is due to the OH, CH, and NH vibrations. The peaks in the range of 1600 to 1690 cm^{-1} are the stretching frequency of amide I band of protein. Amide II is in the range of 1480 – 1575 cm^{-1} and amide III is in between 1229 - 1301 cm^{-1}. Both the Amide I and Amide II bands are sensitive to the secondary structure of a protein (Yang *et al.*, 2015).

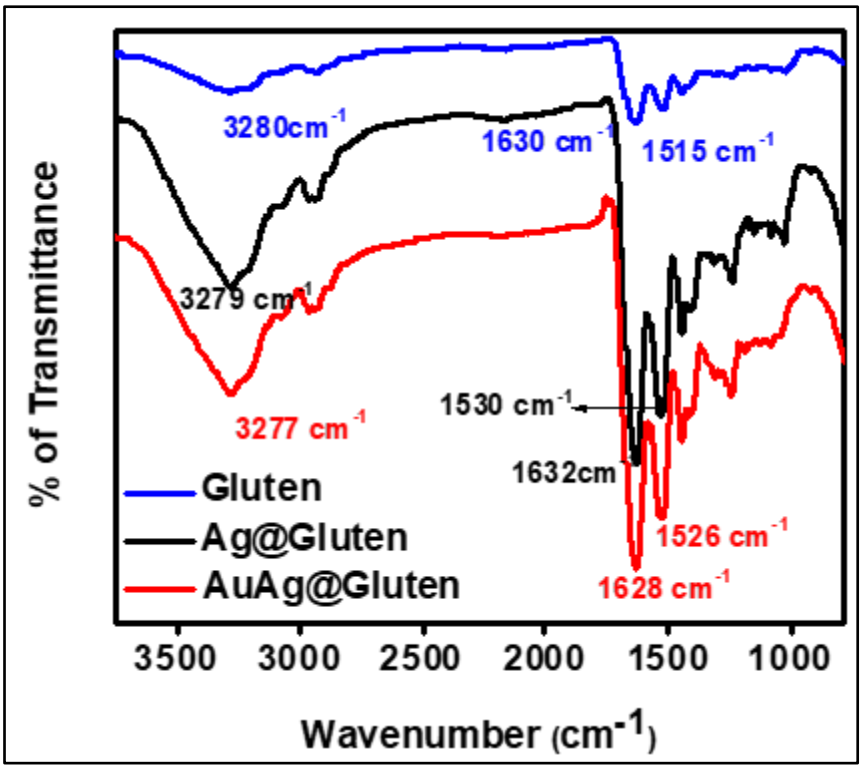

Figure 4.7. FTIR spectra of gluten (blue trace), AgQC@gluten (black trace) and AgAuQC@gluten (red trace).

After formation of AgAuQC at pH 5-6, the confirmation of gluten further changed. The stretching frequency of amide I and amide II shifted to 1628 cm^{-1} and 1526 cm^{-1}, respectively. This change in conformation of gluten in acidic pH can assist the GERs leading to the formation of intense red emitting AgAuQC@gluten.

4.3.2. Sensing of bilirubin

The fluorimetric sensing of bilirubin is schematically illustrated in Figure 4.1. Figure 4.8A illustrates that the fluorescence emission intensity of AgAuQC

quenched as a function of increasing concentration of bilirubin. Specifically, on the addition of 70 µM bilirubin, nearly 90 % of the fluorescence emission intensity of AgAuQC was quenched. A linear correlation between the two quantities, i.e., the emission intensity and concentration, is clearly visible from the Stern–Volmer plot displayed in Figure. 4.8B and 4.8C. The plot is constructed based on the Stern–Volmer equation (Equation 2.1).

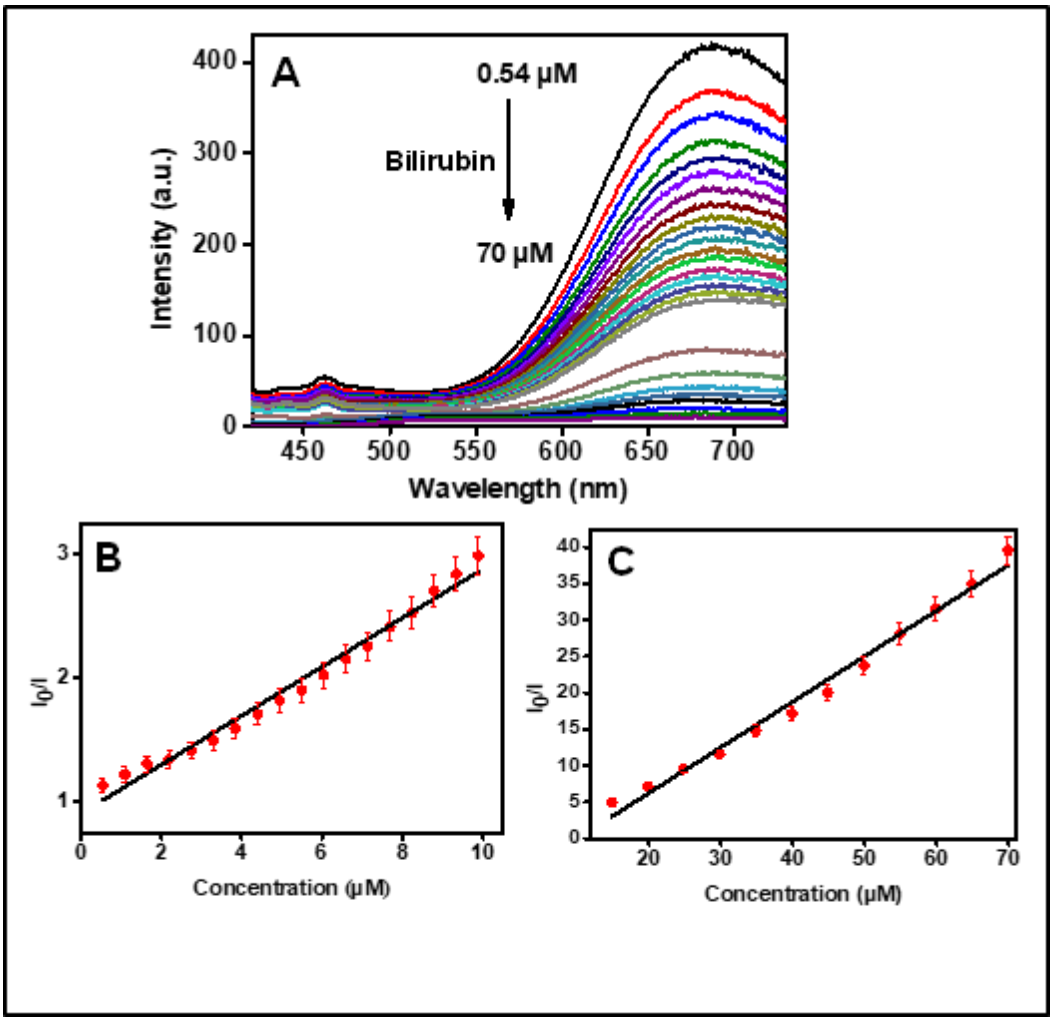

Figure 4.8. (A) Fluorescence response of AgAuQC@gluten with different concentration of bilirubin (0.54-70 µM), (B) and (C) shows the Stern-Volmer plot of AgAuQC@gluten in the concentration range (0.54-10 µM) and (10-70 µM), respectively.

It demonstrates that there is a good linear dependence of fluorescence intensity on bilirubin concentration with R^2= 0.98 over the concentration ranging from 0.5 to 10 µM and 10-70 µM. The detection limit is calculated based on 3σ/K, (Mathew

& Joseph 2017) where σ is the standard deviation from the blank measurement in the absence of bilirubin and K is the slope of the calibration plot and is estimated to be 50 nM, which is much lower than clinically relevant range (25-50 µM) of bilirubin found in human blood (Dubin and Johnson 1954; Nagasue *et al*. 1987). Moreover, we demonstrated the selectivity of the sensor system using various biomolecules (Cholesterol, folic acid (FA), thymine, galactose (gala), creatinine, L-valanine (L-Val), L-alanine (L-ala), L-tyrosine (L-Tyro), L-proline (L-prol), L-serine (L-Ser), stearic acid, lysine, glutathione (GSH), glycine (Gly), urea, glucose, fructose,

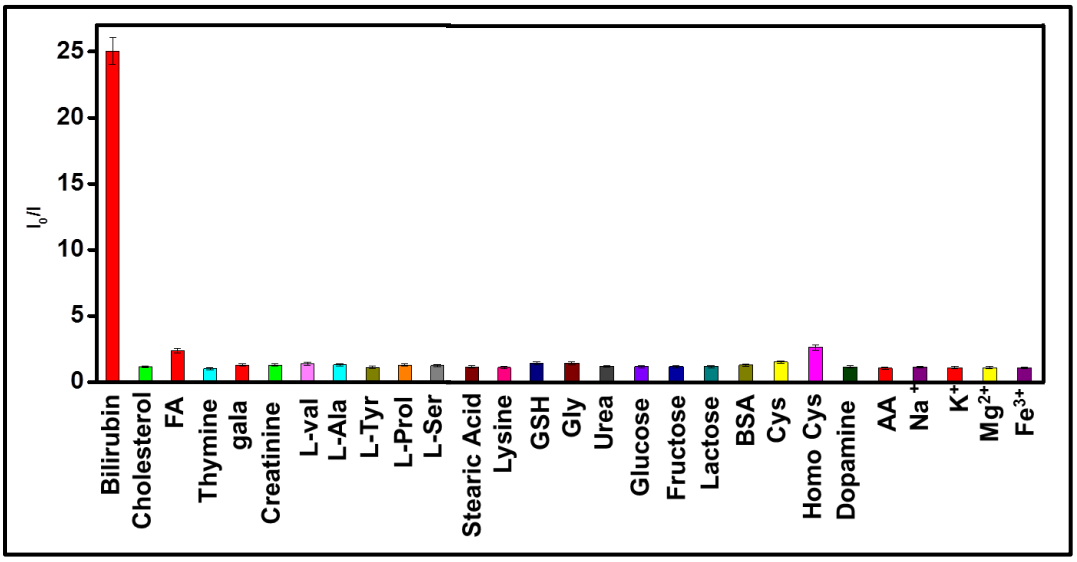

Figure 4.9. Fluorescence response of AgAuQC@gluten with different biologically relevant molecules and metal ions present in the biological system. (Concentration of all analytes were kept at 70 µM).

lactose, bovine serum albumin (BSA), Cysteine (Cys), homocysteine (Homo cys), dopamine and ascorbic acid (AA)) as well as metal ions (Na^+, K^+, Mg^{2+},Fe^{3+}) present in the blood. It was found that bilirubin resulted in an obvious change in the fluorescence, while the fluorescence quenching response of AuAgQC with other biomolecules were negligible (Figure 4.9). These results demonstrate that this approach exhibits an excellent selectivity for bilirubin detection over other competing molecules.

4.3.3. Possible quenching mechanism

A detailed investigation has been carried out to explore the mechanism of fluorescence quenching. Generally, the fluorescence quenching can take place due to three different phenomenon, (a) IFE or FRET between quencher and fluorophore, (b) ground state complex formation leading to static quenching, and (3) PET from the fluorophore to the quencher (Zhang., *et al.*, 2013).

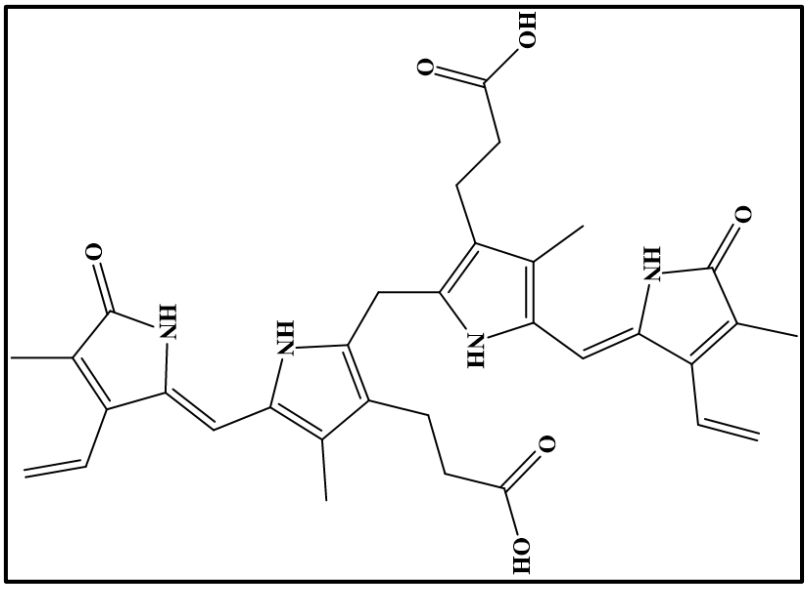

Figure 4.10. Structure of bilirubin

It is well known that the IFE can happen only when a significant spectral overlap between the absorption spectrum of quencher and emission or excitation spectrum of fluorophore takes place (Chang & Ho, 2015). Here the absorption spectrum of bilirubin has a wide range of absorption from 350 nm to 550 nm and showed a significant overlap with the excitation spectrum of AgAuQC@gluten (Figure. 4.11A). Hence the possibility of inner filter effect assisted fluorescence quenching cannot be ruled out, since we have excited the QC at 400 nm. To understand the effect of IFE for fluorescence quenching, we have changed the excitation wavelength to 365 nm, 400 nm, 430 nm, and 530 nm. It is noticed that the quenching is more prominent at 430 nm excitation where the bilirubin has maximum absorption (Figure 4.11B).

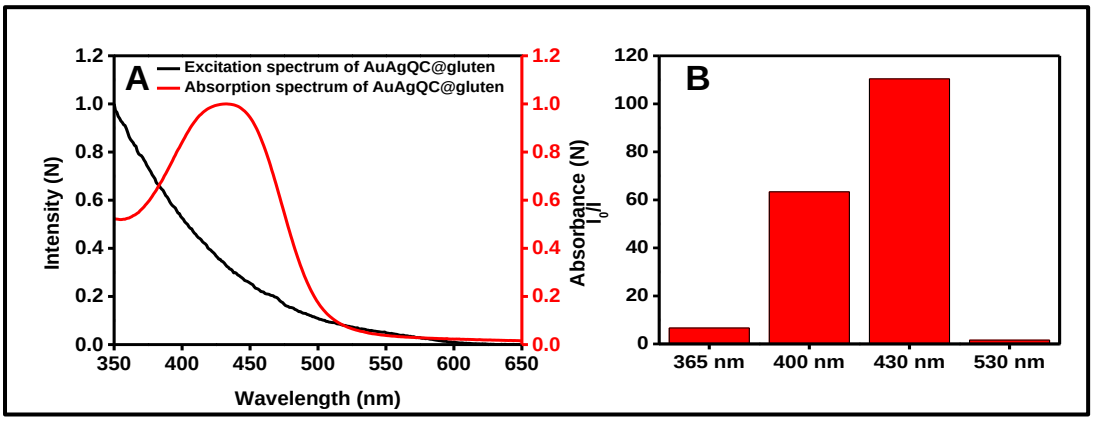

Figure 4.11. (A) Excitation spectrum of AgAuQC@gluten (black trace) and the absorption spectrum of bilirubin (red trace) (B) Fluorescence quenching of AgAuQC@gluten with bilirubin at different excitation wavelength (Concentration of bilirubin maintained as constant-50 mM).

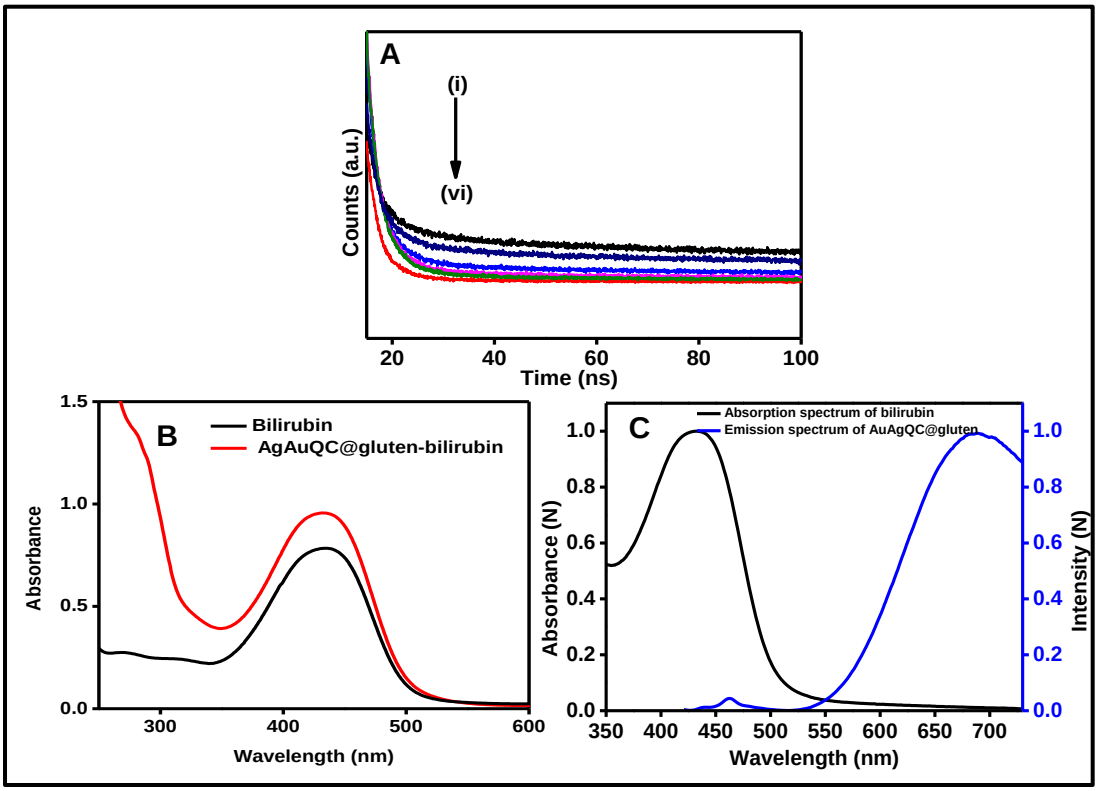

Figure 4.12. Fluorescence decay of AgAuQC@gluten with different concentration of bilirubin. (0, 5, 15, 25, 35, 70 µM from (i) to (vi)). (D) Absorption spectrum of bilirubin and AgAuQC@gluten-bilirubin. (E) Absorption spectra of bilirubin (black trace) and Emission spectra of AgAuQC@gluten (Blue trace).

At 365 nm and 550 nm excitation, the quenching response is comparatively very less. Thus it is confirmed that the inner filter effect is possibly the mechanism behind the fluorescence quenching. To further ascertain whether inner filter effect is the main reason for fluorescence quenching, we have carried out lifetime analysis, since inner filter effect based fluorescence quenching cannot change the lifetime of material after the addition of quencher. Figure 4.12A shows the lifetime analysis of AgAuQC in the presence and absence of bilirubin. The lifetime of AgAuQC@gluten is decreasing with increasing concentration of bilirubin. It is observed that the average lifetime of AgAuQC decreased from 35 ns to 12 ns after the addition of bilirubin (70 µM) (Table. 4.2). Thus inner filter effect cannot be the only reason for fluorescence quenching. The possibility of FRET between QC and bilirubin is ruled out by analyzing the absorption spectrum of bilirubin and emission spectrum of AgAuQC. There is no spectral overlap observed between the fluorophore and the quencher (Figure 4.12C). Thus the decrease in the average lifetime value is due to the PET from AgAuQC to bilirubin. Furthermore, UV-Visible spectra of bilirubin and AgAuQC-bilirubin are given in Figure. 4.12B. A minor broadening of the peak at 430 nm is observed after the addition of bilirubin to the AgAuQC and also no other new peak emerged. This excludes the possibility of any ground state complex formation between bilirubin and AgAuQC.

Table 4.2. Lifetime data of AgAuQC@gluten with different concentration of bilirubin

Sample Name	**τ_1(ns)**	**A_1**	**τ_2(ns)**	**A_2**	**τ_{av}(ns)**	**χ^2**
AuQC@gluten	35.81	80.34	3.03	19.66	35.14	1.24
Bilirubin (5µM)	28.17	66.87	2.7	33.13	27.01	1.24
Bilirubin (15µM)	25.6	52.33	2.8	47.67	23.53	1.3
Bilirubin (25µM)	20.2	38.98	2.7	61.02	17.17	1.18
Bilirubin (35µM)	17.9	34.6	2.7	65.4	14.52	1.18
Bilirubin (70µM)	15.88	32.32	2.4	67.68	12.63	1.22

In addition, we have carried out FT-IR spectroscopy to understand the interaction between bilirubin and AgAuQC (Figure 4.13). The FTIR spectrum of the bilirubin shows a sharp peak at 3404 cm^{-1} band, which is due to the N–H stretching vibration of the pyrrole group present in bilirubin. The spectrum of AgAuQC-bilirubin shows that the peak at 3283 cm^{-1} is broadened with decreased signal intensity with respect to that of the AgAuQCs alone. Bilirubin has two carboxyl side chains (The structure of bilirubin is given Figure 4.10) and produced an intense carboxyl C-O stretching vibration at 1687 cm^{-1}, which is absent in AgAuQC-bilirubin.

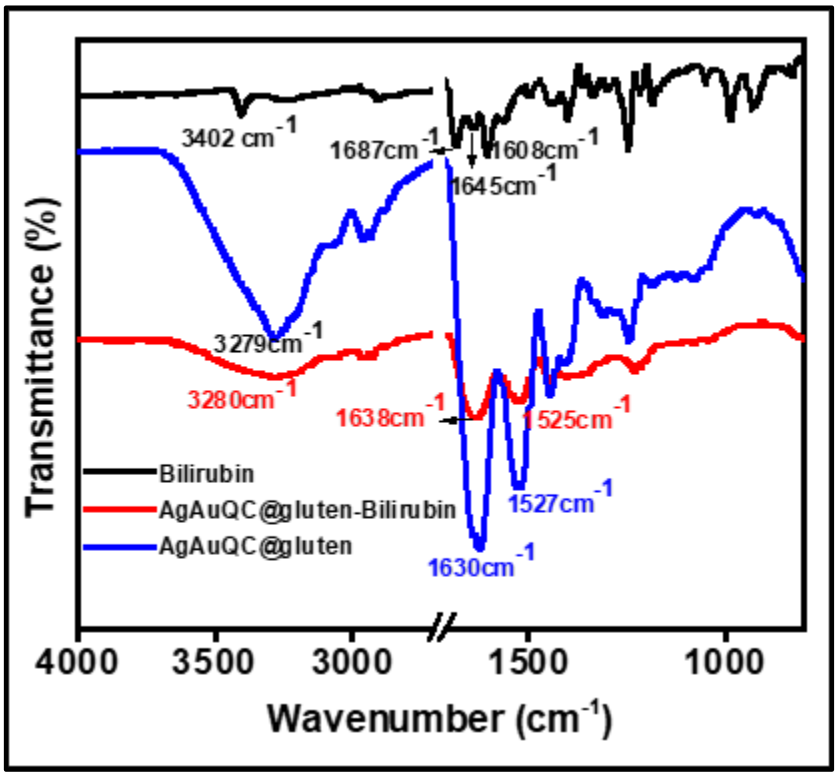

Figure 4.13. FT-IR spectra of bilirubin (black trace), AgAuQC@gluten (blue trace) and AgAuQC@gluten with bilirubin (red trace).

The peaks corresponding to amide I (1630 cm^{-1}) and Amide II (1527 cm^{-1}) in AgAuQC is shifted to 1638 cm^{-1} and 1525 cm^{-1} after the addition of bilirubin. These results indicate that bilirubin can interact with the protein protected AgAuQC either through H-bonding between the carboxyl group of bilirubin and

hydroxyl, nitrogenous and other functional groups on the protein or through hydrophobic interaction. This brings the fluorophore in close proximity to the quencher which further leads to the PET process between AgAuQC and bilirubin.

4.3.4. Sensing of bilirubin in the blood

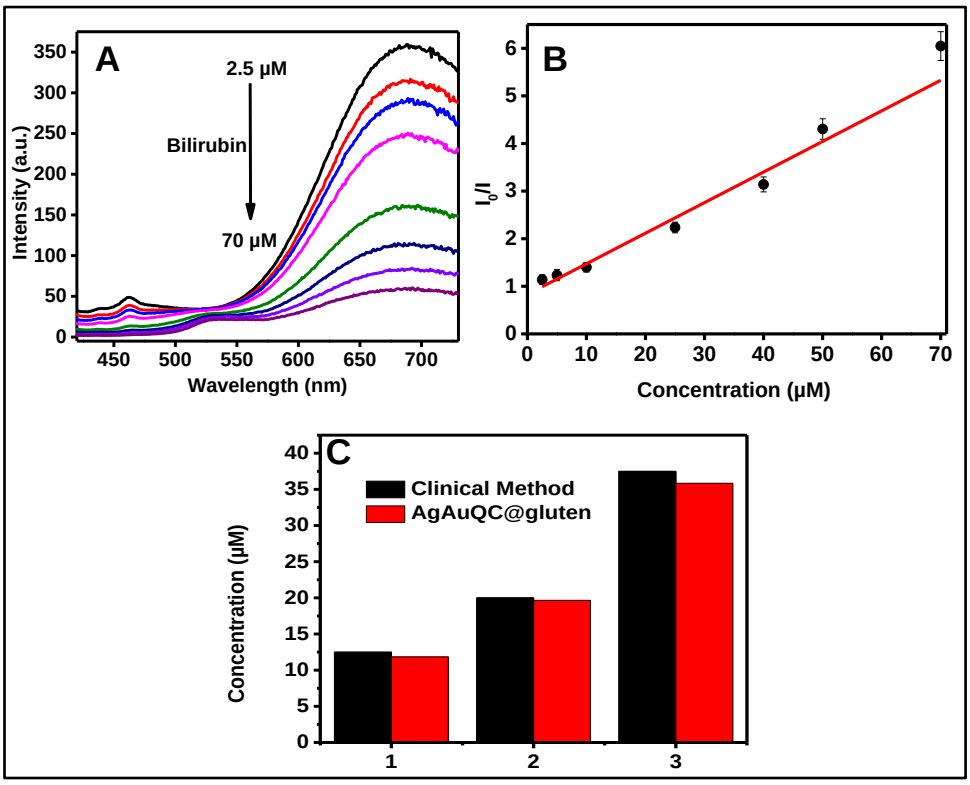

Figure 4.14. (A) Fluorescence response of AgAuQC@gluten with blood spiked with different concentrations of bilirubin (2.5-70 µM). (B) Linear plot of the values of (I_o/I) at 690 nm versus concentration. (C) Comparison of bilirubin levels detected by our method with clinical detection method. 1, 2& 3 are different blood samples containing varying amounts of bilirubin.

To check the feasibility of the developed sensor for the detection of bilirubin in real systems, pre-treated blood samples were spiked with known amounts of bilirubin and fluorescence recovery analysis was performed. Details of the sample preparation is given under the experimental section (Section 4.2.5). An apparent decrease in fluorescent intensity at 690 nm was observed after the introduction of blood spiked with various concentrations of bilirubin (2.5 -70 µM) (Figure 4.14A). A linear graph is obtained by plotting I_0/I Vs the spiked concentration of bilirubin. The recovery of bilirubin in three spiked samples were

analyzed and given in Table 4.3. It exhibits good recovery and acceptable RSD values. From the calibration curve, the concentration of bilirubin in whole blood was estimated to be 11.84± 0.5 µM, 19.65 ± 0.3 µM and 35.84 ± 0.4 µM using our method and the result was compared with conventional clinical method (Figure 4.14C). These results confirm that the proposed method has a great potential for application of creatinine detection in real blood samples.

Table 4.3. Analytical result of bilirubin in the spiked blood sample

Test NO.	**Added(µM)**	**Found (µM)**	**Expected (µM)**	**Recovery (%)**	**RSD**
1	0	11.84	12.50	94.72	2.5
2	6	18.25	18.50	98.64	2.1
3	12	23.80	24.50	97.14	2.8

4.3.5. Sensor development

We have developed a simple and cost effective cotton based sensor for the visual detection of bilirubin by coating AuAgQC@gluten on cotton buds. The cotton buds were soaked in AuAgQC@gluten overnight and then dried. We have noticed that AuAgQC@gluten on cotton buds was stable and maintained its emission intensity for three months. Using the prepared probe, we were able to detect different concentrations of bilirubin. As the concentration of bilirubin increases from 0.5 mM to 70 µM, the red luminescence decreases under UV the light (λ_{Ex} 365 nm) (Figure. 4.15). This observation indicates that the developed probe can be used as an effective platform for the selective and sensitive detection of bilirubin for practical applications.

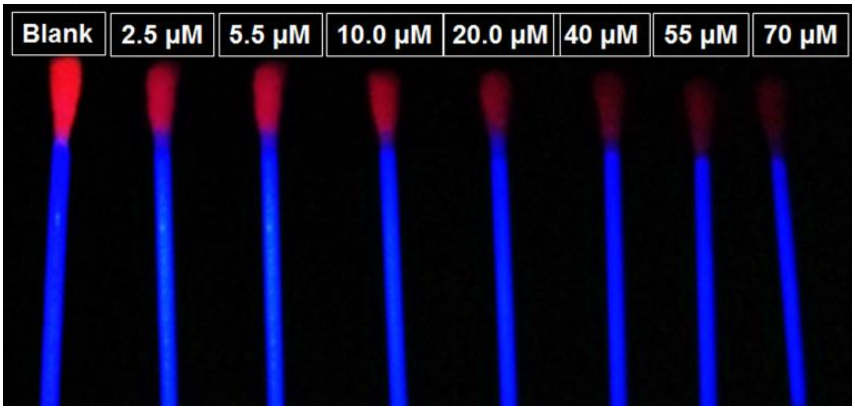

Figure 4.15. Photograph of AgAuQC probe with different concentration of bilirubin taken under UV light.

4.4 Conclusions

In summary, we reported a facile method to synthesis a water-soluble, stable, fluorescent AgAuQC by galvanic exchange reaction in which a naturally abundant, sustainable and cost-effective protein, gluten is used as the protecting and stabilizing agent. The AgAuQC@gluten exhibit 9.5 % QY and is found to be stable in an array of pH (1-12). These red luminescent alloy QCs have been successfully utilized towards the development of a fluorescent sensor for the selective detection of bilirubin. A detailed investigation was carried out to understand the possible quenching mechanism for bilirubin sensing. The IFE and PET are the two major mechanisms behind the fluorescent quenching. A detection limit of 50 nM was achieved for bilirubin by this method. AgAuQC@gluten is stable and they exhibit similar fluorescence on a solid substrate like cotton, which led to the design of a simple and cost-effective fluorescence-based optical sensor for bilirubin. The validity of the proposed method has been tested by detecting the concentration of bilirubin in blood samples, which substantiated its great potential practicality in real samples.

CHAPTER 5

GRAPHENE CARBON DOT ASSISTED SUSTAINABLE SYNTHESIS OF GOLD QUANTUM CLUSTER FOR RATIOMETRIC SENSING OF MERCURY (Hg^{2+})

This chapter deals the synthesis of stable dual light emitting gold quantum cluster-graphene quantum dot (AuQC@GQD) nanocomposite using a single protein, gluten as the raw material. Hydrothermal treatment of wheat gluten protein resulted in the development of a stable blue-green emitting graphene quantum dot (GQD), which was further conjugated with gluten and used for the synthesis of gold quantum clusters (AuQC). Moreover, the gluten conjugated GQD acted as a reducing agent for the fast formation of red emitting AuQC. The resulted AuQC@GQD were characterized by various spectroscopic and microscopic techniques. We further explore the use of AuQC@GQD as a probe for ratiometric detection of mercury (Hg^{2+}). The sensor exhibited a good linear relationship in the Hg^{2+} concentration range from 0.1 to 35.8 ppm with a detection limit of about 0.1 ppm. Moreover, AuQC@GQD were effectively incorporated into electrospun polyvinyl alcohol (PVA) nanofibers for visual colorimetric sensing. We have monitored the visual fluorescent response of AuQC@GQD-PVA mat to Hg^{2+}, and the observed change of color under UV irradiation indicates the utility of the AuQC@GQD-PVA nanofibers for on-site detection of Hg^{2+}. In addition, the formed AuQC@GQD can able to produces white light emission at a particular composition of $HAuCl_4$ and GQD under UV irradiation, which can further extend its applicability in the field of optoelectronics.

Part of this chapter has been published in ChemistrySelect (2018), Vol: 3, 9545-9554

5.1. Introduction

Development of sustainable dual light emitting nanomaterials by an environmentally friendly method is an extremely demanding area of research in biomedical field like biosensing, bio-imaging, due to its enhanced detection specificity, and more quantitative measurements (Chen., *et al.*, 2013; Cui., *et al.*, 2017; Wang *et al.*, 2016). Generally, the dual emitting materials are constructed by embedding fluorophore with fluorescent nanomaterials via covalently or non-covalently (Chen., *et al.*, 2013; Cui., *et al.*, 2017). Moreover, the construction of dual emitting fluorescent nanomaterial involved numerous tedious multistep synthesis, complicated coupling or chemical modification process. Thus, the development of new in-situ methods is essential in order to simplify the construction process by avoiding the tedious chemical methods. In this study, we have given emphasis to the design of a novel dual emitting composite of graphene quantum dot (GQD) and gold quantum clusters (AuQC) for ratiometric sensing of mercury (Hg^{2+}) and production of white light by a simple in-situ method.

AuQC and GQD are two emerging classes of fluorescent nanoprobe, exhibit molecule like optical properties, discrete electronic states, size-tunable emission and excellent biocompatibility (Bacon *et al.*, 2014; Dong *et al.*, 2017; Fang *et al.*, 2017) (Chakraborty & Pradeep, 2017; Zheng *et al.*, 2017). The presence of both AuQCs and GQD in a single system is not only combining the unique properties of the AuQCs and GQDs but they also exhibit new properties arising from interactions between the two entities. Recently Zhang and co-workers developed a gold quantum cluster-carbon dot composite material for ratiometric sensing of ascorbic acid (Zhang., *et al.*, 2016). The report shows that the gold-carbon dot material exhibits unique properties of both gold cluster and carbon dot with dual emission. Barman and co-workers developed a white light emitting composite of carbon dot and dye encapsulated bovine serum albumin (BSA) protected gold quantum clusters (Barman., *et al.*, 2016). They have individually synthesized both carbon dot and coumarin dye encapsulated BSA protected gold quantum cluster and mixing of these systems provided white light generation. In such strategy, the fluorophores are present in solution

independently. However, a better strategy to synthesize color tunable, as well as dual emitting AuQC-GQD composite material from an environmentally friendly method, is still needed. It will be advantageous if plant-derived proteins can be utilized for the preparation of nanoparticles as they are not only abundant, sustainable and renewable but also the least expensive (Li., *et al.*, 2017; Mathew & Joseph, 2017). In chapter 3, we have elaborated the synthesis of wheat gluten protein stabilized AuQC (Mathew & Joseph, 2017).

In the present study, we have demonstrated for the first time a facile, sustainable green synthetic route to prepare dual emitting AuQC@GQD nanocomposite. The GQD were synthesized by hydrothermal method, a facile and green strategy in which, wheat gluten protein as the source. Further, the obtained stable intense blue-green emitting GQD were then functionalized with gluten, which is utilized as a reducing agent for the fast formation of AuQC. In addition, the AuQC@GQD was effectively incorporated into electrospun polyvinyl alcohol nanofibers for ratiometric detection of mercury ion. Ratiometric sensing is a more sensitive and accurate method since the ratio of the fluorescent intensities at two wavelengths is capable of built-in correction to eliminate the environmental interference. Hg (II) is considered the most dangerous and universal pollutants, elevate serious environmental and health concerns, and disrupt many organs like kidney, brain, permanent damage to the central nervous system, DNA damage and so on (Du *et al.*, 2013) Considering the adverse effect of Hg (II) and the fact that Hg (II) can quench AuQC, (Ghosh *et al.*, 2014; Senthamizhan *et al.*, 2014) Hg(II) was used as the target analyte to confirm the proof-of-concept. Herein the red emission from AuQC was completely quenched by Hg (II), while the blue emission from GQD was slightly altered. In the meanwhile, we have observed that AuQC@GQD produces a near white light emission under UV irradiation at a particular composition of GQD and in-situ formed AuQC, revealing its promising applications in optoelectronic devices.

Experimental Section

5.1.1. Materials

All the reagents were used as obtained without further purification. Gluten and $HAuCl_4$ were purchased from Sigma Aldrich. The membrane dialysis tubes (molecular weight cut off 1kDa) were purchased from Spectra/Por®. Sodium dihydrogen phosphate, Disodium hydrogen phosphate, NaOH and all metal ions salts were purchased from Merck, India. Polyvinyl alcohol (PVA) is purchased from Alfa Aesar, India. All solutions were prepared by using Millipore water.

5.1.2. Instrumentation

UV–Visible absorption spectra were recorded in the range of 200–800 nm using the Varian model, Carywin Bio100 spectrometer. All fluorescence measurements were made using the Fluoro Max-4C spectrofluorometer (HoribaInstruments, USA. The slit width for excitation and emission were set at 5nm. TCSPC accessory is used for lifetime analysis with a pulse width of 1.3 ns. HRTEM images were recorded on a JEOL JEM 2100 instrument with an acceleration voltage of 200 kV. The TEM-EDX elemental mapping analysis was carried out using energy dispersive X-ray. FT-IR spectra were recorded using Perkin Elmer FTIR spectrometer. Zeta potential measurements were performed on a particle size analyzer (Zetasizer Nano ZS series, Malvern Instruments). XPS analysis was measured on multilab 2000, Thermo Fisher Scientific using Mg K-α radiation. SEM and EDS analysis were studied using (HR-SEM, Quanta FEG200, FEI, USA) equipped with Energy dispersive spectroscopy. Confocal laser scanning microscope (CLSM) images were recorded using A1R si, NIKON instrument, wherein excitation sources for all experiment were fixed at 405 nm.

5.1.3. Preparation of graphene quantum dot

The GQD were prepared by hydrothermal method. Briefly, 250 mg of gluten protein powder was dissolved in 10 mL, 0.25 M NaOH solution and stirred

for 10 minutes to get complete disperse solution. The gluten solution was transferred to 25 mL Teflon- lined autoclave and heated at 220 ˚C for 3 hours and gradually cooled down to room temperature. A brown colored GQD solution was formed. The purification of GQD was carried out by three steps such as filtration, centrifugation, and dialysis. In the first step, the brown colored solution obtained was filtered to remove unreacted organic moieties. The filtrate collected were centrifuged at 10000 rpm for 20 minutes to separate the less-fluorescent deposit. Further, the supernatant collected were dialyzed for two days to get pure GQD. The resultant solution was further lyophilized to obtain GQD powder which was stored in a desiccator at room temperature until use.

5.1.4. Preparation of AuQC@GQD

The AuQC@GQD was synthesized by using gluten modified GQD. Briefly, about 5mL (5 mg/mL) of the prepared GQD is treated with 5 mL of gluten (5 mg/mL) and stirred at room temperature for 30 minutes. The gluten treated GQD were further reacted with $HAuCl_4$ (5mM, 5 mL) at 55 ºC for 80 minutes. Thus, obtained AuQC@GQD showed a reddish violet emission under UV light. Further purification of AuQC@GQD was carried out by dialyzing against deionized water through a dialysis membrane (MWCO 14 kDa) for 48 hours to remove large particles and unbound GQD. The resultant solution was further lyophilized to obtain the AuQC@GQD powder which was stored in a desiccator at room temperature until use.

5.1.5. Development of AuQC@GQD-PVA nanofibers

The AuQC@GQD-PVA nanofibers were prepared by electrospinning method. The PVA (16 wt %) solution was prepared in 20 mL hot water (80 ºC) by stirring for 5 hours to obtain a transparent homogeneous solution. To the above prepared PVA solution, AuQC@GQD (200 mg) powder was added and a uniform solution was prepared by stirring at room temperature for 2 hours. The prepared AuQC@GQD-PVA mixtures were loaded into a 10 mL plastic syringe fitted with a needle. The electrospinning was performed using a horizontal set up containing

a variable high DC voltage power supply and a programmable syringe pump (ESPIN NANO, Physics Instrument Company, Chennai). A high voltage (12 kV) was applied between the needle and the collector with a flow rate of 0.3 mL/h. The distance between the needle tip and collector are maintained as 15 cm. Nanofibers were collected on an aluminium sheet mounted on a cylindrical drum collector, which rotated at a speed of 2500 rpm.

5.1.6. Cross-linking of AuQC@GQD-PVA

The cross-linking of AuQC@GQD-PVA was carried out based on a reported method (Senthamizhan *et al.*, 2014). Glutaraldehyde (GA) vapor was used as the crosslinking agent. The GA/HCl solution was prepared in the volume ratio of 3:1 (GA–HCl) and was spread out into a petri dish and placed at the bottom of a desiccator. Further, AuQC@GQD-PVA mat was mounted to the desiccator and exposed to GA vapor without physical contact for 24 hours.

5.1.7. Development of sensor

For sensing experiment, the nanofibrous mat was cut uniformly into small pieces of size 2 cm x 2 cm. The mats were treated with different concentration of aqueous solution of Hg^{2+} separately. Thereafter, the change in color was noted under UV lamp. Furthermore, confocal laser scanning microscopy (CLSM) was employed to analyze the change in fluorescence of nanofibers. For that, the nanofibrous coated on a glass slide was used for imaging. The fibers on glass slide are treated with different concentration of Hg^{2+} and fluorescence image of the fibers were taken before and after the addition of Hg^{2+}.

5.2. Results and Discussion

5.2.1. Synthesis and characterizations of AuQC@GQD

According to the previous reports, proteins and biopolymers can serve as precursors to prepare GQDs or carbon nanoparticles through a hydrothermal route (Liu, Xue *et al.*, 2016; Liu, Xin *et al.*, 2016; Roy *et al.*, 2014). Herein the blue-

green emitting GQD was synthesized by a one-step hydrothermal method in which gluten protein is used as the carbon source. Detailed synthesis procedure is given under the experimental section (Section 5.2.3). It is a facile, economic, bottom-up method to synthesize GQDs in mild conditions (220 °C for 3 hours). The blue-green emitting GQD were formed by degradation of large organic molecules to small molecules through hydrothermal hydrolysis followed by hydrothermal carbonization (Wu *et al.*, 2013).

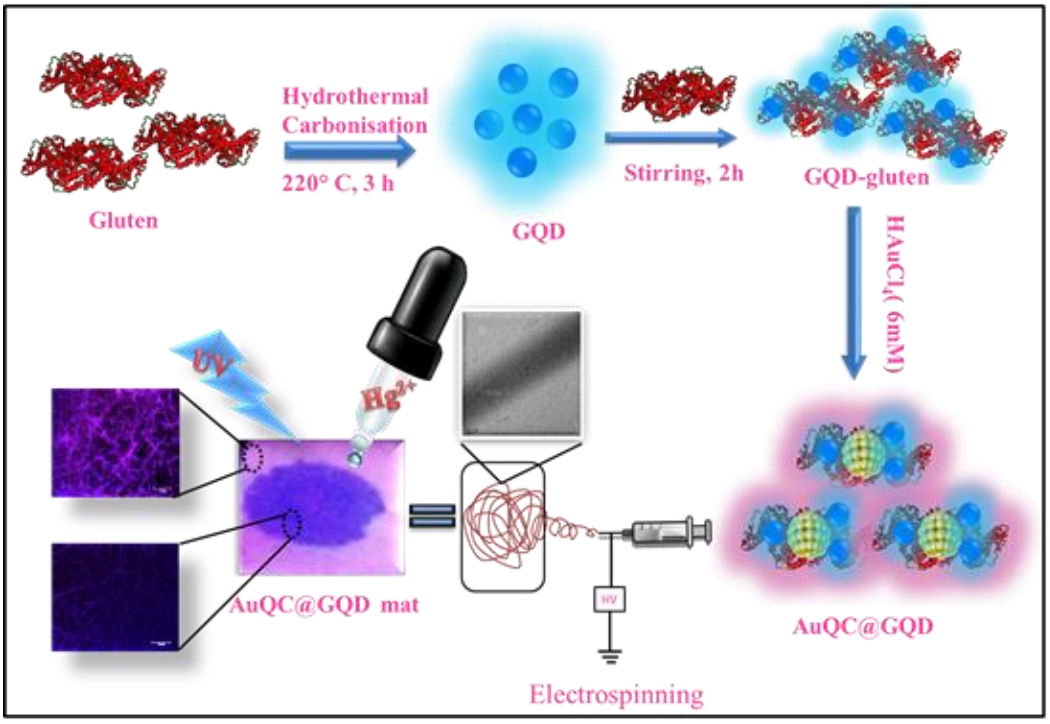

Figure 5.1. Schematic representation for the synthesis of GQD, AuQC@GQD and AuQC@GQD-PVA nano mat for Hg^{2+} detection.

The as-prepared GQD was further used as the reducing agent for the formation of AuNP and AuQC.

Here we serendipitously observed that GQD alone can easily reduce Au (III) to Au (0) state and at the same time generate larger sized gold nanoparticle other than smaller gold quantum clusters, without the addition of reducing agent and stabilizers. The reducing ability of GQD were earlier reported by Wang and his co-workers, which is due to the presence of -OH functional group present on the GQD surface (Wang., *et al.*, 2013). In order to confirm, GQD acts as the

reducing agent and aid in the formation of nanoparticles (AuNP), GQD were treated with $HAuCl_4$. The GQD (2 mL) mixed with $HAuCl_4$ (10 mM, 100 µL) and incubated at 50 °C for 1 h. It is observed that the color of the solution changes from brown to light pink, which is the characteristic color of gold nanoparticle.

The TEM image of obtained AuNP exhibited nearly spherical morphology with size around 60±0.5 nm (Figure 5.2A and 5.2B). The presence of SPR peak at 520 nm further proves the formation of AuNP in the medium (Figure 5.2C). Furthermore, the lack of formation of the gold quantum cluster can be assigned to the absence of bulky protecting/ capping agent in the medium. Since we have reported the protecting and reducing ability of gluten for the synthesis of AuQC (Mathew & Joseph 2017), functionalized the GQD with gluten and monitored the formation of AuQC. According to previous reports, it is well known that the carbon nanomaterials (CNTs, graphene, CD) can be functionalized by protein via non -covalent interaction such as hydrophobic, Vander Waals, and electrostatic interactions (Oliveira *et al.*, 2015). Thus, here also we proposed that the GQD were surface functionalized with gluten via non-covalent interaction. The conjugation of protein towards the GQD was confirmed by zeta potential analysis, UV-Vis absorption spectroscopy and fluorescence study.

The UV-Vis absorption spectra of gluten, GQD and GQD-gluten were compared, as shown in Figure 5.3A. The gluten exhibits absorption around 285 nm, which is due to the aromatic amino acid present in the gluten. Conjugation of gluten towards GQD shows a gradual rise in absorption around 400 nm and peaks from gluten (285 nm) and GQD (270 nm) were merged and exhibited as a single broad peak around 276 nm. From the fluorescence analysis, the conjugation of gluten causes a slight decrease in fluorescent intensity of GQD, which could be due to the interaction of GQD with gluten. To analyze the binding of gluten with GQD, GQDs were treated with different concentration of gluten (25 mg/mL, 0.1 ml to 1 mL) (Figure 5.3B). With increasing concentration of gluten, the fluorescent intensity of GQD at 450 nm is decreased and reached a level of saturation where no further decrease in fluorescence intensity was observed on increasing the gluten concentration.

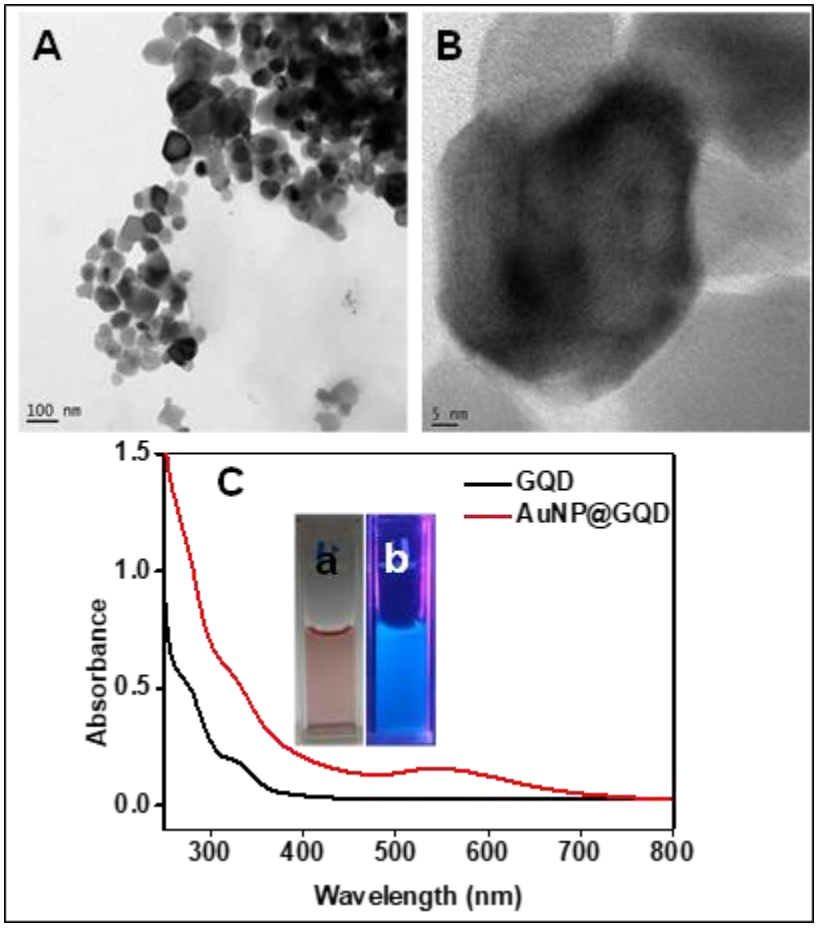

Figure 5.2. (A) and (B) TEM and HR TEM images of AuNP@GQD respectively. (C) UV-Vis absorption spectra of GQD (black trace), AuNP@GQD (red trace). Inset shows the photograph of AuNP@GQD under visible light (a) and UV irradiation (b).

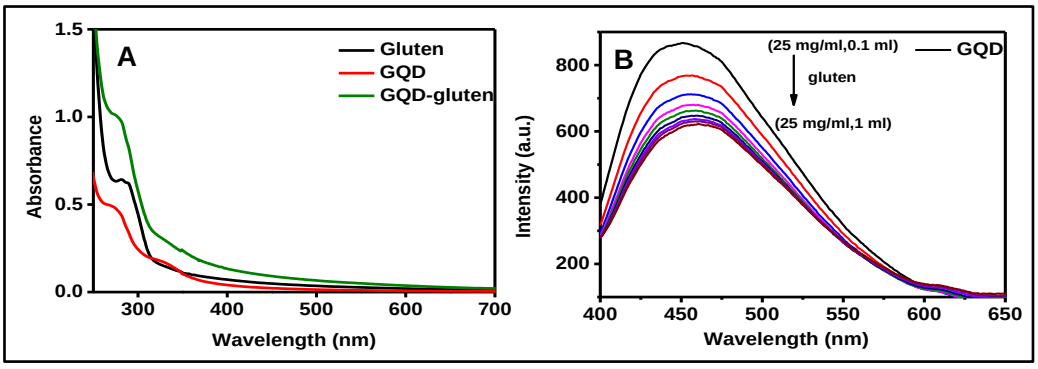

Figure 5.3. (A) UV-Vis absorption spectra of gluten (black trace), GQD (red trace)& GQD-gluten (green trace). (B) Fluorescent emission spectra of GQD with different concentration of gluten.

Zeta potential measurements further confirm the hybrid formation of gluten and GQD. GQD is having average zeta potential around -14.8 mV, upon the addition of gluten the zeta potential changes to -20.45 mV, confirming the conjugation of GQD over gluten. Thus, herein we have proposed that GQD is functionalized with protein via non-covalent interaction, either through electrostatic interaction or by H-bonding interactions between the surface functional group of GQD and the protein.

Then the gluten conjugated GQD were further used for the synthesis of AuQC@GQD. The GQD-gluten conjugate was treated with $HAuCl_4$ to form AuQC@GQD. Figure 5.1. represents the various steps involved in the synthesis of AuQC@GQD.Figure 5.4 shows the HRTEM images of GQD and AuQC@GQD. The TEM images of GQD imply the nearly monodisperse distribution of GQD with an average size around 3±0.5 nm.

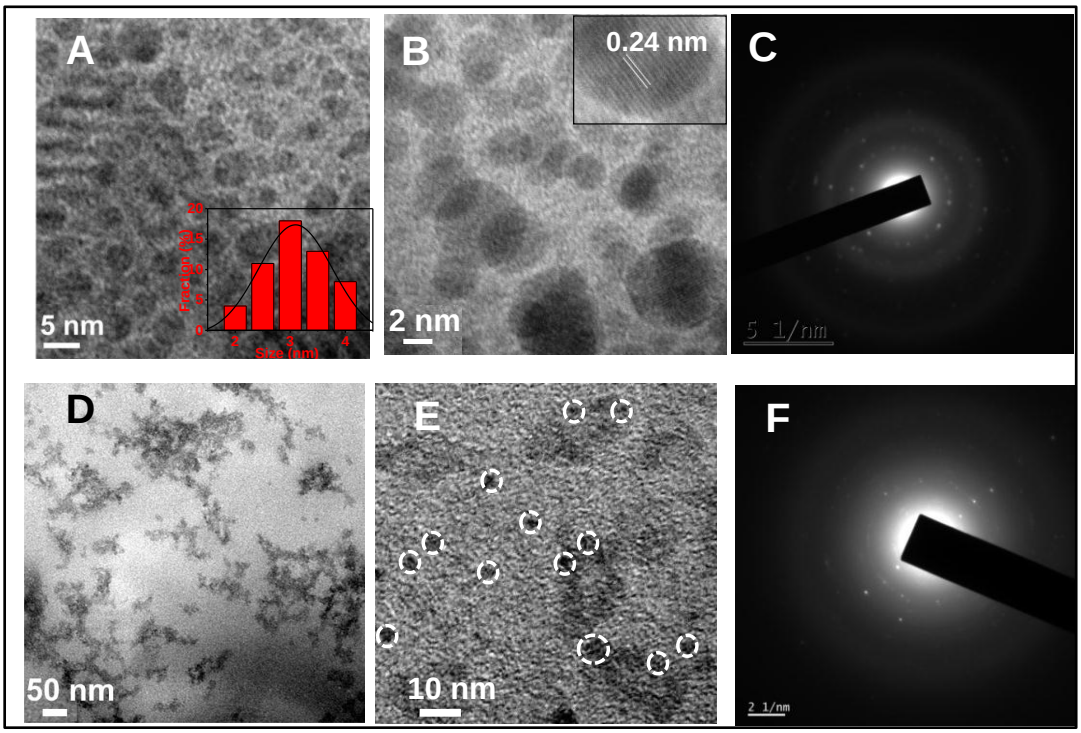

Figure 5.4**.** (A) and (B) shows HRTEM images of GQD. (C) SAED pattern of GQD. (D), E & (F) shows the TEM image and SAED pattern of AuQC@GQD respectively.

HRTEM images and selected area electron diffraction (SAED) pattern implies the crystalline nature of GQD (Figure 5.4C). The measured lattice fringe distance is found to be 0.24 nm, (Figure 5.4B) which corresponds to the (1120) crystal phase of graphite (Roy *et al.*, 2014). When gold quantum clusters grew in GQD-gluten medium, it is found that the AuQC decorated on the surface functionalized GQD. TEM image of AuQC@GQD reveals the distribution of AuQCs above the carbon dot surface (Figure 5.4D&5.4E). The gold quantum clusters most likely bound to the surface of the gluten modified GQD and at the same time, the AuQC@GQD appears to form a chain-like structure. It can be observed that the size of the AuQC (>1.5 nm) much smaller than GQD (3±0.5 nm). The SAED pattern of AuQC@GQD showed a similar pattern as GQD (Figure 5.4F).

Figure 5.5 shows the UV-Vis absorption and emission spectra of GQD and AuQC@GQD. The absorption spectrum of GQD shows two peaks at 270 nm and 325 nm corresponds to π-π* transition of C=C and n- π* transition of C=O bond respectively.

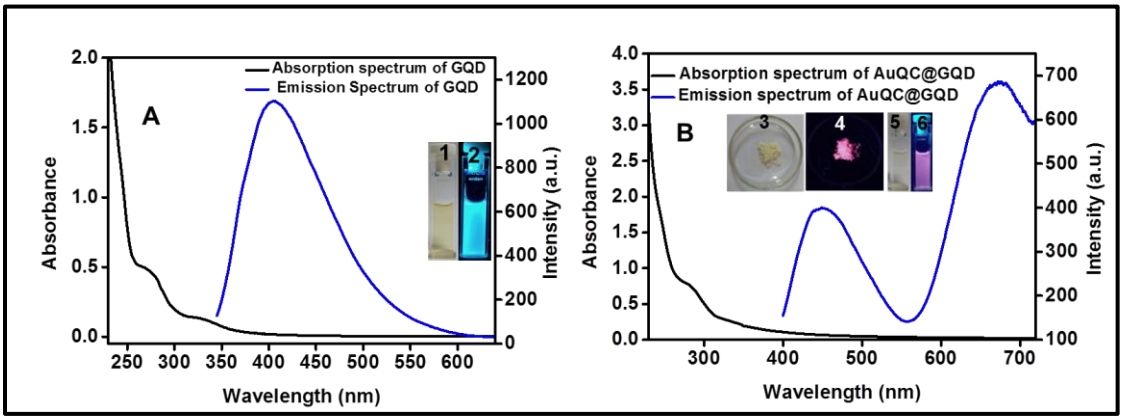

Figure 5.5. (A) Absorption (Black trace) and emission spectrum (Blue trace) of GQD. Inset of 1A shows the photograph of GQD under visible light (1) and UV light (2). (B) Absorption (Black trace) and emission spectrum (Blue trace) of AuQC@GQD. The inset shows the photographs of AuQC@GQD powder and liquid under visible light (3 & 5) and under UV irradiation (4 & 5) respectively.

It has been reported that the AuQC@gluten exhibit a featureless absorption peak and absence of surface plasmon resonance peak provides direct evidence for the formation of smaller quantum clusters (Mathew & Joseph, 2017).

The UV-Vis absorption spectrum of AuQC@GQD retains the characteristics peaks of GQD and its spectrum showed a gradual rise in absorbance from 550 nm which is similar to that of AuQCs, another less intense absorbance was observed around 450 nm which is attributed to be derived from the absorption characteristics of AuQCs. The emission spectrum of GQD shows its emission maximum at 405 nm by an excitation of 330 nm. As anticipated, AuQC@GQD exhibited a dual-emission spectrum with two well-resolved fluorescence peaks at 450 nm and 680 nm, as excited by the same wavelength of 380 nm, corresponds to GQD and AuQC respectively.

The emission spectrum of AuQC@GQD with different excitation wavelengths showed typical excitation-dependent emission property of GQD's and excitation- independent emission property of AuQC's (Mathew & Joseph, 2017; Zhang., *et al.*, 2015).

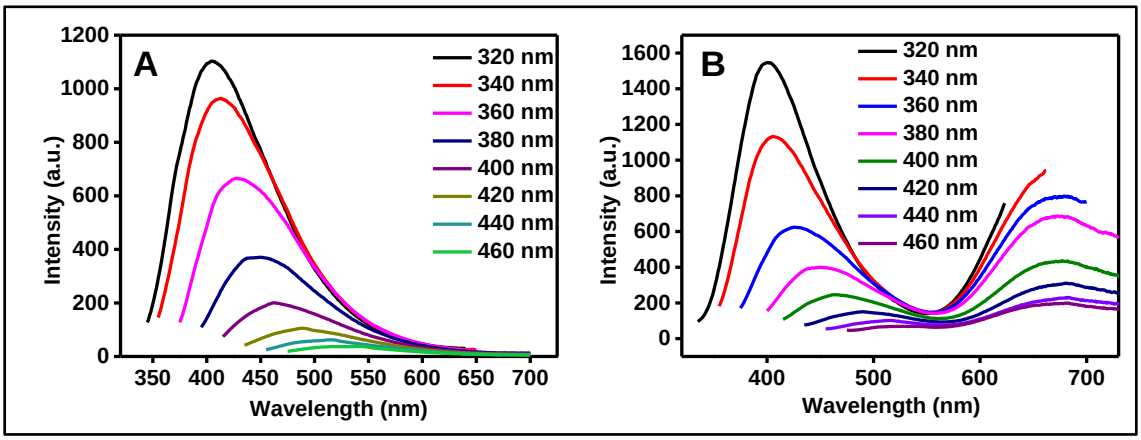

Figure 5.6. Emission spectrum of GQD (A) and AuQC@GQD (B) at the different excitation wavelength.

The emission peak corresponds to GQD was shifted to longer wavelengths (from 400 nm to 525 nm) with the excitation from 320 to 560 nm, whereas the peak corresponds to AuQC not varying with excitation wavelength (Figure 5.6). The diluted aqueous solution of GQD and AuQC@GQD are brownish yellow under daylight, upon irradiation at 365 nm light, the aqueous solution of GQD exhibits blue-green emission and the AuQC@GQD exhibits the reddish violet emission (inset of Figure 5.5B). The Quantum yield of AuQC@GQD and GQD were found

to be 5.53 % and 6%, which was calculated using quinine sulfate as standard (Mathew *et al.*, 2015). The quation for QY calculation is given in Section 3.2.5 (Equation 3.1) and Table 5.1 shows the calculated data.

Table 5.1. Quantum yield calculation

Sample	**λ_{Exc} (nm)**	**Φ_0**	**A_0**	**I_0**	**n_o**	**A_s**	**I_s**	**n_s**	**Φ_s (%)**
GQD	340	0.54	0.063	$2.3x10^8$	1.33	0.073	$2.9x10^7$	1.33	6.0
AuQC@GQD	340	0.54	0.063	$2.3x10^8$	1.33	0.089	$3.4 x10^7$	1.33	5.53

The time-resolved fluorescence study of GQD and AuQC@GQD are shown in Figure 5.7, and Table 5.2. The AuQC@GQD exhibited average lifetimes of 2.02 ns (λ_{ex} - 344 nm and λ_{max} - 450 nm) and 1.39 ns (with respect to λ_{max}- 680 nm).

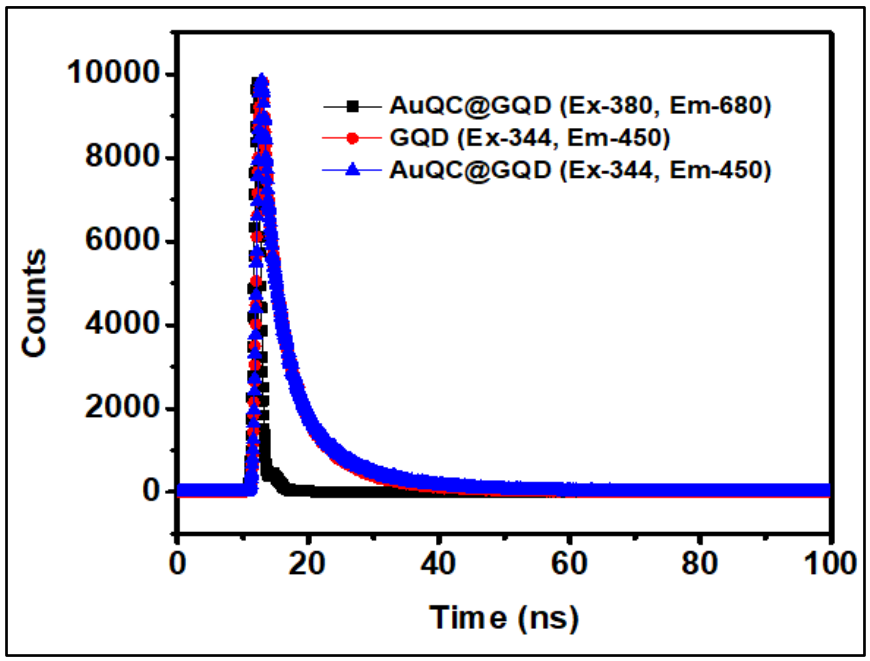

Figure 5.7. The lifetime analysis of GQD (Data collected at λem 450 nm, red trace) and AuQC@GQD (Data collected at λem 680 nm(black trace) and 450 nm (blue trace)).

Additionally, we have observed that the average lifetime of the GQD alone (λ_{ex} - 344 nm and λ_{max} - 450 nm) decreased from 4.33 ns to 2.02 ns after the formation of AuQC@GQD.

Table 5.2. Lifetime analysis of GQD and AuQC@GQD

Name of the sample	**A_1**	**τ_1 (ns)**	**A_2**	**τ_2(ns)**	**$<\tau>$(ns)**	**$\chi 2$**
GQD (λ_{Em} 450 nm)	81.90	0.37	18.10	5.37	4.33	1.34
AuQC@GQD (λ_{Em} 450 nm)	78.69	0.25	21.31	2.647	2.02	1.26
AuQC@GQD (λ_{Em} 680)	3.62	2.41	96.38	0.078	1.39	1.32

This decrease in lifetime can be attributed to the surface changes of GQD by conjugation of gluten and thereafter the formation of AuQC in the medium.

Here we noticed that, compared with the other conventional methods used for the development of dual emitting nanocomposite, the strategy employed here significantly simplified the preparation method and shortened the operation time. When GQD-gluten was treated with gold chloride at 55 °C, within 10 minutes AuQC started forming and formed completely within 100 minutes.

The surface functional groups of GQD and AuQC@GQD were confirmed by Fourier-transform infrared (FT-IR) and X-ray photoelectron spectroscopy (XPS). The FT-IR spectra of gluten, GQD and AuQC@GQD are given in Figure 5.8A. In the FT-IR spectra of gluten, a broad absorption band around 3400-2900 cm^{-1} corresponds to OH, CH and NH vibrations. The major characteristics peaks in the protein infrared spectrum are amide I and amide II bands. The peak at 1636 and 1520 cm^{-1} are assigned to the amide I and amide II stretching vibrations of gluten. A weak peak at 1440 cm^{-1} corresponds to the amide III of C-N stretching.

After the formation of GQD at high temperature and high pressure, the structure and confirmation of gluten protein were destroyed.

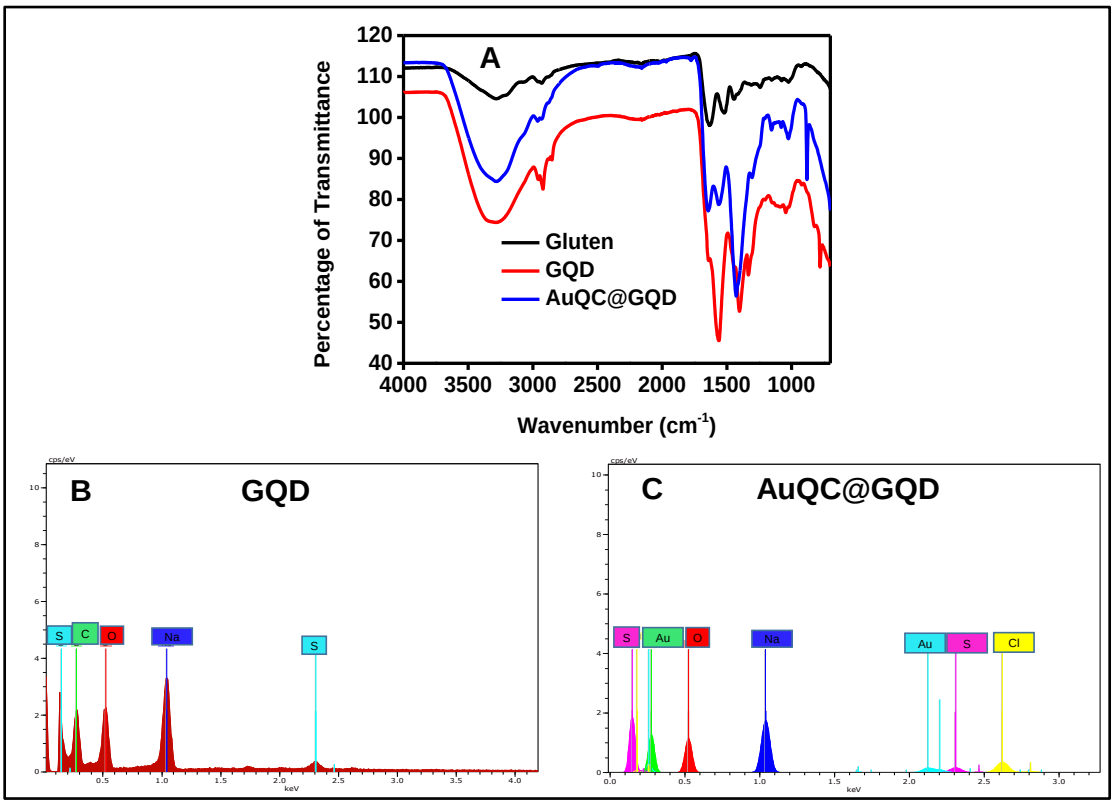

Figure 5.8. (A) FT-IR spectrum of gluten (black trace), GQD (red trace) and AuQC@GQD (blue trace). (C) and (D) shows the EDS data of GQD and AuQC@GQD.

The presence O-H group in GQD was confirmed by observing stretching vibration at 3285 cm $^{-1}$ and the peaks at 3352 and 1560 cm^{-1} are ascribed to the N–H stretching vibrations. Further, a peak was observed at 1333 cm $^{-1}$ which is corresponds to C–O stretching vibration. The peak observed at 1640 and 1402 cm $^{-1}$ corresponds to stretching vibration of C═O of the oxygenic group, and C═C of aromatic hydrocarbon confirmed the carbonization of protein under high pressure and temperature. The peak at 1402 cm^{-1} is attributing to the symmetric stretching vibration of COO^{-}. These results suggest that GQD is made-up of aromatic structure with a large number of amino and phenol hydroxyl groups on the surface, which can serve as an electron donor for the reduction of Au^{+} to Au (0). In the FT-IR spectrum of AuQC@GQD, the presence of characteristic peaks from

gluten (amide I and amide II) and GQD (COO^-, OH, NH_2) confirms that both GQD and AuQC cluster connected by the protein, gluten.

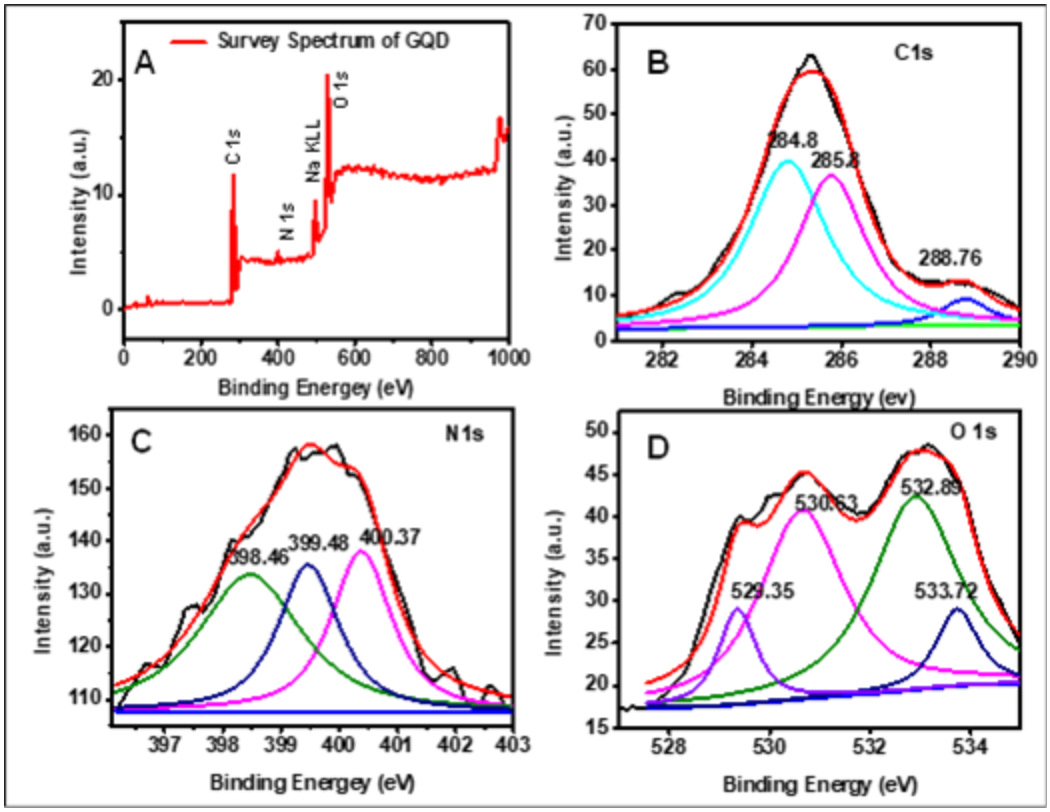

Figure 5.9. (A) XPS survey spectrum, (B) C1s XPS spectrum, (C) N1s XPS spectrum, and (D) O1s XPS spectrum of GQD.

The elemental composition of the GQD and AuQC@GQD were further investigated by EDS and XPS analysis. The presence of elemental gold in AuQC@GQD is shown in EDS data (Figure 5.8C). The XPS survey spectrum of GQD shows the characteristics peak of C1s, N1s, Na auger and O1s spectra at 284.5 eV, 400 eV, 495 eV and 532 eV respectively (Figure 5.9A). The high-resolution spectrum of C1s shows the presence of sp^2 C (C-C or C═C) in graphene at 284.8 eV, sp^3 C from C-O and C-N at 285.8 eV and C═O at 288.76 eV (Figure 5.9B). In the N1s spectrum, the peaks at 398.46 eV, 399.48 eV, and 400.37 eV correspond to pyridinic nitrogen, pyrrolic nitrogen, and graphite-like nitrogen respectively (Figure 5.9C). The high-resolution spectrum of O1s shows the presence of C═O (529.35 eV), -OH (530.63 eV) O═C-OH (532.69 eV), C-O-C (533.72 eV) (Figure 5.9D). The XPS survey spectrum of AuQC@GQD shows

the presence of Au 4f (84.29 eV), C1s (284.2 eV), N1s (398.9 eV) and O1s (529.1eV) (Figure 5.10A). The high-resolution spectra of AuQC@GQD show Au $4f_{7/2}$ and Au $4f_{5/2}$ components at 84.4eV and 88.1 eV, which implies the gold quantum cluster formation in the system (Figure 5.10B). The comparison of high-resolution spectra of C1s of AuQC@GQD with GQD shows a shift in binding energy after formation of AuQC. The binding energy corresponding to the C-C or C═C at 284.8 eV of GQD is shifted to 285.2 eV, and the binding energy corresponding to C-O and C-N at 285.8 eV is shifted to 286.6 eV in AuQC@GQD (Figure 5.10). This increase in binding energy could be attributed to the binding of GQD with gluten and thereafter the formation of AuQC.

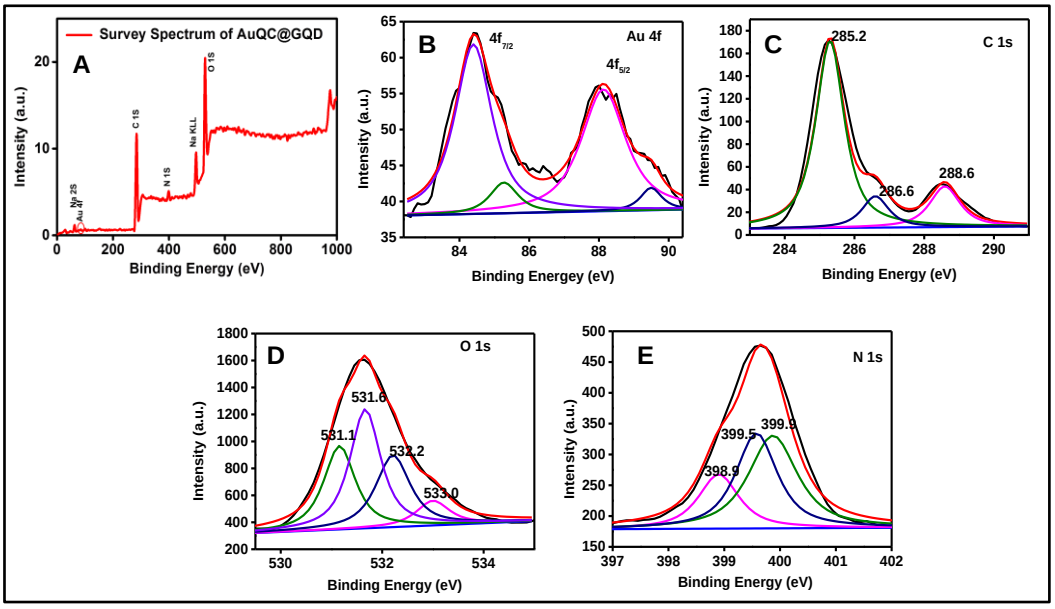

Figure 5.10. (A) XPS survey spectrum, (B) Au 4f XPS spectrum(C) C1s XPS spectrum, (D) O1s XPS spectrum, and (E) N1s XPS spectrum of AuQC@GQD.

Moreover, it is observed that the AuQC@GQD produces near white light emission at a particular composition of $HAuCl_4$. The white light emission generates at the addition of 4 mM $HAuCl_4$ to GQD-gluten medium. Figure 5.11B shows the chromaticity in CIE (Commission Internationale de l'´Eclairage 1931) coordinates of the as-synthesized AuQC@GQD (0.33, 0.25) calculated based on the emission spectra of AuQC@GQD, which is close to the pure white CIE coordinates (0.33, 0.33) and comparable to the many reported values (Singh & Mishra, 2015). Further, a composite film of AuQC@GQD was prepared using

polyvinyl alcohol (PVA) and under UV irradiation, the films produced near white light emission clearly demonstrating its potential application in the field of optoelectronics for the development of white light emitting diode (LED) (Figure 5.11).

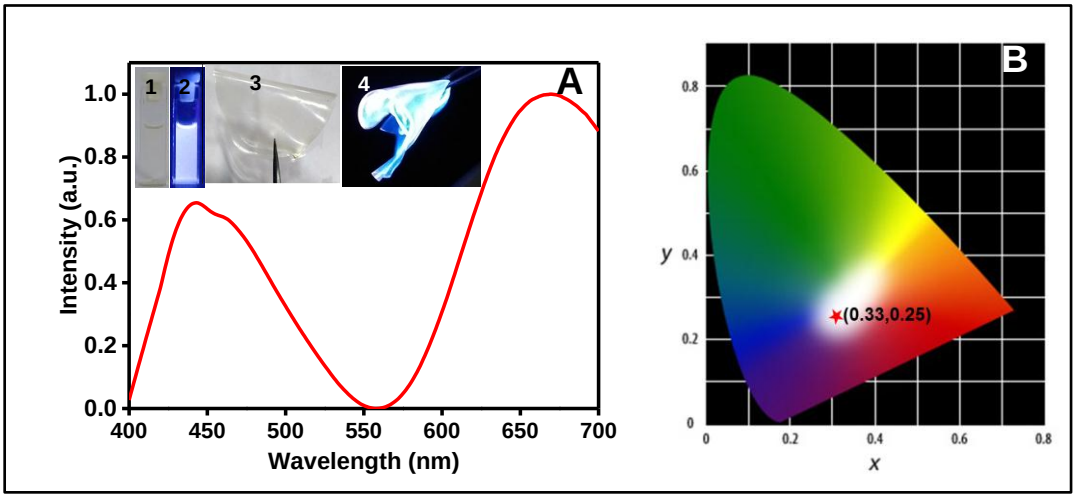

Figure 5.11. (A) & (B) shows the emission spectra of near white light emitting AuQC@GQD and corresponding chromaticity diagram of AuQC@GQD respectively. The inset shows the photograph of AuQC@GQD solution (1&2) and AuQC@GQD-PVA film (3&4) under visible light (1&3) and UV irradiation (2&4).

5.2.2. Controlled assembly of AuQC@GQD on the nanofibers surface for ratiometric sensing of mercury (II)

It is well known that the AuQC can be used for the selective sensing of Hg^{2+} through its ability of oxidation of Au or by metallophilic (Hg^{2+}–Au^{+}) interaction (Ghosh *et al.*, 2014; Xie *et al.*, 2010a). In this work, it was found that Hg^{2+}can selectively quench the red emission of AuQC (680 nm) component of AuQC@GQD and has a slight effect on blue emission of GQD component (460 nm). As shown in Figure 5.12A, upon the addition of Hg^{2+}, the fluorescence at 680 nm was remarkably quenched, while the fluorescence intensity at 460 nm was only slightly altered. Furthermore, when different concentrations of Hg^{2+} were treated with AuQC@GQD, the fluorescence intensity at 680 nm decreased with the increase of Hg^{2+} concentration. The fluorescence intensity ratio at 460 nm and

680 nm exhibited a good linear relationship in the Hg^{2+} concentration range from 0.1 to 1.3 ppm and 1.6-35.8 ppm with a detection limit of about 0.1 ppm (Figure 5.12B &5.12C). The quenching experiments and fluorescence response of AuQC@GQD were conducted with various metal ions. Ions such as Cu^{2+}, Co^{2+}, Mg^{2+}, Zn^{2+}, Ni^{2+}, Ag^{+}, Fe^{2+}, Ca^{2+}, Sn^{2+}, K^{+}, Na^{+}, Al^{3+}, Fe^{3+}, Pb^{2+} and Cd^{2+}, chosen as they could be present in water with Hg^{2+}, did not induce any noticeable variation in the fluorescence.

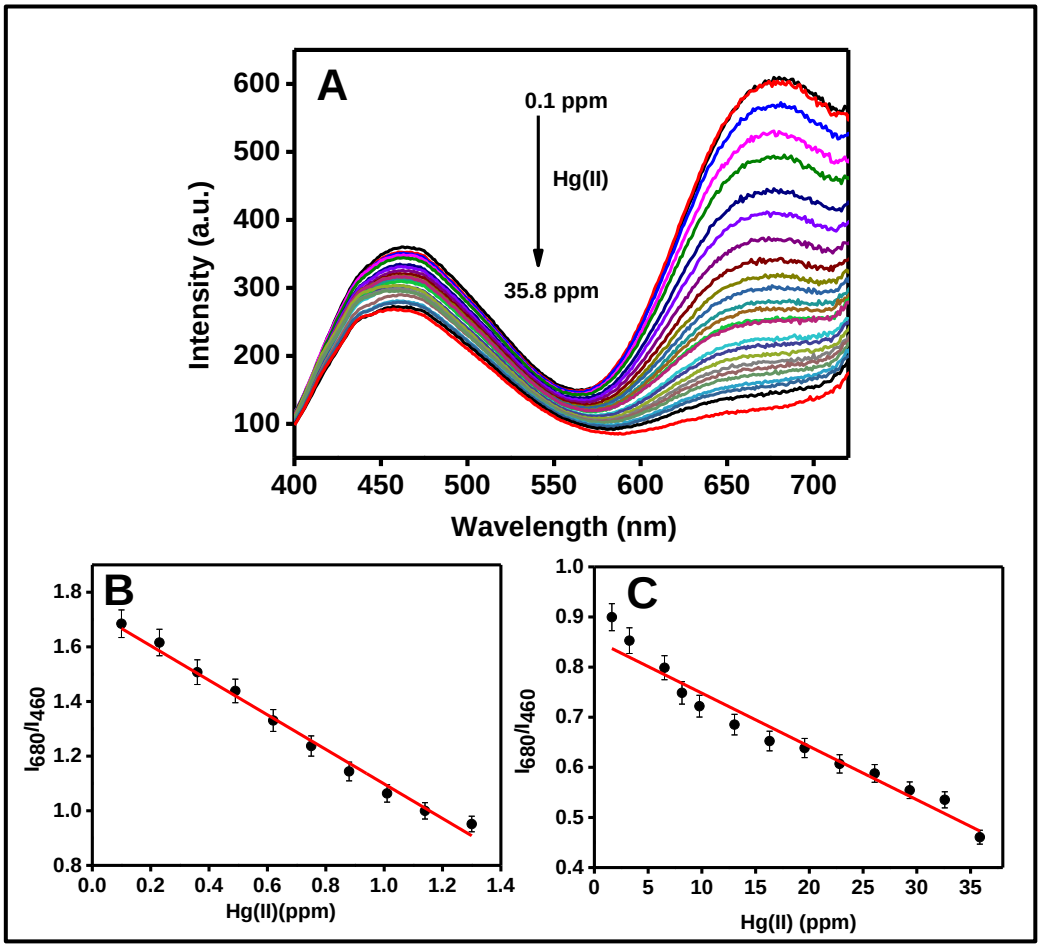

Figure 5.12. (A) Fluorescence response of AuQC@GQD with different concentration of Hg (II) (0.1 ppm- 35.8 ppm). (B) and (C) shows the fluorescence intensity ratio (I_{680}/I_{460}) of AuQC@GQD Vs Hg (II) concentrations in a range of (0.1-1.3 ppm) and (1.6-35.8ppm), respectively.

Thus, it is confirmed that the fluorescence quenching is specific to Hg^{2+} as shown in Figure 5.13. Further, we have developed a sensitive sensor platform by incorporating AuQC@GQD on nanofibers by electrospinning of AuQC@GQD on a PVA matrix. Thus, by developing AuQC@GQD incorporated nanofibers, a

unique sensor having more surface area interaction, better dispersion and better detectability were generated. The detailed method of preparation is given under the experimental section (Section 5.24 & 5.25). Thus, obtained AuQC@GQD mat were found to dissolve rapidly in aqueous solution, further limiting its potential applications as a sensor.

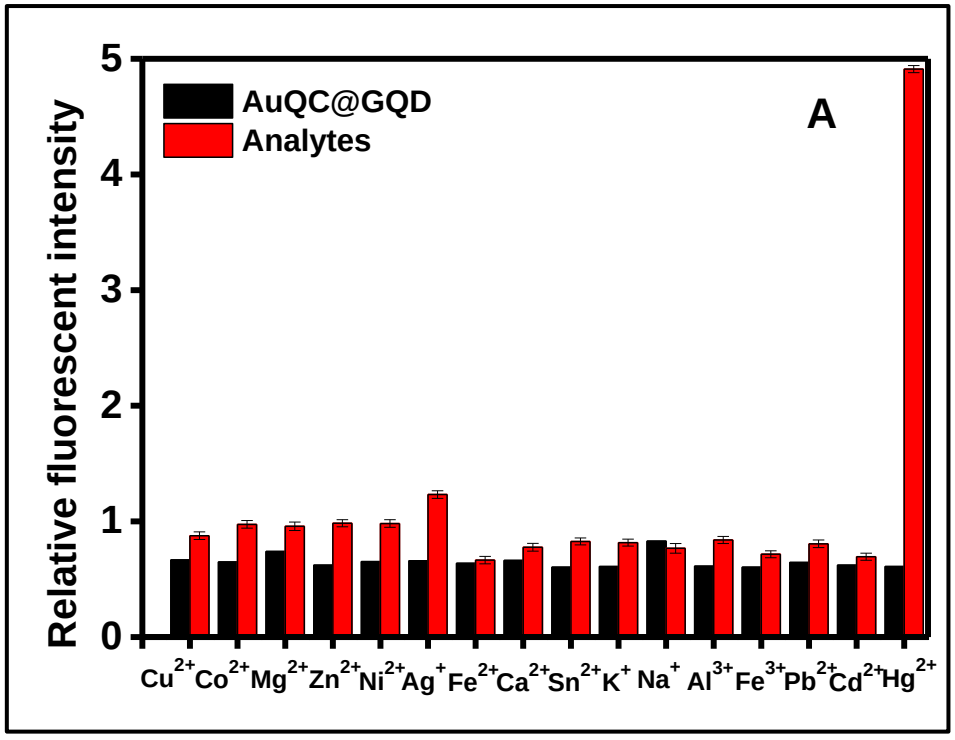

Figure 5.13. Fluorescence response of AgAuQC@gluten with different metal ions. (Concentration of all analytes were kept constant as 35.8 ppm).

In order, to overcome the above drawback, the nanofibrous mat was cross-linked with glutaraldehyde vapor to produce water-insoluble mat. The incorporation of AuQC@GQD on PVA matrix and morphology of nanofiber were characterized using the various optical and microscopic technique. The SEM images of PVA and AuQC@GQD-PVA electrospun mats revealed the generation of uniform and defect-free nanofibers with an average diameter of 130 ± 50 nm. It is noticed that the morphology of the nanofiber was retained the same even after the incorporation of AuQC@GQD (Figure 5.14A & 5.14B). The TEM image of AuQC@GQD-PVA indicated the uniform distribution of AuQC@GQD on the surface of nanofibers (Figure 5.14D & 5.14E).

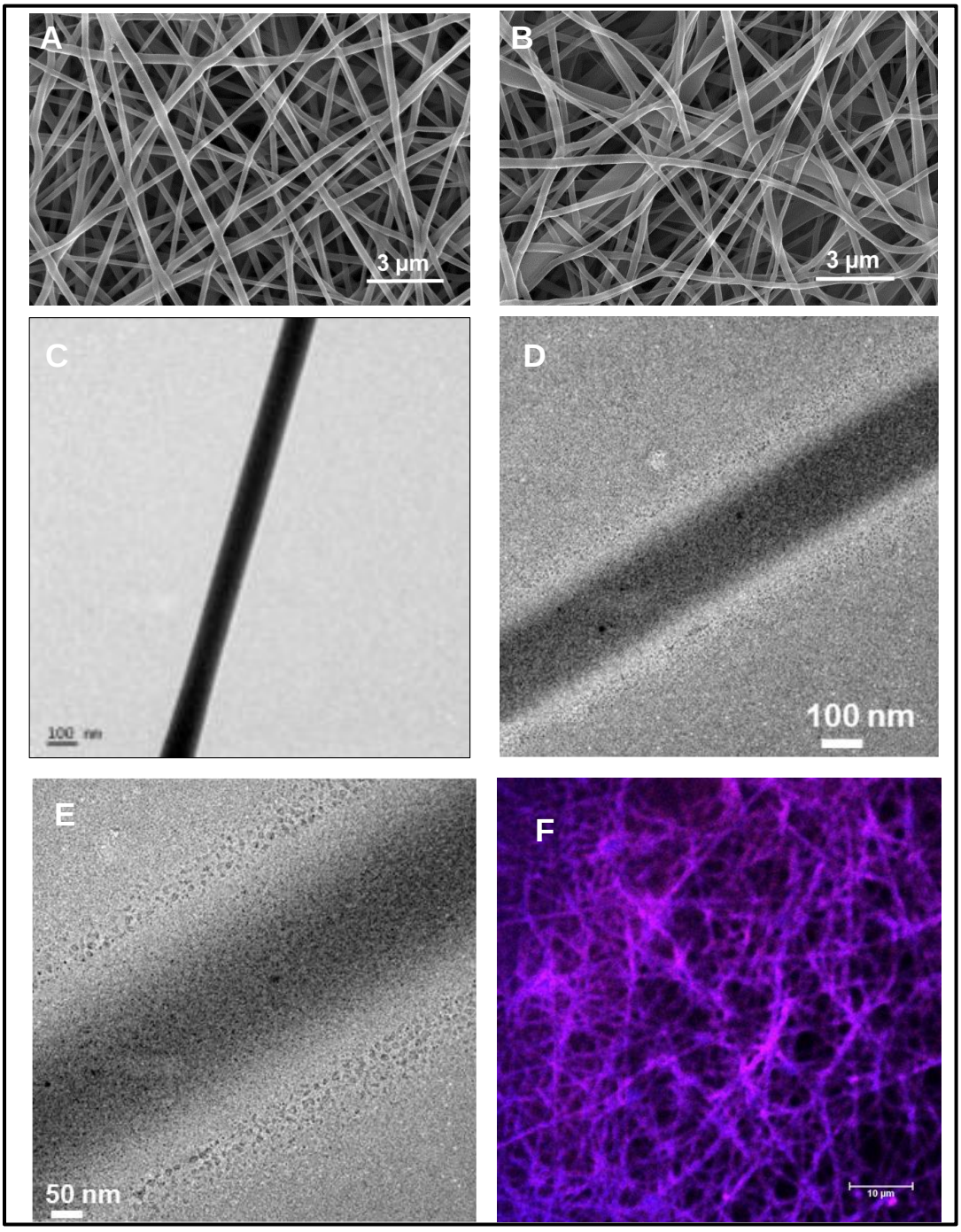

Figure 5.14. (A) & (B) shows the SEM image of PVA & AuQC@GQD-PVA respectively. (C) &(D) shows the TEM image of PVA &AuQC@GQD-PVA respectively. (E) HRTEM image AuQC@GQD-PVA (F) CLSM image of AuQC@GQD-PVA (merged,) excited at 400 nm.

Furthermore, CLSM studies exhibited reddish violet emission of the nanofibrous mat and observed an even luminescence on the nanofibers confirming the uniform dispersion of AuQC@GQD throughout the nanofibre and luminescence property

were not affected on incorporation to PVA mats (Figure 5.14F). The elemental analysis further confirmed the presence of elemental Au, N, C, O, and S on the nanofiber (Figure 5.15). The nanofiber matrix emits reddish violet fluorescence on exposure to UV light (365 nm) further extends its applicability in developing a sensor for the naked eye detection of Hg (II). In order to analyze the applicability of AuQC@GQD-PVA nanofibers as sensor for detecting mercury ions, the nanofibre mat was analyzed via visual calorimetric approach and CLSM based analysis, which led to the observation that AuQC@GQD-PVA nanofiber mat was able to detect the different concentration of Hg (II).

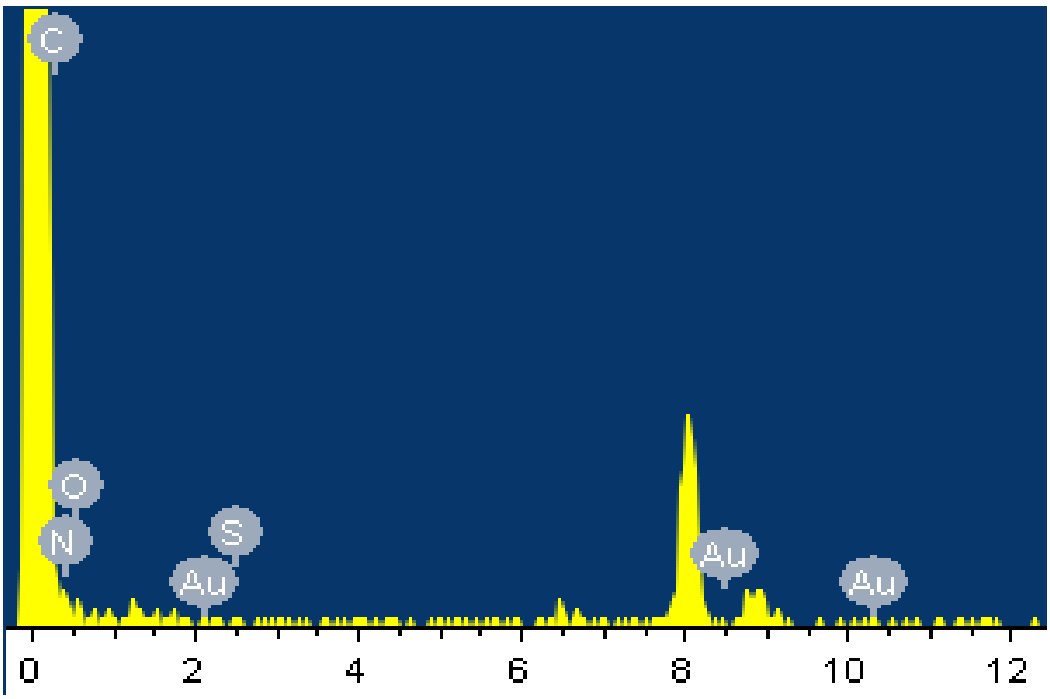

Figure 5.15. EDX analysis of AuQC@GQD-PVA.

For the ease of visualization, independent nanofiber mats were drop cast with different concentration of aqueous solution of Hg (II) and the concentration-dependent fluorescence quenching of AuQC@GQD-PVA nanofibers were noted (Figure 5.16B). At higher concentration of mercury (35 ppm), the red fluorescence completely quenched and blue emission partially retained. The same quenching phenomenon was observed in the case of CLSM images, which is given in Figure 5.16A, upon the addition of different concentration Hg (II), the red emission from the nanofiber is quenched and the fiber became blue emitting.

Thus, this unique developed sensor can be used as an effective platform for the sensitive and selective detection of Hg (II) in practical applications.

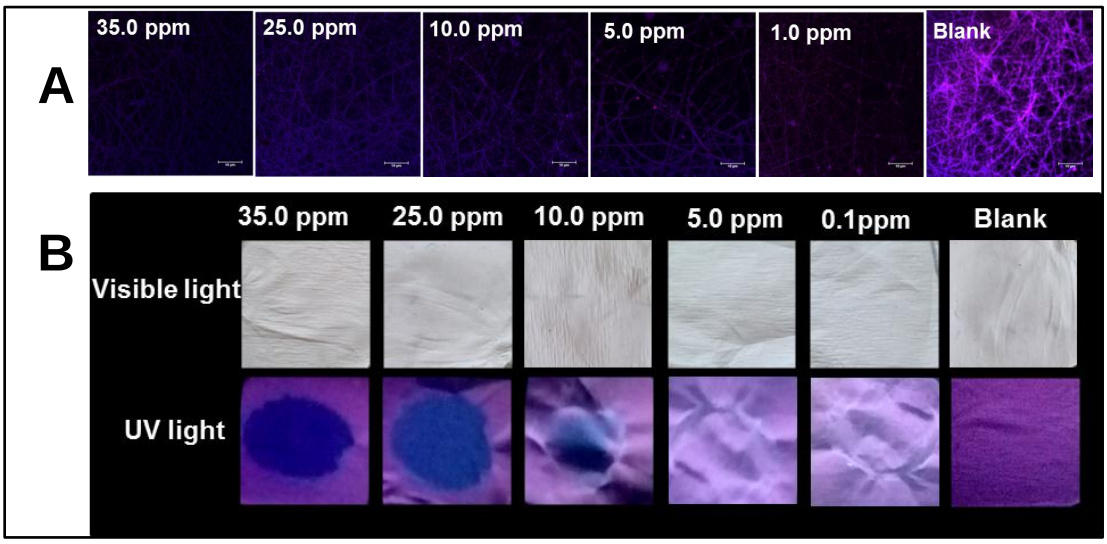

Figure 5.16. (A) CLSM image of AuQC@GQD-PVA nanofibre mat with different concentration of Hg (II). (B) Photograph of AuQC@GQD-PVA mat with different concentration of Hg (II) (35.0 ppm -0.1 ppm) taken under visible light and UV light.

5.2.3. Mechanism of fluorescence sensing

A detailed investigation has been carried out to explore the mechanism of fluorescence quenching. Generally, the fluorescence quenching can take place by two processes (1) electron transfer between fluorophore and quencher and (2) energy transfer between fluorophore and quencher. Here the possibility of energy transfer between Hg (II) and AuQC@GQD can be easily ruled out because there is no spectral overlap between analytes and fluorophore. The possibility of static fluorescence quenching was ruled out by analyzing the absorption of AuQC@GQD with different concentration of Hg (II). The absorption spectra of AuQC@GQD with different concentration of Hg (II) is shown in Figure 5.17A. There was no considerable change in the absorption spectra of AuQC@GQD observed when Hg (II) is introduced. This excludes the possibility of any ground state complex formation between Hg (II) and AuQC@GQD. Further, the possibility of excited state complex formation assisted photo-induced electron transfer mechanism was studied by lifetime analysis. We used pulsed laser

excitation (455 nm) to avoid interference from protein and measure the lifetimes of AuQC@GQD at their fluorescence peak maxima (680 nm) (Figure 5.17B).

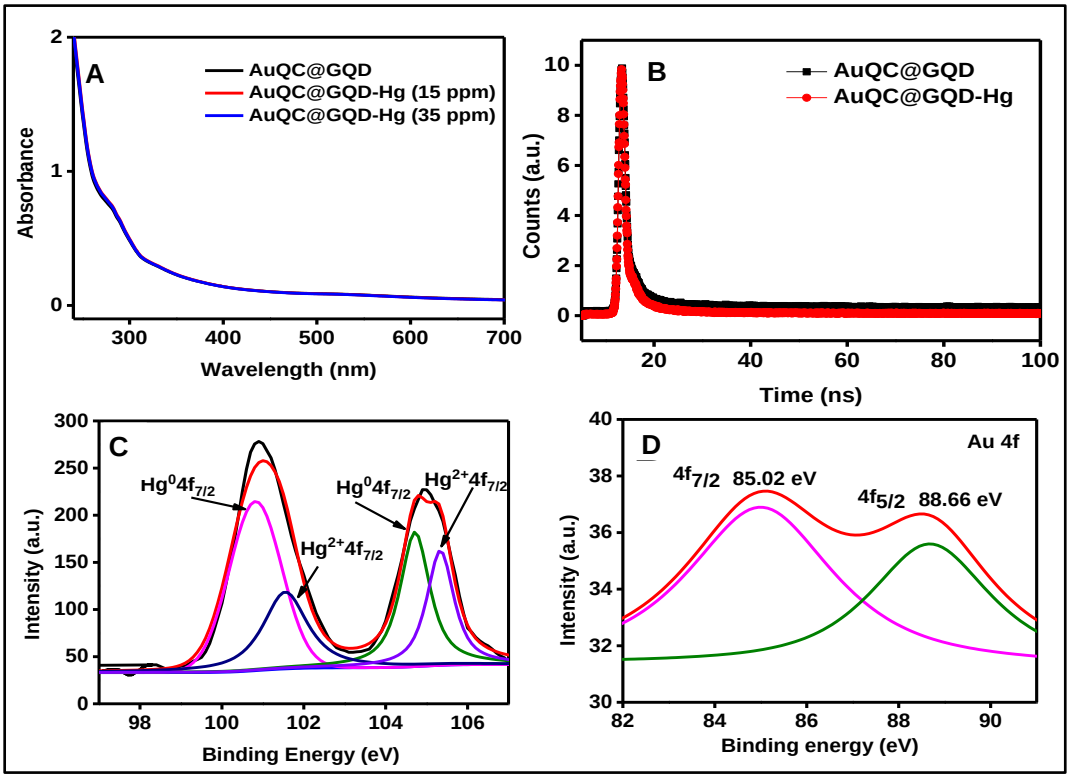

Figure 5.17. (A). UV-Vis Absorption spectra of AuQC@GQD with Hg (II). (B)Life time analysis of AuQC@GQD with Hg (II). (C) XPS high-resolution spectra of Hg 4f after the interaction with AuQC@GQD. (D)Au 4f of AuQC@GQD after the interaction with of Hg (35 ppm).

It is observed that after the interaction of Hg (II), the average lifetime of AuQC@GQD is reduced from 24.113 ns to 14.37 ns. This decrease lifetime is due to the excited state electron transfer between AuQC@GQD and Hg (II), which will further reduce Hg (II) to Hg (0) (The lifetime analysis data is given in table 5.3). This was further supported by XPS analysis. The XPS analysis of AuQC@GQD-PVA nanofiber before and after addition Hg (II) is given in Figure 5.17 C&D. After the introduction of Hg (II), the binding energy of Au increased to 85.02 eV from 84.4 eV, which is corresponding to the Au^{+}. The Hg $4f_{7/2}$ peak was seen at 100.80 eV and 101.5 eV, which shows the binding energy corresponding to metallic mercury (Figure 5.17C). This may be due to the reduction of mercuric ions, in which electrons were supplied by the core atoms of

the Au. This observation was supported by the reported literature (Chai *et al.*, 2010; Ghosh *et al.*, 2014). Moreover, it has been reported that Hg^{2+} can quench the fluorescence of carbon dot through the interaction with electron-rich aromatic ring (Zhao *et al.*, 2017). Thus, the slight decrease in fluorescent intensity of GQD from AuQC@GQD in the presence of Hg^{2+} can be due to the electron transfer from the electron-rich aromatic ring of GQD and Hg (II).

Table 5.3. Lifetime analysis of AuQC@GQD and AuQC@GQD-Hg

Sample Name	τ_1**(ns)**	A_1	τ_2**(ns)**	A_2	χ^2	τ_{av}**(ns)**
AuQC@GQD(680nm)	25.30	65.06	2.6	34.94	1.2	24.113
AuQC@GQD-Hg(II) (680 nm)	16.25	47.9	2.33	52.1	1.21	14.37

5.3. Conclusions

In conclusion, we designed a unique approach for developing sustainable resource-based dual emitting GQD-AuQC (AuQC@GQD) composite for ratiometric sensing of Hg^{2+}, using gluten protein as raw material. The use of plant protein as a raw material makes the preparation simple, inexpensive, and environmentally friendly. The obtained nanocomposite exhibited dual fluorescence emission at 450 nm and 680 nm which originate from the GQD and AuQC respectively. Compared with the conventional method for preparation of AuQC based nanohybrid for the development of ratiometric sensors, herein simplify the construction process, does not require coupling agent for conjugation of other fluorophores, or further mixing of GQD with other fluorophores. Additionally, we have successfully incorporated fluorescent AuQC@GQD nanocomposite in electrospun PVA nanofiber for efficient visual detection of Hg^{2+} in aqueous solutions. The Hg^{2+} could quench the fluorescence at 680 nm remarkably while the fluorescence at 450 nm changed slightly. This nanocomposite sensor has a high sensitivity and a satisfying detection performance can be explored for the practical applications. Moreover, the

obtained AuQC@GQD was able to produce near white light emission at a particular composition under UV irradiation, extending its applicability in the field of optoelectronics.

CHAPTER 6

SYNTHESIS AND CHARACTERIZATION OF GLUTEN PROTECTED COPPER QUANTUM CLUSTER FOR INTRAUTERINE DEVICE APPLICATION

This chapter deals with the synthesis of fluorescent copper quantum clusters (CuQCs) by a simple one-pot green method using gluten as a stabilizing agent. The CuQCs were characterized by UV–Vis absorption, fluorescence, FT-IR, TEM, and XPS. We further incorporated CuQCs on a polymer to study the release rate of a Cu^{2+} ion from CuQC-polymer composite, since copper ion is well known for its fungicidal property and contraceptive action in Copper T (CuT). The CuQCs were incorporated into a model polymer, polyurethane (PU) by melt compounding and the mixtures were extruded. It was observed that the CuQCs were uniformly dispersed within the polymer matrix. The in-vitro experiment was carried out to quantify the potential release of Cu (II) ion for contraceptive applications. The developed nanocomposite releases Cu(II) ion for 90 days, which suggests its potential application of CuQC in the medical field like the development of short-term intrauterine devices (IUD). Compared to conventional IUDs, here the CuQC-PU nanocomposite reduces the burst release of the Cu^{2+} and the release rates can be tuned by changing the composition of the materials. These results suggest that the CuQC-PU nanocomposite have a great potential to replace current commercial intrauterine devices.

Part of this chapter has been published in Analyst (2018), Vol:143, 3841–3849

6.1. Introduction

Contraception is defined as the intentional prevention of conception by the aides of various devices, sexual practices, chemicals, drugs, or surgical procedures (Jain & Muralidhar, 2011). The common contraception methods are barrier methods, hormonal methods, emergency contraception, sterilization and intrauterine methods (Jain & Muralidhar, 2011). Among these, copper-containing intrauterine device (Cu-IUD) is the world's most widely used effective type of long-acting and reversible birth control method and is used by more than 150 million women around the world (Kaneshiro & Aeby, 2010). It is a non-hormonal type of contraception in which a copper-containing wire is placed inside the uterus and prevents fertilization of the egg by disrupting the sperm mobility and damaging the sperm (Kaneshiro & Aeby, 2010). Their contraception action is mainly based on the release of cupric ions from the metallic Cu wire. This released Cu ion induces an inflammatory reaction in the endometrium and creating an unfavorable environment in the uterus that decreases the mobility and viability of sperm and prevent the fertilization (Kaneshiro & Aeby, 2010; Ortiz *et al.*, 1996). Even though it is considered a low cost, high effective and long-lasting method, its having several disadvantage such as burst release of cupric ion in the initial days, the fragmentation of copper wire or copper sleeve after long-term corrosion in uterine secretions, the direct contact between copper and endometrium, the more and more rough surface of copper after long-term etc (Li *et al.*, 2007). These will give side effect such as uterine bleeding, pelvic pain, intermenstrual spotting etc (Li *et al.*, 2007). To overcome the side-effects of conventional Cu-IUDs, polymer matrix copper nanoparticle composites have been developed because of their superiority in controlling the release of the copper ion and the continuous matrix phase (Cai *et al.*, 2007; Li *et al.*, 2007). Cai et al. first introduced the concept of polymer and copper nanoparticles for IUDs development, They have used low-density polyethylene (LDPE) as the matrix material for IUDs and the sample was produced by mixing LDPE powders and copper nanoparticles (Cai *et al.*, 2007). The possibility of direct contact of copper wire or copper sleeve to the endometrium wall can be avoided in the case of

polymer matrix nanocomposite. Another discomfort for using CuT is that the insertion and removal of the device have to carry out by a qualified medical practitioner (Stanback & Grimes, 1998). A major advantage of biodegradable polymer nanocomposite based device is the removal of the device is not required.

Copper QCs have emerged as a new generation of nanomaterial for biomedical and environmental applications in recent years, (Wang *et al.*, 2018) the ultra-small copper quantum clusters (QCs) (∼2 nm) have not yet been used for this particular application. The CuQC contains several tens of Cu atoms, which can be oxidized and Cu(II) ion can be released from the CuQC-polymer composite matrix in uterine fluid and further used for the development CuQC based intrauterine device.

Although the protein directed synthesis of copper quantum clusters are established, unfortunately, most of the copper quantum clusters are synthesized using toxic reducing agents (eg; N_2H_4, H_2O_2), which limit their widespread biomedical applications (Cao *et al.*, 2014; Guo *et al.*, 2016). Apart from the common reductive synthetic techniques which employs reducing agents such as $NaBH_4$, Ascorbic acid, N_2H_4 and H_2O_2 (Cao *et al.*, 2014; Li., *et al.*, 2016; Xiaoqing *et al.*, 2015), here our capping agent gluten itself reduces Cu^{2+} to Cu(0) and hence plays a key role in synthesizing stable CuQCs. The as-synthesized clusters were found to be stable in the solid state which can be exploited in the fabrication of various devices in the biomedical field.

Metal-polymer nanocomposites can be an effective option for such purposes because of the highly dispersed nature of the quantum clusters and its large nanoparticle/polymer interfacial area that guarantees a high reactivity and eventually good metal releasing properties (Cioffi *et al.*, 2005; Palza *et al.*, 2017; Saumya & Rao, 2012; Wang., *et al.*, 2015; Wu., *et al.*, 2015).

Polyurethanes (PU) have been widely used in medical field such as implants for sustained release of drugs, development of intravaginal rings, fabrication of medical devices such as cathedral, heart valves or artificial veins and arteries etc., due to its excellent biocompatibility, swelling property and

flexible nature (Burke & Hasirci, 2004; Lowinger *et al.*, 2018; Shelke *et al.*, 2014).

Herein a novel one-step, facile, synthetic method is presented to prepare copper QCs (CuQCs) in ambient conditions by using an easily available, biocompatible, cost-effective protein, gluten as both the reducing agent and the protective layer preventing the aggregation of the as-formed QCs. Furthermore, CuQCs were loaded on a model polymer, PU for a novel application, the development of an intrauterine device that can be a plausible alternative for conventional Copper T. To the best of our knowledge, polyurethane (PU) embedded CuQCs have never been reported so far for this particular application.

6.2. Experimental Section

6.2.1. Materials

Copper sulfate ($CuSO_4$), sodium hydroxide (NaOH), sodium chloride (NaCl), potassium chloride (KCl), calcium chloride ($CaCl_2$) and glucose were purchased from Merck Specialities Private Ltd., India. Gluten and Diethyl ammonium salt of diethyldithiocarbamic acid were purchased from Sigma-Aldrich. Polyurethane (PU) was purchased from Micku traders, India. Millipore water was used for all of the experiments.

6.2.2. Instrumentation

Fluorescence emission and excitation spectra were recorded using a Fluoro Max – 4C spectrofluorometer (Horiba Instruments, USA) at an excitation wavelength 325 nm and the slit width of 5 nm. UV-visible absorption spectra were recorded using a Varian model Cary win Bio 100 double beam spectrometer (path length 1 cm). Temperature-dependent fluorescent measurements were carried out at the varying temperature from 20 °C to 90 °C by taking data points with an interval of 10 °C by using Fluoro Max – 4C spectrofluorometer (Horiba Instruments, USA) with a temperature controller accessory (Model 300B series). DSM Xplore micro-compounder with a volume capacity of 5 mL was used for the

preparation of CuQC-PU nanocomposite. The morphology of the samples was examined by TEM, JEOL JEM 2011 microscope operating at 200 kV. In the case of liquid, samples were prepared by drop casting on carbon-coated copper grids. For the solid composite, sliced thin sections of CuQC-PU composites with a thickness of about 60–80 nm, prepared by ultra-microtomy, were used to take the TEM images of the composites. XPS analysis was carried out using a Multilab 2000, Thermo Fisher Scientific using Mg K-α radiation. SEM and EDS analysis were carried out using HRSEM, Quanta FEG200, FEI, USA equipped with EDS. FTIR spectra were measured using Perkin Elmer FTIR spectrometer. X-ray diffraction analysis was carried out using XRD, D8 Discover, Bruker with Cu Kα radiation. TGA was done by using, Q-50, TA Instruments, USA in the temperature range of 20–800 °C at a heating rate of 5 °C/ min under N_2 atmosphere.

6.2.3. Preparation of CuQC@gluten

In a typical experiment, Gluten (25mg/mL) was added to 5 mL NaOH (0.25mM) and was stirred for 15 min at 40 °C. 5mL, $CuSO_4$ (1 mM,) was treated with the above solution and was kept stirring for 9 hours at 55 °C. The color of the solution changed from blue to violet within 2 to 5 minutes. Finally, the mixture was allowed to stir for 7-9 hours at 55 °C, while the color of the solution changed from violet to brownish pink, indicating the formation of CuQC. The formed CuQC@gluten was then purified by dialysis against deionized water through a dialysis membrane (14 MWCO) for 48 hours to remove large particles. The powder of CuQC@gluten was obtained by lyophilization and stored at room temperature for further usage.

6.2.4. Preparation of CuQC-PU nanocomposite

CuQC-PU nanocomposite samples prepared by melt mixing of polyurethane (PU) pellets with solid copper quantum cluster powder. The composite was made into a tubular structure for the suitable application, by using micro compounder at a temperature of 80 °C. Particularly CuQCs/PU

nanocomposite were prepared through melt intercalation technique by mixing the 50 wt % CuQCs with the PU matrix in an internal batch mixer (Thermo Scientific Haake PolyLab OS Rheomix, Thermo Electron Corporation, MA, USA) at 80 °C with a rotor speed of 70 rpm and mixing time of 5 minutes. Finally, the extrudate was collected and stored at room temperature for further applications.

6.2.5. MTT assay

L929 cells were obtained from ATCC, Bangalore, India. For MTT assay analysis. In the first step, the CuQC-PU sample was incubated in PBS at 37 ^{o}C for three different time intervals (24, 48, 72 hours). After the specific incubation periods, the samples were removed and the extract was used to carry out cytotoxicity studies in L929 cell lines. The L929 cells were seed into 96 well plates and incubated for 24 hours at 37 ºC. After the incubation, the cells were treated with 10 µL of extract taken from PBS and incubated for 24 hours. After the 24 hours of incubation, the medium was replaced with 90µL of fresh medium and 10µL MTT reagent (5mg/mL) was added. After 4 hours of incubation, the culture was removed. The well was then added with 100µL of DMSO and kept for 30 minutes incubation. The absorbance of color developed was then determined using microplate reader at 570 nM.

6.2.6. Determination of Cu^{2+} release

The release rate of Cu^{2+} was determined by a previously reported method (Cai *et al.*, 2007; Li *et al.*, 2007). Absorbance measurements in simulated uterine solution (SUS) were carried out to measure the release rate. The composition (gm/L) of SUS is given below.

SUS (gm/L): 4.97 NaCl, 0.224 KCl, 0.167 $CaCl_2$, 0.25 $NaHCO_3$, 0.50 Glucose, 0.072 $NaH_2PO_4.2H_2O$. The pH of the medium is adjusted to 6.5 by adding NaOH or HCl. Diethyl ammonium salt of diethyldithiocarbamic acid, with a concentration of $8X10^{\wedge-3}$ mol/L, was used as a chelating agent. This compound formed a yellow chelate with the cupric ion having an absorption maximum at 448 nm. A calibration plot was made by taking the absorbance of the solutions

containing various concentrations of $CuSO_4$ and the chelating reagent. For the estimation of copper ion release, the CuQC-PU wires were suspended and incubated in 5 mL of SUS and kept for continuous shaking at 37 °C. The pH value 6.5 was established by adding diluted hydrochloric acid or sodium hydroxide solution. To avoid retarding oxidation rate, the SUS was replaced by a freshly prepared batch once in a week in the first month and subsequently twice in a month and absorbance reading was taken in every week.

6.3. Results and Discussion

6.3.1. Synthesis and Characterization of CuQC

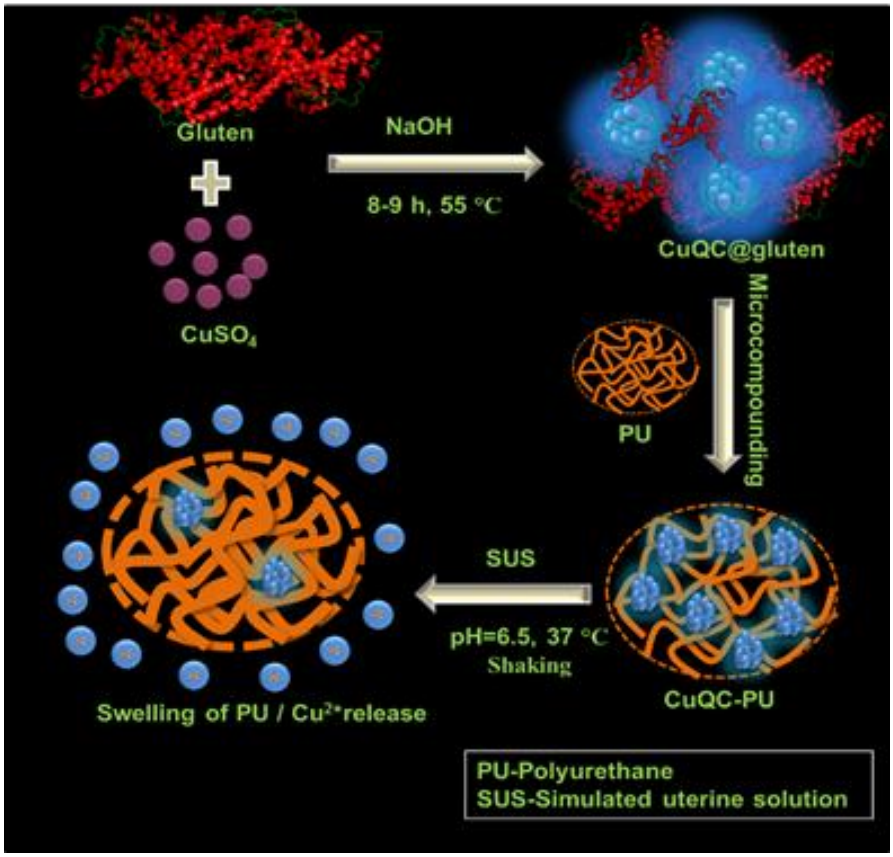

Figure 6.1. Schematic representation for the synthesis of CuQCs, CuQC-PU composite and the release of Cu^{2+} from the nanocomposite.

The method of gluten directed synthesis of stable, water-soluble and fluorescent CuQC is shown in Figure 6.1. Syntheses of CuQCs were accomplished in a single step within 8-9 hours of the reaction. The detailed

procedure for the synthesis of CuQCs is given in the experimental section (Section 6.2.3). Formation of blue emitting Cu QC was confirmed by different spectroscopic and microscopic techniques. Figure 6.2A shows the absorption spectra of pure gluten (black trace) and blue emitting CuQCs (red trace). On comparing the absorption spectra of gluten and CuQC, in addition to a peak at 280 nm, a small hump is observed at 325 nm, which arises from CuQCs. This observation is supported by previously reported literature for BSA protected copper quantum cluster (Goswami *et al.*, 2011).

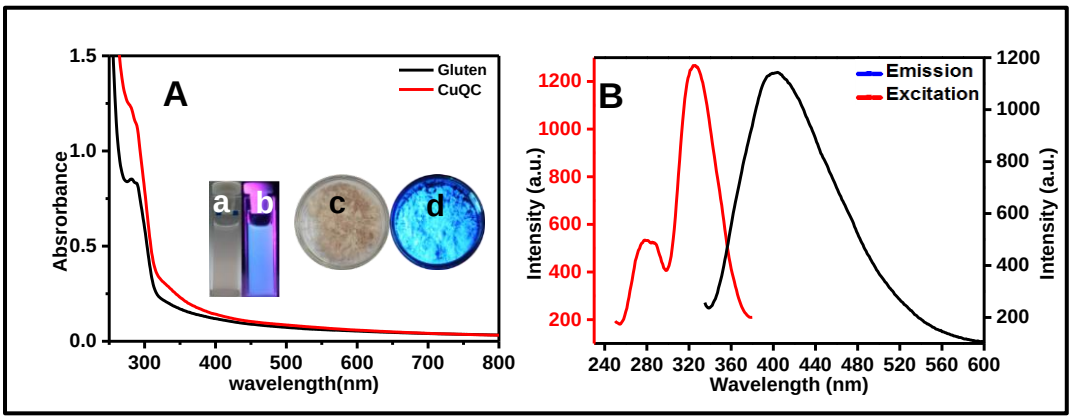

Figure 6.2. (A) UV-Vis absorption spectra of gluten (black trace) and CuQC (red trace). (B) Excitation (red trace) and emission spectra (black trace, λ_{ex} = 320 nm) of CuQC. The inset shows the photographs of aqueous solution CuQC (a&b) and powder (c&d), where (a,c) is taken under visible light and (b&d) taken under UV light.

The peak around 280 nm is due to the aromatic amino acid present in the gluten (Mathew & Kuruvilla, 2017). The absence of surface plasmon resonance peak (around 560-600 nm) clearly rules out the possibility of Cu nanoparticle formation in the solution mixture. The CuQC solution exhibits light brown color under visible light (inset of Figure 6.2, a) and intense blue emission under UV light (365 nm) (inset of Figure 6.2, b). The fluorescent emission spectrum of CuQCs shows a single peak with an emission maximum of 410 nm when excited at 325 nm (Figure 6.2B). The excitation spectrum of the product consists of one major peak at 325 nm and a shoulder peak at 280 nm (Figure 6.2B). Multiple excitation peaks were observed as expected for QCs in proteins due to the cluster core as well as the protein.

Synthesis of stable fluorescent CuQCs has been crucial since Cu ions in aqueous solution usually result in the formation of large nanoparticles (NPs) rather than smaller QCs due to spontaneous aggregation of QCs leading to a significant loss of their photophysical properties (Cao *et al.*, 2014a).

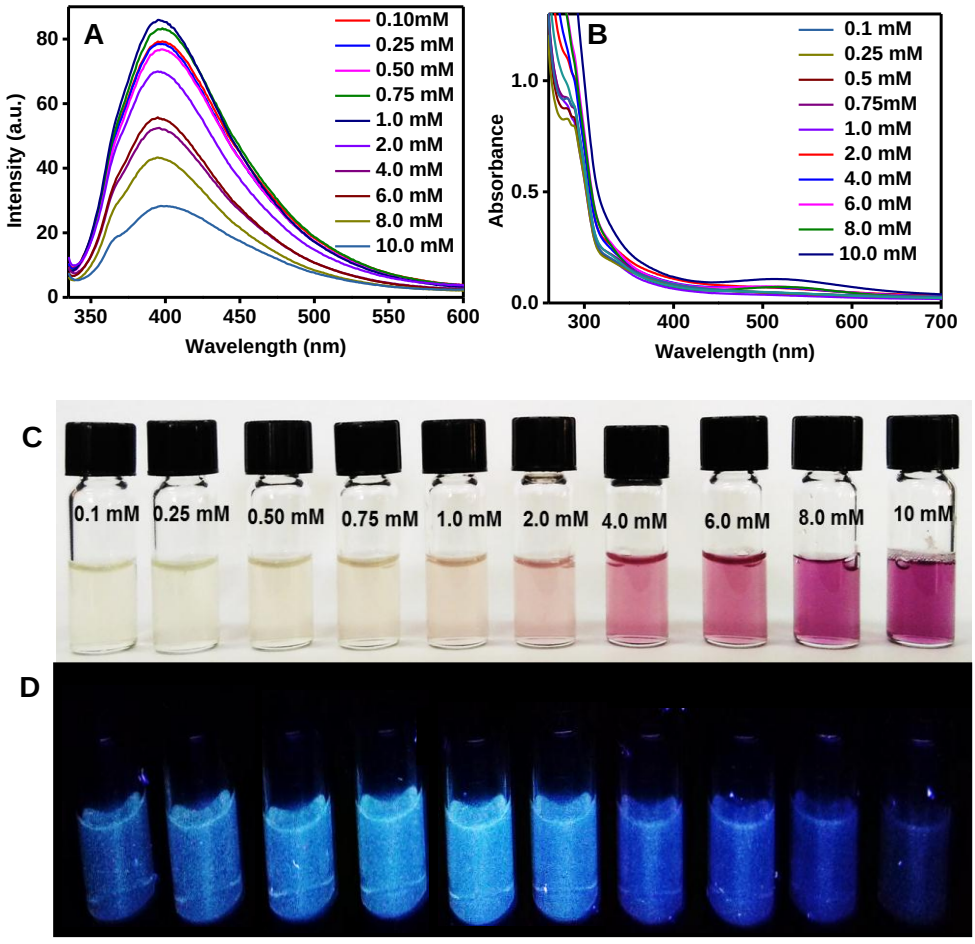

Figure 6.3 (A)&(B) shows the fluorescence emission spectra (λex = 320 nm) and absorption spectra of evaluation of clusters with various concentration of $CuSO_4$ respectively. The concentration of gluten (25 mg/mL) was maintained as constant. The spectra were collected after 7 hours reaction at 55 °C.(C) and (D) shows the photograph of CuQC formation at various concentration of CuSO4 under visible light and UV light (λex = 365 nm) respectively.

Thus it is essential to know the key parameters such as concentration, pH, time and temperature to obtain a highly luminescent CuQCs. Higher the fluorescence intensity represents the higher the reaction rate for the formation of CuQCs (Xue *et al.*, 2008). Hence, a series of control experiments have been

performed to optimize the reaction condition. When we varied the concentration of $CuSO_4$ from 0.1 mM to 10 mM by keeping the concentration of gluten as a constant (25 mg/mL), it was noticed that the maximum emission was obtained at 1 mM concentration of $CuSO_4$ (Figure 6.3A). Upon increasing the concentration of $CuSO_4$ from 1 mM to 10 mM, the flurescent intensity of the CuQC is getting decreased due to the aggregation of smaller QCs resulting in the formation of larger sized nanoparticle at higher concentration. This was further confirmed by analyzing UV-Vis absorption spectrum of product at different concentration of $CuSO_4$. The UV-Vis absorption spectrum clearly indicates the formation of nanoparticles (surface plasmon resonance (SPR) peak at 550 nm) upon increasing the concentration of $CuSO_4$ beyond 2mM (Figure 6.3B). Moreover, the peak observed at 280 nm is arises from the aromatic amino acid present in the gluten. During the formation of nanoparticle, the oxidation of aromatic amino acid is takes place, this leads to the broadening of peak at 280 nm with much higher absorption. This was supported by the following referenceThe photographs of CuQC at various concentration of $CuSO_4$ under visible light and UV light are given in Figure 6.3C&D which further supports the optimum concentration of $CuSO_4$ as 1 mM. In order to further confirm that the blue emission is originating from CuQCs and not from gluten, we have compared the emission spectrum of gluten and CuQC under the same conditions since the aromatic amino acids in the protein are known to emit in the blue region. By comparing the emission spectra of gluten and CuQC, it was noticed that gluten alone shows insignificant emission at 325 nm excitation at pH 12 (Figure 6.4A) confirming the generated blue emission is from CuQCs. We have monitored the optimum time required for the formation of blue emitting QCs by recording fluorescence emission spectra and absorption spectra at different time intervals (1-9 hours). The emission of these QCs started appearing after a few hours from the start of the preparation. As the reaction time progressed to 4-7 h, a gradual increase in the fluorescence intensity from the solution has been observed (Figure 6.4C). After around 8-9 h of the reaction, there is no further enhancement in the fluorescence and the reaction is considered to be completed. UV-Vis absorption spectra show a gradual increase in extinction around 325 nm upon increasing the reaction time (1-9 hour) (Figure

6.4B), which further gives an evidence for the CuQC formation in the medium. The pH of the reaction mixture is another important parameter in the synthesis of fluorescent CuQCs. We have carried out experiments in acidic (pH =5), neutral (pH =7) and basic (pH=12) pH and it was observed that the highly concentrated blue emitting quantum cluster formed only at basic pH (pH=12) (Figure 6.4D). It is reported that at alkaline pH, aromatic amino acids present on the protein donate electrons to reduce metal ion and broken disulfides at elevated pH stabilize through Au–sulfur linkages (Xavier *et al.*, 2012c).

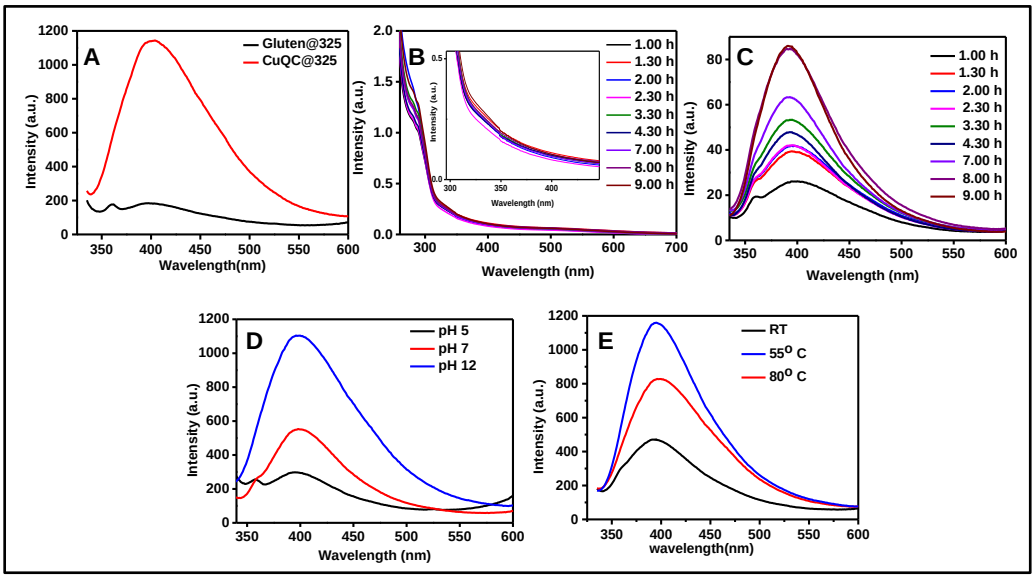

Figure 6.4 A Comparison emission spectra of gluten (black trace) and CuQC (red trace). (B)Absorption spectra and (C) emission spectra (λex = 320 nm) of QC at different time points during their synthesis. Concentration of $CuSO_4$ (1 mM) and gluten (25 mg/mL) maintained as constant. The spectra were collected with different time interval stars from 1h to 9 h. (D) and (E) shows the Fluorescent emission spectra (λex = 325 nm) for CuQC synthesized at different pHs and temperature respectively (λex = 325 nm).

The optimum temperature required for the formation of stable CuQCs was found out by carrying out the reaction at three different temperatures (RT, 55 °C and 80 °C). The fluorescence intensity of CuQCs reached the maximum at 55 °C for 8 h of reaction (Figure 6.4E). These results indicate that the optimum concentration ($CuSO_4$), pH, temperature, and time required for the formation of intense luminescent CuQCs were found to be 1 mM $CuSO_4$ and 25 mg/mL gluten

mixture at pH~ 12 at 55 °C for 8-9 h reaction. Here gluten itself acts as the reducing agent and stabilizes the clusters by providing steric protection.

The particle size of the CuQCs was determined by TEM analysis. TEM images of CuQCs revealed that the formed cluster has an average diameter of around 1.5 nm (Figure 6.5A). The oxidation state of copper in CuQC was determined using XPS analysis. Two distinct and intense peaks were observed at 932.3 and 952.7 eV (Figure 6.5C) corresponding to $2p_{3/2}$ and $2p_{1/2}$ respectively indicating the existence of Cu (0) state in CuQC. However, the absence of the peak at 942 eV corresponding to Cu^{2+} confirms that CuQC does not contain Cu^{2+}.

The formation of the gluten protected CuQC was further confirmed by FTIR spectroscopy (Figure 6.5D) by taking gluten as the control. FTIR spectra of gluten consist of normal protein amide bands (Amide I, II and III).

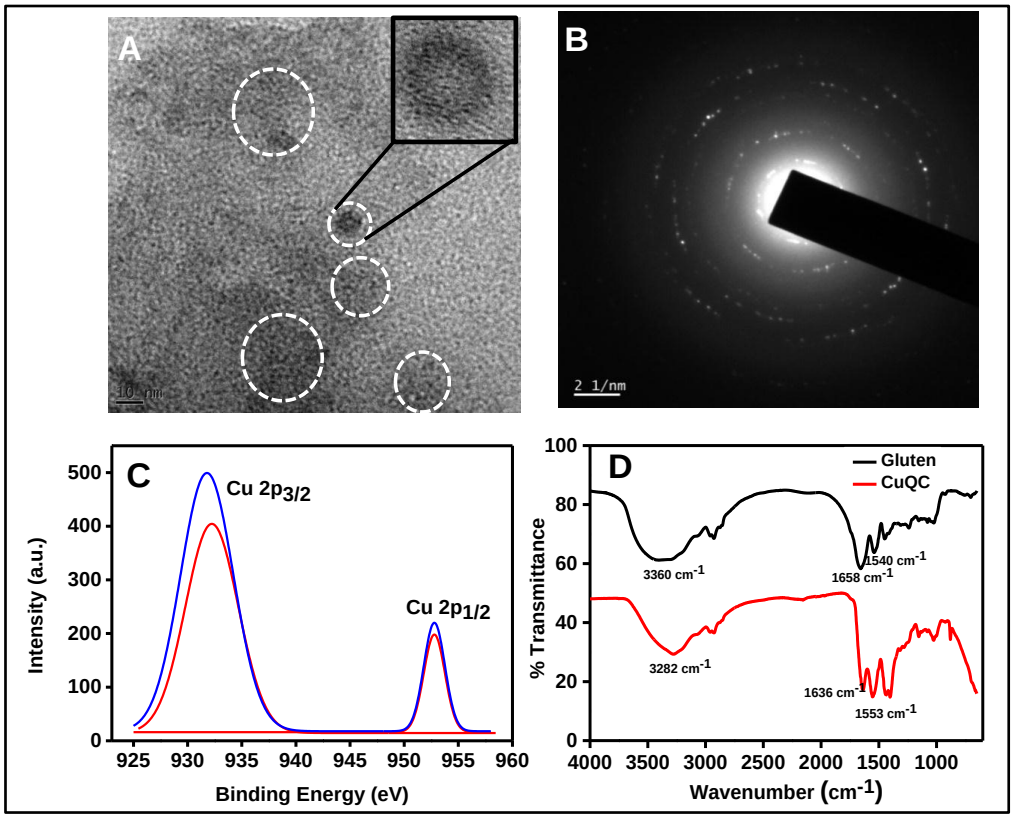

Figure 6.5 (A) TEM images and (B) selected area electron diffraction (SAED) pattern of CuQC showing the crystalline structure of CuQC.(C) XPS spectrum of Cu 2p electrons in CuQC. (D) FTIR spectra of gluten and CuQC.

The peaks in the range of 1600 -1690 cm^{-1} are the stretching frequency of amide I. Amide II is in the range of 1480- 1575 cm^{-1} and amide III is in between 1229-1301 cm^{-1}. In addition, the peak at 3500–2900 cm^{-1} due to –NH and –OH stretching vibrations was also prominent, indicating the existence of free $–NH_2$, -OH and –COOH groups. The secondary structure of the protein will mainly affect the amide I band. Here the peak corresponding to amide I is found to be shifted from 1658 cm^{-1} to 1636 cm^{-1}, which is due to the increase in the disordered structure of the protein. Along with amide I, amide II is also affected here, which is observed by the shift in peak from 1540 to 1553 cm^{-1}.

According to the spherical Jellium model, the wavelength of the fluorescent quantum cluster depends on the size of the cluster core (Goswami *et al.*, 2011; Mathew & Joseph, 2017). The blue emission of CuQCs was observed with an emission maximum at 410 nm by an excitation of 325 nm, which indicates the presence of Cu_{13} quantum clusters based on the spherical Jellium model (Goswami *et al.*, 2011). Due to the complexity of wheat gluten protein (composed of hundreds of different protein), the number of Cu atoms present in the cluster could not be detected using MALDI TOF- MS analysis (Mathew & Kuruvilla, 2017).

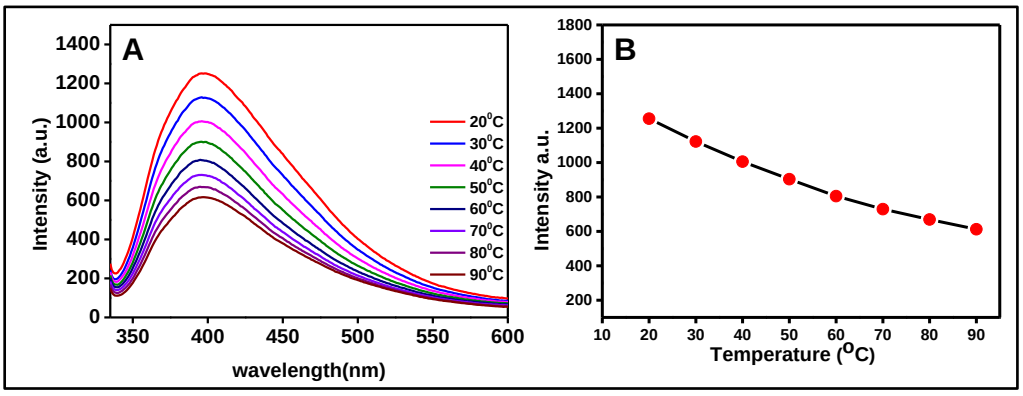

Figure 6.6 (A) Fluorescent Emission spectra of CuQC subjected to various temperature and (B) corresponding intensity Vs temperature data.

Further, the formed CuQC was subjected to various temperatures for understanding the thermal stability of the system. Figure 6.6 shows the variation in the fluorescence intensity within a temperature range of 20-90°C which verifies

the fact that 50% percentage of the cluster is stable up to 80 °C. Thus it can be processed at 80 °C for the particular application.

6.3.2. Fabrication and characterization of CuQCs/PU Nanocomposite for Cu ion release.

The CuQCs@gluten were incorporated into PU via melt-compounding and extrusion of the molten polymer nanocomposite produce 3.00 mm diameter extrudate. The detailed procedure for the preparation of CuQCs-PU nanocomposite is given under the experimental section (Section 6.2.4). The incorporation of CuQC in PU was confirmed by TEM, FTIR, XRD and TGA analysis. The dispersion of CuQC in PU matrix can be visible from the TEM image (Figure 6.7A). Selected area diffraction pattern shows the crystalline nature of CuQC@PU (Inset of Figure 6.7 A).

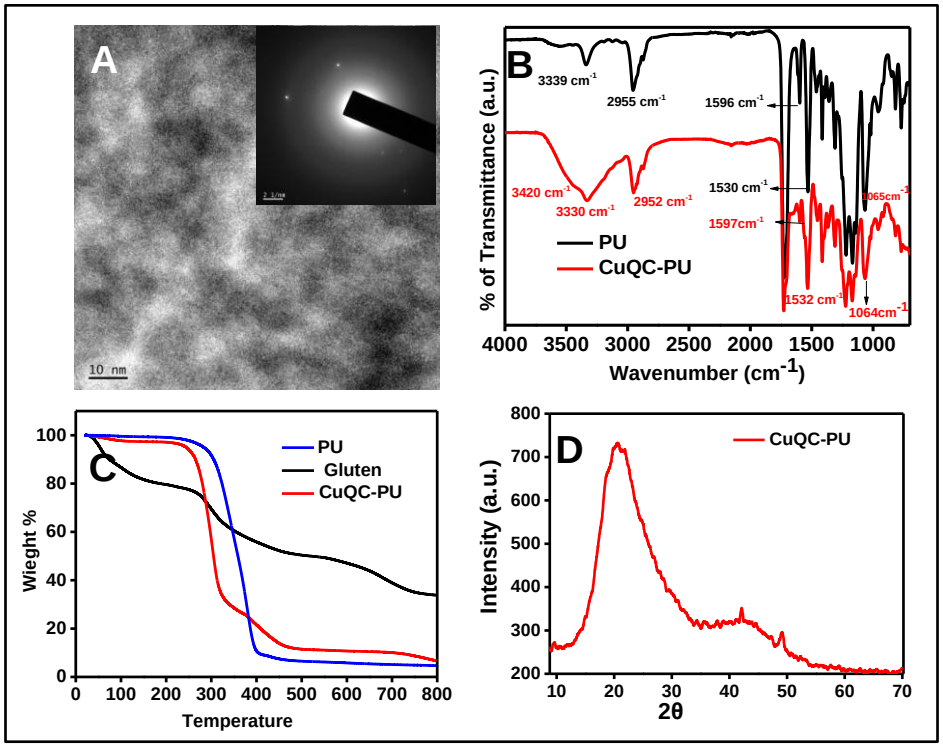

Figure 6.7. (A)The TEM image and SAED pattern (inset of A) of CuQC-PU nanocomposite. (B) FTIR spectra of PU and CuQC-PU nanocomposite. (C) TGA profile of PU, gluten, CuQC-PU. (D) XRD analysis of CuQC-PU.

FTIR spectra of PU and CuQC@PU composite are given in Figure 6.7B. In the FTIR spectrum of PU, the two bands at 3339 and 1530 cm^{-1}, corresponds to the stretching and bending vibrations of the N - H groups. The peaks at 2955 and 2872 cm^{-1} were attributed to CH_2 asymmetric and symmetric stretching vibrations, respectively. The peak at 1726 cm^{-1} indicated the C═O stretching vibrations. Incorporation of gluten protected CuQCs into PU exhibits both the characteristic peaks of CuQC and PU, which further implies the successive incorporation of QC into the polymer matrix. CuQC-PU retains the characteristic peaks of PU and the emergence of a new broad peak in the range of 3400 cm^{-1} to 3600 cm^{-1} is from OH and NH stretching vibrations of gluten.

The Thermogravimetric analysis of CuQC@gluten, PU and CuQC-PU are shown in Figure 6.7C. The neat-PU degradation profile showed two-step degradation, corresponds to the breakdown of a urethane bond and ester decomposition. The PU showed higher thermal stability than CuQC@gluten, because it started degrading at 285 °C and almost completely decomposed (4% w/w char residue) at 470 °C, whereas CuQC@gluten started degrading at 177 °C and was not fully degraded after 800 °C. The degradation profile of CuQC@gluten showed a gradual weight loss rather than a sharp drop in the weight loss. The initial weight loss by the CuQC@gluten samples was observed at around 100 °C due to the moisture loss during the temperature rise. The incorporation of CuQC@gluten changed the degradation profile of PU. The decomposition temperature of PU shifted from 285 to 230 °C after melt mixing of CuQC@gluten. The degradation pattern for CuQC@gluten is present in the TGA profile of CuQC-PU. This implies the successful incorporation of CuQC@gluten in the PU matrix. Figure 6.7D shows the XRD patterns of CuQC-PU with intense and weak broad diffractions at $2\theta = 20°$ and 43°, respectively. The former shows that there is a microcrystalline domain in the hard segment of polyurethanes. The latter is typical of amorphous polymers. The sharp peak at 43° and 50° originates from the copper quantum cluster, which is well agreement with previous literature (Epifani *et al.*, 2001; Tashkhourian *et al.*, 2018; Trovati *et al.*, 2010). These results provide further evidence for the incorporation of CuQC on the polymer matrix.

6.3.3. The release of Cu^{2+} from CuQC-PU composite

We have confirmed the ability of CuQC-PU composite for Cu^{2+} ion release for the development of intrauterine device application by monitoring the UV-Vis absorption study. The release study was carried out in a synthetic uterine fluid originally formulated by Zhang (Li., *et al.*, 2015), has been widely used to test IUD wires. The pH and temperature used for the release medium was 6.5 and 37 °C respectively. The composition of the simulated uterine solution (SUS) is given under the experimental section (Section 6.2.6). Figure 6.8 illustrates the release kinetics of Cu (II) ion by CuQCs-PU composite for 90 days in SUS solution. It is observed that the rate of release of Cu(II) during initial days is comparatively high, which is due to very few CuQCs attached on the surface of the composites that can directly react with the solution, leading to the generation of cupric ions. Then a slow and sustained release is observed during the 20 to 90 days. These findings are in good agreement with previous investigations of copper nanoparticles exposed in SUS (Cai *et al.*, 2007). The cell viability was evaluated by a standard MTT assay. The cytotoxicity analysis of CuQC-PU extract at three different time interval (24 h, 48 h, 72 h) is shown in figure 6.8B. The obtained data suggest that the sample extract at all the three-time points were cytocompatible. The cells showed the least toxicity in all time intervals. Figure 6.9 shows the SEM image and elemental mapping of CuQCs-PU composite before and after immersion in SUS for 90 days. These images clearly demonstrate the formation of large cracks on the surface of PU after immersion (Figure 6.9 A&B). These cracks were developed during the swelling and corrosion of CuQCs-PU in acidic medium, which facilitates easy release of Cu^{2+} into the medium.

Moreover, it is observed that the CuQC-PU composite wire become swollen after immersion in SUS medium at pH 6.5. Thus the swelling of the polymer can have an impact on drug release kinetics (Lowinger *et al.*, 2018). When a polymer swells, the length of the diffusion pathways increases. This will result in the sustained release of Cu^{2+} (Lowinger *et al.*, 2018). It is well-known that copper nanoparticles can be oxidized in aqueous solutions exposed to air (Reaction 6.1

&6.2) resulting in the release of copper ions under acidic condition (Cai *et al.*, 2007).

$$8Cu + O_2 + 2H_2O \rightarrow 4Cu_2O + 4H^+ + 4e^- \quad (6.1)$$

$$Cu_2O + 2H^+ \rightarrow 2Cu^{2+} + H_2O + 2e^- \quad (6.2)$$

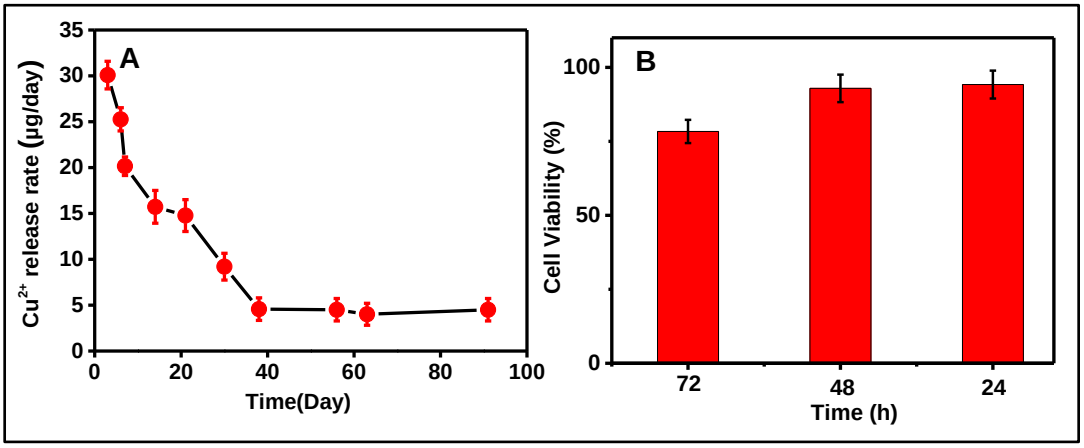

Figure 6.8. (A) Release kinetics of Cu (II) ion by 50 % CuQCs-PU composite for 90 days in SUS solution. (B) In-vitro cell viability of L929 cells with CuQCs-PU extract.

The elemental mappings of CuQC@PU before and after immersion in SUS are depicted in Figure 6.9C, 6.9D, 6.9E and 6.9F respectively. The elements present in the CuQC-PU are O, N, C, S, and Cu. By comparing the mass percentage of Cu in CuQC-PU before and after immersion in SUS, it is observed that the mass percentage of Cu decreased from 5.21 % to 0.20 % after immersion in SUS, which gives further evidence for the copper ion release from the CuQCs-PU nanocomposite. This observation suggests the great potential application of CuQC in the development of short-term IUD. Although this research was conducted with a model polymer (PU), our approach can be extended towards the development of novel short-term IUD with a biodegradable polymer as an implant. Even though CuT is used as a reliable long-acting method of family planning, the abrupt release of copper ion during the initial days causes uterine bleeding, pelvic pain, inter-menstrual spotting, excessive bleeding, etc

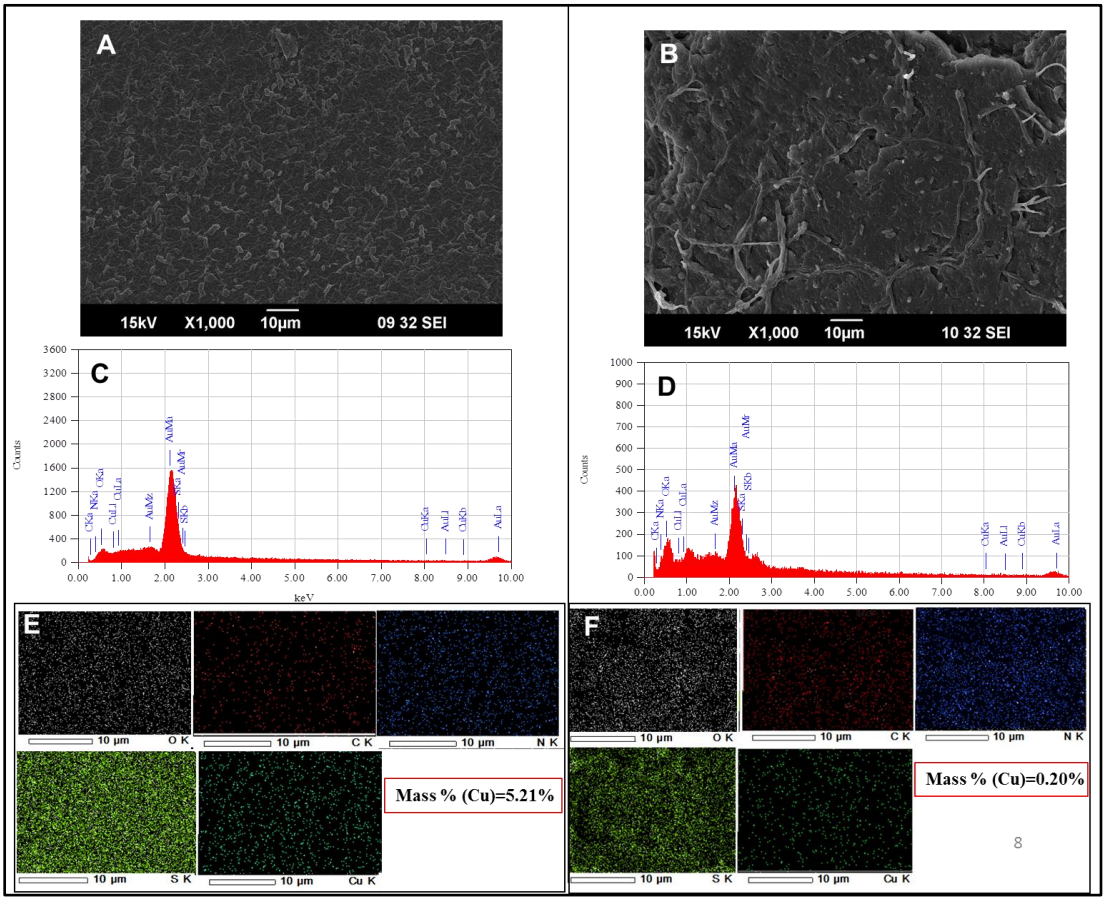

Figure 6.9. (A) & (B) SEM image of CuQCs-PU before and after immersion in SUS respectively. (C) & (D) EDS spectra of CuQCs-PU before and after immersion in SUS respectively. (E) & (F) Elemental mapping of CuQCs-PU before and after immersion in SUS for 90 days respectively.

Similarly, it has been reported that copper ion burst release might affect the surrounding cells because they are exposed to cytotoxic levels of Cu ions (Hatai *et al.*, 2012). Thus a short-term biocompatible user-friendly device could be generated effectively by using polymer nanocomposite based systems. Another advantage of CuQC nanocomposite for this particular application is that the cupric ion release could be controlled by adjusting the composition of CuQC in the composite.

6.4. Conclusions

In summary, this study provides a facile and green method for preparing blue emitting, water-soluble Cu QCs using the protein, gluten as a template. Gluten is a

complex protein derived from wheat. Further, we have investigated Cu ion release from CuQC-PU nanocomposite for contraceptive applications. The CuQCs were uniformly distributed in the polymer matrix. Compared to conventional intrauterine devices here the CuQC-PU nanocomposite reduces the burst release of the Cu^{2+} and the release rates can be tuned by changing the composition of the materials. These results suggest that the CuQC-PU nanocomposite have a great potential to replace current commercial intrauterine devices. Further investigations on device fabrication are still in progress.

CHAPTER 7

IMPROVED BIOAVAILABILITY OF CURCUMIN IN GLIADIN PROTECTED GOLD QUANTUM CLUSTER FOR TARGETED DELIVERY

This chapter deals with the synthesis of gliadin stabilized gold quantum cluster for encapsulation of curcumin and its targeted delivery to the cancer cell. CUR is an anticancer drug containing hydrophobic polyphenol derived from the rhizome of the Curcuma longa. The utilisation of CUR in cancer treatment is limited due to sub-optimal pharmacokinetics and poor bioavailability at the tumor site. In order to improve the bioavailability of CUR, we have encapsulated it into AuQCs stabilized by a proline-rich protein gliadin, since proline-rich protein is having the ability to bind hydrophobic drug CUR. The encapsulation of CUR into the hydrophobic cavity of the protein was confirmed by various spectroscopic techniques. Compared to CUR alone, the encapsulated CUR was stable against degradation and showed higher pH stability, up to 8.5 pH. The encapsulation efficiency of CUR in AuQC was calculated as 98%, which was much higher than the other reported methods. In vitro, drug release experiment exhibited a controlled and pH-dependent CUR release over a period of 60 hours. The encapsulated CUR- QCs exhibited less toxicity in the normal cell line (L929) and high toxicity in the breast cancer (MDA-MB239) cell line. Thus it can be used as a potential material for anticancer therapy and bio-imaging.

The results of this chapter have been communicated for publication in ACS Omega

7.1. Introduction

Cancer is known as an uncontrolled growth of abnormal cell and it is considered as the second leading cause of death globally. The conventional treatments for cancer diseases are surgery, chemotherapy, radiotherapy, and hormone therapy (Palumbo *et al.*, 2013). The major challenge of chemotherapy is the non-specificity of cancer cells, where normal cells are also drastically affected. The common chemotherapeutic agents used for the treatment are platinum derivatives, topoisomerase inhibitors, nucleoside analogues, vinca alkaloids, and taxanes (Dobbelstein & Moll, 2014; Urruticoechea *et al.*, 2010). These chemotherapeutic agents, though effective in treating cancer, exhibit severe toxicity in non-cancer cells as well (Liu, B. *et al.*, 2015). Also, most cancer types show initial susceptibility to chemotherapeutic agents and gain drug resistance through methods like drug efflux and DNA mutation thus increasing the chances of reoccurrence of the disease and thereby questioning the continued administration of these drugs (Housman *et al.*, 2014). Thus, the discovery of natural phytochemicals with effective growth-inhibitory activity in cancer cells and zero toxicity for normal cell lines has been the Holy Grail in the research community.

Among the phytochemicals, curcumin (CUR) [1,7-bis(4-hydroxy-3-methoxyphenyl)-1,6-heptadiene- 3,5-dione], is a worthy candidate which is being explored thoroughly. CUR is a natural hydrophobic polyphenol, isolated from the rhizomes of the perennial herb *Curcuma longa* (Singh *et al.*, 2013). It has been drawn significant interest in the recent past owing to its numerous biological and medicinal activities such as antimicrobial, anti-oxidant, anti-inflammatory, anticarcinogenic, and neuroprotective properties and is also an inhibitor of angiogenesis (Hatcher *et al.*, 2008; Hewlings & Kalman, 2017; Yallapu *et al.*, 2010). However, its poor water solubility, high rate of degradation at the physiological condition and low oral bioavailability, which is essentially due to its hydrophobic nature, limit its use in food and medicine (Yallapu *et al.*, 2010). The poor bioavailability of CUR leads to its low absorption and high rate of

metabolism within the living system and rapid elimination from the biological system (Bansal *et al.*, 2011; Hatcher *et al.*, 2008).

Keeping this insight, various formulations like encapsulating CUR within various carrier systems such as nanoparticles, liposomes, proteins, polymers etc. have been devised (Bansal *et al.*, 2011). In recent times, several research groups have been used biocompatible nanomaterials as drug carriers for targeted therapy. One of the important nanomaterials used as carriers are metal nanoparticles and among them, gold quantum clusters have specifically raised interest among scientists (Ding *et al.*, 2015; Zhang, X. *et al.*, 2015). Recently Govindaraju and co-workers developed CUR conjugated fluorescent gold nanocluster for anticancer therapy (Govindaraju *et al.*, 2018). The excellent properties of AuQCs such as easy one-pot synthesis, intensive fluorescence, good aqueous solubility, excellent biocompatibility, extraordinary photostability, extremely small size, and low cytotoxicity make them as a suitable candidate for bio-imaging, and drug delivery (Song *et al.*, 2016).

Herein, we selected an abundant, low-cost and sustainable plant protein - wheat gliadin employed as a reducing as well as stabilizing agent to facilely produce AuQC and exhibiting a strong red fluorescence. Gliadin is a proline and glutamine-rich monomeric protein component of wheat gluten and has a high amount of non-polar amino acids in its primary structure (Joye *et al.*, 2015). It is well known that the proline-rich proteins have the ability to bind hydrophobic drugs which allow mediated and controlled drug release (Malekzad *et al.*, 2018; Patel *et al.*, 2010). Thus herein we have used gliadin protected gold quantum cluster for enhanced solubilization of CUR in an aqueous medium which exhibits excellent stability at the physiological condition. The AuQC-CUR shows significant results in both bio-imaging and anticancer therapy, which suggest its great potential for anticancer treatment.

7.2. Experimental Section

7.2.1. Materials

All the reagents were used as obtained without further purification unless stated otherwise. $HAuCl_4.3H_2O$, gliadin, folic acid, 1-Ethyl-3-(3-dimethylaminopropyl)carbodiimide (EDC), N-Hydroxysuccinimide (NHS) and the membrane dialysis bag (molecular weight cut-off 14 kDa) were purchased from Sigma-Aldrich. Sodium dihydrogen phosphate, Sodium hydroxide, and disodium hydrogen phosphate were purchased from Merck. CUR was gifted by Synthite industries, Kerala, India. All solutions were prepared using Millipore water.

7.2.2. Instrumentation

UV-Visible absorption spectra were recorded in the range of 200 - 800 nm using the Varian model, Cary wins Bio 100 spectrometer. All luminescence measurements were recorded using the Fluoro Max-4C spectrofluorometer (Horiba Instruments, USA). The slits for excitation and emission were set at 5 nm. TCSPC was used for lifetime analysis with a pulse width of 1.3 ns. HRTEM images were recorded on a JEOL JEM 2100 instrument with an acceleration voltage of 200 kV. XPS analysis was carried out using an Omicron ESCA Probe spectrometer with unmonochromatized Mg Kα X-rays. FTIR spectra were measured using Perkin Elmer FTIR spectrometer. Thermal transition measurements were done using a TA Q100-DSC thermal analyzer (TA Instruments, New Castle, Delaware 19720 USA).

7.2.3. Preparation of AuQC@gliadin

Synthesis of AuQC@gliadin is briefly explained herein. Gliadin (25 mg/mL) protein powder was dissolved in 0.25 M NaOH solution and heated at 40 °C for 15 minutes. 5 mL of gliadin solution is treated with 5 mL (5mM) $AuCl_4$ and kept for vigorous stirring at 55 °C for 3 hours. Purification of AuQC@gliadin was performed by dialysis against distilled water for 24 hours in a dialysis

membrane of molecular weight cut-off 14 kDa. The cleaned gold clusters were then freeze-dried and stored at room temperature for further use.

7.2.4. Encapsulation of curcumin in AuQC@gliadin

The AuQC@gliadin stock solution (5%, w/v) was prepared by dispersing the freeze-dried AuQC@gliadin sample in water. 4 mg/mL CUR stock solution was prepared in distilled ethanol and 14 μL of CUR solution was added per mL of AuQC@gliadin, drop-wise over stirring at room temperature. The CUR solution immediately solubilizes in AuQC@gliadin solution, resulting in a bright yellow solution, which is distinct from the golden-yellow of AuQC@gliadin. The stirring is continued for 30 minutes to stabilize the formulation. The unbound CUR was removed by centrifugation at 10000 rpm for 10 min. The resultant supernatants were then collected and freeze-dried and stored at room temperature for further use.

7.2.5. Preparation of folic acid functionalized AuQC@gliadin-CUR conjugate

Conjugation of FA with protein stabilised AuQC was carried out by EDC/NHS coupling reaction (Nair *et al.*, 2015). 0.25mL of 0.05M aqueous solution of EDC was treated with 5 mL (1mg/mL) of AuQC@gliadin and kept for stirring for 2 hours. To this, 0.25 mL of 0.05M aqueous solution of NHS was added followed by the addition of 150 μL of 4 mM folic acid. After 12 hours of continuous reaction, the reaction mixture is centrifuged at 15000 rpm for 15 minutes in a 1:1 methanol/2-propanol mixture. It is followed by washing twice with DI water to obtain FL-AuQC@gliadin. To this solution, 200 μL of CUR stock solution was added followed by continuous stirring for 30 minutes to get FA-AuQC@gliadin-CUR conjugate.

7.2.6. Calculation of encapsulation efficiency (EE)

Encapsulation efficiency of CUR bound to AuQC@gliadin was determined by adding 200 μL CUR stock solution in 10 mL solution of

AuQC@gliadin and kept stirred for 30 minutes at room temperature. The solution was centrifuged for 10 minutes at 10000 rpm to pelletize the undissolved CUR. The pellet was carefully dissolved in a known amount of ethanol, and CUR was quantified spectrophotometrically at 428 nm. The encapsulation efficiency (EE) was calculated based on equation (1)(Sneharani *et al.*, 2010).

$$\text{Encapsulation efficiency (\%)} = \frac{\text{Total amount of curcumin} - \text{Free curcumin}}{\text{Total amount of curcumin}} \times 100 \quad (1)$$

7.2.7. In-vitro release of curcumin

Direct dispersion method was employed to study the in-vitro drug release of CUR from AuQC@gliadin-CUR (Anitha *et al.*, 2011; Anitha *et al.*, 2012; Bisht *et al.*, 2007). A known quantity of CUR loaded AuQCs was taken in 3 mL 0.1M PBS at pH 5 and 7.4 and incubated in a water bath shaker at 37 ºC. The study was done for a time period of 60 hours where the tubes were taken out at definite time intervals and centrifuged at 10000 rpm for 10 minutes. This was done in order to pelletize the released drug, while the entrapped drug within the gold quantum cluster remains in the supernatant. Subsequently, the pellets were dissolved in 3 mL ethanol and the amount of CUR released was quantified using a spectrometer at a wavelength of 428 nm.

7.2.8. Cell culture

C6 cells were cultured in F-12K basal medium and MDA-MB231 and L929 cells in Dulbecco's modified Eagle's medium (DMEM) and these were supplemented with 10% FBS and 1% penicillin/streptomycin. The cells were incubated at 37 ºC for 24 hours with 5% CO_2 and were observed for healthy growth after incubation. On reaching 80-90% confluency, they were trypsinized using Trypsin-EDTA solution (0.25% w/v trypsin, 0.54 mM EDTA) to detach them from the flask and centrifuged at 3000 rpm for 3 minutes. The cells were then re-suspended in the medium for further studies.

7.2.9. Cytotoxicity study

To evaluate the cytotoxicity of the prepared formulation, MTT [3-(4,5-Dimethylthiazole-2-yl)-2,5-diphenyl tetrazolium] assay was performed. It is a colorimetric test based on the selective ability of viable cells to reduce the tetrazolium component of MTT into formazan crystals, which is purple in colored (Rejinold *et al.*, 2011). For cytotoxicity experiments, MDA-MB231 and L929 cells were seeded on a 96 well plate and incubated at 37 ºC for 24 hours. Subsequently, both the cell lines were added with four different concentrations (25 µg, 50 µg, 100 µg, 200 µg) of FA-conjugated AuQC@gliadin-CUR. After the incubation of FA-AuQC@gliadin-CUR in serum-free media for 24 hours, the media were replaced with 90 µL of fresh media followed by the addition of 10 µL (5mg/mL) MTT reagent. The media were removed after 4-hours incubation at 37 °C. 100 µL of DMSO was then added to the wells and kept for 30 minutes incubation. The optical density (OD) of the solutions were then determined at 570 nm using a micro plate reader. The data was plotted against the concentration of FA-AuQC@gliadin-CUR versus relative cell viability (%).

7.2.10. Cellular uptake studies

Cellular uptake studies were done to monitor the relative uptake of FA-AuQC@gliadin-CUR in different cell lines and also to standardize the time required for the maximum uptake of the formulation by the cells. The study was done in L929 (normal cell line), C6 glioma (brain cancer cell) and MDA-MB231 (breast cancer) cells. These cells were cultured as described above and were seeded into 4-well dishes. The cells were incubated at 37 ºC for 24 hours, so that they can attach well. Followed by the incubation, the cell lines were treated with 100 µg of FA-AuQC@gliadin-CUR at three different time point incubations (1 hour, 2 hours and 4 hours). After each time point incubation, the cells were fixed using 4% para formaldehyde (PFA) solution and were mounded on glass slides. The cellular uptake and the fluorescence property of the FA-conjugated AuQC@gliadin-CUR were observed with HcRed and FITC using a confocal microscope.

7.2.11. Stability measurements

Stability of the prepared formulation in various pH (5, 6, 7, 7.4, 8.6 and 9) buffers were studied spectrometrically. In order to study the stability of the conjugate at pH 7.4 with time, CUR and AuQC@gliadin-CUR were dispersed in phosphate buffer and incubated at room temperature. The concentration of CUR at different time intervals was calculated by measuring the absorbance at 428 nm.

7.3. Results and discussion

7.3.1. Characterization of AuQC@gliadin

The method for the synthesis of AuQC@gliadin is similar to our previous method for the synthesis of gluten protected AuQC (Mathew & Joseph, 2017). Gliadin-protected AuQC were synthesized by in-situ reduction of chloroauric acid. Spectroscopic and microscopic techniques were used to confirm the successful formation of AuQC@gliadin. The UV-Visible absorption and emission spectrum of AuQC@gliadin are shown in Figure 7.2.

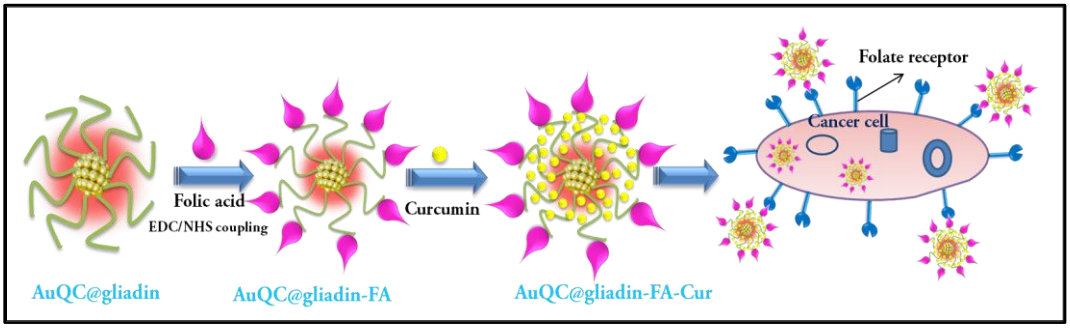

Figure 7.1. Schematic representation for the targeted delivery of CUR by folic acid conjugated AuQC.

AuQC@gliadin showed a characteristic broad featureless absorption peak with a small hump at 280 nm which is due to the presence of aromatic amino acid present in gliadin as like AuQC@gluten (Figure 7.2A) (Mathew, & Joseph 2017; Tao *et al.*, 2015; Xavier *et al.*, 2012a). The possibility of Au nanoparticle formation was eliminated since the surface plasmon resonance peak was not visible at around 520 nm. At an excitation of 380 nm, the fluorescence spectra of the formed cluster

showed an emission maximum centered at 685 nm along with a weak emission peak around 460 nm which is due to the aromatic amino acid present in gliadin (Figure 7.2A). The formed cluster showed an intense red emission under UV light (365 nm) (Inset of Figure 7.2, a) and light brown color under visible light (Inset of Figure 7.2, b). TEM image and XPS analysis further confirmed the formation of AuQC. The TEM image of AuQC@gliadin (Figure 7.2B) demonstrated that the as-prepared AuQC has good monodispersity with a particle size of ~ 2nm.

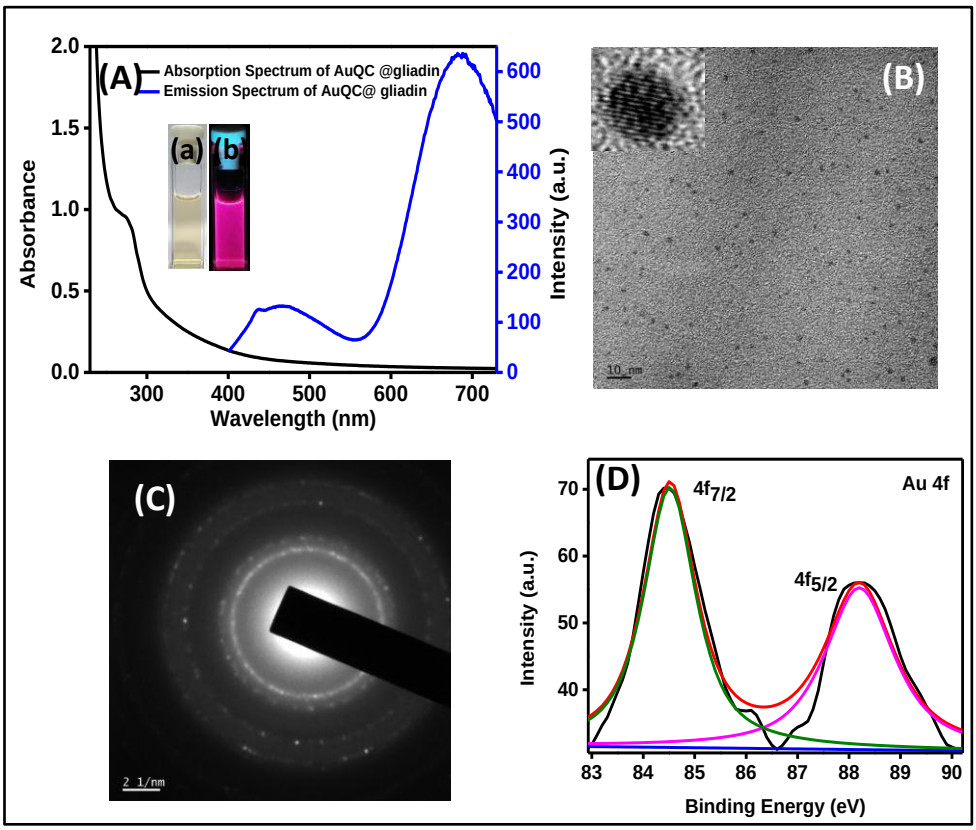

Figure 7.2. (A) Optical absorption (black trace) and emission (blue trace, λex = 380 nm) spectra of AuQC@gliadin. The inset shows the photographs of aqueous solution AuQC@gliadin under (a) UV light and (b) visible light. (B).TEM images of AuQC@gliadin. The inset shows HR-TEM image of AuQC@gliadin in the scale of 2 nm; (C) SAED pattern of AuQC@gliadin. And (D) Binding energy of AuQC@gliadin determined from XPS.

HRTEM and SAED pattern demonstrated the crystallinity of the as-formed QCs. XPS determined the binding energy for Au $4f_{7/2}$ and $4f_{5/2}$ of AuQC@gliadin to be 84.5 and 88.1 eV respectively, which corresponds to Au(0). This confirmed the reduction of Au(III) to Au(0) after the formation of clusters (Figure 7.2B).

7.3.2. Characterization of AuQC@gliadin-CUR

Simple one-step mixing method was used for the loadng of CUR into AuQC@gliadin to form AuQC@gliadin-CUR hybrid. The schematic representation for the encapsulation of CUR into AuQC@gliadin is illustrated in Figure 7.1. The encapsulation efficiency (EE) of CUR in AuQC@gliadin was calculated and found to be 98.17±0.25%. The formed AuQC@gliadin-CUR hybrid was then lyophilized and re-suspended in water. It was found that, lyophilized powder of AuQC@gliadin-CUR hybrid showed a complete dispersion in aqueous medium (Figure 7.3b, inset). Whereas, CUR alone remained completely insoluble in water with un-dissolved flakes clearly visible in the suspension (Figure 7.3b inset).

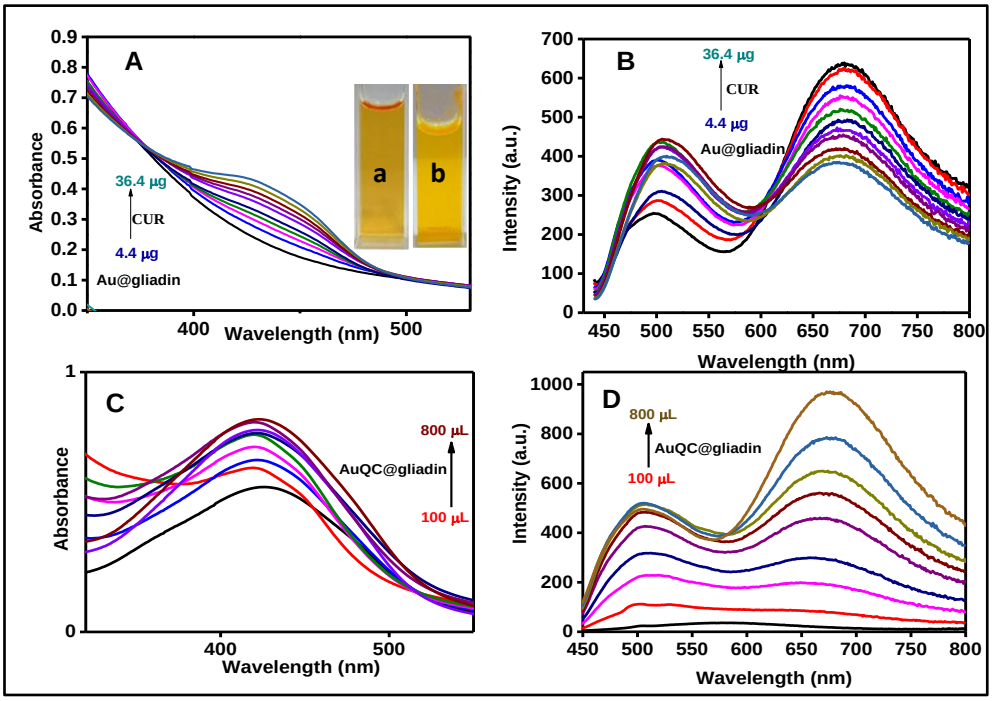

Figure 7.3. (A) and (B) Respective absorption and emission spectra of AuQC@gliadin with different concentrations of CUR (4.4 µM to 36.4 µM). Inset of (A) shows (a) CUR in AuQC@gliadin and (b) CUR in water; (C and D) Respective absorption and emission spectra of CUR with different volumes of AuQC@gliadin (100 µL to 800 µL).

The Photophysical studies of AuQC@gliadin and the hybrid have been carried out to understand the interaction of CUR with the AuQC@gliadin.

Noticeable changes in the absorption and fluorescence spectra of CUR and AuQC@gliadin were observed after interaction of these two entity. Figure 7.3A&B shows the UV-Vis absorption and emission spectra of AuQC@gliadin with different concentrations of CUR. CUR alone showed an absorption peak at 428 nm in the aqueous buffer which is the signature of its basic diaryl heptanoic chromophore group (Gangwar *et al.*, 2012). The inclusion of CUR in AuQC@gliadin showed the broadening with a slight blue shift in the absorption peak and a noticeable increase in the absorption intensity (Figure 7.3A). The blue shift in the absorption maxima is suggest the non-polar vicinity of the CUR molecules (Ghosh *et al.*, 2011; Kunwar *et al.*, 2006). Upon the addition of CUR to AuQC@gliadin, noticeable changes in the fluorescence intensity and peak position at 480 nm of QC was observed. On addition of increasing concentration of CUR to QC, the broadening of the emission peak at 480 nm and its complete shifting to 505 nm was noticed, which is corresponds to CUR emission (Figure 7.3B). CUR alone in buffer showed a weak broad fluorescence peak at 570 nm when excited at 430 nm (black trace of figure 7.3D). The blue shift in the emission spectrum of CUR from 570 nm to 505 nm is due to the entrapment of CUR in AuQC@gliadin. Previous reports for the interaction of CUR with proteins support this observation (Barik *et al.*, 2003; Kunwar *et al.*, 2006; Tapal & Tiku, 2012). The binding of CUR to BSA, human serum albumin (HSA) and soy protein isolate showed fluorescence maxima at 510, 515 and 500 nm, respectively (Barik *et al.*, 2003; Kunwar *et al.*, 2006; Tapal & Tiku, 2012). CUR is known to bind to the hydrophobic domain of the protein molecules and this non-polar environment of CUR in AuQC@gliadin is held responsible for the blue shift in its emission maxima (Banerjee *et al.*, 2014; Barik *et al.*, 2003; Kunwar *et al.*, 2006; Pan *et al.*, 2013). Moreover the interaction of CUR with AuQC@gliadin can be confirmed by the progressive reduction in fluorescence intensity at 680 nm on the addition of increasing concentrations of CUR (Figure 7.3B).

Similarly, the enhanced solubilization of CUR in an aqueous solution of AuQC@gliadin was demonstrated by monitoring the absorption and emission spectra of CUR with various concentrations of AuQC@gliadin. The absorption and emission spectra of CUR at different volume of AuQC@gliadin are shown in

figure 7.3C & D). On addition of increasing volume of AuQC@gliadin to CUR in the buffer, remarkable changes were observed in the absorption and fluorescence spectra of CUR. The increase in absorption intensity at 428 nm along with the broadening in the absorption peak confirmed the improved solubility of CUR in the gold quantum cluster solution. Moreover, the addition of AuQC@gliadin greatly improved the fluorescence intensity of CUR at 505 nm, compared to that in an aqueous medium, together with the blue shift from 575 to 505 nm in the fluorescence peak, which suggests that CUR in AuQC@gliadin binds to the hydrophobic pockets of the protein and thus experiences a non-polar environment. The fluorescence lifetime analysis further supported the encapsulation of CUR in protein stabilized AuQCs. The fluorescence decays of CUR, AuQC@gliadin and AuQC@gliadin-CUR were recorded with an excitation wavelength of 405 nm and the fluorescence decays were monitored to their emission maxima.

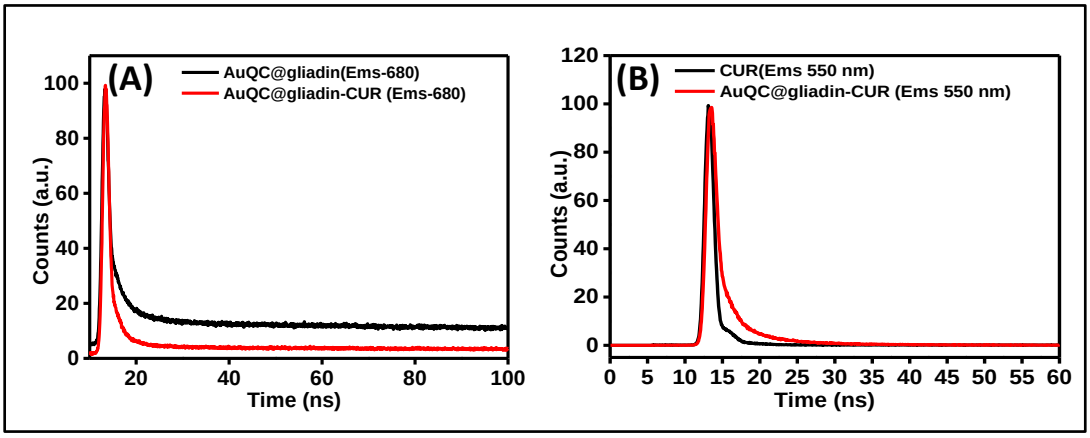

Figure 7.4. (A) Lifetime of AuQC@gliadin and AuQC@gliadin-CUR at 680 nm emission; (B) Lifetime of CUR and AuQC@gliadin-CUR at 550 nm emission.

All the lifetime values were obtained by fitting the fluorescence decay curves bi-exponentially, as tabulated in Table 7.1. When comparing the average lifetime of CUR and encapsulated CUR, the encapsulated CUR shows increased average lifetime value. The increased value of the average lifetime is due to the entrapment of CUR in the hydrophobic pockets of protein which disrupt the excited state intramolecular proton transfer (ESIPT) process. Whereas the average lifetime of AuQC@gliadin decreased when CUR was introduced, which is due to the interaction of CUR with QCs.

Table 7.1. Life-time data of AuQC@gliadin, AuQC@gliadin-CUR and CUR.

Sample Name	**A_1**	**τ_1(ns)**	**A_2**	**τ_2(ns)**	**χ^2**	**τ_{av}**(ns)
CUR (550 nm)	14.96	6.84	85.04	1.48	1.37	3.88
AuQC@Gliadin-CUR (550 nm)	43.74	2.16	56.26	8.2	1.37	7.17
AuQC@Gliadin (680 nm)	84.74	60.25	59.69	3.29	1.39	59.69
AuQC@Gliadin-CUR (680 nm)	78.78	44.5	21.22	2.68	1.1	43.83

The FTIR analysis was carried out to understand the confirmation changes of protein after incorporation of CUR. Figure 7.5A shows FTIR spectra of (i) AuQC@gliadin (black) (ii) AuQC@gliadin-CUR (blue) and (iii) CUR (red). The secondary structure of gliadin was described by the protein amide I band at 1600–1690 cm^{-1} (due to C-O stretching) and amide II band at 1480–1575 cm^{-1} (C–N stretch coupled with N–H bending mode) (Barth, 2007; "Infrared Spectroscopy of Proteins,"). Non-covalent interactions such as Van-der Waals interactions, hydrophobic interactions, and hydrogen bonds are generally known to lower the energy of the corresponding part of the molecule, reduce the force constants of the bonds, and therefore decrease its absorption frequency (Tang *et al.*, 2002). After interaction with CUR, the peak corresponding to amide I shifted to lower wavenumber from 1633 to 1630 cm^{-1} and the amide II band shifted from 1536 to 1528 cm^{-1}. This shift in wavenumber resulted from the binding of CUR to the protein C═O, C-N, and N-H groups. The N-H stretching frequency of gliadin is decreased from 3280 cm^{-1} to 3278 cm^{-1} due to the interaction of CUR with the N-H groups of the protein (Bourassa *et al.*, 2010). Moreover, the decrease in signal intensity of the amide bands of protein furthermore suggested the changes in the protein conformational states upon interaction with CUR (Bourassa *et al.*, 2010). CUR has its phenolic –OH stretching peak at 3504 cm^{-1} and its other

characteristic bands at 1027/857cm^{-1} (C–O–C stretching), 1275cm^{-1} (aromatic C–O stretching), 1428 cm^{-1} (olefinic C–H bending), 1502 cm^{-1} (C=O and C=C vibrations) and at 1602 cm^{-1} stretching vibrations of benzene ring. These peaks were attenuated in the AuQC@gliadin-CUR spectrum due to the higher band width of protein bands which suggests that CUR is located within the macromolecular protein moiety by van-der Waals forces and hydrophobic interactions.

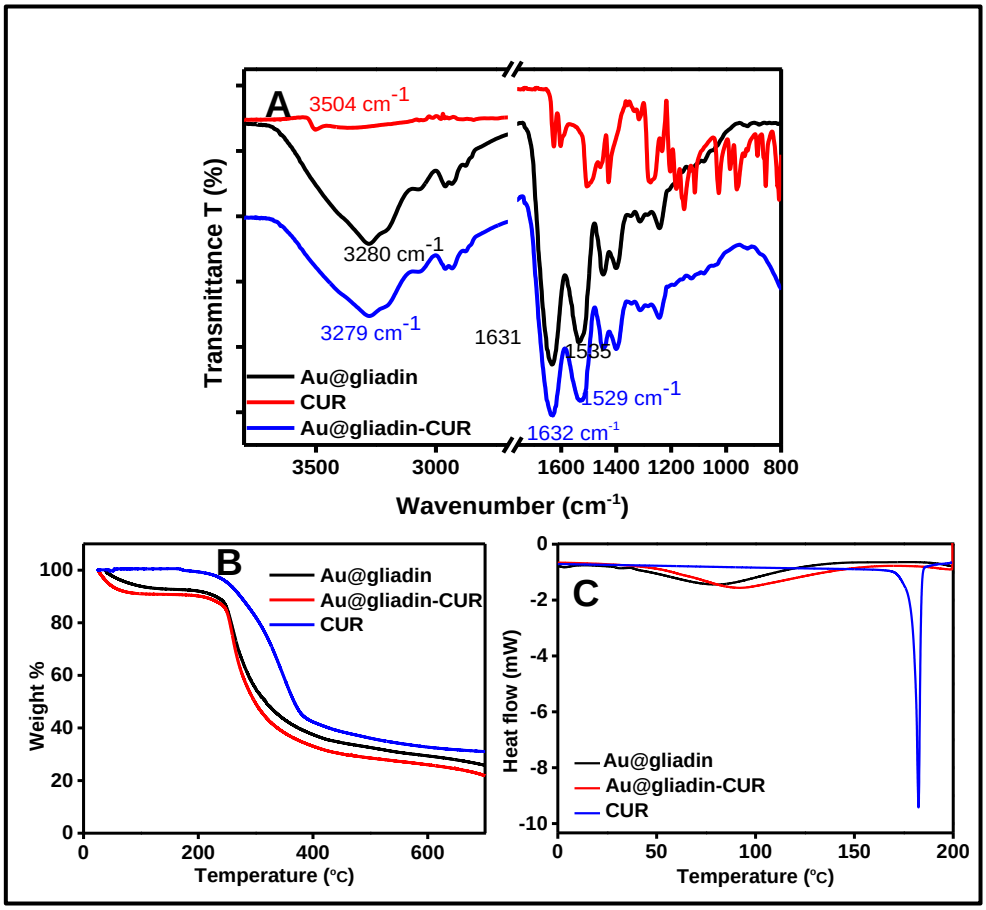

Figure 7.5. (A) FT-IR spectra, (B) TGA and (C)DSC analysis of AuQC@gliadin, CUR, AuQC@gliadin-CUR.

Thermal analysis of AuQC@gliadin, CUR, and AuQC@gliadin-CUR was carried out to understand the changes in the thermal behavior of AuQC@gliadin after incorporation of CUR. Figure 7.5B &C shows the TGA and DSC analysis of AuQC@gliadin, CUR, and AuQC@gliadin-CUR. The Thermo-gravimetric curves of AuQC@gliadin and CUR loaded AuQC demonstrated the first stage weight

loss by the gliadin samples at around 100 °C due to moisture loss at increasing temperature (Khatkar *et al.*, 2013). The second stage weight loss resulted from the decomposition of gliadin at 246 °C in AuQC@gliadin and 249 °C in AuQC@gliadin-CUR. This shift in decomposition temperature is attributed to the incorporation of CUR to AuQC@gliadin and implies the enhanced stability of AuQC@gliadin after CUR incorporation. TGA curve for pure CUR showed rapid weight loss around 260 °C which may be attributed to the decomposition of substituent groups of CUR (Chen., *et al.*, 2014).

The DSC thermograms of AuQC@gliadin showed an endothermic peak at 77 ºC due to the unfolding and denaturisation of protein (Khatkar *et al.*, 2013). The incorporation of CUR increased the thermal stability of gliadin in AuQC since the denaturisation temperature shifted to higher temperature of 92 ºC in the case of AuQC@gliadin-CUR. The DSC of CUR alone shows an endothermic peak at 183 ºC which is corresponding to the melting of CUR (Hu., *et al.*, 2015). The endothermic peak of CUR was absent in the conjugate which confirms the molecular incorporation of CUR in AuQC.

7.3.3. Stability of curcumin

As mentioned earlier CUR has very little solubility in water and is chemically unstable under physiological conditions which is a major issue that concerns its bioavailability (Prasad *et al.*, 2014). It is well known that CUR is highly unstable at physiological pH and undergoes rapid degradation into different products such as bicyclopentadione, vanillin, and ferulic acid (Schneider *et al.*, 2015). It is reported that the binding of CUR to the hydrophobic pockets of protein can greatly improve solubilisation and arrest its degradation (Esmaili *et al.*, 2011; Tapal & Tiku, 2012). In order to investigate the stability/biodegradability of CUR, the changes of the relative intensity of the characteristic absorption maximum of CUR in physiological condition was measured as a function of time (Figure 7.6). The absorption peak at 428 nm of free CUR showed a rapid degradation in PBS solution with only 60 % of CUR remaining after 12 hours of incubation. Whereas in the case of encapsulated CUR

showed remarkable stability under the same condition, with more than 92% of CUR remaining even after 12 hour of incubation (Figure 7.6A). Similarly we have analysed the stability of the encapsulated CUR in different pH conditions. Figure 7.6B shows the absorption spectrum of AuQC@gliadin-CUR at different pH ranging from 5 to 9. Inset shows the photographs of AuQC@gliadin-CUR solution in different buffers. The entrapped CUR is highly stable from pH 5 to 8.6, indicating the protection of CUR from hydrolytic degradation.

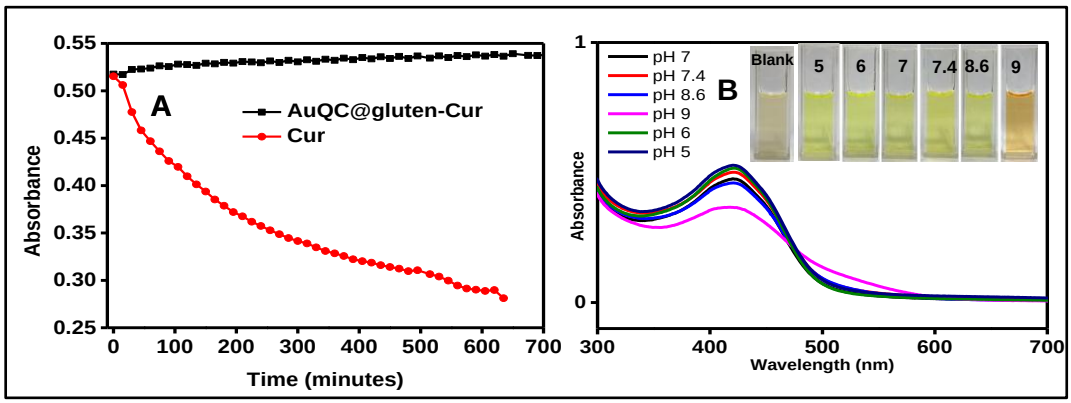

Figure 7.6. (A). Plot showing the stability of AuQC@gliadin-CUR and CUR in aqueous buffer pH 7.4; (B) Absorption spectra indicating the pH stability of AuQC@gliadin-CUR at pH 5, 6, 7, 7.4, 8.6, 9.

At pH 9, slight blue shift of the maximum absorption wavelength with a decrease in absorbance was observed, which is due to the degradation of CUR in more alkaline condition. Thus the hybrid developed in this study shows superior stability over many reported formulations (Jain, 2017; Li., *et al.*, 2017; Manju & Sreenivasan, 2011; Yallapu *et al.*, 2010; Zhang *et al.*, 2011).

7.3.4. In vitro release of CUR from AuQC@gliadin-CUR

Before checking the anti-cancer activity of the drug-loaded quantum cluster, in vitro release kinetics was studied using UV-Vis spectroscopy. The study was carried out with PBS at pH 5 and pH 7.4. The percentage of drug released from AuQC@gliadin-CUR at predetermined time intervals were calculated using the standard curve prepared for CUR. Figure 7.7 shows the in vitro drug release profile of AuQC@gliadin-CUR at pH 5 and pH 7.4. The in vitro

dug release profile shows that CUR release was more at pH 5 compared with at pH 7.4. A sustained release of CUR were observed after the initial burst release and 97.8% of the encapsulated CUR was released at pH 5 within 60 hours. The initial burst release could be due to the attached CUR molecules on the surface of the AuQCs and the sustained release from the entrapped CUR (Anitha *et al.*, 2011). In pH 7.4, the total release was only 35.4% at the same time and the results indicated that the release of CUR was slower at physiological pH than under acidic condition. Since the cancer cells have an acidic extracellular environment, the release of CUR at acidic (pH~5) is more suitable for cancer therapy and non-cancer cells at physiological pH are likely to be least affected by our formulation. The higher release rate CUR at acidic pH could be the conformational changes of gliadin at this pH, which facilitate enhanced CUR release.

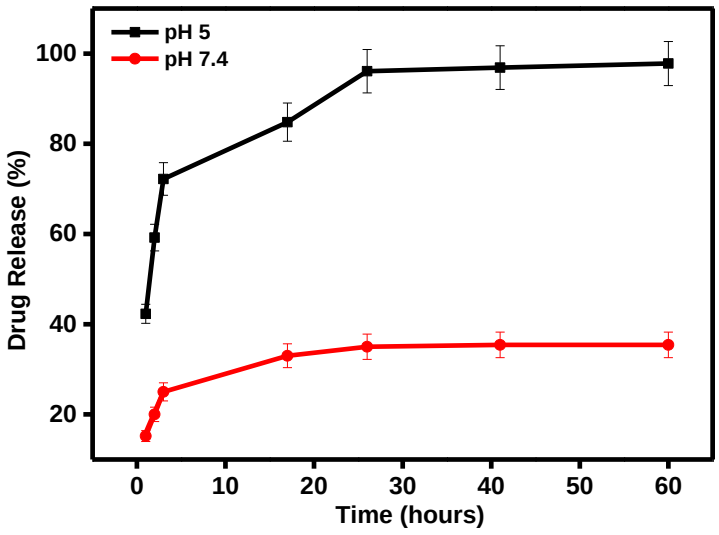

Figure 7.7. Drug release profile showing release percentage of CUR from AuQC@gliadin-CUR over 60 hours at pH 5 and 7.4.

7.3.5. Characterization of folate conjugated AuQC@gliadin-CUR

Folic acid has been conjugated to AuQC@gliadin for targeted delivery of CUR to the cancer cell because the membrane associated FA receptor (FR) is overexpressed in cancer cells but remains at a very low level in most normal

tissues (Meng *et al.*, 2011). FA-AuQC@gliadin-CUR was formed by chemically linking folic acid to the protein via EDC/NHS coupling. The conjugation of FA was confirmed by FTIR spectroscopy and UV-Vis absorption study. Figure 7.8 A & B shows the respective absorption and FT-IR spectra of folic acid (FA) and FA-AuQC@gliadin-CUR. The absorption spectrum of FA-AuQC@gliadin-CUR shows three characteristic peaks at 282 nm, 361 nm and 420 nm. The peaks at 282 nm and 361 nm are accorded with the characteristic absorbance of FA, and the absorbance at 420 nm is originated from CUR. This indicates that FA was successfully conjugated with AuQC@gliadin. Further conjugation of FA towards QC was confirmed by FT-IR spectroscopy. The FT-IR spectra of FA showed characteristic peaks at 3538 cm^{-1} and 3413 cm^{-1} due to the stretching of -OH and –NH of the glutamic acid and pterinic portion, respectively (Sadder El-Leithy *et al.*, 2017). Also, the peak at 1690 cm^{-1} corresponded to the stretching of different –C=O groups and the band at 1604 cm^{-1} resulted from –NH bending (Sadder El-Leithy *et al.*, 2017). Moreover, the band at 1482 cm^{-1} has arisen from the vibration of the pterinic group. On inspecting the spectra of FA-AuQC@gliadin-CUR, the successful conjugation of FA to AuQC@gliadin-CUR was confirmed.

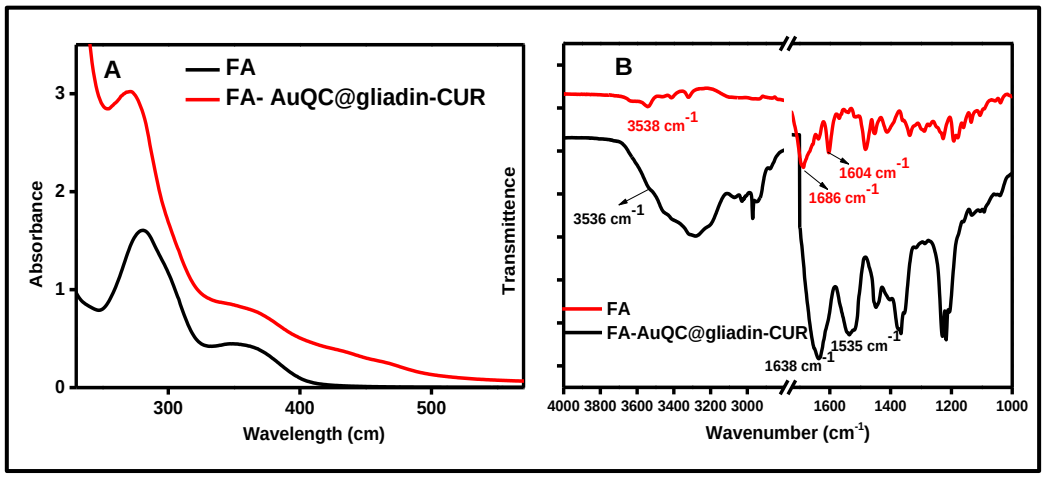

Figure 7.8 (A) Absorption spectra showing Folic acid (FA) and Folic Acid conjugated AuQC@gliadin-CUR (AuQC@gliadin-FA-CUR). (B) FT-IR spectra of (a) Folic acid (FA) and (b) FA conjugated AuQC-CUR.

As evident from Figure 7.8B, the -OH stretching peak of FA at 3538 cm^{-1} and the NH stretching at 3413 cm^{-1} with an increase in intensity could be found in the

FTIR of the FA-AuQC@gliadin-CUR due to the overlapping of these functional groups with those in AuQC@gliadin-CUR. A shift in wavenumber of the amide I group (C−O stretch) from 1630 to 1636 cm^{-1} was observed on conjugation of FA to AuQC@gliadin-CUR. Amide II band of AuQC@gliadin-CUR also showed a shift from 1528 to 1535 cm^{-1} which is attributed to the newly formed C−N bond (Sadder El-Leithy *et al.*, 2017).

7.3.6. In-vitro cytotoxicity to normal and cancer cells

It is necessary to evaluate the toxicity profile of nanoprobe for biomedical applications. To evaluate the cytotoxicity of FA-AuQC@gliadin-CUR we have treated L929 -normal cell line and MDA-MB 231 breast cancer cells to a series of equivalent concentrations of the nanoprobe for 24 hours, and the percentage of viable cells was quantified by the use of MTT assay (Figure 7.9). The results from the MTT assay showed that AuQC@gliadin-FA-CUR exerts a significant concentration dependent cytotoxicity to MDA-MB 231 cells and at the same time it is least toxicity to the normal cell line –L929. This further supports the targeted delivery of CUR to the cancer cell without affecting normal cell and indicate that CUR remains active even after conjugation with AuQC@gliadin.

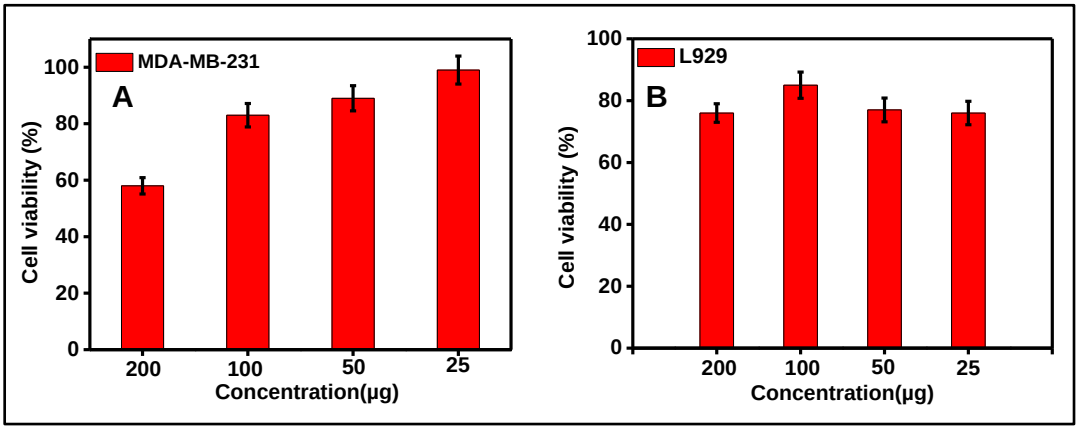

Figure 7.9. Cytotoxicity studies by MTT assay in (A) L929 cell line; (B) MDA-MB-231 cell line.

Herein compared to cancer cells, normal cells are also slightly affected because the immortalized cells cannot sustain continuous treatment for 24 hours

and this could also be a governing factor for the unexpected cell death in these cell lines. Moreover normal cell lines show significant expression of folate receptors and though not over-expressed as these cell lines, there are still distribution of the folate receptors among normal cell lines (Weitman *et al.*, 1992). The least toxicity of L929 cells with that of MDA-MB231 may be attributed to the presence of these folate receptors in the normal cells which on prolonged exposure (24hrs) of FA-AuQC@gliadin-CUR may have facilitated its uptake.

There are several reports on the cytotoxic effects of CUR in several types of cancers and mechanisms by which they act (Cheng *et al.*, 2013; Xu, X. *et al.*, 2015). In C6 cells, CUR is known to reduce the cell survival in a p53- and caspase-independent manner which is an effect correlated with the inhibition of AP-1 and NFB signalling pathways (Dhandapani *et al.*, 2007), whereas in MDA-MB-231 cells, apoptosis is induced through regulation of ROS (Zheng *et al.*, 2012). Thus AuQC@gliadin as a CUR carrier is reassuring to the cancer treatment regime due to its ability to administer CUR without the loss of its medicinal efficacy.

7.3.7. Cellular uptake of FA-AuQC@gliadin-CUR

The in-vitro cellular uptake studies via confocal fluorescent imaging were done after 1st, 2nd and 4th hour of incubation and the images are shown in Figure 7.10, 7.11 and 7.12. On analysing the uptake intensities of all the three cell lines, it is confirmed that maximum uptake was observed in the cancer cells after 4 hours of incubation. It is long known that nanotechnology driven drug delivery systems enhance the delivery to targeted cancer cells by benefitting from the unique vasculature characteristics of tumors (Lei *et al.*, 2011). L929 cells (normal cell line) (Figure 7.12) showed no fluorescence at 4 hours compared to C6 (Figure 7.11) and MDA-MB231(Figure 7.12) (cancer cell lines) suggesting minimal to zero uptake of the formulation by these cells. This makes AuQC@gliadin a felicitous CUR carrier since the undesirable effects of traditional chemotherapeutic agents may be overcome as it augments its availability at the

tumor site alone with least damage on healthy tissues. Also, a gradual increase in the fluorescence intensity was observed with the increase in incubation time (from 1 hour to 4 hours) in cancer cells. The morphological changes in the cells after treatment with the FA-AuQC@gliadin-CUR have been inspected by microscopic observation.

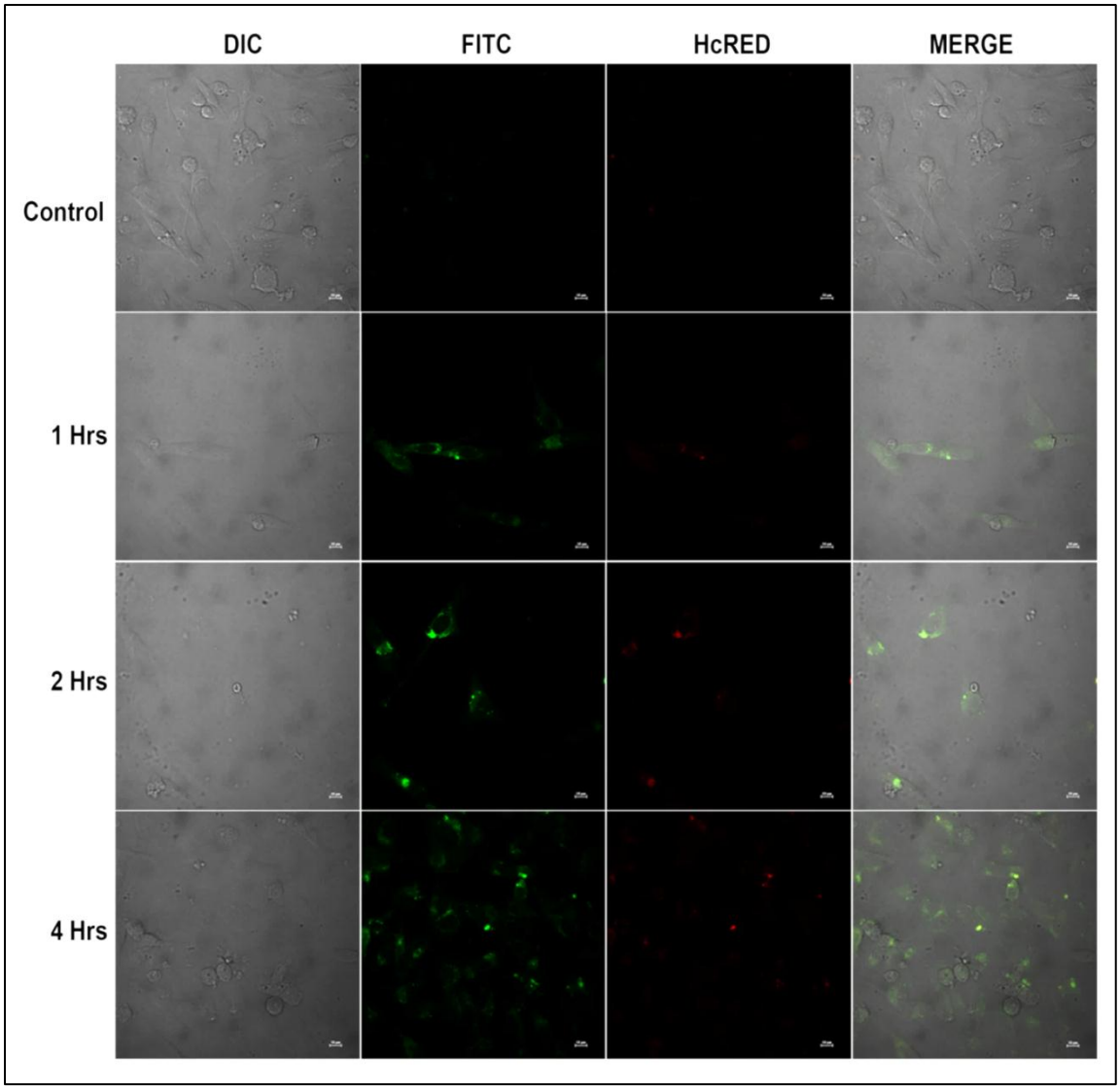

Figure 7.10. The confocal fluorescence images of MDA- MB-231-breast cancer cells treated with AuQC@gliadin-FA-CUR at the 1st, 2nd and 4th hour of incubation.

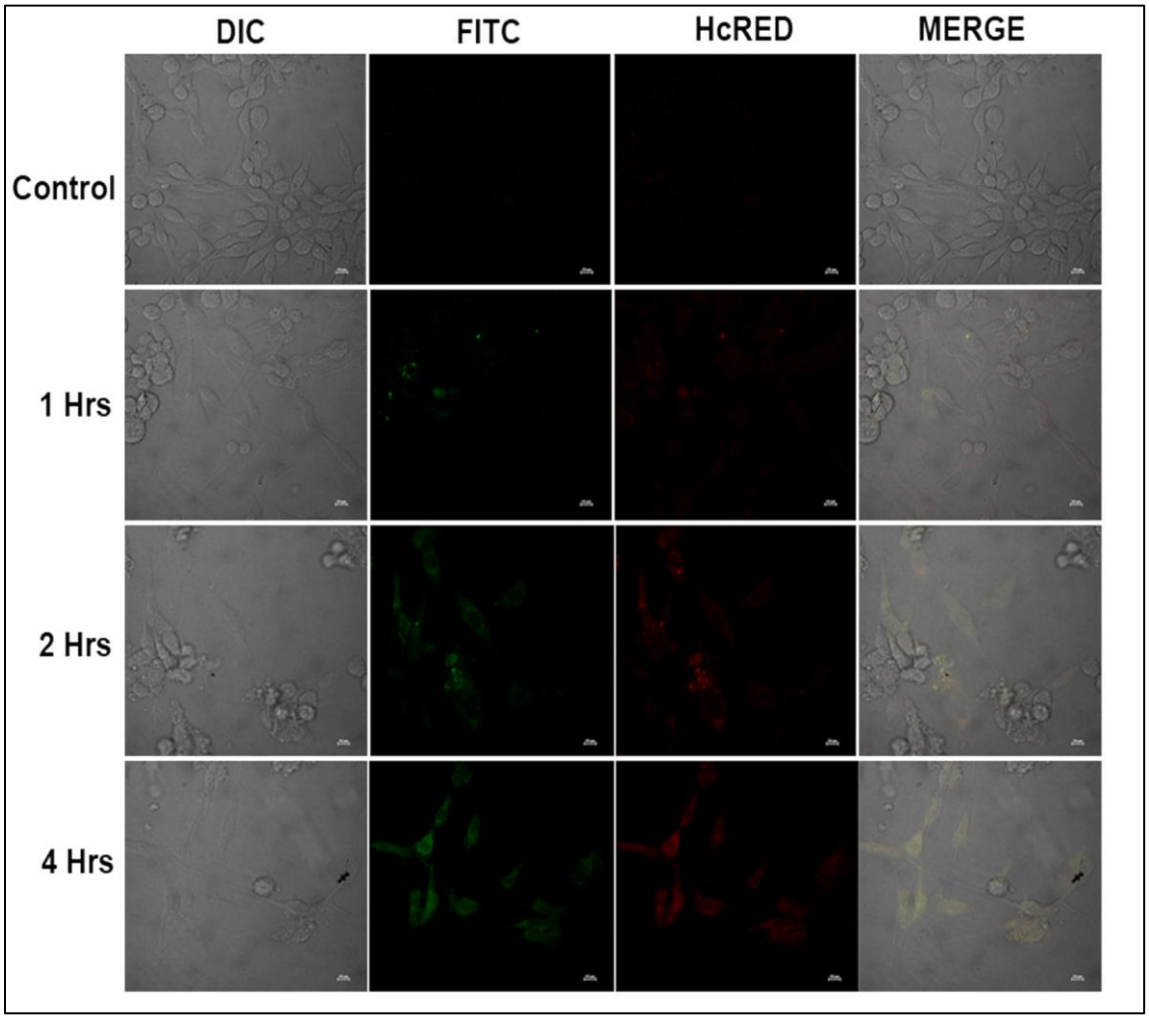

Figure 7.11. The confocal fluorescence images of C6 tumor cells treated with AuQC@gliadin-FA-CUR at the 1st, 2nd and 4th hour of incubation.

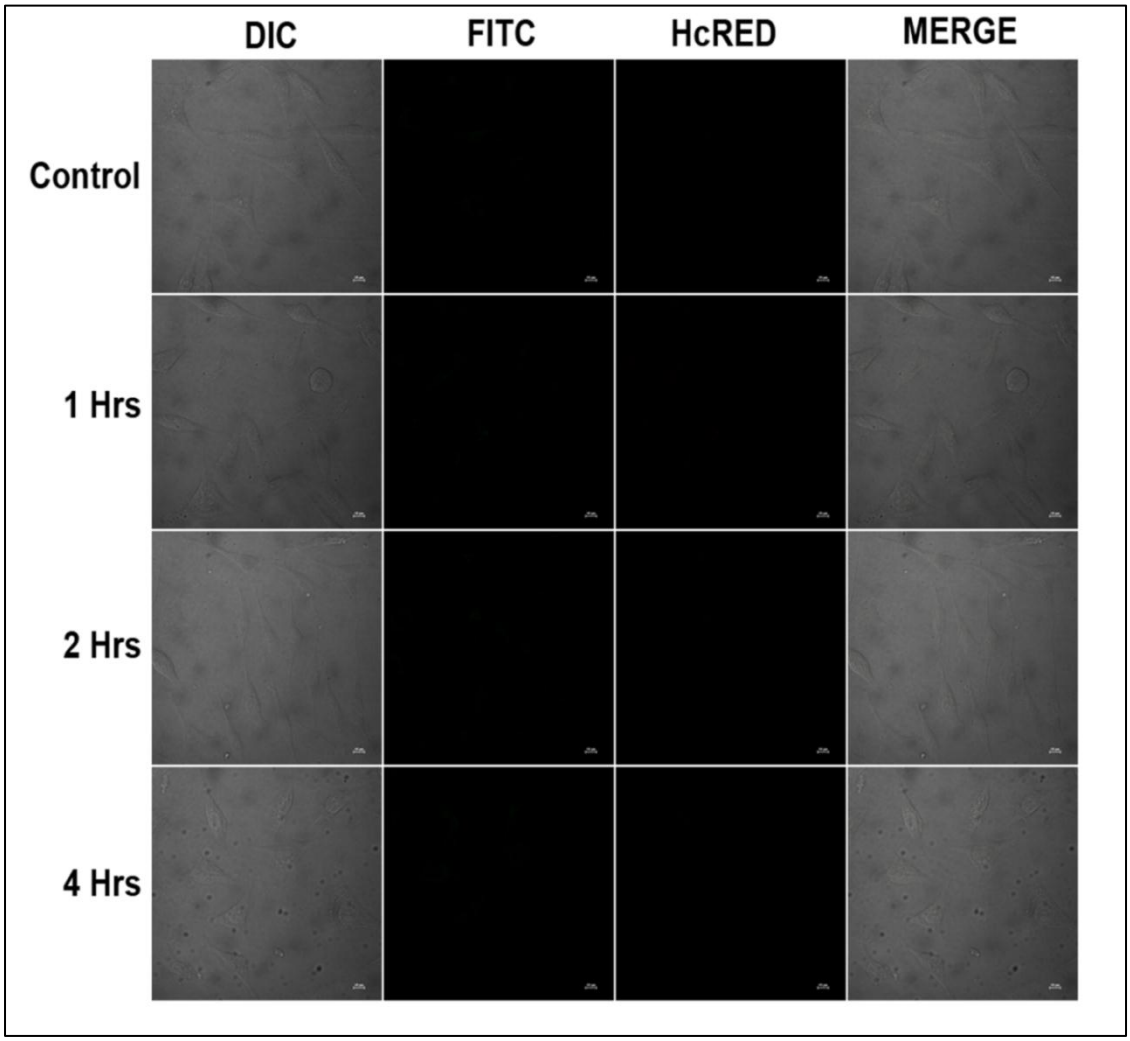

Figure 7.12 The confocal fluorescence images of L929 cells treated with AuQC@gliadin-FA-CUR at the 1st, 2nd and 4th hour of incubation.

Compared to L929 cells, both C6 and MDA-MB231 cells have undergone obvious morphological changes as is evident from Figure 7.10, 7.11 and 7.12. With an increase in incubation time, there was a retraction of cellular processes with appearance of common apoptotic features like cell shrinkage, membrane blebbing, rounding etc. Also, disintegration of the cancer cells was at its peak at 4 hours of incubation and more cells detached from the substratum leaving only a few attached. This confirms the selective toxicity of our conjugate in cancer cell lines.

7.4. Conclusions

We have synthesized gliadin protected gold quantum cluster using a simple, one-pot synthesis strategy and have effectively conjugated CUR to the cluster through instant mixing. Optical and thermal studies, microscopic analysis, encapsulation efficiency, in vitro drug release, cellular uptake and cytotoxicity of the prepared formulation were performed. The encapsulation efficiency of CUR was 98.37± 0.25% and the release study showed 97.8% release of the drug within 60 hours in pH 5. The cellular uptake studies also demonstrated maximum uptake by C6 and MDA-MBA-231 cells and minimum uptake by L929 cells. Poor bioavailability upon oral administration and lack of absorption restricts the therapeutic application of hydrophobic and nearly water insoluble CUR. Despite their phenomenal anti-cancer activity, many pharmaceutical companies refrain from using them as such owing to the fact that they form drug aggregates in highly localized concentrations at the sites of their deposition. This remains tantalizing to the scientific community knowing how active these compounds are toward their molecular targets. CUR, which falls into this category of compounds, is in dire need for a suitable carrier system to overcome these limitations without compromising its activity which AuQC@gliadin is expected to fulfil.

CHAPTER 8
CONCLUSIONS AND FUTURE PERSPECTIVE

8.1. Conclusions

Owing to the ultra-small size, excellent biocompatibility, and intriguing optical properties, noble metal QCs shows significant interest in the biomedical fields like biosensing, imaging, and therapy. Thus precise synthesis of the NMQCs using novel synthetic strategies are highly demanded. The biocompatible metal QCs produced via biological synthesis, particularly template-assisted synthesis are suitable candidates for biolabeling and imaging. Several biomolecules such as amino acids, peptides, enzymes, DNA, and proteins have been used as templates for the synthesis of NMQCs. Among these, protein templated synthesis has received much attention due to its simplicity in preparation, one-pot and green synthetic strategy, good aqueous solubility, relatively low environmental impact, mild reaction conditions, excellent biocompatibility, and versatile surface chemistry. Thus marriage of unique optical and electronic properties of the metal quantum cluster with inherent biological properties of protein make them superior candidates over other conventional nanomaterial used in bio-nanotechnology. However, to achieve the promising applications, there are still a number of issues that have to be further explored:

(1) The cost of the conventional protein used for the synthesis of QC is comparatively high, such as the protein derived from animals (BSA, HSA, Lysozyme etc).
(2) The relatively low QY of the cluster
(3) Low stability of QC in the biological systems. For example degradation of protein under acidic condition, which can reduce the optical properties of QC. Less stability of QC in the presence of reactive oxygen species, which limit the bio-labeling due to oxidative decomposition.

(4) The biological applications could be widened by exploring the use of fluorescent AuQC@Protein in clinical diagnosis.
(5) The immobilization of AuQCs on solid substrates could provide a useful platform and can be used to develop photochemical sensors.

Our work aims to address a few of the aforementioned issues by synthesizing different protein stabilized noble metal QC and also to develop fluorescent sensors and drug delivery vehicles using the synthesized QC@protein.

Chapter 1 summarizes the recent progress in the synthesis of protein stabilized noble metal QC and its formation mechanisms, general characterization, structural investigation, purification, surface functionalization and key applications in the biomedical field. The major application of QCs discussed here are (1) the development of biosensor using the QC like the metal ions sensing, anion sensing, small biomolecule sensing, and bacterial sensing. (2) The biological labeling, imaging and cancer therapy by using QC@protein is also discussed

The development of an enzymatic sensor using protein stabilized AuQCs is discussed in chapter 2. Acetylcholine sensor was developed using Acetylcholinesterase (AChE) conjugated BSA protected Au QC. AChE hydrolyzes acetylcholine (ACh) to choline (Ch) which in turn interacts with AuQC@BSA-AChE and quenches its fluorescence, enabling sensing. The limit of detection of ACh was found to be 10 nM. Real-time analysis of ACh in blood is also demonstrated in this chapter.

Chapter 3 demonstrated a sustainable synthesis of fluorescent gold quantum clusters with a plant protein, gluten, as a protecting and stabilizing ligand. The formation of QC was confirmed by various spectroscopic and microscopic techniques. The AuQC@gluten was further used for the selective turn-on detection of creatinine in the human blood. A detailed investigation was carried out to understand the mechanism for detection. Here picric acid is used as a fluorescent quencher and electron transfer from AuQC@protein to PA leads to fluorescent quenching. Further, the interaction of creatinine block the electron

transfer by forming a creatinine-picrate complex and a concentration-dependent recovery of fluorescence is observed, which enable the sensing.

Preparation of highly stable, intense red emitting gold-silver alloy quantum cluster using gluten as a protecting and stabilizing ligand is discussed in chapter 4. The AgAuQC@gluten was prepared by a galvanic exchange reaction. The optimization of reaction condition and stability of QC was studied. It shows excellent photostability and pH stability and has 9.5 % quantum yield. Further, a bilirubin sensor was also developed using AgAuQC@gluten based on fluorescence quenching strategy. The major reasons for fluorescence quenching are inner filter effect and electron transfer between QC and bilirubin. It shows excellent selectivity towards other biomolecules usually present in blood.

Design of a dual emitting GQD-AuQC (AuQC@GQD) composite for ratiometric sensing of Hg^{2+} is discussed in chapter 5. Herein the first step, blue-green emitting GQD was synthesized by hydrothermal carbonization of gluten. In the second step, the GQD acted as a reducing agent for the formation of AuQC. The resulting composite exhibited dual fluorescence emission at 450 nm and 680 nm which originated from the GQD and AuQCs respectively. Further AuQC@GQD was successfully incorporated into PVA nanofibre by electrospinning method. The resultant fluorescent mat was used for efficient visual detection of Hg^{2+}. Mercury (II) quenches the red emission from AuQC@GQD, whereas the blue-green emission is retained. The mechanism for selective quenching of red fluorescence is the metallophilic interaction assisted electron transfer process between mercury (II) and Au (I).

The process of copper ion release from CuQC@gluten was elaborated in Chapter 6. The blue emitting Cu QC was formed inside gluten by biomineralisation process and the prepared QCs were characterized by spectroscopic and microscopic technique. For the fabrication CuQC-Polymer strip for Cu (II) ion release, the melt mixing of CuQC and polyurethane was done using micro compounding technique. The composite shows a slow and steady release of the copper ions from this composite for 90 days, which can be used for intrauterine device fabrication. Moreover the composite is cytocompatable.

Synthesis of gliadin protected AuQC for the targeted delivery of CUR is discussed in chapter 7. Gliadin stabilized AuQC (AuQC@gliadin) was encapsulated CUR into hydrophobic pockets of protein provide enhanced stability and solubility of CUR at physiological condition. It prevents the intrinsic degradation nature of CUR, which reduce its therapeutic effect. A 98 % encapsulation efficiency is acquired by this method. Folic acid was conjugated to the QC for targeted delivery of CUR. The cytotoxicity study shows least toxicity of the encapsulated CUR to the normal cell and toxicity to the cancer cell. Cellular uptake study indicates noticeable uptake of CUR in the cancer cell. After prolonged incubation, cell damage and shrinkage was observed in the cancel cells, whereas normal cell was least affected.

8.2. Scope for the future work

Although there is a significant understanding about the protein stabilized QCs, the fundamental knowledge about the origin of luminescence of QCs is not well analyzed. Since, the protein stabilized QCs are not crystalized so far, we aim to explore the crystal structure of gluten stabilized QCs and find the origin of luminescence in the nanocluster. In the biomedical application of QCs@protein, most of the application focuses on employing them as a probe for sensing and imaging. Henceforth more focus could be given for therapy of tumor. Owing to the cytocompatability of gliadin stabilized AuQCs, the in vivo study can be done for anti-cancer drug delivery. In addition, it is necessary to know how these proteins together with clusters are going to interact with the biological environment and what would be the intracellular fate of the untaken clusters.

In addition to biomedical applications, the application of QC in the field of opto-electronics and energy harvesting is yet to be explored.

REFERENCES

1. Anitha, A., Deepagan, V.G., Divya Rani, V.V., Menon, D., Nair, S.V., & Jayakumar, R. (2011). Preparation, characterization, in vitro drug release and biological studies of curcumin loaded dextran sulphate–chitosan nanoparticles. Carbohydrate Polymers, 84(3), 1158-1164.
2. Anitha, A., Maya, S., Deepa, N., Chennazhi, K.P., Nair, S.V., & Jayakumar, R. (2012). Curcumin-Loaded N,O-Carboxymethyl Chitosan Nanoparticles for Cancer Drug Delivery. Journal of Biomaterials Science, Polymer Edition, 23(11), 1381-1400.
3. Archana, R., Sonali, S., Deepthy, M., Prasanth, R., Habeeb, M., Thalappil, P., Shantikumar, N., & Manzoor, K. (2010). Molecular-receptor-specific, non-toxic, near-infrared-emitting Au cluster-protein nanoconjugates for targeted cancer imaging. Nanotechnology, 21(5), 055103.
4. Bacon, M., Bradley, S.J., & Nann, T. (2014). Graphene quantum dots. Particle & Particle Systems Characterization, 31(4), 415-428.
5. Baksi, A., Mitra, A., Mohanty, J.S., Lee, H., De, G., & Pradeep, T. (2015). Size Evolution of Protein-Protected Gold Clusters in Solution: A Combined SAXS–MS Investigation. The Journal of Physical Chemistry C, 119(4), 2148-2157.
6. Baksi, A., Xavier, P.L., Chaudhari, K., Goswami, N., Pal, S.K., & Pradeep, T. (2013). Protein-encapsulated gold cluster aggregates: the case of lysozyme. [10.1039/C2NR33180B]. Nanoscale, 5(5), 2009-2016.
7. Banerjee, C., Maiti, S., Mustafi, M., Kuchlyan, J., Banik, D., Kundu, N., Dhara, D., & Sarkar, N. (2014). Effect of Encapsulation of Curcumin in Polymeric Nanoparticles: How Efficient to Control ESIPT Process? Langmuir, 30(36), 10834-10844.
8. Bansal, S.S., Goel, M., Aqil, F., Vadhanam, M.V., & Gupta, R.C. (2011). Advanced Drug-Delivery Systems of Curcumin for Cancer Chemoprevention. Cancer prevention research (Philadelphia, Pa.), 4(8), 1158-1171.

9. Barcaro, G., Sementa, L., Fortunelli, A., & Stener, M. (2015). Optical properties of nanoalloys. [10.1039/C5CP00498E]. Physical Chemistry Chemical Physics, 17(42), 27952-27967.
10. Barik, A., Priyadarsini, K.I., & Mohan, H. (2003). Photophysical studies on binding of curcumin to bovine serum albumins. Photochem Photobiol, 77(6), 597-603.
11. Barman, M.K., Paramanik, B., Bain, D., & Patra, A. (2016). Light Harvesting and White- Light Generation in a Composite of Carbon Dots and Dye- Encapsulated BSA- Protein- Capped Gold Nanoclusters. Chemistry-A European Journal, 22(33), 11699-11705.
12. Barsoum, B.N., Watson, W.M., Mahdi, I.M., & Khalid, E. (2004). Electrometric assay for the determination of acetylcholine using a sensitive sensor based on carbon paste. Journal of Electroanalytical Chemistry, 567(2), 277-281.
13. Barth, A. (2007). Infrared spectroscopy of proteins. Biochimica et Biophysica Acta (BBA) - Bioenergetics, 1767(9), 1073-1101.
14. Basu, S., Sahoo, A.K., Paul, A., & Chattopadhyay, A. (2016). Thumb Imprint Based Detection of Hyperbilirubinemia Using Luminescent Gold Nanoclusters. Scientific reports, 39005, 6.
15. Bhandari, S., Pramanik, S., Khandelia, R., & Chattopadhyay, A. (2016). Gold nanocluster and quantum dot complex in protein for biofriendly white-light-emitting material. ACS Applied Materials & Interfaces, 8(3), 1600-1605.
16. Bhattacharyya, K., & Mukherjee, S. (2018). Fluorescent Metal Nano-Clusters as Next Generation Fluorescent Probes for Cell Imaging and Drug Delivery. Bulletin of the Chemical Society of Japan, 91(3), 447-454.
17. Bietz, J., & Wall, J. (1972). Wheat gluten subunits: Molecular weights determined by sodium dodecyl sulfate-polyacrylamide gel electrophoresis. Cereal Chem, 49(4), 416-430.
18. Bisht, S., Feldmann, G., Soni, S., Ravi, R., Karikar, C., Maitra, A., & Maitra, A. (2007). Polymeric nanoparticle-encapsulated curcumin

("nanocurcumin"): a novel strategy for human cancer therapy. J Nanobiotechnology, 5, 3.

19. Blokland, A. (1995). Acetylcholine: a neurotransmitter for learning and memory? Brain Research Reviews, 21(3), 285-300.
20. Bothra, S., Babu, L.T., Paira, P., Ashok Kumar, S., Kumar, R., & Sahoo, S.K. (2018). A biomimetic approach to conjugate vitamin B6 cofactor with the lysozyme cocooned fluorescent AuNCs and its application in turn-on sensing of zinc(II) in environmental and biological samples, Analytical and Bioanalytical Chemistry, 410(1), 201-210.
21. Bourassa, P., Kanakis, C.D., Tarantilis, P., Pollissiou, M.G., & Tajmir-Riahi, H.A. (2010). Resveratrol, genistein, and curcumin bind bovine serum albumin. J Phys Chem B, 114(9), 3348-3354.
22. Burke A., Hasirci N. (2004) Polyurethanes in Biomedical Applications. In: Hasirci N., Hasirci V. (eds) *Biomaterials. Advances in Experimental Medicine and Biology*, vol 553. Springer, Boston, MA
23. Cai, S., Xia, X., Zhu, C., & Xie, C. (2007). Cupric ion release controlled by copper/low- density polyethylene nanocomposite in simulated uterine solution. Journal of Biomedical Materials Research Part B: Applied Biomaterials, 80(1), 220-225.
24. Cantelli, A., Battistelli, G., Guidetti, G., Manzi, J., Di Giosia, M., & Montalti, M. (2016). Luminescent gold nanoclusters as biocompatible probes for optical imaging and theranostics. Dyes and Pigments, 135, 64-79.
25. Cao, H., Chen, Z., Zheng, H., & Huang, Y. (2014). Copper nanoclusters as a highly sensitive and selective fluorescence sensor for ferric ions in serum and living cells by imaging. Biosensors and Bioelectronics, 62, 189-195.
26. Cao, X.-L., Li, H.-W., Yue, Y., & Wu, Y. (2013). pH-Induced conformational changes of BSA in fluorescent AuNCs@ BSA and its effects on NCs emission. Vibrational Spectroscopy, 65, 186-192.
27. Cao, X.-L., Luo, Y.-N., Lian, L.-L., Wu, Y.-Q., & Lou, D.-W. (2015). Selective Detection of Iodine/Iodide Using BSA-stabilized Gold

Nanoclusters-based Fluorescence Probe. Chemistry Letters, 44(10), 1392-1394.

28. Cathcart, N., & Kitaev, V. (2010). Silver Nanoclusters: Single-Stage Scaleable Synthesis of Monodisperse Species and Their Chirooptical Properties. The Journal of Physical Chemistry C, 114(38), 16010-16017.
29. Chai, F., Wang, T., Li, L., Liu, H., Zhang, L., Su, Z., & Wang, C. (2010). Fluorescent Gold Nanoprobes for the Sensitive and Selective Detection for Hg2+. Nanoscale Res. Lett., 5(11), 1856-1860.
30. Chakraborty, I., & Pradeep, T. (2017). Atomically Precise Clusters of Noble Metals: Emerging Link between Atoms and Nanoparticles. Chemical Reviews, 117(12), 8208-8271
31. Chan, P.-H., & Chen, Y.-C. (2012a). Human Serum Albumin Stabilized Gold Nanoclusters as Selective Luminescent Probes for Staphylococcus aureus and Methicillin-Resistant Staphylococcus aureus. Analytical Chemistry, 84(21), 8952-8956.
32. Chan, W.C., Maxwell, D.J., Gao, X., Bailey, R.E., Han, M., & Nie, S. (2002). Luminescent quantum dots for multiplexed biological detection and imaging. Current opinion in biotechnology, 13(1), 40-46.
33. Chang, H.-C., & Ho, J.-a.A. (2015). Gold Nanocluster-Assisted Fluorescent Detection for Hydrogen Peroxide and Cholesterol Based on the Inner Filter Effect of Gold Nanoparticles. Analytical Chemistry, 87(20), 10362-10367.
34. Chattoraj, S., Amin, A., Jana, B., Mohapatra, S., Ghosh, S., & Bhattacharyya, K. (2016). Selective Killing of Breast Cancer Cells by Doxorubicin-Loaded Fluorescent Gold Nanoclusters: Confocal Microscopy and FRET. ChemPhysChem, 17(2), 253-259.
35. Chattoraj, S., & Bhattacharyya, K. (2014). Fluorescent Gold Nanocluster Inside a Live Breast Cell: Etching and Higher Uptake in Cancer Cell. The Journal of Physical Chemistry C, 118(38), 22339-22346.
36. Chaudhari, K., Xavier, P.L., & Pradeep, T. (2011). Understanding the Evolution of Luminescent Gold Quantum Clusters in Protein Templates. ACS Nano, 5(11), 8816-8827.

37. Chen, C.-H., & Lin, M.S. (2012). A novel structural specific creatinine sensing scheme for the determination of the urine creatinine. Biosensors and Bioelectronics, 31(1), 90-94.
38. Chen, H., Li, B., Ren, X., Li, S., Ma, Y., Cui, S., & Gu, Y. (2012). Multifunctional near-infrared-emitting nano-conjugates based on gold clusters for tumor imaging and therapy. Biomaterials, 33(33), 8461-8476.
39. Chen, H., Li, S., Li, B., Ren, X., Li, S., Mahounga, D.M., Cui, S., Gu, Y., & Achilefu, S. (2012). Folate-modified gold nanoclusters as near-infrared fluorescent probes for tumor imaging and therapy. Nanoscale, 4(19), 6050-6064.
40. Chen, L.-Y., Wang, C.-W., Yuan, Z., & Chang, H.-T. (2014). Fluorescent Gold Nanoclusters: Recent Advances in Sensing and Imaging. Analytical Chemistry, 87(1), 216-229.
41. Chen, P.-C., Periasamy, A.P., Harroun, S.G., Wu, W.-P., & Chang, H.-T. (2016). Photoluminescence sensing systems based on copper, gold and silver nanomaterials. Coordination Chemistry Reviews, 320-321, 129-138.
42. Chen, T.-H., & Tseng, W.-L. (2012). (Lysozyme Type VI)-Stabilized Au8 Clusters: Synthesis Mechanism and Application for Sensing of Glutathione in a Single Drop of Blood. Small, 8(12), 1912-1919.
43. Chen, T., Hu, Y., Cen, Y., Chu, X., & Lu, Y. (2013). A dual-emission fluorescent nanocomplex of gold-cluster-decorated silica particles for live cell imaging of highly reactive oxygen species. Journal of the American Chemical Society, 135(31), 11595-11602.
44. Chen, T., Xu, S., Zhao, T., Zhu, L., Wei, D., Li, Y., Zhang, H., & Zhao, C. (2012). Gold Nanocluster-Conjugated Amphiphilic Block Copolymer for Tumor-Targeted Drug Delivery. ACS Applied Materials & Interfaces, 4(11), 5766-5774.
45. Chen, Y., Wang, Y., Wang, C., Li, W., Zhou, H., Jiao, H., Lin, Q., & Yu, C. (2013). Papain-directed synthesis of luminescent gold nanoclusters and the sensitive detection of Cu2+. J. Colloid Interface Sci., 396(0), 63-68.

46. Chen, Z., Qian, S., Chen, X., Gao, W., & Lin, Y. (2012). Protein-templated gold nanoclusters as fluorescence probes for the detection of methotrexate. Analyst, 137(18), 4356-4361.
47. Chen, Z., Ren, X., Meng, X., Chen, D., Yan, C., Ren, J., Yuan, Y., & Tang, F. (2011). Optical detection of choline and acetylcholine based on H2O2-sensitive quantum dots. Biosensors and Bioelectronics, 28(1), 50-55.
48. Chen, Z., Xia, Y., Liao, S., Huang, Y., Li, Y., He, Y., Tong, Z., & Li, B. (2014). Thermal degradation kinetics study of curcumin with nonlinear methods. Food Chemistry, 155, 81-86.
49. Cheng, K.-W., Wong, C.C., Mattheolabakis, G., Xie, G., Huang, L., & Rigas, B. (2013). Curcumin enhances the lung cancer chemopreventive efficacy of phospho-sulindac by improving its pharmacokinetics. International Journal of Oncology, 43(3), 895-902.
50. Cheng, L., Wang, C., Feng, L., Yang, K., & Liu, Z. (2014). Functional Nanomaterials for Phototherapies of Cancer. Chemical Reviews, 114(21), 10869-10939.
51. Chevrier, D.M., Chatt, A., & Zhang, P. (2012). Properties and applications of protein-stabilized fluorescent gold nanoclusters: short review. J. Nanophoton., 6(1), 064504-064516.
52. Chevrier, D.M., Thanthirige, V.D., Luo, Z., Driscoll, S., Cho, P., MacDonald, M.A., Yao, Q., Guda, R., Xie, J., Johnson, E.R., Chatt, A., Zheng, N., & Zhang, P. (2018). Structure and formation of highly luminescent protein-stabilized gold clusters. Chemical Science, 9(10), 2782-2790.
53. Cioffi, N., Torsi, L., Ditaranto, N., Tantillo, G., Ghibelli, L., Sabbatini, L., Bleve-Zacheo, T., D'Alessio, M., Zambonin, P.G., & Traversa, E. (2005). Copper Nanoparticle/Polymer Composites with Antifungal and Bacteriostatic Properties. Chemistry of Materials, 17(21), 5255-5262.
54. Cui, H.-D., Hu, D.-H., Zhang, J.-N., Gao, G.-H., Zheng, C.-F., Gong, P., Xi, X.-H., Sheng, Z.-H., & Cai, L.-T. (2017). Theranostic gold cluster

nanoassembly for simultaneous enhanced cancer imaging and photodynamic therapy. Chinese Chemical Letters, 28(7), 1391-1398.

55. Cui, J., Liu, T., Liang, D., Liu, J., Zhang, K., Yang, B., & Ning, Y. (2017). A novel dual-emission QDs/PCDs assembled composite nanoparticle for high sensitive visual detection of Hg 2+. RSC Advances, 7(78), 49330-49336.
56. Cui, M., Zhao, Y., & Song, Q. (2014). Synthesis, optical properties and applications of ultra-small luminescent gold nanoclusters. TrAC Trends in Analytical Chemistry, 57, 73-82.
57. Dawson, W.R., & Windsor, M.W. (1968). Fluorescence yields of aromatic compounds. The Journal of Physical Chemistry, 72(9), 3251-3260.
58. Day, L., Augustin, M., Batey, I., & Wrigley, C. (2006). Wheat-gluten uses and industry needs. Trends in Food Science & Technology, 17(2), 82-90.
59. Dayan, A., & Paine, A. (2001). Mechanisms of chromium toxicity, carcinogenicity and allergenicity: review of the literature from 1985 to 2000. Human & experimental toxicology, 20(9), 439-451.
60. de Araújo, W.R., Salles, M.O., & Paixão, T.R. (2012). Development of an enzymeless electroanalytical method for the indirect detection of creatinine in urine samples. Sensors and Actuators B: Chemical, 173, 847-851.
61. Debus, B., Kirsanov, D., Yaroshenko, I., Sidorova, A., Piven, A., & Legin, A. (2015). Two low-cost digital camera-based platforms for quantitative creatinine analysis in urine. Analytica Chimica Acta, 895, 71-79.
62. Dhandapani, K.M., Mahesh, V.B., & Brann, D.W. (2007). Curcumin suppresses growth and chemoresistance of human glioblastoma cells via AP-1 and NFkappaB transcription factors. J Neurochem, 102(2), 522-538.
63. Ding, H., Yang, D., Zhao, C., Song, Z., Liu, P., Wang, Y., Chen, Z., & Shen, J. (2015). Protein–Gold Hybrid Nanocubes for Cell Imaging and Drug Delivery. ACS Applied Materials & Interfaces, 7(8), 4713-4719.
64. Dobbelstein, M., & Moll, U. (2014). Targeting tumour-supportive cellular machineries in anticancer drug development. Nat Rev Drug Discov, 13(3), 179-196.

65. Dong, Y., Chen, Y., You, X., Lin, W., Lu, C.-H., Yang, H.-H., & Chi, Y. (2017). High photoluminescent carbon based dots with tunable emission color from orange to green. Nanoscale, 9(3), 1028-1032.
66. Du, J., Jiang, L., Shao, Q., Liu, X., Marks, R.S., Ma, J., & Chen, X. (2013). Colorimetric detection of mercury ions based on plasmonic nanoparticles. Small, 9(9- 10), 1467-1481.
67. Du, Y., Li, X., Lv, X., & Jia, Q. (2017). Highly Sensitive and Selective Sensing of Free Bilirubin Using Metal–Organic Frameworks-Based Energy Transfer Process. ACS Applied Materials & Interfaces, 9(36), 30925-30932.
68. Durgadas, C.V., Sharma, C.P., & Sreenivasan, K. (2011). Fluorescent gold clusters as nanosensors for copper ions in live cells. [10.1039/C0AN00424C]. Analyst, 136(5), 933-940.
69. Dutta, D., Chattopadhyay, A., & Ghosh, S.S. (2016). Cationic BSA Templated Au–Ag Bimetallic Nanoclusters As a Theranostic Gene Delivery Vector for HeLa Cancer Cells. ACS Biomaterials Science & Engineering, 2(11), 2090-2098.
70. Dwivedi, N., Kumar, S., Carey, J.D., & Dhand, C. (2015). Functional Nanomaterials for Electronics, Optoelectronics, and Bioelectronics. Journal of Nanomaterials, 2015, 2.
71. Ellairaja, S., Shenbagavalli, K., Ponmariappan, S., & Vasantha, V.S. (2017). A green and facile approach for synthesizing imine to develop optical biosensor for wide range detection of bilirubin in human biofluids. Biosensors and Bioelectronics, 91, 82-88.
72. Epifani, M., De, G., Licciulli, A., & Vasanelli, L. (2001). Preparation of uniformly dispersed copper nanocluster doped silica glasses by the sol–gel process. Journal of Materials Chemistry, 11(12), 3326-3332.
73. Esmaili, M., Ghaffari, S.M., Moosavi-Movahedi, Z., Atri, M.S., Sharifizadeh, A., Farhadi, M., Yousefi, R., Chobert, J.-M., Haertlé, T., & Moosavi-Movahedi, A.A. (2011). Beta casein-micelle as a nano vehicle for solubility enhancement of curcumin; food industry application. LWT - Food Science and Technology, 44(10), 2166-2172.

74. Fang, Q., Dong, Y., Chen, Y., Lu, C.-H., Chi, Y., Yang, H.-H., & Yu, T. (2017). Luminescence origin of carbon based dots obtained from citric acid and amino group-containing molecules. Carbon, 118, 319-326.
75. Fevery, J. (2008). Bilirubin in clinical practice: a review. Liver International, 28(5), 592-605. doi: doi:10.1111/j.1478-3231.2008.01716.x
76. Ganguly, M., Jana, J., Pal, A., & Pal, T. (2016). Synergism of gold and silver invites enhanced fluorescence for practical applications. RSC Advances, 6(21), 17683-17703.
77. Gangwar, R.K., Dhumale, V.A., Kumari, D., Nakate, U.T., Gosavi, S.W., Sharma, R.B., Kale, S.N., & Datar, S. (2012). Conjugation of curcumin with PVP capped gold nanoparticles for improving bioavailability. Materials Science and Engineering: C, 32(8), 2659-2663.
78. Gao, Z., Liu, F., Hu, R., Zhao, M., & Shao, N. (2016). Lysozyme-stabilized Ag nanoclusters: synthesis of different compositions and fluorescent responses to sulfide ions with distinct modes. RSC Advances, 6(70), 66233-66241.
79. George, A., Shibu, E.S., Maliyekkal, S.M., Bootharaju, M.S., & Pradeep, T. (2012). Luminescent, Freestanding Composite Films of Au15 for Specific Metal Ion Sensing. ACS Applied Materials & Interfaces, 4(2), 639-644.
80. Ghosh, A., Jeseentharani, V., Ganayee, M.A., Hemalatha, R.G., Chaudhari, K., Vijayan, C., & Pradeep, T. (2014). Approaching Sensitivity of Tens of Ions Using Atomically Precise Cluster–Nanofiber Composites. Analytical Chemistry, 86(22), 10996-11001.
81. Ghosh, M., Singh, A.T.K., Xu, W., Sulchek, T., Gordon, L.I., & Ryan, R.O. (2011). Curcumin nanodisks: formulation and characterization. Nanomedicine : nanotechnology, biology, and medicine, 7(2), 162-167.
82. Goswami, N., Giri, A., Bootharaju, M., Xavier, P.L., Pradeep, T., & Pal, S.K. (2011). Copper quantum clusters in protein matrix: potential sensor of Pb2+ ion. Analytical Chemistry, 83(24), 9676-9680.
83. Goswami, N., Zheng, K., & Xie, J. (2014a). Bio-NCs - the marriage of ultrasmall metal nanoclusters with biomolecules. Nanoscale.

84. Goswami, N., Zheng, K., & Xie, J. (2014b). Bio-NCs - the marriage of ultrasmall metal nanoclusters with biomolecules. [10.1039/C4NR04561K]. Nanoscale, 6(22), 13328-13347.
85. Govindaraju, S., Ankireddy, S.R., Viswanath, B., Kim, J., & Yun, K. (2017). Fluorescent Gold Nanoclusters for Selective Detection of Dopamine in Cerebrospinal fluid. Scientific reports, 7, 40298.
86. Govindaraju, S., Rengaraj, A., Arivazhagan, R., Huh, Y.-S., & Yun, K. (2018). Curcumin-Conjugated Gold Clusters for Bioimaging and Anticancer Applications. Bioconjugate Chemistry, 29(2), 363-370.
87. Guan, G., Zhang, S.-Y., Cai, Y., Liu, S., Bharathi, M.S., Low, M., Yu, Y., Xie, J., Zheng, Y., Zhang, Y.-W., & Han, M.-Y. (2014). Convenient purification of gold clusters by co-precipitation for improved sensing of hydrogen peroxide, mercury ions and pesticides. [10.1039/C4CC02008A]. Chemical Communications, 50(43), 5703-5705
88. Gui, R., & Jin, H. (2013). Aqueous synthesis of human serum albumin-stabilized fluorescent Au/Ag core/shell nanocrystals for highly sensitive and selective sensing of copper(ii). [10.1039/C3AN01397A]. Analyst, 138(23), 7197-7205.
89. Guo, C., & Irudayaraj, J. (2011). Fluorescent Ag clusters via a protein-directed approach as a Hg(II) ion sensor. Anal. Chem., 83(8), 2883-2889.
90. Guo, Y., Cao, F., Lei, X., Mang, L., Cheng, S., & Song, J. (2016). Fluorescent copper nanoparticles: recent advances in synthesis and applications for sensing metal ions. Nanoscale, 8(9), 4852-4863.
91. Habeeb Muhammed, M.A., Verma, P.K., Pal, S.K., Retnakumari, A., Koyakutty, M., Nair, S., & Pradeep, T. (2010). Luminescent Quantum Clusters of Gold in Bulk by Albumin-Induced Core Etching of Nanoparticles: Metal Ion Sensing, Metal-Enhanced Luminescence, and Biolabeling. Chem. - Eur. J., 16(33), 10103-10112.
92. Halawa, M.I., Gao, W., Saqib, M., Kitte, S.A., Wu, F., & Xu, G. (2017). Sensitive detection of alkaline phosphatase by switching on gold nanoclusters fluorescence quenched by pyridoxal phosphate. Biosensors and Bioelectronics, 95, 8-14.

93. Hanif, S., John, P., Gao, W., Saqib, M., Qi, L., & Xu, G. (2016). Chemiluminescence of creatinine/H2O2/Co2+ and its application for selective creatinine detection. Biosensors and Bioelectronics, 75, 347-351.
94. Hatai, J., Pal, S., Jose, G.P., & Bandyopadhyay, S. (2012). Histidine Based Fluorescence Sensor Detects Hg2+ in Solution, Paper Strips, and in Cells. Inorganic Chemistry, 51(19), 10129-10135
95. Hatcher, H., Planalp, R., Cho, J., Torti, F.M., & Torti, S.V. (2008). Curcumin: From ancient medicine to current clinical trials. Cellular and molecular life sciences : CMLS, 65(11), 1631-1652.
96. Haveli, S.D., Walter, P., Patriarche, G., Ayache, J., Castaing, J., Van Elslande, E., Tsoucaris, G., Wang, P.-A., & Kagan, H.B. (2012). Hair Fiber as a Nanoreactor in Controlled Synthesis of Fluorescent Gold Nanoparticles. Nano Letters, 12(12), 6212-6217.
97. He, S.-B., Wu, G.-W., Deng, H.-H., Liu, A.-L., Lin, X.-H., Xia, X.-H., & Chen, W. (2014). Choline and acetylcholine detection based on peroxidase-like activity and protein antifouling property of platinum nanoparticles in bovine serum albumin scaffold. Biosens. Bioelectron., 62(0), 331-336.
98. He, Y., Zhang, X., & Yu, H. (2015). Gold nanoparticles-based colorimetric and visual creatinine assay. Microchimica Acta, 182(11-12), 2037-2043.
99. Hemmateenejad, B., Shakerizadeh-shirazi, F., & Samari, F. (2014). BSA-modified gold nanoclusters for sensing of folic acid. Sensors and Actuators B: Chemical, 199, 42-46.
100. Hewlings, S.J., & Kalman, D.S. (2017). Curcumin: A Review of Its' Effects on Human Health. Foods, 6(10), 92.
101. Hopkins, P.N., Wu, L.L., Hunt, S.C., James, B.C., Vincent, G.M., & Williams, R.R. (1996). Higher serum bilirubin is associated with decreased risk for early familial coronary artery disease. Arteriosclerosis, Thrombosis, and Vascular Biology, 16(2), 250-255.
102. Hou, S., Ou, Z., Chen, Q., & Wu, B. (2012). Amperometric acetylcholine biosensor based on self-assembly of gold nanoparticles and acetylcholinesterase on the sol–gel/multi-walled carbon nanotubes/choline

oxidase composite-modified platinum electrode. Biosensors and Bioelectronics, 33(1), 44-49.

103. Housman, G., Byler, S., Heerboth, S., Lapinska, K., Longacre, M., Snyder, N., & Sarkar, S. (2014). Drug resistance in cancer: an overview. Cancers (Basel), 6(3), 1769-1792.

104. Hu, D.-H., Sheng, Z.-H., Zhang, P.-F., Yang, D.-Z., Liu, S.-H., Gong, P., Gao, D.-Y., Fang, S.-T., Ma, Y.-F., & Cai, L.-T. (2013a). Hybrid gold-gadolinium nanoclusters for tumor-targeted NIRF/CT/MRI triple-modal imaging in vivo. [10.1039/C2NR33543C]. Nanoscale, 5(4), 1624-1628.

105. Hu, D.-H., Sheng, Z.-H., Zhang, P.-F., Yang, D.-Z., Liu, S.-H., Gong, P., Gao, D.-Y., Fang, S.-T., Ma, Y.-F., & Cai, L.-T. (2013b). Hybrid gold–gadolinium nanoclusters for tumor-targeted NIRF/CT/MRI triple-modal imaging in vivo. [10.1039/C2NR33543C]. Nanoscale, 5(4), 1624-1628.

106. Hu, D., Sheng, Z., Gong, P., Zhang, P., & Cai, L. (2010). Highly selective fluorescent sensors for Hg2+ based on bovine serum albumin-capped gold nanoclusters. Analyst, 135(6), 1411-1416.

107. Hu, L., Deng, L., Alsaiari, S., Zhang, D., & Khashab, N.M. (2014). “Light-on” Sensing of Antioxidants Using Gold Nanoclusters. Analytical Chemistry, 86(10), 4989-4994.

108. Hu, L., Shi, Y., Li, J.H., Gao, N., Ji, J., Niu, F., Chen, Q., Yang, X., & Wang, S. (2015). Enhancement of Oral Bioavailability of Curcumin by a Novel Solid Dispersion System. AAPS PharmSciTech, 16(6), 1327-1334.

109. Hu, L., Yuan, Y., Zhang, L., Zhao, J., Majeed, S., & Xu, G. (2013). Copper nanoclusters as peroxidase mimetics and their applications to H2O2 and glucose detection. Anal. Chim. Acta, 762(0), 83-86.

110. Hu, Y., Guo, W., & Wei, H. (2015a). Protein- and Peptide-directed Approaches to Fluorescent Metal Nanoclusters. Israel Journal of Chemistry, 55(6- 7), 682-697.

111. Hu, Y., Guo, W., & Wei, H. (2015b). Protein- and Peptide- directed Approaches to Fluorescent Metal Nanoclusters. Israel Journal of Chemistry, 55(6- 7), 682-697.

112. Huang, P., Lin, J., Wang, S., Zhou, Z., Li, Z., Wang, Z., Zhang, C., Yue, X., Niu, G., Yang, M., Cui, D., & Chen, X. (2013). Photosensitizer-conjugated silica-coated gold nanoclusters for fluorescence imaging-guided photodynamic therapy. Biomaterials, 34(19), 4643-4654.
113. Huang, Y., Lin, Q., Wu, J., & Fu, N. (2013). Design and synthesis of a squaraine based near-infrared fluorescent probe for the ratiometric detection of Zn2+ ions. Dyes and Pigments, 99(3), 699-704.
114. Heinz Fabian and Werner Mäntele (2006), Infrared Spectroscopy of Proteins. Handbook of Vibrational Spectroscopy Handbook of Vibrational Spectroscopy, Wiley online library
115. Jain, B. (2017). A spectroscopic study on stability of curcumin as a function of pH in silica nanoformulations, liposome and serum protein. Journal of Molecular Structure, 1130, 194-198.
116. Jain, R., & Muralidhar, S. (2011). Contraceptive Methods: Needs, Options and Utilization. Journal of Obstetrics and Gynaecology of India, 61(6), 626-634.
117. Jian-feng, G., Chang-jun, H., Mei, Y., Dan-qun, H., & Huan-bao, F. (2016). Ultra-sensitive fluorescence determination of chromium (VI) in aqueous solution based on selectively etching of protein-stabled gold nanoclusters. RSC Advances, 6(106), 104693-104698.
118. Jiang, X., Du, B., Huang, Y., & Zheng, J. (2018). Ultrasmall noble metal nanoparticles: Breakthroughs and biomedical implications. Nano Today, 21, 106-125.
119. Jin, L., Shang, L., Guo, S., Fang, Y., Wen, D., Wang, L., Yin, J., & Dong, S. (2011). Biomolecule-stabilized Au nanoclusters as a fluorescence probe for sensitive detection of glucose. Biosens. Bioelectron., 26(5), 1965-1969.
120. Jin, R., & Nobusada, K. (2014). Doping and alloying in atomically precise gold nanoparticles. [journal article]. Nano Research, 7(3), 285-300.
121. Joye, I.J., Davidov-Pardo, G., Ludescher, R.D., & McClements, D.J. (2015). Fluorescence quenching study of resveratrol binding to zein and gliadin: Towards a more rational approach to resveratrol encapsulation using water-insoluble proteins. Food chemistry, 185, 261-267.

122. Jupally, V.R., & Dass, A. (2014). Synthesis of Au130(SR)50 and Au130-xAgx(SR)50 nanomolecules through core size conversion of larger metal clusters. [10.1039/C3CP54343A]. Physical Chemistry Chemical Physics, 16(22), 10473-10479.
123. Kaneshiro, B., & Aeby, T. (2010). Long-term safety, efficacy, and patient acceptability of the intrauterine Copper T-380A contraceptive device. International Journal of Women's Health, 2, 211-220.
124. Kauffman, D.R., Alfonso, D., Matranga, C., Qian, H., & Jin, R. (2013). A Quantum Alloy: The Ligand-Protected Au25–xAgx(SR)18 Cluster. The Journal of Physical Chemistry C, 117(15), 7914-7923.
125. Kawasaki, H., Hamaguchi, K., Osaka, I., & Arakawa, R. (2011). ph-Dependent Synthesis of Pepsin-Mediated Gold Nanoclusters with Blue Green and Red Fluorescent Emission. Adv. Funct. Mater., 21(18), 3508-3515.
126. Khandelia, R., Bhandari, S., Pan, U.N., Ghosh, S.S., & Chattopadhyay, A. (2015). Gold Nanocluster Embedded Albumin Nanoparticles for Two-Photon Imaging of Cancer Cells Accompanying Drug Delivery. Small, 11(33), 4075-4081.
127. Khatkar, B.S., Barak, S., & Mudgil, D. (2013). Effects of gliadin addition on the rheological, microscopic and thermal characteristics of wheat gluten. Int J Biol Macromol, 53, 38-41.
128. Kong, Y., Chen, J., Gao, F., Brydson, R., Johnson, B., Heath, G., Zhang, Y., Wu, L., & Zhou, D. (2013). Near-infrared fluorescent ribonuclease-A-encapsulated gold nanoclusters: preparation, characterization, cancer targeting and imaging. Nanoscale, 5(3), 1009-1017.
129. Kumara, C., & Dass, A. (2011). (AuAg)144(SR)60 alloy nanomolecules. Nanoscale, 3(8), 3064.
130. Kunwar, A., Barik, A., Pandey, R., & Priyadarsini, K.I. (2006). Transport of liposomal and albumin loaded curcumin to living cells: an absorption and fluorescence spectroscopic study. Biochim Biophys Acta, 1760(10), 1513-1520.

131. Lakowicz, J.R. (2013). Principles of fluorescence spectroscopy: Springer Science & Business Media.
132. Le GueÌvel, X., HoÌˆtzer, B., Jung, G., Hollemeyer, K., Trouillet, V., & Schneider, M. (2011). Formation of Fluorescent Metal (Au, Ag) Nanoclusters Capped in Bovine Serum Albumin Followed by Fluorescence and Spectroscopy. J. Phys. Chem. C, 115(22), 10955-10963.
133. Le Guevel, X., Trouillet, V., Spies, C., Li, K., Laaksonen, T., Auerbach, D., Jung, G., & Schneider, M. (2012). High photostability and enhanced fluorescence of gold nanoclusters by silver doping. [10.1039/C2NR30653K]. Nanoscale, 4(24), 7624-7631.
134. Le, G.X., Daum, N., & Schneider, M. (2011). Synthesis and characterization of human transferrin-stabilized gold nanoclusters. Nanotechnology, 22(27), 275103.
135. Le, G.X., Hoetzer, B., Jung, G., & Schneider, M. (2010). NIR-emitting fluorescent gold nanoclusters doped in silica nanoparticles. J. Mater. Chem., 21(9), 2974.
136. Le, G.X., Hotzer, B., Jung, G., Hollemeyer, K., Trouillet, V., & Schneider, M. (2011). Formation of Fluorescent Metal (Au, Ag) Nanoclusters Capped in Bovine Serum Albumin Followed by Fluorescence and Spectroscopy. J. Phys. Chem. C, 115(22), 10955.
137. Lee, C.-Y., Hsu, N.-Y., Wu, M.-Y., & Lin, Y.-W. (2016). Microwave-assisted synthesis of BSA-stabilised gold nanoclusters for the sensitive and selective detection of lead(ii) and melamine in aqueous solution. [10.1039/C6RA16043C]. RSC Advances, 6(82), 79020-79027.
138. Lei, T., Srinivasan, S., Tang, Y., Manchanda, R., Nagesetti, A., Fernandez-Fernandez, A., & McGoron, A.J. (2011). Comparing cellular uptake and cytotoxicity of targeted drug carriers in cancer cell lines with different drug resistance mechanisms. Nanomedicine : nanotechnology, biology, and medicine, 7(3), 324-332.
139. Li, C., Chen, H., Chen, B., & Zhao, G. (2018). Highly fluorescent gold nanoclusters stabilized by food proteins: From preparation to application in

detection of food contaminants and bioactive nutrients. Critical reviews in food science and nutrition, 58(5), 689-699.

140. Li, D., Chen, Z., Wan, Z., Yang, T., Wang, H., & Mei, X. (2016). One-pot development of water soluble copper nanoclusters with red emission and aggregation induced fluorescence enhancement. [10.1039/C6RA01499B]. RSC Advances, 6(41), 34090-34095.
141. Li, G., Fu, H., Chen, X., Gong, P., Chen, G., Xia, L., Wang, H., You, J., & Wu, Y. (2016). Facile and sensitive fluorescence sensing of alkaline phosphatase activity with photoluminescent carbon dots based on inner filter effect. Analytical Chemistry, 88(5), 2720-2726.
142. Li, H.-W., Yue, Y., Liu, T.-Y., Li, D., & Wu, Y. (2013). Fluorescence-enhanced Sensing Mechanism of BSA-protected Small Gold-nanoclusters to Silver(I) Ions in Aqueous Solutions. J. Phys. Chem. C, 117, 16159-16165.
143. Li, H., Guo, Y., Xiao, L., & Chen, B. (2014). Selective and sensitive detection of acetylcholinesterase activity using denatured protein-protected gold nanoclusters as a label-free probe. [10.1039/C3AN01736B]. Analyst, 139(1), 285-289.
144. Li, H., Zhu, W., Wan, A., & Liu, L. (2017). The mechanism and application of the protein-stabilized gold nanocluster sensing system. [10.1039/C6AN02112C]. Analyst, 142(4), 567-581.
145. Li, J., Suo, J., Huang, X., Ye, C., & Wu, X. (2007). Release behavior of copper ion in a novel contraceptive composite. Contraception, 76(3), 233-237.
146. Li, L., Yu, B., & You, T. (2015). Nitrogen and sulfur co-doped carbon dots for highly selective and sensitive detection of Hg (Ⅱ) ions. Biosensors and Bioelectronics, 74, 263-269.
147. Li, M., Xin, M., Guo, C., Lin, G., & Wu, X. (2017). New nanomicelle curcumin formulation for ocular delivery: improved stability, solubility, and ocular anti-inflammatory treatment. Drug Dev Ind Pharm, 43(11), 1846-1857.

148. Li, M., Yang, D.-P., Wang, X., Lu, J., & Cui, D. (2013). Mixed protein-templated luminescent metal clusters (Au and Pt) for H2O2 sensing. Nanoscale Res. Lett., 8(1), 182.
149. Li, R., Xu, P., Fan, J., Di, J., Tu, Y., & Yan, J. (2014). Sensitive iodate sensor based on fluorescence quenching of gold nanocluster. Analytica Chimica Acta, 827, 80-85.
150. Li, Y., Chen, Y., Huang, L., Ma, L., Lin, Q., & Chen, G. (2015). A fluorescent sensor based on ovalbumin-modified Au nanoclusters for sensitive detection of ascorbic acid. [10.1039/C5AY00798D]. Analytical Methods, 7(10), 4123-4129.
151. Li, Z., Peng, H., Liu, J., Tian, Y., Yang, W., Yao, J., Shao, Z., & Chen, X. (2018). Plant Protein-Directed Synthesis of Luminescent Gold Nanocluster Hybrids for Tumor Imaging. ACS Applied Materials & Interfaces, 10(1), 83-90.
152. Lin, H., Li, L., Lei, C., Xu, X., Nie, Z., Guo, M., Huang, Y., & Yao, S. (2013). Immune-independent and label-free fluorescent assay for Cystatin C detection based on protein-stabilized Au nanoclusters. Biosensors and Bioelectronics, 41, 256-261.
153. Lin, Y.-H., & Tseng, W.-L. (2010a). Ultrasensitive sensing of Hg2+ and CH3Hg+ based on the fluorescence quenching of lysozyme type VI-stabilized gold nanoclusters. Analytical Chemistry, 82(22), 9194-9200.
154. Liu, B., Ezeogu, L., Zellmer, L., Yu, B., Xu, N., & Joshua Liao, D. (2015). Protecting the normal in order to better kill the cancer. Cancer Medicine, 4(9), 1394-1403.
155. Liu, C.-L., Wu, H.-T., Hsiao, Y.-H., Lai, C.-W., Shih, C.-W., Peng, Y.-K., Tang, K.-C., Chang, H.-W., Chien, Y.-C., Hsiao, J.-K., Cheng, J.-T., & Chou, P.-T. (2011). Insulin-Directed Synthesis of Fluorescent Gold Nanoclusters: Preservation of Insulin Bioactivity and Versatility in Cell Imaging. Angew. Chem., Int. Ed., 50(31), 7056-7060.
156. Liu, D., Chen, W., Tian, Y., He, S., Zheng, W., Sun, J., Wang, Z., & Jiang, X. (2012). A Highly Sensitive Gold-Nanoparticle-Based Assay for

Acetylcholinesterase in Cerebrospinal Fluid of Transgenic Mice with Alzheimer's Disease. Adv Healthc Mater., 1(1), 90-95.

157. Liu, F., Bing, T., Shangguan, D., Zhao, M., & Shao, N. (2016). Ratiometric Fluorescent Biosensing of Hydrogen Peroxide and Hydroxyl Radical in Living Cells with Lysozyme–Silver Nanoclusters: Lysozyme as Stabilizing Ligand and Fluorescence Signal Unit. Analytical Chemistry, 88(21), 10631-10638.
158. Liu, H., Yang, G., Abdel-Halim, E., & Zhu, J.-J. (2013). Highly selective and ultrasensitive detection of nitrite based on fluorescent gold nanoclusters. Talanta, 104, 135-139.
159. Liu, J.-M., Cui, M.-L., Wang, X.-X., Lin, L.-P., Jiao, L., Zheng, Z.-Y., Zhang, L.-H., & Jiang, S.-L. (2013). A Promising gold nanoclusters fluorescence sensor for highly sensitive and selective detection of S2−. Sens. Actuators, B: Chemical(0).
160. Liu, J.-M., Hu, Y., Yang, Y.-K., Liu, H., Fang, G.-Z., Lu, X., & Wang, S. (2018). Emerging functional nanomaterials for the detection of food contaminants. Trends in Food Science & Technology, 71, 94-106.
161. Liu, J., Krishna, K.S., Kumara, C., Chattopadhyay, S., Shibata, T., Dass, A., & Kumar, C.S.S.R. (2016). Understanding Au[similar]98Ag[similar]46(SR)60 nanoclusters through investigation of their electronic and local structure by X-ray absorption fine structure. [10.1039/C5RA27396J]. RSC Advances, 6(30), 25368-25374.
162. Liu, J., Lu, L., Xu, S., & Wang, L. (2015). One-pot synthesis of gold nanoclusters with bright red fluorescence and good biorecognition Abilities for visualization fluorescence enhancement detection of E. coli. Talanta, 134, 54-59.
163. Liu, P., Shang, L., Li, H., Cui, Y., Qin, Y., Wu, Y., Hiltunen, J.K., Chen, Z., & Shen, J. (2014). Synthesis of fluorescent α-chymotrypsin A-functionalized gold nanoclusters and their application to blot-based technology for Hg 2+ detection. RSC Advances, 4(60), 31536-31543.
164. Liu, S.G., Luo, D., Li, N., Zhang, W., Lei, J.L., Li, N.B., & Luo, H.Q. (2016). Water-soluble nonconjugated polymer nanoparticles with strong

fluorescence emission for selective and sensitive detection of nitro-explosive picric acid in aqueous medium. ACS Applied Materials & Interfaces, 8(33), 21700-21709.

165. Liu, X., Fu, C., Ren, X., Liu, H., Li, L., & Meng, X. (2015). Fluorescence switching method for cascade detection of salicylaldehyde and zinc(II) ion using protein protected gold nanoclusters. Biosensors and Bioelectronics, 74, 322-328.
166. Liu, X., Li, T., Hou, Y., Wu, Q., Yi, J., & Zhang, G. (2016). Microwave synthesis of carbon dots with multi-response using denatured proteins as carbon source. [10.1039/C5RA23081K]. RSC Advances, 6(14), 11711-11718.
167. Liu, X., Pang, J., Xu, F., & Zhang, X. (2016). Simple Approach to Synthesize Amino-Functionalized Carbon Dots by Carbonization of Chitosan. [Article]. Scientific reports, 6, 31100.
168. Liu, Y., Ai, K., Cheng, X., Huo, L., & Lu, L. (2010). Gold-Nanocluster-Based Fluorescent Sensors for Highly Sensitive and Selective Detection of Cyanide in Water. Adv. Funct. Mater., 20(6), 951-956.
169. Liu, Y., Li, H., Guo, B., Wei, L., Chen, B., & Zhang, Y. (2017). Gold nanoclusters as switch-off fluorescent probe for detection of uric acid based on the inner filter effect of hydrogen peroxide-mediated enlargement of gold nanoparticles. Biosensors and Bioelectronics, 91, 734-740.
170. Lowinger, M., Barrett, S., & Zhang, F. (2018). Sustained Release Drug Delivery Applications of Polyurethanes. Pharmaceutics, 10(2).
171. Lu, D., Liu, L., Li, F., Shuang, S., Li, Y., Choi, M.M.F., & Dong, C. (2014). Lysozyme-stabilized gold nanoclusters as a novel fluorescence probe for cyanide recognition. Spectrochimica Acta Part A: Molecular and Biomolecular Spectroscopy, 121, 77-80.
172. Lu, Y., & Chen, W. (2012). Sub-nanometre sized metal clusters: from synthetic challenges to the unique property discoveries. [10.1039/C2CS15325D]. Chemical Society Reviews, 41(9), 3594-3623.
173. Luo, J., Wu, C., Xu, T., & Wu, Y. (2011). Diffusion dialysis-concept, principle and applications. Journal of Membrane Science, 366(1), 1-16.

174. Malekzad, H., Mirshekari, H., Sahandi Zangabad, P., Moosavi Basri, S.M., Baniasadi, F., Sharifi Aghdam, M., Karimi, M., & Hamblin, M.R. (2017). Plant protein-based hydrophobic fine and ultrafine carrier particles in drug delivery systems. Critical Reviews in Biotechnology, 1-21.
175. Malekzad, H., Mirshekari, H., Sahandi Zangabad, P., Moosavi Basri, S.M., Baniasadi, F., Sharifi Aghdam, M., Karimi, M., & Hamblin, M.R. (2018). Plant protein-based hydrophobic fine and ultrafine carrier particles in drug delivery systems. Crit Rev Biotechnol, 38(1), 47-67.
176. Mali, B., & Ncholas, P.C. (1988). Jaffes' reaction for creatinine: kinetic study and spectrophotometric characteristics of the product of the reactions of creatinine, acetoacetate and creatinine and acetoacetate with alkaline picrate: Portland Press Limited.
177. Manju, S., & Sreenivasan, K. (2011). Conjugation of curcumin onto hyaluronic acid enhances its aqueous solubility and stability. J Colloid Interface Sci, 359(1), 318-325.
178. Mathew, A., & Pradeep, T. (2014). Noble Metal Clusters: Applications in Energy, Environment, and Biology. Part. Part. Syst. Charact., 31,1017-1053
179. Mathew, M.S., Baksi, A., Pradeep, T., & Joseph, K. (2016). Choline-induced selective fluorescence quenching of acetylcholinesterase conjugated Au@ BSA clusters. Biosensors and Bioelectronics, 81, 68-74.
180. Mathew, M.S., & Joseph, K. (2017). Green Synthesis of Gluten-Stabilized Fluorescent Gold Quantum Clusters: Application As Turn-On Sensing of Human Blood Creatinine. ACS Sustainable Chemistry & Engineering, 5(6), 4837-4845.
181. Mathew, M.S., Sreenivasan, K., & Joseph, K. (2015). Hydrogen-bond assisted, aggregation-induced emission of digitonin. RSC Advances, 5(121), 100176-100183.
182. Meng, F., Yin, H., Li, Y., Zheng, S., Gan, F., & Ye, G. (2018). One-step synthesis of enzyme-stabilized gold nanoclusters for fluorescent ratiometric detection of hydrogen peroxide, glucose and uric acid. Microchemical Journal, 141, 431-437.

183. Meng, H., Chen, J.-Y., Mi, L., Wang, P.-N., Ge, M.-Y., Yue, Y., & Dai, N. (2011). Conjugates of folic acids with BSA-coated quantum dots for cancer cell targeting and imaging by single-photon and two-photon excitation. [journal article]. JBIC Journal of Biological Inorganic Chemistry, 16(1), 117-123.
184. Miao, Z., Hou, W., Liu, M., Zhang, Y., & Yao, S. (2018). BSA capped bi-functional fluorescent Cu nanoclusters as pH sensor and selective detection of dopamine. [10.1039/C7NJ03524A]. New Journal of Chemistry, 42(2), 1446-1456.
185. Mohanty, J.S., Baksi, A., Lee, H., & Pradeep, T. (2015). Noble metal clusters protected with mixed proteins exhibit intense photoluminescence. [10.1039/C5RA06964E]. RSC Advances, 5(59), 48039-48045.
186. Mohanty, J.S., Xavier, P.L., Chaudhari, K., Bootharaju, M., Goswami, N., Pal, S., & Pradeep, T. (2012a). Luminescent, bimetallic AuAg alloy quantum clusters in protein templates. Nanoscale, 4(14), 4255-4262.
187. Mohanty, J.S., Xavier, P.L., Chaudhari, K., Bootharaju, M.S., Goswami, N., Pal, S.K., & Pradeep, T. (2012b). Luminescent, bimetallic AuAg alloy quantum clusters in protein templates. [10.1039/C2NR30729D]. Nanoscale, 4(14), 4255-4262.
188. Mueller, S.G., Weiner, M.W., Thal, L.J., Petersen, R.C., Jack, C.R., Jagust, W., Trojanowski, J.Q., Toga, A.W., & Beckett, L. (2005). Ways toward an early diagnosis in Alzheimer's disease: The Alzheimer's Disease Neuroimaging Initiative (ADNI). Alzheimer's & Dementia, 1(1), 55-66.
189. Muhammed, M.A.H., Verma, P.K., Pal, S.K., Kumar, R.C.A., Paul, S., Omkumar, R.V., & Pradeep, T. (2009). Bright, NIR-Emitting Au23 from Au25: Characterization and Applications Including Biolabeling. Chem.--Eur. J., 15(39), 10110.
190. Murugadoss, A., Kai, N., & Sakurai, H. (2012). Synthesis of bimetallic gold–silver alloy nanoclusters by simple mortar grinding. Nanoscale, 4(4), 1280-1282.
191. Nair, L.V., Nazeer, S.S., Jayasree, R.S., & Ajayaghosh, A. (2015). Fluorescence Imaging Assisted Photodynamic Therapy Using

Photosensitizer-Linked Gold Quantum Clusters. ACS Nano, 9(6), 5825-5832.

192. Nair, L.V., Philips, D.S., Jayasree, R.S., & Ajayaghosh, A. (2013). A Near-Infrared Fluorescent Nanosensor (AuC@Urease) for the Selective Detection of Blood Urea. Small, 9(16), 2673-2677.

193. Nawrot, W., Drzozga, K., Baluta, S., Cabaj, J., & Malecha, K. (2018). A Fluorescent Biosensors for Detection Vital Body Fluids' Agents. Sensors, 18(8), 2357.

194. Nebu, J., Anjali Devi, J.S., Aparna, R.S., Abha, K., & Sony, G. (2018). Erlotinib conjugated gold nanocluster enveloped magnetic iron oxide nanoparticles–A targeted probe for imaging pancreatic cancer cells. Sensors and Actuators B: Chemical, 257, 1035-1043.

195. Negishi, Y., Nobusada, K., & Tsukuda, T. (2005). Glutathione-Protected Gold Clusters Revisited: Bridging the Gap between Gold(I)−Thiolate Complexes and Thiolate-Protected Gold Nanocrystals. Journal of the American Chemical Society, 127(14), 5261-5270.

196. Negishi, Y., Takasugi, Y., Sato, S., Yao, H., Kimura, K., & Tsukuda, T. (2004). Magic-Numbered Aun Clusters Protected by Glutathione Monolayers (n = 18, 21, 25, 28, 32, 39): Isolation and Spectroscopic Characterization. Journal of the American Chemical Society, 126(21), 6518-6519.

197. Nishida, N., Yao, H., Ueda, T., Sasaki, A., & Kimura, K. (2007). Synthesis and Chiroptical Study of d/l-Penicillamine-Capped Silver Nanoclusters. Chemistry of Materials, 19(11), 2831-2841. doi: 10.1021/cm0700192

198. Oliveira, S.F., Bisker, G., Bakh, N.A., Gibbs, S.L., Landry, M.P., & Strano, M.S. (2015). Protein functionalized carbon nanomaterials for biomedical applications. Carbon, 95, 767-779.

199. Ortiz, M.E., Croxatto, H.B., & Bardin, C.W. (1996). Mechanisms of action of intrauterine devices. Obstetrical & gynecological survey, 51(12), 42S-51S.

200. Palumbo, M.O., Kavan, P., Miller, W.H., Jr., Panasci, L., Assouline, S., Johnson, N., Cohen, V., Patenaude, F., Pollak, M., Jagoe, R.T., & Batist, G. (2013). Systemic cancer therapy: achievements and challenges that lie ahead. Frontiers in pharmacology, 4, 57-57.
201. Palza, H., Galarce, N., Bejarano, J., Beltran, M., & Caviedes, P. (2017). Effect of copper nanoparticles on the cell viability of polymer composites. International Journal of Polymeric Materials and Polymeric Biomaterials, 66(9), 462-468.
202. Pan, K., Zhong, Q., & Baek, S.J. (2013). Enhanced Dispersibility and Bioactivity of Curcumin by Encapsulation in Casein Nanocapsules. Journal of Agricultural and Food Chemistry, 61(25), 6036-6043.
203. Pandya, A., Lad, A.N., Singh, S.P., & Shanker, R. (2016). DNA assembled metal nanoclusters: synthesis to novel applications. [10.1039/C6RA24098D]. RSC Advances, 6(114), 113095-113114.
204. Parmar, A.K., Valand, N.N., Solanki, K.B., & Menon, S.K. (2016). Picric acid capped silver nanoparticles as a probe for colorimetric sensing of creatinine in human blood and cerebrospinal fluid samples. Analyst, 141(4), 1488-1498.
205. Patel, A., Hu, Y., Tiwari, J.K., & Velikov, K.P. (2010). Synthesis and Characterization of zein-curcumin colloidal particles. [10.1039/C0SM00800A]. Soft Matter, 6(24), 6192-6199.
206. Pradeep, T., Baksi, A., & Xavier, P.L. (2014a). CHAPTER 7 Noble Metal Clusters in Protein Templates Functional Nanometer-Sized Clusters of Transition Metals: Synthesis, Properties and Applications (pp. 169-225): The Royal Society of Chemistry.
207. Pradeep, T., Baksi, A., & Xavier, P.L. (2014b). Noble Metal Clusters in Protein Templates. Functional Nanometer-Sized Clusters of Transition Metals: Synthesis, Properties and Applications, 169-225.
208. Prasad, S., Tyagi, A.K., & Aggarwal, B.B. (2014). Recent Developments in Delivery, Bioavailability, Absorption and Metabolism of Curcumin: the Golden Pigment from Golden Spice. Cancer Research and Treatment : Official Journal of Korean Cancer Association, 46(1), 2-18.

209. Pyng, Y., Xiaoming, W., Yon-Rui, T., Jane, H., & Jau, T. (2013). Metallophilic Bond-Induced Quenching of Delayed Fluorescence in Au25@BSA Nanoclusters. Particle & Particle Systems Characterization, 30(5), 467-472.
210. Qian, H., Zhu, M., Wu, Z., & Jin, R. (2012). Quantum Sized Gold Nanoclusters with Atomic Precision. Accounts of Chemical Research, 45(9), 1470-1479.
211. Qiao, J., Mu, X., Qi, L., Deng, J., & Mao, L. (2013). Folic acid-functionalized fluorescent gold nanoclusters with polymers as linkers for cancer cell imaging. [10.1039/C3CC44256J]. Chemical Communications, 49(73), 8030-8032.
212. Qin, L., He, X., Chen, L., & Zhang, Y. (2015). Turn-on Fluorescent Sensing of Glutathione S-Transferase at near-Infrared Region Based on FRET between Gold Nanoclusters and Gold Nanorods. ACS Applied Materials & Interfaces, 7(10), 5965-5971.
213. Rajamanikandan, R., & Ilanchelian, M. (2018). Protein-protected red emittive copper nanoclusters as a fluorometric probe for highly sensitive biosensing of creatinine. [10.1039/C8AY00827B]. Analytical Methods, 10(29), 3666-3674.
214. Reddy, N., & Yang, Y. (2007). Novel protein fibers from wheat gluten. Biomacromolecules, 8(2), 638-643.
215. Rejinold, N.S., Muthunarayanan, M., Chennazhi, K.P., Nair, S.V., & Jayakumar, R. (2011). Curcumin loaded fibrinogen nanoparticles for cancer drug delivery. J Biomed Nanotechnol, 7(4), 521-534.
216. Retnakumari, A.P., Hanumanthu, P.L., Malarvizhi, G.L., Prabhu, R., Sidharthan, N., Thampi, M.V., Menon, D., Mony, U., Menon, K., Keechilat, P., Nair, S., & Koyakutty, M. (2012). Rationally Designed Aberrant Kinase-Targeted Endogenous Protein Nanomedicine against Oncogene Mutated/Amplified Refractory Chronic Myeloid Leukemia. Molecular Pharmaceutics, 9(11), 3062-3078.
217. Richards, C.I., Choi, S., Hsiang, J.-C., Antoku, Y., Vosch, T., Bongiorno, A., Tzeng, Y.-L., & Dickson, R.M. (2008). Oligonucleotide-stabilized Ag

nanocluster fluorophores. Journal of the American Chemical Society, 130(15), 5038-5039.

218. Rong, L., Zhaoyang, W., Yuanlian, Y., Shuzhen, L., & Ruqin, Y. (2018). Application of gold–silver nanocluster based fluorescent sensors for determination of acetylcholinesterase activity and its inhibitor. Materials Research Express, 5(6), 065027.

219. Roy, P., Periasamy, A.P., Chuang, C., Liou, Y.-R., Chen, Y.-F., Joly, J., Liang, C.-T., & Chang, H.-T. (2014). Plant leaf-derived graphene quantum dots and applications for white LEDs. [10.1039/C4NJ01185F]. New Journal of Chemistry, 38(10), 4946-4951.

220. Ruedas-Rama, M.J., & Hall, E.A. (2010). Analytical nanosphere sensors using quantum dot− enzyme conjugates for urea and creatinine. Analytical Chemistry, 82(21), 9043-9049.

221. Rurack, K., & Spieles, M. (2011). Fluorescence Quantum Yields of a Series of Red and Near-Infrared Dyes Emitting at 600−1000 nm. Analytical Chemistry, 83(4), 1232-1242.

222. Sadder El-Leithy, E., Mohamed, H., & Abd el-Moneum, R. (2017). Synthesis, Optimization and Characterization of Folate-Chitosan polymer conjugate for Possible Oral delivery of Macromolecular drugs (Vol. 7).

223. Santhosh, M., Chinnadayyala, S.R., Kakoti, A., & Goswami, P. (2014). Selective and sensitive detection of free bilirubin in blood serum using human serum albumin stabilized gold nanoclusters as fluorometric and colorimetric probe. Biosensors and Bioelectronics, 59, 370-376.

224. Sattarahmady, N., Heli, H., & Moosavi-Movahedi, A.A. (2010). An electrochemical acetylcholine biosensor based on nanoshells of hollow nickel microspheres-carbon microparticles-Nafion nanocomposite. Biosensors and Bioelectronics, 25(10), 2329-2335.

225. Saumya, V., & Rao, T.P. (2012). Copper quantum cluster-polypyrrole composite film based zero current chronopotentiometric sensor for glutathione. [10.1039/C2AY25342A]. Analytical Methods, 4(7), 1976-1982.

226. Schaaff, T.G., Knight, G., Shafigullin, M.N., Borkman, R.F., & Whetten, R.L. (1998). Isolation and Selected Properties of a 10.4 kDa Gold:Glutathione Cluster Compound. The Journal of Physical Chemistry B, 102(52), 10643-10646.
227. Schena, A., & Johnsson, K. (2014). Sensing Acetylcholine and Anticholinesterase Compounds. Angew. Chem. Int. Ed.
228. , 53(5), 1302-1305.
229. Schneider, C., Gordon, O.N., Edwards, R.L., & Luis, P.B. (2015). Degradation of Curcumin: From Mechanism to Biological Implications. J Agric Food Chem, 63(35), 7606-7614.
230. Schneider, J., Gründig, B., Renneberg, R., Cammann, K., Madaras, M., Buck, R., & Vorlop, K.-D. (1996). Hydrogel matrix for three enzyme entrapment in creatine/creatinine amperometric biosensing. Analytica Chimica Acta, 325(3), 161-167.
231. Selvaprakash, K., & Chen, Y.-C. (2014). Using protein-encapsulated gold nanoclusters as photoluminescent sensing probes for biomolecules. Biosensors and Bioelectronics, 61, 88-94.
232. Senthamizhan, A., Celebioglu, A., & Uyar, T. (2014). Flexible and highly stable electrospun nanofibrous membrane incorporating gold nanoclusters as an efficient probe for visual colorimetric detection of Hg (II). Journal of Materials Chemistry A, 2(32), 12717-12723.
233. Senthilkumar, T., & Asha, S.K. (2015). Selective and Sensitive Sensing of Free Bilirubin in Human Serum Using Water-Soluble Polyfluorene as Fluorescent Probe. Macromolecules, 48(11), 3449-3461.
234. Shamsipur, M., Molaabasi, F., Sarparast, M., Roshani, E., Vaezi, Z., Alipour, M., Molaei, K., Naderi-Manesh, H., & Hosseinkhani, S. (2018). Photoluminescence Mechanisms of Dual-Emission Fluorescent Silver Nanoclusters Fabricated by Human Hemoglobin Template: From Oxidation- and Aggregation-Induced Emission Enhancement to Targeted Drug Delivery and Cell Imaging. ACS Sustainable Chemistry & Engineering, 6(8), 11123-11137.

235. Shamsipur, M., Molaabasi, F., Shanehsaz, M., & Moosavi-Movahedi, A.A. (2015). Novel blue-emitting gold nanoclusters confined in human hemoglobin, and their use as fluorescent probes for copper (II) and histidine. Microchimica Acta, 182(5-6), 1131-1141.
236. Shang, L., Dong, S., & Nienhaus, G.U. (2011). Ultra-small fluorescent metal nanoclusters: Synthesis and biological applications. Nano Today, 6(4), 401-418.
237. Shao, C., Yuan, B., Wang, H., Zhou, Q., Li, Y., Guan, Y., & Deng, Z. (2011). Eggshell membrane as a multimodal solid state platform for generating fluorescent metal nanoclusters. [10.1039/C0JM04071A]. Journal of Materials Chemistry, 21(9), 2863-2866.
238. Shelke, N.B., Nagarale, R.K., & Kumbar, S.G. (2014). Chapter 7 - Polyurethanes Natural and Synthetic Biomedical Polymers (pp. 123-144). Oxford: Elsevier.
239. Shewry, P., & Tatham, A. (1997). Disulphide bonds in wheat gluten proteins. Journal of Cereal Science, 25(3), 207-227.
240. Shewry, P.R., Halford, N.G., Belton, P.S., & Tatham, A.S. (2002). The structure and properties of gluten: an elastic protein from wheat grain. Philosophical Transactions of the Royal Society of London B: Biological Sciences, 357(1418), 133-142.
241. Shi, H., Ou, M.Y., Cao, J.P., & Chen, G.F. (2015). Synthesis of ovalbumin-stabilized highly fluorescent gold nanoclusters and their application as an Hg2+ sensor. [10.1039/C5RA15559B]. RSC Advances, 5(105), 86740-86745.
242. Shibu, E.S., Sugino, S., Ono, K., Saito, H., Nishioka, A., Yamamura, S., Sawada, M., Nosaka, Y., & Biju, V. (2013). Singlet-Oxygen-Sensitizing Near-Infrared-Fluorescent Multimodal Nanoparticles. Angewandte Chemie International Edition, 52(40), 10559-10563.
243. Shichibu, Y., Negishi, Y., Tsunoyama, H., Kanehara, M., Teranishi, T., & Tsukuda, T. (2007). Extremely High Stability of Glutathionate-Protected Au25 Clusters Against Core Etching. Small, 3(5), 835-839

244. Singh, D.K., Jagannathan, R., Khandelwal, P., Abraham, P.M., & Poddar, P. (2013). In situ synthesis and surface functionalization of gold nanoparticles with curcumin and their antioxidant properties: an experimental and density functional theory investigation. [10.1039/C2NR33776B]. Nanoscale, 5(5), 1882-1893.

245. Singh, V., & Mishra, A.K. (2015). White light emission from vegetable extracts. Scientific reports, 5.

246. Sneharani, A.H., Karakkat, J.V., Singh, S.A., & Rao, A.G.A. (2010). Interaction of Curcumin with β-Lactoglobulin—Stability, Spectroscopic Analysis, and Molecular Modeling of the Complex. Journal of Agricultural and Food Chemistry, 58(20), 11130-11139.

247. Sommer, M.E., Elgeti, M., Hildebrand, P.W., Szczepek, M., Hofmann, K.P., & Scheerer, P. (2015). Chapter Twenty-Six - Structure-Based Biophysical Analysis of the Interaction of Rhodopsin with G Protein and Arrestin. In A. K. Shukla (Ed.), Methods in Enzymology (Vol. 556, pp. 563-608): Academic Press.

248. Song, X.-R., Goswami, N., Yang, H.-H., & Xie, J. (2016). Functionalization of metal nanoclusters for biomedical applications. [10.1039/C6AN00773B]. Analyst, 141(11), 3126-3140.

249. Stanback, J., & Grimes, D. (1998). Can intrauterine device removals for bleeding or pain be predicted at a one-month follow-up visit?: A multivariate analysis. Contraception, 58(6), 357-360.

250. Stocker, R., Yamamoto, Y., McDonagh, A.F., Glazer, A.N., & Ames, B.N. (1987). Bilirubin is an antioxidant of possible physiological importance. Science, 235, 1043-1047.

251. Sun, J., & Jin, Y. (2014). Fluorescent Au nanoclusters: recent progress and sensing applications. [10.1039/C4TC01489H]. Journal of Materials Chemistry C, 2(38), 8000-8011.

252. Sun, J., Yue, Y., Wang, P., He, H., & Jin, Y. (2013). Facile and rapid synthesis of water-soluble fluorescent gold nanoclusters for sensitive and

selective detection of Ag^{+}. [10.1039/C2TC00207H]. Journal of Materials Chemistry C, 1(5), 908-913. doi:

253. Sun, X., Jiang, X., Dong, S., & Wang, E. (2003). One-step synthesis and size control of dendrimer-protected gold nanoparticles: A heat-treatment-based strategy. Macromol. Rapid Commun., 24(17), 1024.
254. Sun, X., Ma, X., Kumar, C.V., & Lei, Y. (2014). Protein-based sensitive, selective and rapid fluorescence detection of picric acid in aqueous media. Analytical Methods, 6(21), 8464-8468.
255. Sun, X., Wang, Y., & Lei, Y. (2015). Fluorescence based explosive detection: from mechanisms to sensory materials. [10.1039/C5CS00496A]. Chemical Society Reviews, 44(22), 8019-8061.
256. Susman, M.D., Popovitz- Biro, R., Vaskevich, A., & Rubinstein, I. (2015). pH- Dependent Galvanic Replacement of Supported and Colloidal Cu2O Nanocrystals with Gold and Palladium. Small, 11(32), 3942-3953.
257. Tang, B., Ma, L., Wang, H.-y., & Zhang, G.-y. (2002). Study on the Supramolecular Interaction of Curcumin and β-cyclodextrin by Spectrophotometry and Its Analytical Application. Journal of Agricultural and Food Chemistry, 50(6), 1355-1361.
258. Tao, Y., Li, M., Ren, J., & Qu, X. (2015). Metal nanoclusters: novel probes for diagnostic and therapeutic applications. [10.1039/C5CS00607D]. Chemical Society Reviews, 44(23), 8636-8663.
259. Tao, Y., Lin, Y., Ren, J., & Qu, X. (2013). A dual fluorometric and colorimetric sensor for dopamine based on BSA-stabilized Aunanoclusters. Biosens. Bioelectron., 42(0), 41-46.
260. Tapal, A., & Tiku, P.K. (2012). Complexation of curcumin with soy protein isolate and its implications on solubility and stability of curcumin. Food Chemistry, 130(4), 960-965.
261. Tashkhourian, J., Sheydaei, O., & Nami- Ana, S. (2018). Copper nanoclusters conjugated silica nanoparticles modified on carbon paste as an electrochemical sensor for the determination of dopamine. Applied Organometallic Chemistry, 32(3), e4196.

262. Thangamuthu, M., Gabriel, W.E., Santschi, C., & Martin, O.J.F. (2018). Electrochemical Sensor for Bilirubin Detection Using Screen Printed Electrodes Functionalized with Carbon Nanotubes and Graphene. Sensors (Basel, Switzerland), 18(3), 800.
263. Trovati, G., Sanches, E.A., Neto, S.C., Mascarenhas, Y.P., & Chierice, G.O. (2010). Characterization of polyurethane resins by FTIR, TGA, and XRD. Journal of Applied Polymer Science, 115(1), 263-268.
264. Tsai, H.-c., & Doong, R.-a. (2005). Simultaneous determination of pH, urea, acetylcholine and heavy metals using array-based enzymatic optical biosensor. Biosensors and Bioelectronics, 20(9), 1796-1804.
265. Udayabhaskararao, T., Sun, Y., Goswami, N., Pal, S.K., Balasubramanian, K., & Pradeep, T. (2012). Ag7Au6: A 13- Atom Alloy Quantum Cluster. Angewandte Chemie International Edition, 51(9), 2155-2159.
266. Unnikrishnan, B., Wei, S.-C., Chiu, W.-J., Cang, J., Hsu, P.-H., & Huang, C.-C. (2014). Nitrite ion-induced fluorescence quenching of luminescent BSA-Au25 nanoclusters: mechanism and application. [10.1039/C3AN02291A]. Analyst, 139(9), 2221-2228.
267. Urruticoechea, A., Alemany, R., Balart, J., Villanueva, A., Vinals, F., & Capella, G. (2010). Recent advances in cancer therapy: an overview. Curr Pharm Des, 16(1), 3-10.
268. Wang, C., Cheng, H., Sun, Y., Xu, Z., Lin, H., Lin, Q., & Zhang, C. (2015). Nanoclusters prepared from a silver/gold alloy as a fluorescent probe for selective and sensitive determination of lead(II). [journal article]. Microchimica Acta, 182(3), 695-701.
269. Wang, C., Lin, H., Xu, Z., Huang, Y., Humphrey, M.G., & Zhang, C. (2016). Tunable carbon-dot-based dual-emission fluorescent nanohybrids for ratiometric optical thermometry in living cells. ACS Applied Materials & Interfaces, 8(10), 6621-6628.
270. Wang, C., Shu, S., Yao, Y., & Song, Q. (2015). A fluorescent biosensor of lysozyme-stabilized copper nanoclusters for the selective detection of glucose. [10.1039/C5RA19421K]. RSC Advances, 5(123), 101599-101606.

271. Wang, C., Wang, Y., Xu, L., Shi, X., Li, X., Xu, X., Sun, H., Yang, B., & Lin, Q. (2013). A galvanic replacement route to prepare strongly fluorescent and highly stable gold nanodots for cellular imaging. Small, 9(3), 413-420.
272. Wang, C., Xu, L., Xu, X., Cheng, H., Sun, H., Lin, Q., & Zhang, C. (2014). Near infrared Ag/Au alloy nanoclusters: Tunable photoluminescence and cellular imaging. Journal of Colloid and Interface Science, 416, 274-279.
273. Wang, G.-L., Jin, L.-Y., Dong, Y.-M., Wu, X.-M., & Li, Z.-J. (2015). Intrinsic enzyme mimicking activity of gold nanoclusters upon visible light triggering and its application for colorimetric trypsin detection. Biosensors and Bioelectronics, 64, 523-529.
274. Wang, H.-B., Li, Y., Chen, Y., Zhang, Z.-P., Gan, T., & Liu, Y.-M. (2018). Determination of the activity of alkaline phosphatase by using nanoclusters composed of flower-like cobalt oxyhydroxide and copper nanoclusters as fluorescent probes. Microchimica Acta, 185(2), 102.
275. Wang, M., Mei, Q., Zhang, K., & Zhang, Z. (2012). Protein-gold nanoclusters for identification of amino acids by metal ions modulated ratiometric fluorescence. [10.1039/C2AN16302K]. Analyst, 137(7), 1618-1623.
276. Wang, X.-R., Li, B.-W., You, H.-Y., & Chen, L.-X. (2015). An Ion Imprinted Polymers Grafted Paper-based Fluorescent Sensor Based on Quantum Dots for Detection of Cu2+ Ions. Chinese Journal of Analytical Chemistry, 43(10), 1499-1504.
277. Wang, X.-X., Wu, Q., Shan, Z., & Huang, Q.-M. (2011). BSA-stabilized Au clusters as peroxidase mimetics for use in xanthine detection. Biosensors and Bioelectronics, 26(8), 3614-3619.
278. Wang, X.-y., Zhu, G.-b., Cao, W.-d., Liu, Z.-j., Pan, C.-g., Hu, W.-j., Zhao, W.-y., & Sun, J.-f. (2019). A novel ratiometric fluorescent probe for the detection of uric acid in human blood based on H2O2-mediated fluorescence quenching of gold/silver nanoclusters. Talanta, 191, 46-53.

279. Wang, X., Long, Y., Wang, Q., Zhang, H., Huang, X., Zhu, R., Teng, P., Liang, L., & Zheng, H. (2013). Reduced state carbon dots as both reductant and stabilizer for the synthesis of gold nanoparticles. Carbon, 64(Supplement C), 499-506.
280. Wang, Y.-Q., Zhao, T., He, X.-W., Li, W.-Y., & Zhang, Y.-K. (2014). A novel core-satellite CdTe/Silica/Au NCs hybrid sphere as dual-emission ratiometric fluorescent probe for Cu2+. Biosensors and Bioelectronics, 51, 40-46.
281. Wang, Y., Chen, J.-T., & Yan, X.-P. (2013). Fabrication of Transferrin Functionalized Gold Nanoclusters/Graphene Oxide Nanocomposite for Turn-On Near-Infrared Fluorescent Bioimaging of Cancer Cells and Small Animals. Anal. Chem., 85(4), 2529-2535.
282. Wang, Y., Chen, J., & Irudayaraj, J. (2011). Nuclear Targeting Dynamics of Gold Nanoclusters for Enhanced Therapy of HER2+ Breast Cancer. ACS Nano, 5(12), 9718-9725.
283. Wang, Z., Chen, B., Duan, J., Hao, T., Jiang, X., Guo, Z., & Wang, S. (2015). A test strip for lead(II) based on gold nanoparticles multi-functionalized by DNAzyme and barcode DNA. [journal article]. Journal of Analytical Chemistry, 70(3), 339-345. doi: 10.1134/s1061934815030247
284. Watanabe, M., Kimura, A., Akasaka, K., & Hayashi, S. (1986). Determination of acetylcholine in human blood. Biochemical medicine and metabolic biology, 36(3), 355-362.
285. Wei, J., Ren, J., Liu, J., Meng, X., Ren, X., Chen, Z., & Tang, F. (2014). An eco-friendly, simple, and sensitive fluorescence biosensor for the detection of choline and acetylcholine based on C-dots and the Fenton reaction. Biosensors and Bioelectronics, 52, 304-309.
286. Weitman, S.D., Lark, R.H., Coney, L.R., Fort, D.W., Frasca, V., Zurawski, V.R., Jr., & Kamen, B.A. (1992). Distribution of the folate receptor GP38 in normal and malignant cell lines and tissues. Cancer Res, 52(12), 3396-3401.

287. Wen, F., Dong, Y., Feng, L., Wang, S., Zhang, S., & Zhang, X. (2011). Horseradish peroxidase functionalized fluorescent gold nanoclusters for hydrogen peroxide sensing. Analytical Chemistry, 83(4), 1193-1196.
288. Wen, X., Yu, P., Toh, Y.-R., Hsu, A.-C., Lee, Y.-C., & Tang, J. (2012). Fluorescence Dynamics in BSA-Protected Au25 Nanoclusters. J. Phys. Chem. C, 116(35), 19032-19038.
289. Whetten, R.L., Khoury, J.T., Alvarez, M.M., Murthy, S., Vezmar, I., Wang, Z.L., Stephens, P.W., Cleveland, C.L., Luedtke, W.D., & Landman, U. (1996). Nanocrystal gold molecules. Advanced materials, 8(5), 428-433.
290. Wieser, H. (2007). Chemistry of gluten proteins. Food microbiology, 24(2), 115-119.
291. Wu, B., Xu, L., Wang, S., Wang, Y., & Zhang, W. (2015). A PEGylated colorimetric and turn-on fluorescent sensor based on BODIPY for Hg (II) detection in water. Polymer Chemistry, 6(23), 4279-4289.
292. Wu, X., He, X., Wang, K., Xie, C., Zhou, B., & Qing, Z. (2010). Ultrasmall near-infrared gold nanoclusters for tumor fluorescence imaging in vivo. [10.1039/C0NR00359J]. Nanoscale, 2(10), 2244-2249.
293. Wu, X., Zhang, Z., Li, J., You, H., Li, Y., & Chen, L. (2015). Molecularly imprinted polymers-coated gold nanoclusters for fluorescent detection of bisphenol A. Sensors and Actuators B: Chemical, 211, 507-514.
294. Wu, Z.L., Zhang, P., Gao, M.X., Liu, C.F., Wang, W., Leng, F., & Huang, C.Z. (2013). One-pot hydrothermal synthesis of highly luminescent nitrogen-doped amphoteric carbon dots for bioimaging from Bombyx mori silk - natural proteins. [10.1039/C3TB20418A]. Journal of Materials Chemistry B, 1(22), 2868-2873.
295. Xavier Le, G., Nicole, D., & Marc, S. (2011). Synthesis and characterization of human transferrin-stabilized gold nanoclusters. Nanotechnology, 22(27), 275103.
296. Xavier, P.L., Chaudhari, K., Baksi, A., & Pradeep, T. (2012). Protein-protected luminescent noble metal quantum clusters: an emerging trend in atomic cluster nanoscience. Nano reviews, 3(1), 14767.

297. Xavier, P.L., Chaudhari, K., Verma, P.K., Pal, S.K., & Pradeep, T. (2010). Luminescent quantum clusters of gold in transferrin family protein, lactoferrin exhibiting FRET. Nanoscale, 2(12), 2769-2776.
298. Xia, X., Long, Y., & Wang, J. (2013). Glucose oxidase-functionalized fluorescent gold nanoclusters as probes for glucose. Anal. Chim. Acta, 772(0), 81-86.
299. Xiaoqing, L., Ruiyi, L., Zaijun, L., Xiulan, S., Zhouping, W., & Junkang, L. (2015). Fast synthesis of copper nanoclusters through the use of hydrogen peroxide additive and their application for the fluorescence detection of Hg2+ in water samples. [10.1039/C5NJ00831J]. New Journal of Chemistry, 39(7), 5240-5248.
300. Xie, J., Zheng, Y., & Ying, J.Y. (2009). Protein-Directed Synthesis of Highly Fluorescent Gold Nanoclusters. J. Am. Chem. Soc., 131(3), 888-889.
301. Xie, J., Zheng, Y., & Ying, J.Y. (2010). Highly selective and ultrasensitive detection of Hg2+ based on fluorescence quenching of Au nanoclusters by Hg2+–Au+ interactions. Chemical Communications, 46(6), 961-963.
302. Xiong, H., Wang, W., Liang, J., Wen, W., Zhang, X., & Wang, S. (2017). A convenient purification method for metal nanoclusters based on pH-induced aggregation and cyclic regeneration and its applications in fluorescent pH sensors. Sensors and Actuators B: Chemical, 239, 988-992.
303. Xiong, X., Tang, Y., Zhang, L., & Zhao, S. (2015). A label-free fluorescent assay for free chlorine in drinking water based on protein-stabilized gold nanoclusters. Talanta, 132, 790-795.
304. Xu, H., Zhu, H., Sun, M., Yu, H., Li, H., Ma, F., & Wang, S. (2015). Graphene oxide supported gold nanoclusters for the sensitive and selective detection of nitrite ions. [10.1039/C4AN02181A]. Analyst, 140(5), 1678-1685.
305. Xu, S., Feng, X., Gao, T., Wang, R., Mao, Y., Lin, J., Yu, X., & Luo, X. (2017). A novel dual-functional biosensor for fluorometric detection of inorganic pyrophosphate and pyrophosphatase activity based on globulin stabilized gold nanoclusters. Analytica Chimica Acta, 958, 22-29.

306. Xu, X., Chen, D., Ye, B., Zhong, F., & Chen, G. (2015). Curcumin induces the apoptosis of non-small cell lung cancer cells through a calcium signaling pathway. Int J Mol Med, 35(6), 1610-1616.
307. Xu, Y., Sherwood, J., Qin, Y., Crowley, D., Bonizzoni, M., & Bao, Y. (2014). The role of protein characteristics in the formation and fluorescence of Au nanoclusters. [10.1039/C3NR06040C]. Nanoscale, 6(3), 1515-1524.
308. Xue, X., Wang, F., & Liu, X. (2008). One-Step, Room Temperature, Colorimetric Detection of Mercury (Hg2+) Using DNA/Nanoparticle Conjugates. Journal of the American Chemical Society, 130(11), 3244-3245.
309. Yallapu, M.M., Jaggi, M., & Chauhan, S.C. (2010). β-Cyclodextrin-curcumin self-assembly enhances curcumin delivery in prostate cancer cells. Colloids and Surfaces B: Biointerfaces, 79(1), 113-125.
310. Yan, L., Cai, Y., Zheng, B., Yuan, H., Guo, Y., Xiao, D., & Choi, M.M. (2012). Microwave-assisted synthesis of BSA-stabilized and HSA-protected gold nanoclusters with red emission. Journal of Materials Chemistry, 22(3), 1000-1005.
311. Yang, G., Zhang, H., Wang, Y., Liu, X., Luo, Z., & Yao, J. (2017). Enhanced stability and fluorescence of mixed-proteins-protected gold/silver clusters used for mercury ions detection. Sensors and Actuators B: Chemical, 251, 773-780.
312. Yang, H., Yang, S., Kong, J., Dong, A., & Yu, S. (2015). Obtaining information about protein secondary structures in aqueous solution using Fourier transform IR spectroscopy. [Protocol]. Nat. Protocols, 10(3), 382-396.
313. Yang, K., Wang, S., Wang, Y., Miao, H., & Yang, X. (2017). Dual-channel probe of carbon dots cooperating with gold nanoclusters employed for assaying multiple targets. Biosensors and Bioelectronics, 91, 566-573.
314. Yang, W., Guo, W., Chang, J., & Zhang, B. (2017). Protein/peptide-templated biomimetic synthesis of inorganic nanoparticles for biomedical applications. [10.1039/C6TB02308H]. Journal of Materials Chemistry B, 5(3), 401-417.

315. Yoo, E.-H., & Lee, S.-Y. (2010). Glucose biosensors: an overview of use in clinical practice. Sensors (Basel, Switzerland), 10(5), 4558-4576.
316. You, Q., Sun, Q., Yu, M., Wang, J., Wang, S., Liu, L., Cheng, Y., Wang, Y., Song, Y., Tan, F., & Li, N. (2017). BSA–Bioinspired Gadolinium Hybrid-Functionalized Hollow Gold Nanoshells for NIRF/PA/CT/MR Quadmodal Diagnostic Imaging-Guided Photothermal/Photodynamic Cancer Therapy. ACS Applied Materials & Interfaces, 9(46), 40017-40030.
317. Yu, P., Wen, X., Toh, Y.-R., Ma, X., & Tang, J. (2015). Fluorescent Metallic Nanoclusters: Electron Dynamics, Structure, and Applications. Particle & Particle Systems Characterization, 32(2), 142-163.
318. Yu, Y., Geng, J., Ong, E.Y.X., Chellappan, V., & Tan, Y.N. (2016). Bovine Serum Albulmin Protein-Templated Silver Nanocluster (BSA-Ag13): An Effective Singlet Oxygen Generator for Photodynamic Cancer Therapy. Advanced Healthcare Materials, 5(19), 2528-2535.
319. Yu, Y., Luo, Z., Teo, C.S., Tan, Y.N., & Xie, J. (2013). Tailoring the protein conformation to synthesize different-sized gold nanoclusters. Chemical Communications, 49(84), 9740-9742.
320. Yuan, X., Dou, X., Zheng, K., & Xie, J. (2015). Recent Advances in the Synthesis and Applications of Ultrasmall Bimetallic Nanoclusters. Particle & Particle Systems Characterization, 32(6), 613-629.
321. Yuan, Z., Peng, M., Shi, L., Du, Y., Cai, N., He, Y., Chang, H.-T., & Yeung, E.S. (2013). Disassembly mediated fluorescence recovery of gold nanodots for selective sulfide sensing. [10.1039/C2NR33202G]. Nanoscale, 5(11), 4683-4686.
322. Yue, Q., Sun, L., Shen, T., Gu, X., Zhang, S., & Liu, J. (2013). Synthesis of Fluorescent Gold Nanoclusters Directed by Bovine Serum Albumin and Application for Nitrite Detection. Journal of Fluorescence, 1-6.
323. Yue, Y., Liu, T.-Y., Li, H.-W., Liu, Z., & Wu, Y. (2012a). Microwave-assisted synthesis of BSA-protected small gold nanoclusters and their fluorescence-enhanced sensing of silver (I) ions. Nanoscale, 4(7), 2251-2254.

324. Zhai, Q., Xing, H., Fan, D., Zhang, X., Li, J., & Wang, E. (2018). Gold-silver bimetallic nanoclusters with enhanced fluorescence for highly selective and sensitive detection of glutathione. Sensors and Actuators B: Chemical, 273, 1827-1832.
325. Zhang, F., Koh, G.Y., Jeansonne, D.P., Hollingsworth, J., Russo, P.S., Vicente, G., Stout, R.W., & Liu, Z. (2011). A Novel Solubility-Enhanced Curcumin Formulation Showing Stability and Maintenance of Anticancer Activity. Journal of Pharmaceutical Sciences, 100(7), 2778-2789.
326. Zhang, J., Chen, C., Xu, X., Wang, X., & Yang, X. (2013). Use of fluorescent gold nanoclusters for the construction of a NAND logic gate for nitrite. [10.1039/C3CC38298B]. Chem. Commun., 49(26), 2691-2693.
327. Zhang, J.R., Yue, Y.Y., Luo, H.Q., & Li, N.B. (2016). Supersensitive and selective detection of picric acid explosive by fluorescent Ag nanoclusters. Analyst, 141(3), 1091-1097.
328. Zhang, J.R., Zeng, A.L., Luo, H.Q., & Li, N.B. (2016). Fluorescent silver nanoclusters for ultrasensitive determination of chromium (VI) in aqueous solution. Journal of hazardous materials, 304, 66-72.
329. Zhang, K., Yu, T., Liu, F., Sun, M., Yu, H., Liu, B., Zhang, Z., Jiang, H., & Wang, S. (2014). Selective Fluorescence Turn-On and Ratiometric Detection of Organophosphate Using Dual-Emitting Mn-Doped ZnS Nanocrystal Probe. Analytical Chemistry, 86(23), 11727-11733.
330. Zhang, L., Qv, S., Wang, Z., & Cheng, J. (2003). Determination of dopamine in single rat pheochromocytoma cell by capillary electrophoresis with amperometric detection. Journal of Chromatography B, 792(2), 381-385.
331. Zhang, L., Wang, D., Huang, H., Liu, L., Zhou, Y., Xia, X., Deng, K., & Liu, X. (2016). Preparation of Gold–Carbon Dots and Ratiometric Fluorescence Cellular Imaging. ACS Applied Materials & Interfaces, 8(10), 6646-6655.
332. Zhang, L., & Wang, E. (2014). Metal nanoclusters: New fluorescent probes for sensors and bioimaging. Nano Today, 9(1), 132-157.

333. Zhang, L., Zhu, J., Guo, S., Li, T., Li, J., & Wang, E. (2013). Photoinduced electron transfer of DNA/Ag nanoclusters modulated by G-quadruplex/hemin complex for the construction of versatile biosensors. Journal of the American Chemical Society, 135(7), 2403-2406.
334. Zhang, X., Wu, F.-G., Liu, P., Wang, H.-Y., Gu, N., & Chen, Z. (2015). Synthesis of ultrastable and multifunctional gold nanoclusters with enhanced fluorescence and potential anticancer drug delivery application. Journal of Colloid and Interface Science, 455, 6-15.
335. Zhang, Y., Jiang, H., & Wang, X. (2015). Cytidine-stabilized gold nanocluster as a fluorescence turn-on and turn-off probe for dual functional detection of Ag+ and Hg2+. Analytica Chimica Acta, 870, 1-7.
336. Zhang, Y., Jiang, J., Li, M., Gao, P., Shi, L., Zhang, G., Dong, C., & Shuang, S. (2017). Bright far-red/near-infrared gold nanoclusters for highly selective and ultra-sensitive detection of Hg2+. Sensors and Actuators B: Chemical, 238, 683-692.
337. Zhang, Z., Sun, W., & Wu, P. (2015). Highly photoluminescent carbon dots derived from egg white: facile and green synthesis, photoluminescence properties, and multiple applications. ACS Sustainable Chemistry & Engineering, 3(7), 1412-1418.
338. Zhao, J., Huang, M., Zhang, L., Zou, M., Chen, D., Huang, Y., & Zhao, S. (2017). Unique Approach To Develop Carbon Dot-Based Nanohybrid Near-Infrared Ratiometric Fluorescent Sensor for the Detection of Mercury Ions. Analytical Chemistry, 89(15), 8044-8049.
339. Zheng, B., Zheng, J., Yu, T., Sang, A., Du, J., Guo, Y., Xiao, D., & Choi, M.M. (2015). Fast microwave-assisted synthesis of AuAg bimetallic nanoclusters with strong yellow emission and their response to mercury (II) ions. Sensors and Actuators B: Chemical, 221, 386-392.
340. Zheng, J., Nicovich, P.R., & Dickson, R.M. (2007). Highly fluorescent noble-metal quantum dots. Annu. Rev. Phys. Chem., 58, 409-431.
341. Zheng, J., Payne, K., Taggart, J.E., Jiang, H., Lind, S.E., & Ding, W.Q. (2012). Trolox enhances curcumin's cytotoxicity through induction of oxidative stress. Cell Physiol Biochem, 29(3-4), 353-360.

342. Zheng, J., Zhang, C., & Dickson, R.M. (2004). Highly fluorescent, water-soluble, size-tunable gold quantum dots. Physical Review Letters, 93(7), 077402.
343. Zheng, Y., Lai, L., Liu, W., Jiang, H., & Wang, X. (2017). Recent advances in biomedical applications of fluorescent gold nanoclusters. Advances in Colloid and Interface Science, 242, 1-16.
344. Zhong, G., Liu, J., & Liu, X. (2015). A fast colourimetric assay for lead detection using label-free gold nanoparticles (AuNPs). Micromachines, 6(4), 462-472.
345. Zhou, F., Feng, B., Yu, H., Wang, D., Wang, T., Liu, J., Meng, Q., Wang, S., Zhang, P., Zhang, Z., & Li, Y. (2016). Cisplatin Prodrug-Conjugated Gold Nanocluster for Fluorescence Imaging and Targeted Therapy of the Breast Cancer. Theranostics, 6(5), 679-687.
346. Zhou, Q., Lin, Y., Xu, M., Gao, Z., Yang, H., & Tang, D. (2016). Facile Synthesis of Enhanced Fluorescent Gold–Silver Bimetallic Nanocluster and Its Application for Highly Sensitive Detection of Inorganic Pyrophosphatase Activity. Analytical Chemistry, 88(17), 8886-8892.
347. Zhou, T.-y., Lin, L.-p., Rong, M.-c., Jiang, Y.-q., & Chen, X. (2013). Silver–Gold Alloy Nanoclusters as a Fluorescence-Enhanced Probe for Aluminum Ion Sensing. Analytical Chemistry, 85(20), 9839-9844.
348. Zhou, W., Cao, Y., Sui, D., Guan, W., Lu, C., & Xie, J. (2016). Ultrastable BSA-capped gold nanoclusters with a polymer-like shielding layer against reactive oxygen species in living cells. [10.1039/C6NR02178F]. Nanoscale, 8(18), 9614-9620.
349. Zhou, Z., Zhang, C., Qian, Q., Ma, J., Huang, P., zhang, X., Pan, L., Gao, G., Fu, H., Fu, S., Song, H., Zhi, X., Ni, J., & Cui, D. (2013). Folic acid-conjugated silica capped gold nanoclusters for targeted fluorescence/X-ray computed tomography imaging. Journal of Nanobiotechnology, 11(1), 17.

LIST OF PUBLICATIONS

Publication based on thesis

1. Meegle S. Mathew, Ananya Baksi, T. Pradeep and Kuruvilla Joseph (2016), Choline-induced Selective Fluorescence Quenching of Acetylcholinesterase Conjugated Au@BSA Clusters. ***Biosensors and Bioelectronics***, 8168–74
2. Meegle S. Mathew and Kuruvilla Joseph (2017), Green Synthesis of Gluten-Stabilized Fluorescent Gold Quantum Clusters: Application As Turn-On Sensing of Human Blood Creatinine; ***ACS Sustainable Chem. Eng***., 5 (6), 4837–4845.
3. Meegle S. Mathew, Joyal Davis, and Kuruvilla Joseph (2018), Green Synthesis of Plant-Derived Protein Protected Copper Quantum Cluster for Intrauterine Device Application, ***Analyst,*** 2018, 143, 3841–3849
4. Meegle S. Mathew, Kiran.S and Kuruvilla Joseph (2018), Graphene Carbon Dot (GQD) Assisted Fast Synthesis of Gold Quantum Cluster in a Protein for Bio-Friendly Near White Light Emitting Material and Ratiometric Sensing of Mercury (Hg2+), ***ChemistrySelect,*** 3, 9545-9554.
5. Meegle S. Mathew, Anoop Philip and Kuruvilla Joseph, Wheat gluten directed synthesis and probing electron transfer and Inner Filter Effects in AgAuQC for bilirubin detection, *Particle and Particle System Characterisation* (Communicated)
6. Meegle S. Mathew, Kavya Vinod, and Kuruvilla Joseph, the Improved bioavailability of curcumin in Gliadin Protected Gold Quantum Cluster (AuQC@gliadin): Delivery, Imaging and Anticancer Applications, ACS Sustainable Chemistry and Engineering (Under revision, ACS Omega).

Other publications

1. Meegle S. Mathew, K. Sreenivasan and Kuruvilla Joseph (2015), Hydrogen-bond assisted aggregation-induced emission of digitonin. *RSC Adv*.5, 5, 100176–100183

Patent

1. Meegle S Mathew and Kuruvilla Joseph, "Novel biosensor for the detection of creatinine, Indian Patent (Patent File No. 201741000489).

Awards/honours

1. Awarded best poster award for the presentation of poster entitled "Facile Synthesis of Protein Protected Luminescent Noble Metal Quantum Clusters for Biomedical Applications' in *International conference on recent trends in material science and technology* (ICMST 2018)October 10-13

CONFERENCES/SEMINARS

Oral presentation

1. Meegle S. Mathew and Kuruvilla Joseph, Choline induced selective fluorescence quenching of Acetylcholinesterase conjugated Au@BSA quantum clusters" *International Symposium on Photonics Applications and Nanomaterials (ISPAN-2015),* Thiruvananthapuram.
2. Meegle S. Mathew and Kuruvilla Joseph, "Fluorescent nanomaterial for Biosensing", *National Meeting of Material Research Society (MRSI),* Trivandrum Chapter, March 2016.
3. Meegle S. Mathew and Kuruvilla Joseph, "Facile Synthesis of Protein Protected Fluorescent Metal Quantum Cluster for Use as Sensing Probes and Drug Delivery Vehicle" International Conference on Optoelectronic and Nano Material for Advanced Technology, at CUSAT 2nd January 2019.

Poster presentations

1. Meegle S. Mathew and Kuruvilla Joseph, Choline induced selective fluorescence quenching of Acetylcholinesterase conjugated Au@BSA quantum clusters" in *International Symposium on Clusters, Cluster-*

Assemblies, and Nanomaterials (ISCAN 2016) IISER, Thiruvananthapuram.

2. Meegle S. Mathew and Kuruvilla Joseph, pH assisted aggregation-induced emission (AIE) of digitonin" in *National Conference on Material Science and Technology (NCMST 2016),* IIST, Thiruvananthapuram on July 12 – 14, 2016.
3. Meegle S. Mathew and Kuruvilla Joseph, Protein Stabilized Fluorescent Gold Quantum clusters for Turn-on Sensing of Human Blood Creatinine in *IUMRS ICYRAM 2016*" IISC, Bangalore.
4. Meegle S. Mathew and Kuruvilla Joseph, Plant Protein Directed Synthesis Luminescent Noble Metal Quantum Clusters and Their Application in Biosensors" *International Conference on Nanomaterials and Their Applications,* University of Mysore, Mysore on March 1-2, 2018.
5. Meegle S. Mathew and Kuruvilla Joseph, Facile Synthesis of Protein Protected Luminescent Noble Metal Quantum Clusters for Biomedical Applications, *International Conference on Recent Trends in Material Science and Technology* (ICMST 2018)October 10-13

Attended conferences

1. Participated in *National Conference on recent trends in material science and technology (NCMST-14)* organised by Department of Chemistry, Indian Institute of Space Science and Technology, *Thiruvanthapuram, July 28th-30*
2. *Participated IIST Research Scholars Day organised by* organised by Department of Chemistry, Indian Institute of Space Science and Technology, *Thiruvanthapuram December 16-17, 2013*